Globular clusters as probes of galaxy formation

Beasley, Michael Andrew

Globular Clusters as Probes of Galaxy Formation

Michael Andrew Beasley

A thesis submitted to the University of Durham
in accordance with the regulations for
admittance to the Degree of Doctor of Philosophy.

Department of Physics
University of Durham
January 19, 2001

'...as observations have accumulated, the subject has become, to my mind at least, more mysterious and more inapproachable.'

William Parsons, Third Earl of Rosse

Abstract

Globular Clusters as Probes of Galaxy Formation

by Michael Andrew Beasley

Observations and analysis of globular cluster systems associated with three galaxy types are presented.

Spectroscopy of globular cluster (GC) candidates in the Sculptor spirals NGC 253 and NGC 55 has identified 15 GCs in these galaxies. This spectroscopic sample, combined with plate scans, indicates total GC populations consistent with that expected for their luminosity and morphological type. From these data, we define new GC samples for spectroscopy.

Radial velocities of 87 GCs in the Virgo elliptical NGC 4472 have been obtained, yielding data for 144 GCs when combined with previous studies. We find the blue GCs have significantly higher velocity dispersion than the red GCs, with little rotation in either population. The GCs dispersion profile declines slowly, yielding mass profiles consistent with X-ray data. We find a steeply rising $\mathcal{M}/L$ ratio, indicative of a massive dark halo surrounding this galaxy. From line-strengths of the GCs, we derive ages and metallicities for the GCs using simple stellar population (SSP) models. We find that the GCs are old and coeval and the bimodality seen in their colours reflects metallicity rather than age differences. The GCs exhibit solar abundance ratios, and both subpopulations show evidence for radial metallicity gradients.

We have obtained high S/N spectra for 64 star clusters in the Large Magellanic Cloud. We measure their Lick indices to test the age and metallicity calibration of SSP models by comparison with literature values. We find our metallicities are consistent, although the values from our integrated spectra are slightly higher. The agreement of the ages for the old GCs is good, but is somewhat poorer for the youngest clusters. We obtain an age-metallicity relation for the clusters consistent with the galaxy's field stars.

We show first results of a project to investigate the age and metallicity distributions of globular cluster systems using semi-analytic models of galaxy formation.

Declaration

The research undertaken in this thesis was performed during the period 1997–2000 whilst the author was a research student under the supervision of Dr Ray Sharples in the Department of Physics at the University of Durham. This work has not been submitted for any other degree at the University of Durham or at any other University. The work shown in this thesis is entirely my own with the following exceptions : Chapter 2.0 was undertaken with Dr. Ray Sharples. Chapter 3 represents the results of a project initiated in 1996 in collaboration with Ray Sharples, Terry Bridges, Steve Zepf, Doug Geisler, Keith Ashman and Dave Hanes. The semi-analytic results in Chapter 5 are very much an ongoing project, and would not have been possible without the work of Carlton Baugh.

Much of the material in Chapters 2 and 3 has appeared in the following publications:

- Beasley M.A., Sharples R.M., 2000, MNRAS, 331, 673
- Beasley M.A., Sharples R.M., Bridges T.J., Hanes, D.A., Zepf, S.E., Ashman, K.M., 2000, MNRAS, 318, 1249
- Stephen E. Zepf, Michael A. Beasley, Terry J. Bridges, David A. Hanes, Ray M. Sharples, Keith M. Ashman, Doug Geisler, 2000 AJ, in press

To my Mum and Dad

Acknowledgements

The PhD process is not simply an academic work, but rather like being set adrift on a raft in the ocean. Without the tremendous support of mermen and mermaids (well, friends, family and colleagues), I'd be amazed if anyone ever finished, er ever.

The person I have to thank most is Ray Sharples, my supervisor. If he hadn't told me to stop being silly the night before I went out for my first observing run in Hawaii, I wouldn't have made it to my second year. I am also indebted to two people at LJMU without whom I'd never have started a PhD, Phil James and Tim O'Brien.

On the science front, I must also thank my collaborators, Terry Bridges, Dave Hanes (I remember the jelly worms), Doug Geisler, Keith Ashman and Steve Zepf. Also thanks to Harald for his vast knowledge of spectroscopic things, Alex for his endless enthusiasm, and to Carlton who works very hard.

Hi and thanks to the people who have gone on to do even bigger and better stuff; Fiona–I miss your *joi de vive*, Andrew (well I always new you'd do well), Scott Kay (printer repair expertise), SJH (for his dodgy jacket), Steve Burby, DJ Simon Shaw, and Seb. Thanks to people in the department who provide entertainment; Geoff, Rich, Dave, Kev, Dijana, Infra-Red Peder Norberg, Carlos (nice $mole$), Graham $\times$ 2, Mike^2, Joy, Sam, Harald, Chris, Pat and Fraser. To Dan & Ade I say 'pies' and thanks for the moral support. To the mountain bikers Davey, Michael, Ian...., why did *I* always eat the mud??

James and Louisa deserve special mention; James for his fantastic curries and punctuality, Louisa for broadening certain horizons.

There's not enough space here to thank my Mum and Dad properly, so I'll just say 'thanks'. Mum, keep acting, politicking and smiling, Dad - keep flying those planes! Also, a BIG thanks to my long-suffering brothers Gareth and David and also to Jitka for putting up with the rest of the family.

Oh, and Amaya, *mas caramelos por favor.*

Contents

List of Figures

List of Tables

Chapter 1

Introduction

Abstract. Globular clusters are massive, roughly spherical, gravitationally bound aggregates of stars. They provide important insights into many branches of astronomy, and have played a pivotal rôle in areas as diverse as aiding our understanding of the size and shape of the Galaxy, to placing lower limits on the age of the Universe. In the form of globular cluster systems, they are inextricably linked with the formation of their host galaxies. Their colour, spatial and number distributions, kinematics and line-strengths all yield unique insights into the dynamical, temporal and chemical state of the galaxy with which they are associated. In this introduction, we discuss the principle characteristics of globular clusters as single entities, and as entire globular cluster systems. We then look at the information which can be obtained from observations of globular cluster systems, in the context of the formation and evolution of their host galaxies.

1.1 Preamble

Palaeontologists have long recognised the importance of the fossil record in aiding our understanding of the Earth's biological history. Indeed, the discovery of Iguanadon[1] teeth at a site in Cuckfield, Sussex, in 1822 lead to the recognition that previously unknown giant reptiles, *dinosaurs*, had once walked the planet. It is not only the characteristics of such fossils which have provided us with insights into our past, but also their location with respect to one another in the earth, the fossil record.

In astronomy, perhaps the closest analogy to terrestrial fossils are globular clusters (GCs), and to the fossil record are globular cluster systems (GCS). By looking back at these ancient swarms of hundreds of thousands (sometimes millions) of stars clustered about their parent galaxy, we look back to a time when the galaxies were young. Detailed analysis of GCs and their systems; their sizes, shapes, colours and dynamics, provide us with powerful insights into the formation, and subsequent evolution of their host galaxies.

[1] Literally 'lizard tooth'

For the nearest GCs, such as one of the 147 known in the Milky Way, individual stars can now be detected down to the very faintest limits. By plotting the colours of these stars against magnitude yields what is essentially a one-parameter sequence, a Hertzsprung-Russell (HR) diagram. Careful comparison of such a diagram to theoretical models has lead to a detailed knowledge of many aspects of the various stages of stellar evolution. However, the HR diagram provides much more information than these important insights into the physics of stars. Reaching past the main-sequence turn-off in the HR diagram leads to age estimates for GCs and hence to some of the strongest lower limits on the age of the Universe. These limits, derived for the oldest galactic GCs, have traditionally been the benchmark against which cosmological models have been tested.

Globular cluster *systems* are known to be associated with all bright galaxies, and many dwarfs; they number from a few to tens of thousands. For the very nearest galaxies, individual GCs may be resolved, and the entire GCS may subtend several degrees on the sky. For more distant galaxies, such as the nearest giant ellipticals, the brightest GCs appear point-like on ground-based images, generally detected as a statistical excess above the background level. From space, these clusters may be marginally resolved, and their physical dimensions can be measured. Significant numbers of globular clusters have now been imaged using Hubble Space Telescope (*HST*) out to Coma ($\sim$ 100 Mpc) and with surface brightness fluctuation measurements, GCs have been detected out to redshifts of $z \sim 0.066$, to date the most distant GCS known (Blakeslee, Tonry, & Metzger 1997).[2]

To first order, several properties of GCS are known to correlate with the mass of their host galaxies, such as mean colour and absolute number. Therefore, the integrated properties of GCS yield insights not only into their own dynamical and chemical evolution, but also for that of their host galaxies. Moreover, some properties of GCS seem to be constant from one galaxy to another, such as the brightness of the turn-over in the globular cluster luminosity function (GCLF). If the GCLF is truly universal, then providing that the turn-over can be reached it presents itself as a standard candle, an independent approach to estimating the distance scale of the Universe (see Harris 1999 for a thorough review).

In this Chapter, we begin by looking at the principle characteristics of globular clusters as individual stellar systems. Then, in Section 1.3, we proceed to examine the properties of GCS,

[2] Elson, Santiago, & Gilmore (1996) performed a survey of all the unresolved objects in the Hubble deep field north with $I \leq 28$. They identified 11 GC candidates possibly associated with an elliptical galaxy at $z \sim 0.16$, which would make them by far the most distant GCs detected. However, the true identity of these objects, and the redshift of their parent galaxy, have yet to be confirmed.

and look at the correlations between GCS and host galaxy in Section 1.4. Finally, in Section 1.5, we outline the structure and goals of this thesis.

1.2 What is a Globular Cluster?

The GCs for which we have the most extensive information upon are those within our own Galaxy. Until recently, most of our knowledge about these systems was based upon observations taken from this single sample. However, in the past few years increasingly detailed studies have been undertaken for nearby extragalactic GCs, such as for those in Large Magellanic Cloud (e.g. Mighell et al. 1996; Johnson & Bolte 1996; Geisler et al. 1997; Olsen et al. 1998), the Small Magellanic Cloud (e.g. Shara et al. 1998), the Fornax dwarf spheroidal (Buonanno et al. 1998, Buonanno et al. 1999), the WLM galaxy (Hodge et al. 1999), M 31 (Ajhar, Blakeslee, & Tonry 1994; Pecci et al. 1996; Holland 1998), M 33 (Sarajedini et al. 1998) and Centaurus A (Harris, Poole, & Harris 1998). All these studies have shown that these GCs exhibit dynamical, structural and chemical properties very similar to GCs in the Milky Way.

1.2.1 Physical Characteristics

Classically, GCs are metal-poor and old, gravitationally bound systems of 'population-II' stars. They are chemically homogeneous and coeval, effectively the embodiment of the idealized 'simple stellar population'. Being population-II systems, they contain no dust, gas or young stars, whilst dynamical studies indicate that they contain little or no dark matter, with mass-to-light ratios ($\mathcal{M}/L_V$) of typically $\sim$ 2 (Heggie & Hut 1996). GCs in the Galaxy show a wide variation in luminosity (and hence mass), from the faint AM 4 with M_V = -1.50 (M $\leq 10^3$ $M_\odot$), to the massive ω Cen with M_V = -10.2 (M $\sim 5 \times 10^6$ $M_\odot$). In Figure 1.1, we show an image of the well-studied metal-poor Galactic GC M 92, taken from the Digitized Sky Survey (DSS).

Typically, stellar densities in the centres of globular clusters are $\sim 10^4$ $M_\odot$ pc^{-3}, much higher than those of open (population I) clusters which typically have $\rho_o \sim 10^2$ $M_\odot$ pc^{-3}. Because GCs are not uniformly spherical systems, and are actually rather inhomogeneous in shape, several empirical parameters are commonly employed in order to describe their physical dimensions. The *core radius* (r_c) is the radius at which the central surface brightness of the GC has dropped by half; the *half-light radius* (r_h) is the radius at which half the total light of the cluster is enclosed and the *tidal*, or *limiting* radius (r_t) is the point where the density of the cluster falls to zero - stars

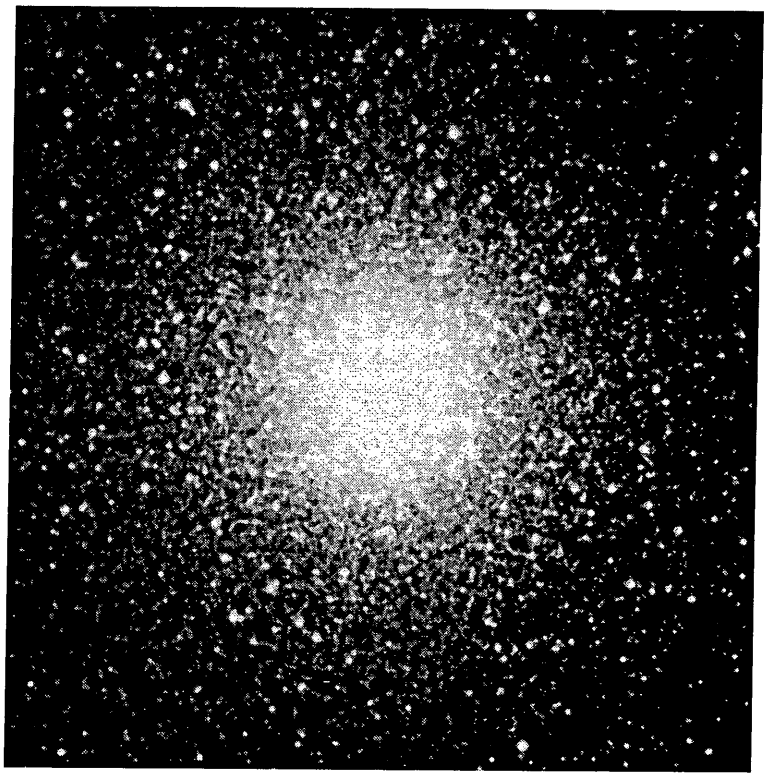

Figure 1.1: DSS image of M 92, one of the most metal-poor globular clusters known with [Fe/H] $\sim$ -2.3. The compact nature and spherical symmetry of the GC is clear. The image is approximately 10′× 10′.

are no longer bound to the GC. Median values of these radii for Milky Way GCs are: $r_c \sim 1.5$ pc, $r_h \sim 10$ pc and $r_t \sim 50$ pc respectively (Peterson & King 1975).

Whilst they appear essentially spherical, the Milky Way GCs are actually somewhat flattened, with a mean minor-to-major axis ratio ($\bar{\epsilon}$) of $\sim$0.93 (White & Shawl 1987). Interestingly, the GCs in the LMC appear even more flattened than their Galactic counterparts, with $\bar{\epsilon} = 0.85$. Frenk & Fall (1982) proposed that this was due to an ellipticity-age relation, in the sense that as the clusters age, they become more spherical. Recently, however, Goodwin (1997) has argued that the difference in ellipticities are probably due to the weaker tidal field of the LMC, in that it is unable to significantly alter the clusters *intrinsic* ellipticity.

1.2.2 Metallicities of Globular Clusters

The metallicities of GCs are traditionally measured as the abundance of iron to hydrogen, with respect to the solar value:

$$[\mathrm{Fe/H}] = \log_{10}\left(\frac{\mathrm{Fe}}{\mathrm{H}}\right)_{\mathrm{GC}} - \log_{10}\left(\frac{\mathrm{Fe}}{\mathrm{H}}\right)_{\odot} \tag{1.1}$$

All the other elements, the 'metals', are assumed to behave in a similar fashion to iron. However, it has become increasingly clear that using a single parameter, [Fe/H], to measure GC metallicity is an oversimplification. High resolution studies employing fine analysis and/or spectral synthesis indicate that abundance ratios of individual elements vary significantly, independent of [Fe/H] (see R. Gratton in Martinez-Roger, Perez-Fournon, & Sanchez 1999 for a good review). A striking example is the oxygen abundance in GCs, which typically have [O/Fe] $\sim$ 0.4. Such an enhancement in the α-elements is generally explained by the excess production of α-nuclides in the supernovae of massive stars, indicating that the GCs in the Galaxy must have formed early in order to have been enriched to an observable level. However, despite these obvious variations, GCs are generally considered to be chemically homogeneous.[3].

For faint, unresolved GCs (essentially those outside the Local Group), high-resolution metallicity determinations can no longer be performed, and *integrated* parameters must be measured, taking the form of either broad-band colours, or low-resolution spectral indices such as those defined by the Lick group (e.g. Trager et al. 1998 and references therein). However, there are significant uncertainties implicit in deriving metallicities using such integrated techniques, which are discussed further in § 1.3.3.

1.2.3 The Hertzsprung-Russell Diagram

Independently developed by E. Hertzsprung and H.N. Russell in 1911, the HR diagram was perhaps the single most important advance in our understanding of stellar evolution. Originally shown as stellar (absolute) magnitude against spectral type, it now generally takes the form of magnitude against colour index or, in the theoretical plane, luminosity against effective temperature. Since GCs are coeval, such a diagram effectively shows a snapshot of stellar evolution in the cluster, where the position of any star in the diagram is largely determined by its mass. In Figure 1.2 we show the colour-magnitude diagram (CMD) of NGC 6205 (M 13), a Galactic GC approximately 7 Kpc distant.

The principle features of the CMD play important parts in both stellar evolution studies and cosmology. For example, the RR Lyrae variables provide accurate distance measurements for

[3] The most massive GC in the Galaxy, ω Cen, shows significant inhomogeneities in its heavy elements. It has been argued that due to the mass and low central concentration of this cluster, it may have undergone significant self-enrichment (Trager, King, & Djorgovski 1995) Also, Langer et al. (1998) have recently found that giant stars in M 92 also show abundance differences of $\sim$ 0.1 dex, which they attribute to a proto-cluster ISM which was not well-mixed.

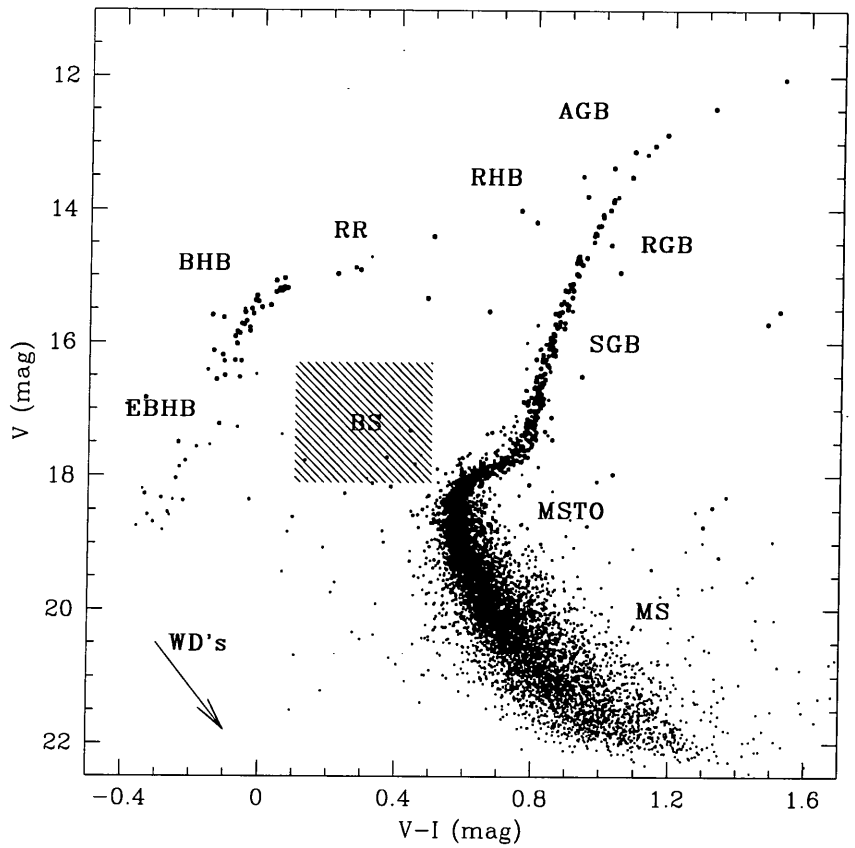

Figure 1.2: A colour-magnitude diagram of NGC 6205 (M 13), which has a metallicity of -1.6 (Zinn 1985). The CMD of M 13 is notable in that it has an extremely extended blue horizontal branch (EBHB), but little or no red horizontal branch. These data were obtained with the 1.5-m Nordic telescope and was kindly supplied by A.R.Gonzaléz. All points shown have $\sigma_{V-I} \leq 0.1$ mag, and their sizes are roughly inversely proportional to the photometric errors.

Galactic GCs, allowing their physical parameters to be accurately assessed (e.g. Vandenberg, Stetson, & Bolte 1996). Moreover, the RR Lyraes in Magellanic Cloud GCs provide distances supplemental to those derived from other sources, such as Cepheids and RGB-tip methods, a vital step on the cosmic distance ladder (e.g. Walker 1992).

However, with regards to determining ages for GCs, the most important regions in the CMD are the main sequence (MS), the subgiant branch (SGB) and the horizontal branch (HB). The MS stretches from the hydrogen burning limit ($M_H \sim 0.08\ M_\odot$) to the MSTO, and its locus is determined principly by the metallicity of the cluster. Metal-rich GCs have a redder MS than their metal-poor cousins, although other physical processes also effect the precise location of the MS, of which perhaps the most important is diffusion (e.g. Castellani & degl'Innocenti 1999; Salaris, Groenewegen, & Weiss 2000).

From the CMD, ages may be derived directly from the observed position of the MSTO, which is determined by the stellar mass at the turnoff and cluster metallicity. An extension of this is to fit isochrones (lines of constant age) to the MSTO and subgiant branch (SGB) simultaneously, which yields an age for the cluster whilst leaving the distance modulus to the cluster as a free parameter. Other age estimates rely on either a comparison between the luminosity of the MSTO and the horizontal-branch (HB), or between the colour of the MSTO and the SGB. Whilst these two latter techniques have the principle advantage in that they yield distance-independent age estimates, it is important to recognise that all the above methods are affected by uncertainties in the input physics of stellar evolution models (e.g. Buonanno et al. 1998; Freytag & Salaris 1999; Salaris, Groenewegen, & Weiss 2000).

In integrated spectra, the Balmer lines are sensitive to the temperature (and hence mass and age) of stars on the MSTO. For a given metallicity, the strength of these indices decrease with increasing age. It has often been assumed that besides metallicity, the temperature of MSTO is the only significant contributer to Balmer line-strengths and is therefore an accurate probe of age in simple stellar populations. However, many workers have a questioned this assumption since a significantly brighter, although much less numerous population of stars exist on the HB of GCs (e.g. Rabin 1983; Burstein et al. 1984; Fisher, Franx, & Illingworth 1995).

The morphologies of GC HBs are determined by several parameters, the 'first' of which is metallicity; as metallicity decreases, HBs generally become bluer. Unfortunately, this is a non-monotonic relation, several Galactic GCs have similar metallicities but very different HB morphologies. This 'second parameter effect', first noticed by Sandage & Wallerstein in 1960, is now generally attributed to age differences (e.g. Bolte 1989; Dickens et al. 1991; Buonanno 1993). However, even a combination of metallicity and age variations does not explain the entire range of observed HB morphologies, and other physical effects such as mass-loss on the RGB and variations in He abundance have been cited (e.g. Catelan & de Freitas Pacheco 1993).

So, whilst the temperature of the MSTO decreases with age, resulting in weaker Balmer lines, variations in HB morphology lead to uncertain contributions to these same indices. Whilst these effects are of little significance for stellar populations with [Fe/H] $>$ -0.5, which have HBs which are 'red clumps', the majority of Galactic (and extragalactic) GCs are more metal-poor than this. Needless to say, this is still an active area of research, particularly with regards to constructing stellar population models for integrated indices (e.g. Bressan, Chiosi, & Tantalo 1996; Jorgensen 1997; Lee, Yoon, & Lee 2000; Maraston & Thomas 2000).

1.3 Globular Cluster Systems

1.3.1 Historical Background

Whilst GCs had been identified in the Magellanic Clouds by Shapley several years earlier, the study of extragalactic globular cluster systems did not begin in earnest until the work of Edwin Hubble in 1932. Using the 100-inch telescope at Mount Wilson, he identified 140 objects associated with the Andromeda galaxy (M 31) for which he stated *"...from their forms, structure, colours, luminosities and dimensions they are provisionally identified as globular clusters."* From the spectrum of "object No. 62", he derived a radial velocity of -210 $\pm$ 100 km s^{-1}, consistent with the radial velocity of M 31, thereby reinforcing the notion that the clusters were associated with the galaxy, and not seen in projection (or indeed were background galaxies). He found that the M 31 GCLF peaked at $\sim$ 1.5 magnitudes fainter than that of the Galactic globular clusters, although he did note that the absolute ranges in luminosity were essentially very similar. It was later discovered that Hubble's derivation of the distance to M 31, based on Shapley's calibration of Cepheids, was too small by a factor of 2 due to the (then unknown) effects of reddening, and therefore his observed M 31 globulars actually had intrinsic luminosities identical to their Galactic counterparts.[4] This was the first evidence of the existence of a substantial extragalactic GCS.

Evidence for GCS in early-type galaxies was more controversial, and was first suggested by Baum (1955). From deep exposure photographic plates of M 87, the central cD in the Virgo cluster, he identified numerous star-like objects and stated *"...it* [M 87] *possesses a very large number of globular clusters-more than a thousand of them..."* [5] Racine (1968) proceeded to obtain colours and magnitudes for 360 GC candidates associated with this galaxy, measured from 200-inch plates. From comparison with the GCs which had been identified in the Galaxy, M 31 and the Large Magellanic Cloud, he concluded that their colours were consistent (although slightly redder) than the known GCs in other galaxies. Increasingly more detailed analyses of the M 87 GCS was subsequently performed by Ables, Newell, & O'Neil (1974) and Harris & Smith (1976), whilst Smith & Weedmann (1976) had just detected GC candidates around the gE in the Hydra cluster, NGC 3311, from deep B-band exposures.

As extragalactic GCS research gathered pace, in a pioneering study in 1976, Hanes analysed the luminosity distributions of GCs in 20 galaxies in Virgo, covering a variety of morphological types.

[4] In the same paper, he also provisionally identified GCs associated with NGC 6822, M 33, M 81 and M 101.

[5] M 87 is now thought to host 13000 $\pm$ 500 GCs (McLaughlin, Harris, & Hanes 1994).

In a series of papers (Hanes 1976; 1977a; 1977b; 1979) he showed that the position of the peak of the GCLF was essentially universal and independent of host galaxy morphology, a phenomenon suggested by previous studies, but with significantly poorer data sets (e.g. Racine 1968; Sandage 1968; de Vaucouleurs 1970; Harris 1974). He then proceeded to apply this 'universality' of the GCLF by deriving a distance to Virgo of $m - M_o = 30.4 \pm 0.5$.

Probably the first comprehensive comparison between a GCS and its host galaxy was performed by Strom et al. (1981) who re-observed the M 87 GCS with photographic UBR photometry and identified $\sim$ 1700 GC candidates. Not only was this study deeper than previous work, but also had greatly increased spatial coverage. Its major findings were: (*i*) the GCs were bluer than the integrated halo light at all radii and (*ii*) the GCs themselves became bluer with increasing galactocentric radius. On this basis these authors concluded that the chemical enrichment and dynamical histories of the clusters and galaxy were more decoupled than previously thought (see also Forte, Strom, & Strom 1981). Considering the sensitivity of the photographic plates used, it was a remarkable achievement to detect the presence of any significant gradient in the cluster system, a fact which has since been confirmed (e.g. Lee & Geisler 1993).

At about this time, the first reliable integrated spectra of extragalactic GCs were obtained, all for the very brightest clusters of the GCS (e.g. Racine, Oke, & Searle 1978; Hanes & Brodie 1980; Cohen 1982). Although these studies were rather limited in scope due to the lack of efficient, multiplexing spectrographs, they illustrated the potential of these observations both in terms of kinematical and abundance analyses. Recent technological advances in spectrograph, detector and telescope design have much improved this situation. There are now statistically significant samples of accurate radial velocities and line-strengths for several galaxies outside the Local Group (e.g. Sharples 1988; Harris, Harris, & Hesser 1988; Mould et al. 1990; Grillmair et al. 1994; Cohen & Ryzhov 1997; Cohen, Blakeslee, & Ryzhov 1998; Sharples et al. 1998; Kissler-Patig et al. 1998; Zepf et al. 2000). We return to the subject of the spectroscopy of extragalactic GCS in Chapter 3.

Similarly, large format CCDs and bigger, better telescopes (one in space...) have lead to a situation where we now have information on the GCS of over 100 galaxies (Harris 1999). We are now in an excellent position to study the GCS of galaxies in detail, and see what we may learn about the processes of galaxy formation and evolution.

1.3.2 Colour Distributions

From the analysis of the colours of GCs associated with bright ellipticals, a number of studies had found than the colour distributions were broad and appeared non-Gaussian (e.g. Cohen 1988; Geisler & Forte 1990; Couture, Harris, & Allwright 1991; Ajhar, Blakeslee, & Tonry 1994). Whilst these studies demonstrated that the colour distribution of these ellipticals' GCS was broader than that of the Local Group spirals, little or no structure could be discerned.

In 1993, Zepf and Ashman applied a robust statistical test based on mixture-modelling to the $B-I$ colours of GCs in the giant Virgo elliptical NGC 4472 (Couture, Harris, & Allwright 1991) and $C-T_1$ colours of GCs associated with Centaurus A (Harris et al. 1992), the closest giant elliptical galaxy to the Milky Way. They found that both of these colour distributions were more likely bimodal as opposed to unimodal at high confidence. Subsequent ground-based studies with increased metallicity sensitivity and/or larger sample sizes have since confirmed this result for these GCS, and have identified several other bimodal/multimodal GCS associated with galaxies: NGC 1399 (Ostrov, Geisler, & Forte 1993), NGC 4486 (Lee & Geisler 1993), NGC 3311 (Secker et al. 1995), NGC 3923 (Zepf, Ashman, & Geisler 1995), NGC 4472 (Geisler, Lee, & Kim 1996). We show in Figure 1.3 examples of the colour distributions for two bright ellipticals, M 87 and NGC 3923. Both distributions are clearly bimodal, although the numbers of clusters in the M 87 dataset is significantly larger.

The application of *HST* to the studies of these colour distributions has yielded important results, in addition to significantly increasing the number of GCS with accurate two-colour photometry. Beginning with Whitmore & Schweizer's (1995) study of M 87 using the F555W and F814W filters (approximating to Johnson V and I) in which they found clear bimodality, many workers have now successfully studied the GCS of various galaxy types in two colours (e.g. Elson & Santiago 1996; Forbes, Brodie, & Huchra 1997; Forbes et al. 1998; Elson et al. 1998; Grillmair et al. 1999; Neilsen & Tsvetanov 1999; Kundu 1999; Kissler-Patig et al. 1999; Puzia et al. 2000). The location and superb spatial resolution of *HST* allows the GCLF turnover at Virgo distances to be easily reached, and since at these distances GCs are partially resolved, allows accurate contamination corrections to be performed. Besides these obvious advantages, the *HST* data archive has also proved a boon to this area of GCS research. Large-scale projects to observe other aspects of galaxy evolution (e.g. Kormendy et al. 1996) have left a rich library of multicolour WFPC-2 images of galaxies in the local Universe. Kundu (1999) exploited this database to obtain colour distributions for 60 early-type galaxies. He found that 30–60% of ellipticals showed signs

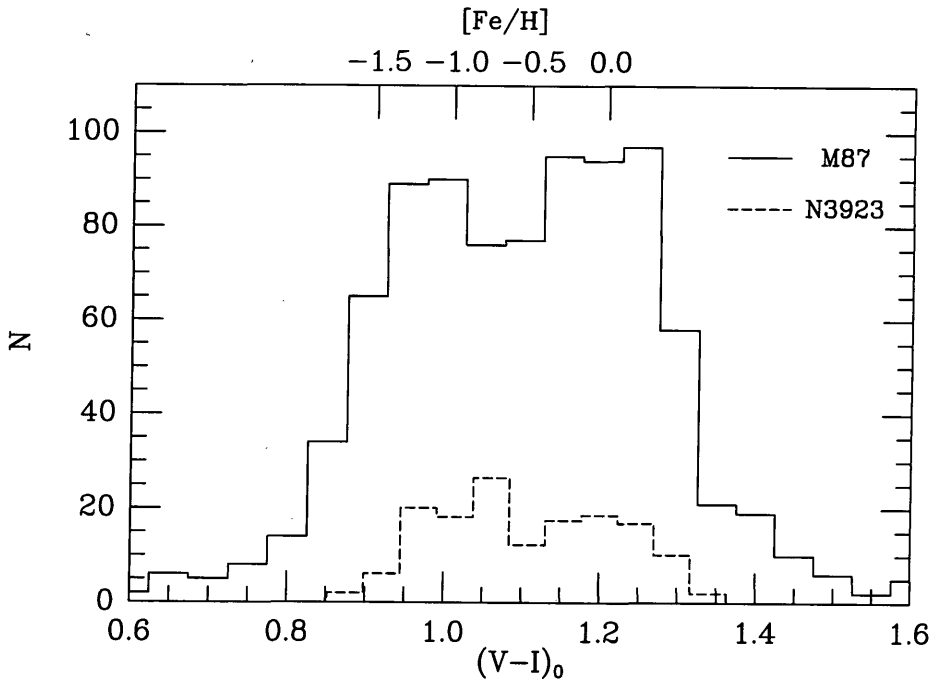

Figure 1.3: Colour histograms for the GCSs of NGC 3923 (Zepf, Ashman, & Geisler 1995) and M 87 (Whitmore & Schweizer 1995). The top scale assumes that the $V - I$ colours reflect metallicity only (taken from Ashman & Zepf 1998).

of bimodality or multimodality, as did $\sim$ 10% of the S0's in his sample. In a similar study, Gebhardt & Kissler-Patig (1999) analysed archival WFPC-2 data of 50 galaxies, 43 of which were S0's or ellipticals[6]. These authors found that nearly half their sample were bimodal, and followed the general trend in that the bright galaxies generally exhibited bimodality, whilst their fainter counterparts did not. Furthermore, some galaxies showed only a single-peaked blue GCS, whilst some exhibited only a single red GCS peak.

1.3.3 Metallicity Distributions

The colour distributions of GCs in early-type galaxies imply that many GCs have metallicities of solar and above. However, the principle concern associated with deriving metallicities from broad-band colours is that the colour calibrations are based upon observations of Galactic GCs. Since these clusters do not reach to solar values, it is precisely this high-metallicity end which

[6] Data for 15 of Gebhardt & Kissler-Patig's galaxies were in common with Kundu, presumably both studies were undertaken concurrently - the main peril of archival data.

is poorly known. Moreover, there is no *a priori* reason why these calibrations should be linearly extrapolated for the very metal-rich GCs, indeed Kissler-Patig et al. (1998) indicate that doing so probably overestimates their metallicities significantly. The same difficulties apply to spectroscopic metallicity determinations based upon Galactic calibrations. This problem can be circumvented by employing stellar population models, which, whilst generally scaled-solar in terms of abundance *ratios* (e.g. Worthey 1994; Vazdekis et al. 1996; Kurth, Fritze-v. Alvensleben, & Fricke 1999), are based upon observations of individual stars which reach to population-I type metallicity values. For example, Cohen, Blakeslee, & Ryzhov (1998) recently use the stellar population models of Worthey (1994) to derive metallicities from spectra of $\sim$ 150 GCs associated with the giant elliptical M 87, the central cD of the Virgo cluster. They found that a small, but significant fraction of GCs had metallicities at solar values or above, whilst avoiding calibrations based on Galactic GCs.

Perhaps a more fundamental concern is the assumption that integrated indices are uniquely determined by one parameter alone, i.e. the metal abundance of the cluster. Other effects may be contributing to the integrated light which we observe, such as differences in HB morphology (see § 1.2.3) and age. As a stellar population ages it becomes redder, since its stellar content becomes intrinsically cooler. Moreover, as a stellar population becomes more chemically enriched it also becomes redder, since the atmospheres of its individual stars become more opaque, increasing their surface area and thereby decreasing their surface temperature. Worthey (1994) quantified this age-metallicity degeneracy with the relation, $\Delta\mathrm{age}/\Delta\mathrm{Z} = 3/2$. The above relation implies that, if a stellar population ages by a factor 2, then a corresponding decrease in its metallicity by a factor of 3 will conspire to make the population look the same in most broadband colours and indices. However, for old stellar populations integrated indices generally become much less sensitive to age differences than metallicity differences, so providing the stellar populations are older than several Gyr, colour-metallicity relations remain valid.

GCs are traditionally regarded as being old, since they were initially characterized by those present in the Galaxy. Indeed, GCs in the Milky Way *are* very old, post-*HIPPARCOS* age estimates from sub-dwarf fitting now yield mean ages for the Galactic GCs of 12.9 ± 2.9 Gyr (Carretta et al. 2000). Moreover, recent age determinations of the GCs in giant ellipticals also point towards old ages (e.g. Harris, Poole, & Harris 1998; Cohen, Blakeslee, & Ryzhov 1998; Kissler-Patig et al. 1998; Puzia et al. 1999). Whilst there is increasing evidence for the existence or young GCs

in interacting galaxies (see § 1.3.4), in the majority of galaxies, GCs may safely be considered old, with their colours corresponding purely to their metallicity.

One final consideration is that, at least for spectroscopy, we can currently sample only the very brightest GCs outside the Local Group. There may be some property of the most luminous (i.e. most massive) clusters, not exhibited by the rest of the population. For example, if self-enrichment occurs in the most massive GCs (e.g. ω Cen), then we may not be getting a true representation of the GCS as a whole. Whilst this is probably not a particular problem for colour distributions, it may pose difficulties for future studies of abundance ratios in extragalactic GCs.

1.3.4 Young Globular Clusters

In the past decade or so, observational evidence has been mounting for the existence of what appear to be *young* GCs. First hinted at by Schweizer (1982), who identified a series of 'blue knots' in the galaxy merger NGC 7252, Lutz (1991) was the first to use the term 'young globular clusters' for what appeared to be 14 luminous blue clusters in the merging galaxy NGC 3597. Since then, many systems have been seen to possess young GC candidates, largely thanks to the superb spatial resolution provided by *HST* : NGC 1275 (Holtzman et al. 1992), NGC 1316 (Goudfrooij et al. 2000), NGC 3256 (Zepf et al. 1999), NGC 3597 (Carlson et al. 1999; Forbes & Hau 2000), NGC 3921 (Schweizer et al. 1996), NGC 4038/4039 (Whitmore & Schweizer 1995), NGC 4449 (Gelatt, Hunter, & Gallagher 2000), NGC 6946 (Elmegreen, Efremov, & Larsen 2000), NGC 7252 (Schweizer & Seitzer 1998). Interestingly, the existence of such young GCs was predicted *prior* to their first identification by Schweizer (1987), and discussed in the context of forming GC subpopulations by Ashman & Zepf (1992). The issue of whether or not these young clusters are truly precursors to GCs, and if they will avoid dissolution or disruption is as yet undecided. However, until stronger constraints are placed upon the physical characteristics of these systems, it suffices to say that we see objects forming in the local Universe which have the physical characteristics expected of young GCs.

1.4 Correlations with the Host Galaxy

1.4.1 Specific Frequency

In 1981, Harris & van den Bergh introduced specific frequency (S_N), applied to the GC systems of galaxies. The specific frequency is a method of normalising the number of GCs by the luminosity of the host galaxy:

$$S_N \equiv N_{GC} \times 10^{0.4(M_V+15)} \tag{1.2}$$

where N_{GC} is the total number of GCs in the galaxy. The specific frequency is normalised to the characteristic luminosity of a dwarf elliptical galaxy (M_V=-15). We show the specific frequencies for a compilation of early-type galaxies in Figure 1.4.

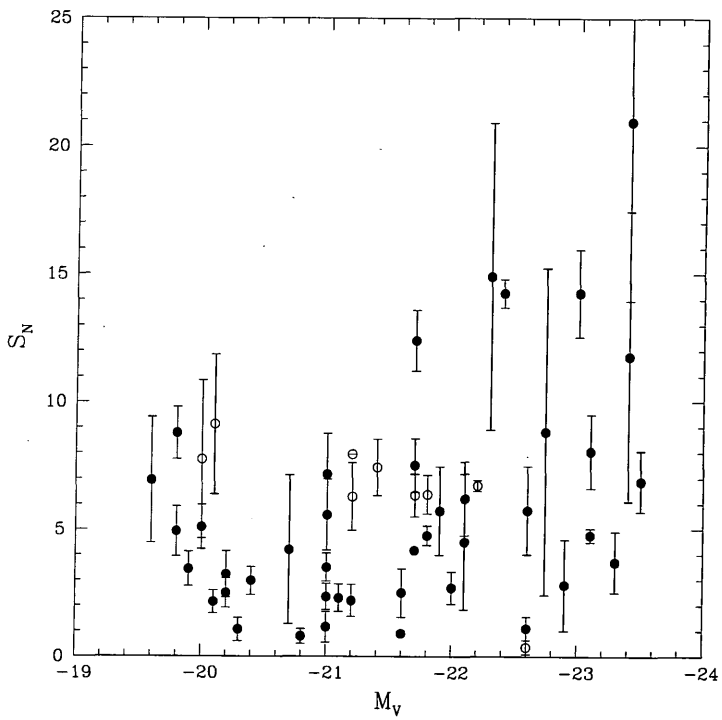

Figure 1.4: The S_N values of elliptical galaxies versus their absolute V-band magnitudes. Open circles indicate that the completeness of the GCS survey was less than 10% of the total (taken from Kissler-Patig 1997).

Figure 1.4 highlights several facts about the specific frequencies of *early-type* galaxies which have become increasingly apparent: (*i*) the plot of S_N versus magnitude is flat, indicating that to first order, the number of GCs scales with host galaxy luminosity, (*ii*) the scatter in S_N is larger

than the observational uncertainties, perhaps not surprising if galaxy (and GC) formation is truly a stochastic process (e.g. Cole et al. 1994; Kauffmann 1996), and (*iii*) S_N seemingly increases with increasing local density–to the point where cDs in rich clusters have hugely elevated S_N. Blakeslee, Tonry, & Metzger (1997) found that from SBF observations of 23 bright galaxies in 19 Abell clusters, S_N increased with mass tracers such as X-ray luminosity and cluster velocity dispersion. Interestingly, rather than having an excess of GCs, perhaps accreted from the surrounding cluster (e.g. Cote, Marzke, & West 1998), it has been suggested that these 'Brightest Cluster Galaxies' are under-luminous for their GCS (e.g. Blakeslee, Tonry, & Metzger 1997; McLaughlin 1999). Moreover, this correlation between the number of GCs and local density is not restricted to the richest Abell clusters, similarly 'field' ellipticals have mean $S_N \sim 2$ whilst those in groups and clusters typically have $S_N \sim 4$ (e.g. Ashman & Zepf 1998; Harris 1999 and references therein).

A related issue is the spatial distribution of GCs in ellipticals. The brightest, 'high-S_N' galaxies seemingly have GCS significantly more extended than the spheroid, whilst fainter ellipticals tend to have GCS which closely follow the galaxy starlight (e.g. Racine, Oke, & Searle 1978; Strom et al. 1981; Harris 1986). Whilst direct comparison between galaxy light profiles and the surface density of the GCS is difficult, since the stellar brightness falls rapidly beyond an effective radius (by definition), for the few cases which have been studied it appears that GCs associated with high-S_N galaxies are preferentially found at large radii (Forbes 1996).

The situation for late-type spirals and irregulars seems somewhat different. Amongst these morphological types, there appears to be significantly less scatter in S_N (about a factor of two), with a mean value of $S_N \sim 0.5$ (Kissler-Patig et al. 1999). As pointed out by Harris (1999), in view of the difficulties of identifying GCs in systems with large amounts of gas and dust, and which are intrinsically poorer in terms of their GCS, the observed scatter could be consistent purely with observational uncertainties. If real however, lower values of S_N in late-type spirals either indicates that they are less adept at forming GCs than early-type spirals and ellipticals, or GC destruction processes in these galaxies are significantly more efficient.

However, comparison of the specific frequencies between galaxy types is complicated by the differing content of their stellar populations, and hence $\mathcal{M}/L$ ratios. Zepf & Ashman (1993) introduced the mass-normalized specific frequency (see § 2.6.1 in Chapter 2) in an effort to correct for this. Whilst such an approach implicitly requires an assumption about the $\mathcal{M}/L$ ratio of each galaxy type, one finds that elliptical galaxies do seem to have factors of $2 \sim 3$ more GCs than

spirals of the same luminosity. Unfortunately, few late-type spirals have well-characterized GCS, and firm conclusions cannot be drawn until more data is obtained for these systems.

1.4.2 A Metallicity-Luminosity Relation?

Since the first quantitative comparisons were performed in the late seventies, the issue of whether or not the star formation history of a galaxy and its GCS are related has been a controversial one.

In 1975, van den Bergh suggested that there may be a correlation between the mean metallicity of a GCS and the luminosity of the host galaxy (Z-L relation). He based this conclusion upon a rather small dataset; observations of the GCS of the Milky Way and Andromeda spirals, two Local Group dwarfs (Fornax and NGC 205) and the dominant Virgo elliptical M 87 (see also Racine 1980). In contrast, the findings of Hanes (1977), Strom et al. (1981) and Forte, Strom, & Strom (1981) that the GCs associated with M 87 were bluer than the halo light at all radii (by $\sim$ 0.5 dex), lead Forte et al. (1981) to conclude that the chemical enrichment of the M 87 GCs was probably decoupled from that of the spheroid. This issue was re-addressed by Brodie & Huchra (1991), who found that, based upon the integrated spectra of 10 GCS, the mean metallicity of the GCS *did* increase with the absolute blue magnitude of the parent galaxy. Subsequent studies with increasingly large datasets have since confirmed these findings (e.g. Secker et al. 1995; Forbes et al. 1996; Durrell et al. 1996), with the Z-L relation roughly scaling as $Z \propto L^{0.4}$ (Brodie & Huchra 1991).

However, the discovery of red and blue subpopulations in many bright ellipticals (see § 1.3.2) somewhat complicated matters. It explained the difference in colour between the galaxy and GCS of M 87 found by Forte et al., since the blue clusters were found to be $\sim$ 1.0 dex more metal-poor than the stellar light, whilst the red clusters had comparable metallicities (Lee & Geisler 1993). But this lead Ashman & Bird (1993) to argue that the Z-L relation was purely a result of brighter galaxies having larger fractions of red (metal-rich) globular clusters-essentially a numerical artefact, rather than any profound physical relation.

The key to resolving this problem is to decompose and analyse the blue and red GC subpopulations, which requires a number of high-quality bimodal datasets covering a range of luminosities. Such an analysis was performed by Forbes, Brodie, & Grillmair (1997) and subsequently updated by Forbes & Forte (2000). These authors found that red GCs showed a strong correlation with parent galaxy magnitude and velocity dispersion (i.e. galaxy mass), and had identical colours (within the uncertainties) to the spheroid light. In contrast, the blue GCs showed no such correlation, with

mean colours similar to the halo GCs in the Milky Way and M 31. If real, this result indicates that red GCs share a common chemical enrichment history with their parent galaxy, whereas the blue GCs originate from a somewhat different star formation process. However, Kundu (1999) found little or no evidence for such a relation between the red GCs and their host galaxies in his sample of 60 early-type galaxies. He argued that if any correlation did exist, it either stemmed from some level of enrichment of the red GCs, or in common with Ashman & Bird, the relative fraction of red GCs increased with increasing luminosity.

Beyond issues of galaxy formation, this result has important consequences for the use of the GCLF as a distance indicator. By measuring the luminosity function of the entire GCS, the observer will perhaps measure different mass functions in the GC subpopulations, arising from the variable metallicity (and perhaps age) of the red clusters. This implies that the position of the GCLF peak may change with the luminosity of the host galaxy, and thus will no longer be a standard candle. A method of side-stepping this problem would be to measure the luminosity function the more homogeneous *blue* clusters only, however this is clearly a more observationally expensive pastime (e.g. Burgarella, Kissler-Patig, & Buat 2000).

In any event, whilst some of the evidence for the red clusters is compelling, it is by no means a clear-cut case and awaits better data.

1.5 Outline of this Thesis

In this thesis, we investigate the properties of the GCS associated with galaxies of three different morphological types.

In Chapter 2, we describe the results of a spectroscopic survey of published GC candidates associated with the Sculptor Group spirals NGC 253 and NGC 55. Based upon our results, we define new catalogues of GC candidates associated with these galaxies, and obtain specific frequencies for their GCS.

Chapter 3 represents the results of a four-year project to obtain a statistically significant sample of radial velocities for GCs associated with the giant Virgo elliptical NGC 4472 using multi-object spectroscopy. We measure and analyse line-strengths of the GCs in order to derive ages and metallicities using simple stellar population models. Additionally, we analyse the kinematics of the sample, and obtain a mass profile for the dark halo of the galaxy. Drawing the results of the

metallicity, age and kinematical analyses of the globular cluster system together, we look at their implications for the formation of this important galaxy.

In Chapter 4 we obtain high signal-to-noise integrated spectra for 64 star clusters in the Large Magellanic Cloud. We measure the line-strengths of these clusters, and place them unto the Lick/IDS system. By using literature data for a subset of these star clusters derived from colour-magnitude diagrams and spectroscopy, we assess the ability of simple stellar population models to reproduce their ages and metallicities. We then use these stellar population models to predict ages and metallicities for the entire sample, and derive an age-metallicity relation for the Large Cloud star clusters.

To round it all off, in Chapter 5 we discuss our conclusions for what are essentially three self-contained chapters. We first discuss further work required in order to characterize the GCS of late-type spirals–a neglected galaxy type in GC research. We then try and understand the origins of the subpopulations in NGC 4472 and other giant ellipticals. We introduce a nascent project using the results of semi-analytic models of galaxy formation to try and predict colour distributions of GCS, and possible correlations with their host galaxies. Finally, we discuss the use of stellar population models in the context of predicting ages and metallicities for extragalactic GCs from integrated spectra, and future avenues for research in this area.

Chapter 2

Globular Clusters in the Sculptor Group

Abstract. We have obtained spectra for 103 published GC candidates in the Sculptor Group galaxies NGC 253 and NGC 55. On the basis of radial velocities and digitized plate images, 14 GCs are identified in NGC 253 and one probable GC is identified in NGC 55. The majority of the objects in the sample appear to be background galaxies. We have obtained and analysed COSMOS plate scans of NGC 253 and NGC 55 and use these along with the spectroscopically identified clusters to define new samples of GC candidates in the two galaxies which should have reduced contamination. From co-added spectra, we obtain a spectroscopic mean metallicity of the NGC 253 GCS of [Fe/H] = -1.23 ± 0.19. We estimate the total GC populations to be 24 ± 12 for NGC 55 and 68 ± 18 for NGC 253, yielding specific frequencies for NGC 55 and NGC 253 of 0.4 ± 0.2 and 0.7 ± 0.2 respectively.

2.1 Introduction

The search for GCs in external galaxies has progressed to the point where GCS have now been studied in over 100 galaxies (e.g. Harris 1999).

To date, the majority of galaxies for which GCS have been investigated are of early-type. This situation has arisen since, at least in principle, the detection of GCs belonging to elliptical galaxies is somewhat more straightforward than that in their late-type counterparts. Ellipticals typically have specific frequencies of $S_N \sim 2$–5, whereas for spirals the value is ~ 0.5. Moreover, GCs are generally associated with the bulge/halo component of galaxies, whereas spirals are not decomposed into bulge/disk components when their total luminosity is determined. As a result, whilst spirals typically count their GCs in hundreds, luminous elliptical galaxies usually possess several thousands of GCs, with the GCS of central cluster cD's often numbering *tens* of thousands (Ashman & Zepf 1998). By way of illustration, compare our nearby neighbour, the Andromeda spiral galaxy (M 31), with the Virgo elliptical NGC 4365. Both M 31 and NGC 4365 have approximately the same V-band absolute magnitude ($M_V \simeq$ -21.8), however the former, an

Sb spiral, has a GCS of 450 $\pm$ 100 (Barmby et al. 2000), whereas NGC 4365, an E2 galaxy, plays host to some 2500 $\pm$ 200 GCs.

Furthermore, it is not simply the total number of GCs between galaxy types which determines the detectability of their GCS. In comparison to late-type galaxies, ellipticals are morphologically simple systems. Not only does their spheroidal nature facilitate relatively straightforward correction for the underlying galaxy light, but also their GCS typically extend to out to several effective radii (Ashman & Zepf 1998). In the case of spirals, unless the galaxy is effectively edge-on to our line-of-sight, GCs are projected onto the disk of the galaxy, rendering them difficult to detect and affected by reddening, crowding and contamination. This requirement is fairly rigid; again taking M 31 as an example, at an inclination to the line-of-sight of $i \sim 78°$, approximately 50% of its GCs are projected against the disk, and this for a galaxy only $\sim$ 0.7 Mpc distant (e.g. Harris 1999). In the light of these difficulties, the nature of the GCS of even some of the closest spiral galaxies is poorly known.

Experience shows that, for ground based observations, the limit for *resolving* GCs is D $\sim$ 5.0 Mpc. At this distance, typical GC core radii of 2 pc and half-light radii of 10 pc will subtend angular diameters of 0.08″ and 0.41″ respectively. From the observers' point of view, the next logical step from looking for GCs in the Local Group, is going to the Sculptor group of galaxies at a distance of 2.5 Mpc (Puche & Carignan 1988). Searches for GCs have been undertaken for the two nearby Sculptor spirals NGC 55 (Liller & Alcaino 1983a) (henceforth LA83a) and NGC 253 (Liller & Alcaino 1983, henceforth LA83b and Blecha 1986 henceforth B86) on the basis of visual inspection and image analysis of photographic plates. LA83a identify 51 objects in NGC 55 and 63 objects in NGC 253 (LA83b) which have magnitudes, colours and sizes comparable to GCs in the Galaxy. B86 identify a further 25 candidates in the field of NGC 253, using a more quantitative technique of profile analysis.

However, the true nature of these GC candidates can only be established via spectroscopy, in order to determine accurate radial velocities. Since these objects are marginally resolved, there is not the same level of confusion with Galactic stars as is the case with more distant cluster systems. Moreover, because the parent galaxies have low systemic velocities ($V_{\rm N55}$=121 km s^{-1}; $V_{\rm N253}$ = 240 km s^{-1}) (de Vaucouleurs et al. 1991), there is little uncertainty in identifying background galaxies. In this Chapter, we present a spectroscopic survey of the LA83a, LA83b and B86 samples.

The plan of this Chapter is as follows: In the remainder of this section, we look at the current understanding of GCS in Sculptor group, paying particular attention to NGC 55 and NGC 253. Next, in Section 2.2, we describe the sample selection and observations of the GC candidates, before proceeding to give details of the reduction of our data. In Section 2.3, we describe the method by which we obtain radial velocities from our spectra and the identification of foreground stars, background galaxies and GCs on this basis. In Section 2.4, we examine the spatial and velocity distributions of the identified GCs, in addition to deriving a mean metallicity of the NGC 253 cluster system. We then describe the definition of a new sample of cluster candidates in Section 2.5, based on the characteristics of the spectroscopic sample and digitized COSMOS plate scans. Next, in Section 2.6, we discuss the properties of the GC of NGC 55 and NGC 253, in the context of correlations between GCS and their host galaxy. Finally, we present our conclusions from this work and a summary in Section 2.7.

2.1.1 The Sculptor Group

The Sculptor group of galaxies forms a loose physical association of about 15 members (de Vaucouleurs 1959, 1978). At a distance of 2.5 Mpc (Puche & Carignan 1988) it is generally believed to be the nearest aggregate of galaxies to our own Local Group (de Vaucouleurs 1975). The group covers an area on the sky of approximately 100π deg^2 and is located at α=0^h 30^m, δ=-30°.

Despite its relative proximity, very little is known of the GCS surrounding the major galaxies in the Sculptor group (NGC 45, 55, 247, 253, 300 and 7793). Da Costa & Graham (1982) obtained spectroscopy of three resolved cluster candidates in the field of NGC 55, an Sb(s)m galaxy, and found all three to have velocities which agree with that of NGC 55 itself. These authors conclude that one of these clusters is perhaps very young ($\tau \leq 10^7$ yr), whilst the other two are at least several Gyr old. Young luminous star clusters have also been discovered in the central regions of the bright starburst spiral NGC 253 by Watson et al. (1996). They find that at least one of these clusters is an excellent candidate for 'young globular cluster' status, with $M \sim 1.5\times10^6$ M$_\odot$ and a half-light radius of $\sim$ 2.5 pc. Larsen & Richtler (1998) undertook a multi-colour imaging survey of 23 nearby galaxies, in order to search for young clusters, which included the Sa(s)d spiral NGC 300. However, these authors found *no* young globular cluster candidates in this galaxy.

Moreover, the nature of the classical (i.e. old) GCs in Sculptor is poorly understood. As mentioned in the introduction to this Chapter, a visual search for old GC candidates around the Sculptor

spirals NGC 55 and NGC 253 has been undertaken by LA83a and LA83b using plates from the ESO 3.6 m telescope. These authors found a total of 114 slightly diffuse objects with the $B - V$ colours, magnitudes and sizes appropriate to those of a GC population similar to that in the Galaxy. A somewhat more quantitative selection of candidates was later derived by Blecha (1986) using profile analysis of images from the Danish 1.5 m telescope, based upon the known properties of Galactic GCs.

For this project we adopt a distance to NGC 55 of 2.0 Mpc, and to NGC 253 of 2.5 Mpc after Graham (1982). At these distances, $1''$ corresponds to 9.7 pc and 12.1 pc respectively. We show DSS images of the two galaxies in Figure 2.1. The spiral structure of NGC 253 is discernable, despite its inclination angle of $i \sim 80°$, as is the irregular nature of NGC 55. In addition to foreground stars, many of the faint sources in the images are background galaxies. In Table 2.1 we list the basic properties of NGC 55 and NGC 253.

Table 2.1. Basic data for NGC 55 and NGC 253.

Sources : 1) de Vaucouleurs et al. (1991), 2) Puche, Carignan, & Wainscoat (1991), 3) Puche, Carignan, & van Gorkom (1991a), 4) Pence (1980), 5) this study.

Quantity	NGC 55	NGC 253	Source
Hubble Type	Sb(s)m	Sab(s)c	1
RA (2000.0)	00 15 08.6	00 47 33.2	1
DEC (2000.0)	-39 13 13	-25 17 18	1
Adopted Distance (Mpc)	2.0	2.5	2,4
M_B	-19.0	-19.5	1
Position Angle (deg)	108	52	1
Angle of Inclination, i (deg)	79 ± 4	73 ± 5	2,3
Heliocentric Velocity, V_h ($km\,s^{-1}$)	121 ± 13	240 ± 15	1
N_{GC}	24 ± 12	68 ± 18	5
S_N	0.4 ± 0.2	0.7 ± 0.2	5

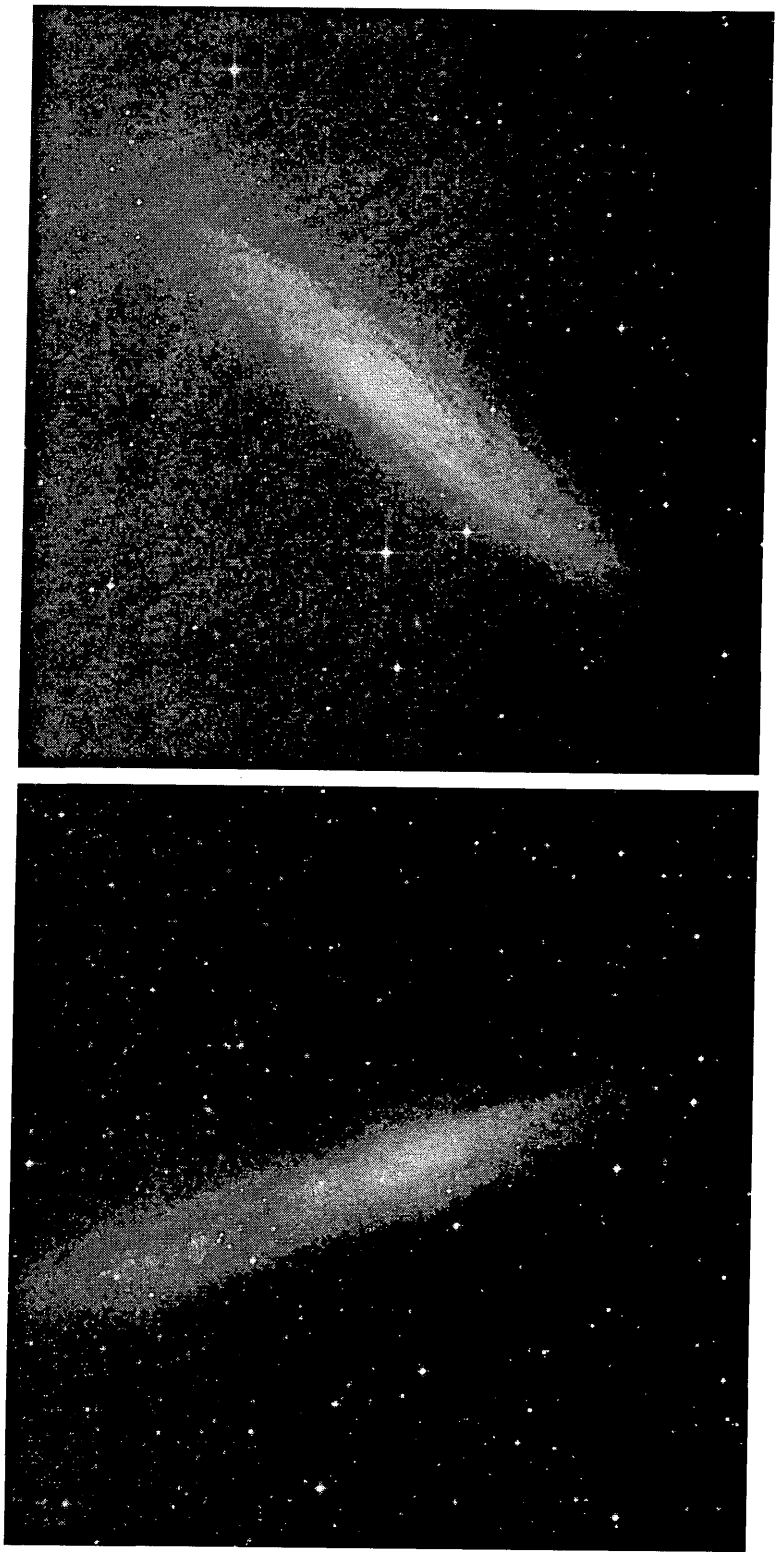

Figure 2.1: DSS images of NGC 253 and NGC 55. The image dimensions are 30 × 30 arcmin.

2.2 Spectroscopy of Globular Clusters in NGC 55 and NGC 253

2.2.1 Selection of the Sample

The sample for our survey was selected from the list of GC candidates published by LA83a for NGC 55, and spectroscopy from LA83b and B86 for NGC 253. The GC candidates were taken within the radial limits $0 < R < 20$ arcmin from the centres of each galaxy (the maximum field of the spectrograph). For a high spectroscopic return, we took magnitude limits of $18 < B < 20.5$ in the published catalogues. However, for completeness we additionally included twenty extra objects. Six candidates were labelled labelled 'bright' and fourteen labelled 'blue' in LA83a and LA83b. As a result, the faintest cluster candidates went down to $B \sim 21.6$. Accurate astrometric positions ($\pm$ 0.3 arcsec) for each target were obtained using a PDS measuring machine and reference stars from the Perth70 catalogue. Any obvious galaxies (usually low surface brightness objects showing spiral structure) were expunged from the lists. Our final list of candidates for spectroscopy contained 57 objects in NGC 55 and 58 in NGC 253.

2.2.2 Observations

The observations were obtained with the 3.9 m Anglo–Australian Telescope (AAT) and the AUTOFIB fibre positioner (Parry & Sharples 1988). This automatic fibre-positioner is capable of obtaining intermediate dispersion spectra of up to 64 objects within a 40 arcminute diameter field. In Table 2.2 we summarize the observational setup.

In addition to our target objects, we assigned several fibres to monitor the sky background spectrum and the faint background light from the parent galaxy halo. We used a 600 lines mm^{-1} grating in the first order with the RGO spectrograph. This allowed us to obtain spectra covering the range 3850–5700 Å at a resolution of 4 Å using the Image Photon Counting System (IPCS) as the detector. We obtained 5×3000 second exposures for each galaxy. These were interspersed with 200 second exposures of a Cu–Ar–He calibration lamp for wavelength calibration and 300 second exposures of blank sky regions for accurate sky-subtraction. Unfortunately, the majority of the observations were obtained in rather poor seeing conditions (2.″3 arcsec) so the final spectra had S/N ratios typically in the range 4$\sim$20.

Table 2.2. Summary of observations at the AAT.

Telescope	3.9-metre AAT
Instrument	AUTOFIB/RGO Spectrograph
Dates	October 1986
Spectral range	3850–5700 Å
Grating	600 V
Dispersion	2.2 Å pixel^{-1}
Resolution (FWHM)	$\sim$ 4.0 Å
Detector	IPCS
Seeing	2–3 $''$
Exposure Time	5 $\times$ 3000s per galaxy

2.2.3 Data Reduction

In Chapter 4 we give a thorough discussion of spectroscopic fibre-based data reduction. Here, we briefly summarize the procedure.

The basic data was primarily reduced using the FIGARO data reduction package. The individual spectra were extracted from the data frame and wavelength calibrated using the exposures of the Cu–Ar–He hollow cathode lamp. The rms residuals of the wavelength calibration were typically 0.2 Å. Sky subtraction was based on dedicated sky fibres in each frame, with the fibre–to–fibre transmission variations and vignetting along the spectrograph slit being removed by using the blank sky exposures. In addition, we corrected for the fibre–to–fibre *spectral* response (most of which is introduced when the spectra are extracted) using exposures of the twilight sky spectrum whose shape was assumed to be constant across the field. During the observations, exposures were obtained of several Galactic GCs and bright stars to act as radial velocity standards. This was achieved by offsetting the standards into individual fibres. For the spatially extended Galactic globulars, groups of adjacent fibres where raster-scanned by 10$\sim$20$''$ and the individual spectra averaged. We summarizes the velocity standards observed for the two galaxies in Table 2.3 .

The final extracted spectra consisted of 925 channels at 2 Å pixel^{-1} and prior to cross–correlation analysis were rebinned onto a logarithmic wavelength scale with a velocity step of 127 km s^{-1} per bin.

Table 2.3. Radial velocity standards observed for NGC 55[1] and NGC 253[2]. †From the SIMBAD database.

ID	Object Type	Spectral Type†	V_h ($km\,s^{-1}$)†
HD 136010[1]	galactic star	K0 II	+1.0
HD 136406[1]	galactic star	K0 III	-20.3
NGC 6356[1]	globular cluster	G3	+27.0
NGC 6809[1]	globular cluster	F4	+174.9
NGC 6981[1]	globular cluster	F4	-288.8
NGC 1851[1]	globular cluster	F4	+320.9
HD 223647[2]	galactic star	G7 III	+14.5
47 Tuc[2]	globular cluster	G4	-18.7
NGC 2298[2]	globular cluster	F5	+149.4
HD 35410[2]	galactic star	G9 III-IV	+20.3

2.3 Velocities of the Spectroscopic Sample

The majority of the radial velocity analysis described in this section was performed using IRAF.

2.3.1 Radial Velocities

We obtained radial velocities from the spectra using two methods. For obvious emission–line objects (i.e. galaxies), identified lines were interactively fit with a Gaussian profile and the position of the centroid measured. The final velocity for these objects was then taken to be the straight mean of these measurements, with the uncertainty being the rms between measurements. For absorption spectra, radial velocities were determined by the cross–correlation of the object spectrum against a template (Tonry & Davis 1979) with the task FXCOR in IRAF. The templates (listed in Table 2.3) were first corrected to the rest-frame using their literature radial velocities obtained from the SIMBAD database. By experimentation with different object–template combinations, we determined that the cross–correlations should have normalised peak heights in the correlation function of > 0.1; below this threshold it was found that returned velocities were unreliable and should therefore be discarded. Furthermore we specified that each spectrum should have at least two reliable cross–correlations against different templates of similar spectral type. The final velocities derived for the absorption-line spectra were taken to be the mean velocity weighted by the cross–correlation peak height of each correlation. The uncertainties in our velocities are the rms between measurements,

added in quadrature to the formal uncertainty derived from the cross-correlation task. As a final step, the velocities were heliocentrically corrected on the basis of their date of observation.

Tables 2.4 and 2.5 show the final velocities obtained from the candidate cluster spectra for the two galaxies.

The uncertainties in the radial velocities derived from the emission lines are generally much lower than those obtained from the cross–correlation. This arises because, whilst the absorption lines are often wide features, the finite width of the emission is due to the instrumental resolution of the spectroscopic system. For spectra which showed emission superimposed unto absorption, we derived velocities using both techniques mainly as a consistency check. Emission lines more than 4 σ from the pseudo–continuum (determined by fitting a polynomial to the spectra) where either interpolated across by hand or removed with the LINECLEAN task in IRAF. In all cases, the agreement was excellent.

Table 2.4.: Globular cluster candidates in NGC 253.
Columns are: ID (fibre #), heliocentric velocity, velocity error, right ascension, declination, other designation, B magnitude and classification.
♣ LA ≡ (Liller & Alcaino 1983b) LAb & LAc are 'blue' candidates from their sample. LAA, LAB & LAC are labelled as 'bright' objects. B ≡ (Blecha 1986).
♡ magnitudes from LA83b and B86

ID	v_h ($km\,s^{-1}$)	v_{err} ($km\,s^{-1}$)	α(1950)	δ(1950)	Alternative ID♣	$B^{\heartsuit}$ (mag)	Classification
1	62081	21	00 45 55.42	-25 14 19.1	LA33	18.9	galaxy
2	33731	79	00 45 17.95	-25 24 59.1	B3	20.1	galaxy
4	23061	117	00 45 19.30	-25 24 02.1	B2	21.2	galaxy
5	29601	30	00 45 19.29	-25 19 11.2	LA38	18.8	galaxy
7	212	74	00 45 35.09	-25 26 58.8	B1	21.1	cluster
8	235	28	00 45 45.79	-25 22 18.0	LA26	20.0	cluster
9	90390	12	00 46 02.22	-25 15 54.7	LAc	19.4	galaxy
10	44826	21	00 45 46.53	-25 13 02.9	LA41	19.6	galaxy
11	75687	21	00 45 00.52	-25 22 02.2	B5	20.8	galaxy
12	266	12	00 44 50.23	-25 23 24.9	LA40	19.3	cluster
13	6552	70	00 44 39.18	-25 29 28.9	B7	20.1	galaxy

continued from previous page

ID	v_h ($km\,s^{-1}$)	v_{err} ($km\,s^{-1}$)	α(1950)	δ(1950)	Alternative ID	B (mag)	Classification
14	64590	18	00 44 39.52	-25 23 43.2	B8	20.4	galaxy
17	49540	89	00 45 33.02	-25 15 14.1	LA43	19.6	galaxy
18	40825	96	00 44 58.63	-25 29 35.0	B6	21.4	galaxy
19	10230	84	00 44 44.08	-25 31 32.6	B10	21.6	galaxy
20	17940	46	00 45 54.02	-25 37 01.9	B30	19.1	galaxy
21	28484	32	00 45 58.44	-25 31 42.2	B31	19.6	galaxy
22	16857	52	00 46 11.56	-25 33 27.1	LAA	16.0	galaxy
23	72749	21	00 46 22.16	-25 32 31.8	LA12	20.0	galaxy
24	55775	117	00 45 56.23	-25 32 31.3	LA20	19.5	galaxy
25	11	50	00 46 02.64	-25 33 47.8	LA17	18.4	star
26	64353	27	00 45 38.92	-25 31 33.8	B32	20.9	galaxy
27	5	45	00 45 49.27	-25 31 00.7	B33	16.5	star
28	228	85	00 46 17.91	-25 34 48.4	LA11	20.1	cluster
29	28629	50	00 45 57.56	-25 35 47.1	LAB	16.8	galaxy
30	44961	90	00 43 51.17	-25 30 12.4	LA51	18.1	galaxy
31	41919	102	00 44 03.39	-25 25 34.5	LA52	19.2	galaxy
32	19830	7	00 43 50.18	-25 36 11.2	LA34	19.2	galaxy
33	230	14	00 43 47.77	-25 36 29.0	LA35	17.6	cluster
35	33206	167	00 43 51.01	-25 38 50.1	LA29	19.6	galaxy
36	352	26	00 44 18.06	-25 34 05.8	B15	21.0	cluster
38	70834	30	00 44 14.58	-25 20 39.9	LA56	20.0	galaxy
39	339	56	00 44 13.07	-25 20 51.9	LA57	20.3	cluster
40	401	117	00 45 05.84	-25 39 53.7	LA24	19.4	cluster
41	218	22	00 45 20.65	-25 34 03.7	B29	22.3	cluster
42	313	85	00 45 05.14	-25 37 56.2	B24	21.0	cluster
43	40796	187	00 45 52.57	-25 42 13.9	LA8	19.3	galaxy
44	447	102	00 46 04.90	-25 45 18.7	LA3	19.7	cluster
45	57852	59	00 45 45.80	-25 39 51.5	B27	19.5	galaxy
46	89151	24	00 45 20.39	-25 34 59.1	B28	21.5	galaxy
47	38485	300	00 45 24.26	-25 36 59.2	B25	21.2	galaxy

continued from previous page

ID	v_h ($km\,s^{-1}$)	v_{err} ($km\,s^{-1}$)	α(1950)	δ(1950)	Alternative ID	B (mag)	Classification
50	28236	4	00 44 44.24	-25 40 59.8	B22	21.1	galaxy
51	10233	91	00 44 38.69	-25 34 57.5	LAb	19.4	galaxy
52	20863	82	00 44 49.22	-25 32 06.3	B11	19.6	galaxy
54	22927	27	00 44 34.79	-25 40 47.3	B20	18.8	galaxy
55	9865	364	00 44 19.47	-25 40 00.8	B19	20.7	galaxy
56	39522	102	00 44 38.88	-25 34 26.6	B16	21.6	galaxy
57	361	45	00 44 55.95	-25 32 03.2	B12	20.6	cluster
58	261	52	00 44 55.64	-25 32 44.6	B13	21.4	cluster
60	21522	76	00 43 48.08	-25 38 32.7	LAC	16.1	galaxy
61	302	22	00 44 55.98	-25 33 03.1	B14	20.2	cluster
62	71064	15	00 44 34.94	-25 36 03.6	B18	21.2	galaxy
63	21020	7	00 44 32.99	-25 43 48.5	B21	20.9	galaxy
64	406	10	00 44 47.76	-25 38 49.3	B23	20.3	galaxy

Table 2.5.: Globular cluster candidates in NGC 55.

Columns are: ID (fibre #), heliocentric velocity, velocity error, right ascension, declination, other designation, B magnitude and classification.

♣ LA ≡ (Liller & Alcaino 1983a) LAb & LAd are labelled as 'blue' objects in their paper. LAA, LAB & LAC are labelled as 'bright' objects.

Objects here denoted n,q,k,o,h,g,t,a & f were considered by Liller & Alcaino as being too blue for classical GCs, but were included for completeness.

♡ magnitudes from LA83a and B86

ID	v_h ($km\,s^{-1}$)	v_{err} ($km\,s^{-1}$)	α(1950)	δ(1950)	Alternative ID♣	$B^{\heartsuit}$ (mag)	Classification
1	66700	108	00 12 50.86	-39 17 25.9	LA61	19.0	galaxy
2	35229	101	00 12 43.09	-39 16 42.3	n	–	galaxy
3	68	45	00 12 40.60	-39 11 45.0	q	–	star
5	48	49	00 12 26.54	-39 22 12.1	k	–	star

continued from previous page

ID	v_h ($km\,s^{-1}$)	v_{err} ($km\,s^{-1}$)	α(1950)	δ(1950)	Alternative ID	B (mag)	Classification
7	32936	89	00 11 06.35	-39 39 43.8	LA5	19.8	galaxy
8	-58	80	00 12 43.35	-39 14 59.8	o	–	star
11	–	–	00 11 19.98	-39 24 55.2	LA46	19.6	QSO
12	49388	136	00 11 22.17	-39 24 23.3	LA48	19.6	galaxy
13	34933	84	00 11 05.77	-39 20 49.3	h	–	galaxy
15	26170	194	00 11 02.95	-39 16 20.8	LA58	20.7	galaxy
16	38076	123	00 11 09.12	-39 23 50.0	LA47	18.2	galaxy
17	19941	194	00 12 10.22	-39 26 17.8	g	–	galaxy
21	52918	18	00 11 08.98	-39 34 11.9	LA27	20.3	galaxy
23	96708	24	00 11 51.76	-39 32 44.5	LA36	20.6	galaxy
24	52935	24	00 11 12.27	-39 34 55.6	LA25	20.1	galaxy
25	17282	109	00 11 18.63	-39 36 06.9	LA20	19.7	galaxy
26	88804	24	00 11 13.40	-39 35 32.8	LA21	20.2	galaxy
27	-60	72	00 12 03.76	-39 29 43.2	LA45	19.8	star
29	35624	21	00 11 40.46	-39 32 56.6	LA32	18.9	galaxy
30	30855	94	00 12 28.05	-39 42 33.8	LA11	18.3	galaxy
31	26016	179	00 12 25.96	-39 42 50.8	LA9	20.5	galaxy
32	35060	14	00 12 38.50	-39 39 20.7	LA30	19.3	galaxy
33	47568	90	00 12 37.40	-39 40 28.2	LA26	19.5	galaxy
35	48265	18	00 12 09.95	-39 39 53.0	LA18	19.7	galaxy
36	71400	200	00 12 21.16	-39 42 38.3	LA8	20.2	galaxy
38	49814	108	00 12 19.71	-39 40 39.9	LA16	18.6	galaxy
39	30811	70	00 12 55.13	-39 41 44.8	t	–	galaxy
41	75000	144	00 12 57.40	-39 42 10.0	LA22	19.6	galaxy
42	74215	24	00 12 46.90	-39 44 50.0	LAd	–	galaxy
43	81546	103	00 11 55.57	-39 43 20.9	LA3	20.2	galaxy
44	32767	24	00 11 14.67	-39 40 35.8	LAb	–	galaxy
46	60311	305	00 11 54.10	-39 40 35.8	LA10	20.2	galaxy
47	30857	74	00 13 03.05	-39 43 37.4	LA15	16.9	galaxy
48	30868	62	00 13 00.49	-39 43 34.3	LA14	17.9	galaxy

continued from previous page

ID	v_h ($km\,s^{-1}$)	v_{err} ($km\,s^{-1}$)	α(1950)	δ(1950)	Alternative ID	B (mag)	Classification
49	60695	18	00 11 50.07	-39 46 19.8	a	–	galaxy
51	5089	122	00 12 52.95	-39 33 55.0	LA42	20.3	galaxy
52	52710	177	00 12 46.37	-39 35 20.7	LA39	19.2	galaxy
53	246	58	00 13 17.91	-39 35 19.7	LA43	17.1	cluster
54	37210	118	00 12 57.89	-39 36 43.5	LA37	20.4	galaxy
55	75407	27	00 12 24.29	-39 35 37.7	LA34	19.8	galaxy
56	92448	24	00 13 35.81	-39 25 23.7	LA59	20.3	galaxy
57	-142	70	00 12 28.78	-39 37 46.9	LA31	20.3	star
58	-111	53	00 13 23.85	-39 29 50.7	LA51	18.8	star
59	75971	104	00 13 29.40	-39 36 33.2	LA41	20.3	galaxy
60	31305	18	00 13 12.09	-39 37 15.9	f	–	galaxy
61	8763	39	00 11 55.37	-39 40 07.5	LAB	16.4	galaxy
62	32793	111	00 11 16.82	-39 39 21.0	LAA	16.7	galaxy
63	-29	56	00 13 02.95	-39 23 51.2	LAC	16.1	star
64	56585	12	00 12 44.39	-39 35 03.3	LA40	20.6	galaxy

Even without consideration of their radial velocities (see § 2.3.2), inspection of the spectra reveals much about the nature of the candidate clusters. In Figure 2.2 we show spectra of three GC candidates in NGC 253. Candidate #27 in NGC 253 (B 33), presents the spectrum of a K2 dwarf, and shows strong metal lines (e.g. magnesium at $\sim$ 5200 Å). Candidate #32 (LA 34) is a background galaxy, with strong emission in [O II], [O III] and Hβ. In the top panel of Figure 2.2, we show the spectrum of the brightest identified GC #33, (LA 35) with B $\sim$17.6. Its spectrum appears metal-poor and absorption in calcium K & H and Hβ (4861 Å) is evident.

2.3.2 Identification of Globular Clusters

All our GC candidates have been classified as extended objects on the basis of visual inspection of photographic plates (e.g. LA83a, LA83b) or profile analysis (B86). The main source of contamination in the samples should therefore stem from background galaxies. The systemic velocity

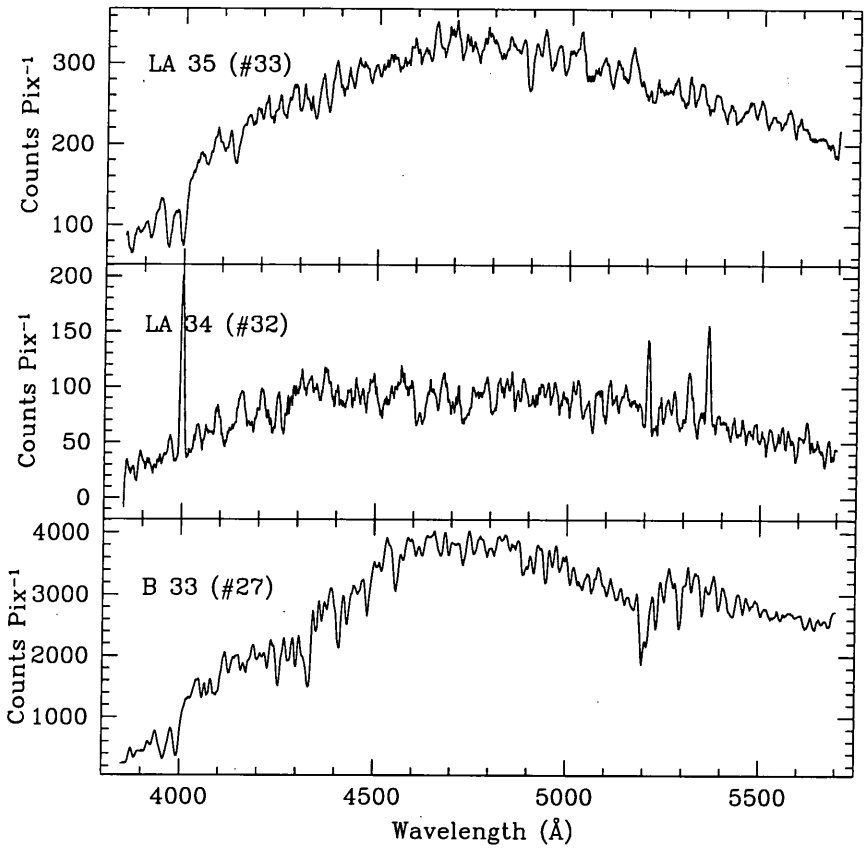

Figure 2.2: Spectra of globular cluster candidates around NGC 253. From top to bottom they are identified as: a GC, v_h = 228 ± 85 km s^{-1}, a background galaxy, v_h = 19830 ± 7 km s^{-1} and a foreground galactic star, v_h = 5 ± 45 km s^{-1}. The galaxy shows emission lines of [O II], [O III] and Hβ, whilst the spectrum of the GC shows clear absorption in H&K, Hβ and magnesium. The spectra have been smoothed with a 3–pixel boxcar filter.

of the Sculptor group is low, (V_{N55} = 121 km s^{-1}; V_{N253} = 240 km s^{-1}), so we have taken a velocity cut at v_h = 1000 km s^{-1}. We assume that all objects above this threshold are background galaxies. A large number of the spectra exhibit emission lines of [O II], [O III], Hβ or Hγ and, with the exception of candidate #64 in NGC 253 (see later), these objects all have $v_h > 1000$ km s^{-1}.

Having removed background galaxies in such a manner should effectively leave a sample consisting of objects which are either contaminating foreground Galactic stars, or GCs within the Sculptor group. For GCs in the Milky Way, Armandroff (1988) gives a velocity dispersion of σ = 100 km s^{-1}. Under the assumption that mass scales approximately with σ^2, and the $\mathcal{M}/L$ ratios of the Milky Way and the two Sculptor spirals are comparable, then the expected velocity dispersion for the halo clusters in NGC 55 and NGC 253 will be $\sim$ 70 km s^{-1}. This value is the same as that found by Schommer et al. (1991) for the GCS of the nearby Sc spiral M 33, which has

a comparable magnitude ($M_V \sim$ -19.4) to NGC 253 and NGC 55. Therefore, we take the velocity ranges ($\pm$ 3 σ from the mean velocity) for possible clusters to be: -80 $\leq V_{\rm N55} \leq$ 340 km s^{-1} and 35 $\leq V_{\rm N253} \leq$ 455 km s^{-1} for NGC 55 and NGC 253 respectively. We show histograms for the velocities from Tables 2.4 and 2.5 in Figure 2.3. The shaded areas in the figure indicate the velocity space in which we expect GCs to fall for the two galaxies. Figure 2.3 illustrates that background galaxies and stars/GCs are clearly delineated on the basis of velocity.

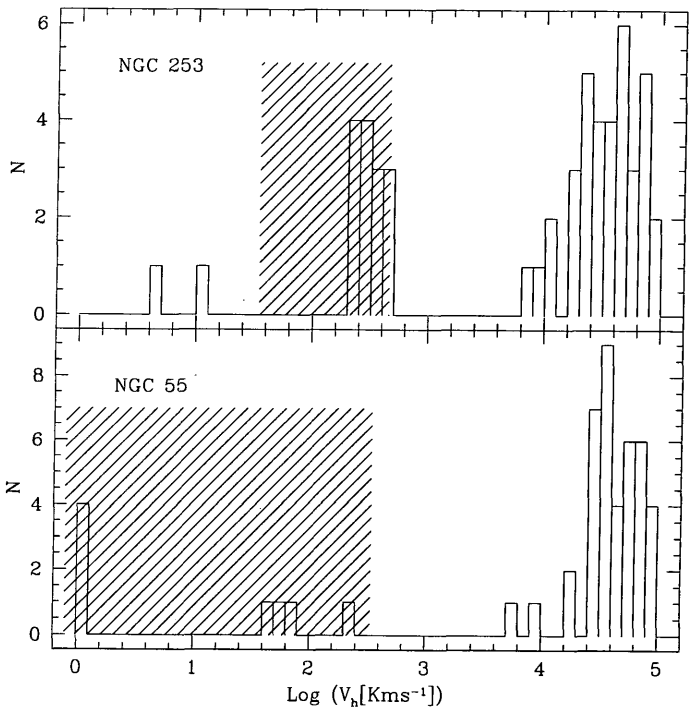

Figure 2.3: Histogram of logarithmic velocities for our globular cluster candidates in NGC 253 and NGC 55. The shaded region indicates the velocity space where we expect to find genuine GCs.

Since at some level there will be an overlap between high velocity foreground stars and GCs in the Sculptor group, distinguishing between these two cases relies on identifying true clusters as marginally extended objects.

Fifteen NGC 253 cluster candidates fall within the velocity range expected for GCs, and appear marginally resolved on images from the DSS. Object #64 has a radial velocity of $v_{\rm h} = 404 \pm 10$ km s^{-1}, but shows emission lines of [O III], Hβ and Hγ. DSS images of this object reveal no real clues as to its nature, but do show that it is projected against the bright background of the galaxy. The radial velocities derived from its emission lines and from cross-correlation (after interpolation over the emission lines) are in excellent agreement, arguing against a superposition

of objects. We have therefore classified object #64 as 'a galaxy'. Two of the candidates, #25 and #27, have radial velocities which fall just short of the velocity cut. The appearance of their images, spectra (e.g. see lower panel of Figure 2.2) and their COSMOS image parameters (see § 2.5.1) point towards a Galactic origin; on this basis they have been identified as foreground stars. Objects #40 and #44 both have relatively large radial velocities in comparison to the systemic velocity of NGC 253, with $v_{\rm h} = 401 \pm 117$ km s^{-1} and $v_{\rm h} = 447 \pm 102$ km s^{-1} respectively. However, the large errors reflect the significant degree of scatter between velocity templates, where their cross–correlations were close to the normalised peak height cut–off at 0.1 (both spectra were of rather low S/N). Since they fall within the velocity range expected, and appear marginally extended in DSS images, they have been left in the sample. In Table 2.6 we list those objects in NGC 253 which we identify as GCs.

Table 2.6. Objects in the NGC 253 sample identified as globular clusters. From left to right the columns give: ID, radial velocity, velocity error, other identification, B magnitude, $B - V$ colour and COSMOS ellipticity.

ID	$v_{\rm h}$	$v_{\rm err}$	Other ID	B	$B-V$	ϵ
	km s^{-1}	km s^{-1}		(mag)	(mag)	
7	212	74	B1	21.1	0.19	–
8	235	28	LA26	20.0	0.68	0.28
12	266	12	LA40	19.3	0.89	0.07
28	228	85	LA11	20.1	0.70	0.12
33	230	14	LA35	17.6	0.77	–
36	352	26	B15	21.0	0.94	0.23
39	339	56	LA57	20.3	0.85	0.08
40	401	117	LA24	19.4	0.97	–
41	218	22	B29	22.3	1.80	0.22
42	313	85	B24	21.0	0.86	0.22
44	447	102	LA3	19.7	0.94	–
57	361	45	B12	20.6	0.85	0.19
58	261	52	B13	21.4	0.74	0.10
61	302	22	B14	20.2	0.54	–

In the NGC 55 sample, there are six objects that are not galaxies and fall within the velocity cut for GCs. However, all but one of these appear point–like and lie on the stellar locus of the COSMOS plate scans. Object #53 has $v_{\rm h} = 246 \pm 58$ km s^{-1} and lies within 2 σ of the galaxies' systemic velocity. Images of this object show some elongation, and an isophotal plot indicates a round, marginally extended source blended with another object.[1] On the basis of this, we classify #53 as a likely GC. At $B = 17.1$ $(B - V = 0.76)$, cluster #53 is bright but not unreasonably so. At the adopted distance to NGC 55 of 2.0 Mpc, $(m - M)_o = 26.5$, gives the cluster M_B = -9.4, similar to the luminous Galactic globular cluster ω Cen (Harris 1996).

Object #11 presents an interesting spectrum, which we show in Figure. 2.4. We have identified this objects as a broad absorption line (BAL) QSO with redshift, z ~2.7. Emission in N V and C IV is shown, although absorption shortward of N V is so strong in this QSO that no Lyα emission is observed. This type of spectrum is occasionally seen in 'peculiar' BAL QSOs (e.g. Korista et al. 1995).

We note that there are a number of galaxies in Tables 2.4 and 2.5 which have very similar radial velocities. These are perhaps members of background galaxy clusters. In particular, in the NGC 55 sample there are four galaxies (#30, #39, #47 and #48) with mean velocity $v_{\rm h} = 30848$ km s^{-1}, $\sigma = 13$ km s^{-1} ($z \sim 0.1$). These galaxies are all located in the region $\alpha = 00^{\rm h}12^{\rm m}30^{\rm s}$, $\delta = -39°42'$ (1950.0 epoch), covering an angular diameter of $\sim 1.9'$ on the sky. At an assumed distance of 470 Mpc (65 km s^{-1} Mpc^{-1}), this corresponds to a separation of $\sim$ 260 Kpc.

2.4 Properties of the Globular Cluster Systems

2.4.1 Velocity and Spatial Distribution

We find that the sample in Table 2.6 has a mean velocity $\bar{v_{\rm h}} = 297$ km s^{-1} with a velocity dispersion, $\sigma = 74$ km s^{-1}. Omitting objects #40 and #44 yields $\bar{v_{\rm h}} = 276$ km s^{-1} and $\sigma = 55$ km s^{-1}. Both the mean velocity of the clusters, and their velocity dispersion is entirely consistent with values expected for the NGC 253 GCS. Twelve of the clusters fall into the 'classical' colour region for GCs, with $0.5 < B - V < 1.25$ (e.g. B86; Ashman & Zepf 1998). Cluster #7 (B1) is very blue, with $B - V = 0.19$. Its spectrum shows strong Balmer absorption lines, and may be analogous to the blue clusters seen in the Magellanic Clouds (e.g. Bica, Claria, & Dottori 1992). Indeed, cross-correlation with spectra of LMC star clusters (see Chapter 4), gives the best agreement with

[1] In their catalogue, LA83a indicate that object #53 (LA43) is separated by 5.″9 from a fainter companion.

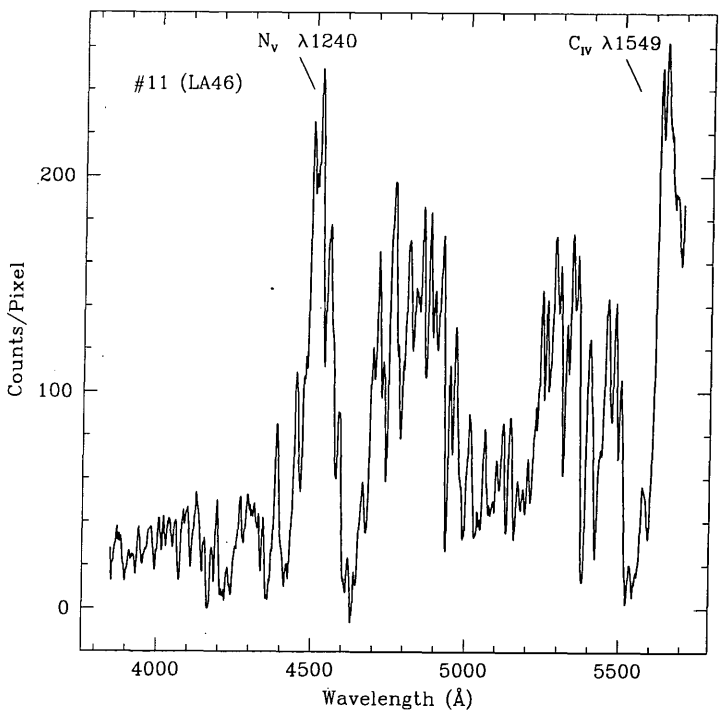

Figure 2.4: Object #11 in the NGC 55 spectroscopic sample, identified as a broad absorption line (BAL) QSO at $z \sim 2.7$. Emission in N V and C IV is indicated, with their corresponding UV rest–frame wavelengths.

SWB II-III types (i.e. young, $\sim$ 100 Myr). We additionally note that this clusters it is close to the disk of NGC 253.

The colour of cluster #41 is surprisingly red, with $B - V = 1.8$. The stellar population models of Worthey (1994) predict ages > 12 Gyr and [Fe/H] $\geq +0.2$ for this colour. However, we believe this interpretation is unlikely, and that the cluster is probably highly reddened due to its proximity to the disk of NGC 253.

We show the spatial distribution of the 14 objects identified as GCs in NGC 253 in Figure 2.5, the field is 40 $'$ on a side. The distribution of cluster velocities is interesting; the clusters predominantly recede with respect to the galaxy rest–frame in the SW part of the galaxy and approach in the NE. This is consistent with the direction of rotation of the galaxy, as measured from Hα rotation curves (Pence 1980). However, due to the small numbers of clusters, the level of rotation is not statistically significant.

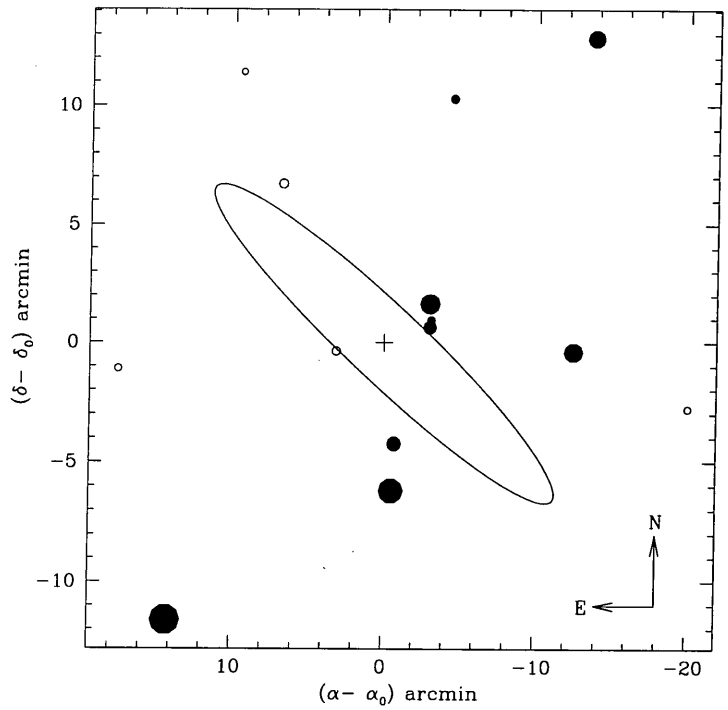

Figure 2.5: Distribution of identified globular clusters about NGC 253. Symbol size represents the magnitude of the globular cluster radial velocity with respect to the galaxy rest frame (systemic velocity $V_{\rm N253} = 240$ kms^{-1}). Open circles represent approaching clusters, filled circles indicate receding clusters in this scheme. The centre of the coordinate system is that of NGC 253, $\alpha(2000) = 00^{\rm h}47^{\rm m}33^{\rm s}$, $\delta(2000) = -25°17'18''$. The ellipse indicates the orientation of the galaxy on the sky, with a position angle of the major axis of 52° (de Vaucouleurs et al. 1991).

2.4.2 Metallicities of the Globular Clusters

The S/N of our cluster spectra is 4∼18, precluding individual measurements of their line-strengths. However, by combining them into a composite spectrum, yields a higher S/N 'mean' spectrum from which we may measure metallicities from individual indices. There is no known correlation between the absolute magnitude and metallicity of GCs in the Galaxy or M 31 (e.g. Perelmuter, Brodie, & Huchra 1995). Therefore, whilst we almost certainly sample the brightest clusters in NGC 253, their mean metallicity should give some insight into the global mean metallicity of the NGC 253 GCS.

In Figure 2.6 we show the spectra of the NGC 253 GCs, arranged in ascending order of S/N (top–left to bottom–right). The spectrum in the bottom–right of Figure 2.6 is the final, co-added spectrum with a resulting S/N of ~ 40. Prior to co-addition, all these spectra were corrected to the rest-frame via their respective radial velocities.

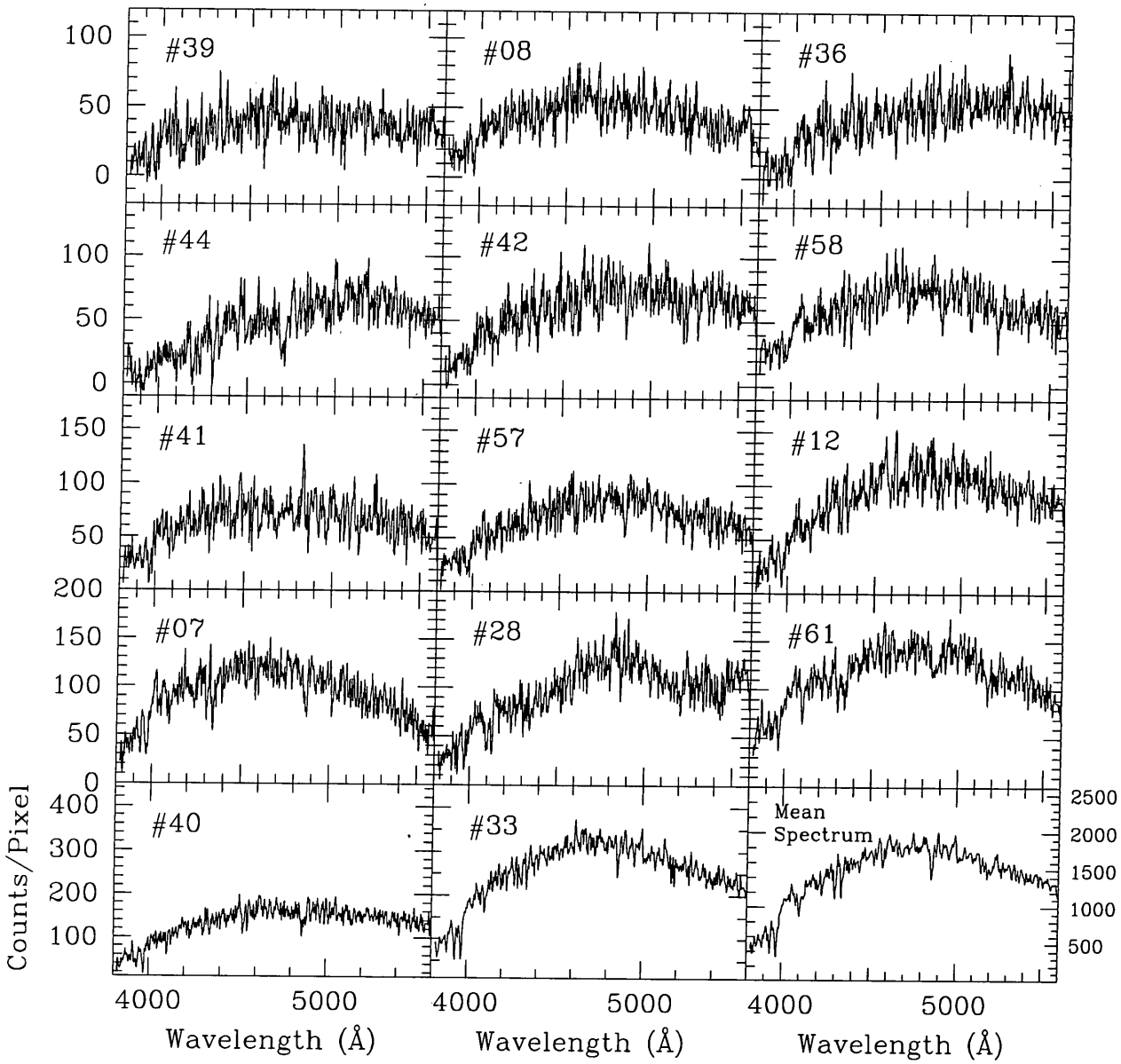

Figure 2.6: The spectra of the NGC 253 globular clusters, arranged in ascending order of signal-to-noise (from top–left to bottom–right). The bottom–right spectrum is the resultant, co-added spectrum of all the clusters. The spectra have been smoothed with a 3–pixel boxcar filter. Note the change of scale on the final, co-added spectrum.

We measure line-strength indices defined by Brodie & Huchra (1990), and use these author's metallicity calibration, based on Galactic and M 31 GCs, to obtain metallicities for our mean spectrum (see Chapter 3 for more details on the line-strength measurement, and metallicity calibration of Brodie & Huchra 1990). Brodie & Huchra define six 'primary calibrators' for metallicity in optical spectra, four of which fall within our useful spectral range (4000–5600 Å), these are Mg_2,

MgH, the G band (CH) and Fe52 (using the nomenclature of Brodie & Huchra 1990). In addition, they also give two 'secondary' calibrators, CNR (cyanogen) and HK (the calcium H and K lines) which we have measured in our co-added spectrum. We measure the (pseudo) equivalent widths of each index, and convert them into line-strength magnitudes (with the exception of Mg_2, which is measured as a magnitude). Then, using the empirical calibrations of Brodie & Huchra (1990), we convert these indices into metallicities. We weight the measured indices by their respective uncertainties obtained from the bootstrap procedure described in Chapter 3, and in accordance with the prescription of Brodie & Huchra (1990). We list the measured indices, their respective weights and resultant metallicity predictions in Table 2.7. From the co-added spectrum, we obtain a mean metallicity of Fe/H = -1.23 $\pm$ 0.19.

Table 2.7. Line-strengths of NGC 253 globular clusters.

Index	I(mag)	w_i	[Fe/H]
HK	0.241	0.115	-1.32
CNR	-0.088	0.050	-1.84
G Band	0.123	0.235	-1.04
MgH	0.016	0.200	-1.52
Mg_2	0.075	0.180	-1.47
Fe52	0.071	0.220	-0.64
$\overline{[Fe/H]}$			-1.23 $\pm$ 0.19

For comparison, the $B - V$ colours of the GCs in Table 2.6 may be translated in metallicities using an appropriate colour-metallicity relation. Couture, Harris, & Allwright (1990) derive such a relation for 64 Galactic GCs, using metallicities from Zinn & West (1984) and the $B - V$ colours given by Reed, Hesser, & Shawl (1988). With the benefit of updated colours and metallicities (and with a larger sample size) we re-examine this relation.[2] For this purpose, we have taken $B - V$ colours and metallicities for Galactic GCs from the McMaster database (Harris 1996) and plot them in Figure 2.7.

[2] It would be desirable to have the addition of a bluer bandpass (e.g. U) both in terms of greater metallicity sensitivity and to determine the reddening vector in the $U - B : B - V$ plane. Unfortunately, the data of LA83a,LA83b and B86 only consists of the $B - V$ colours.

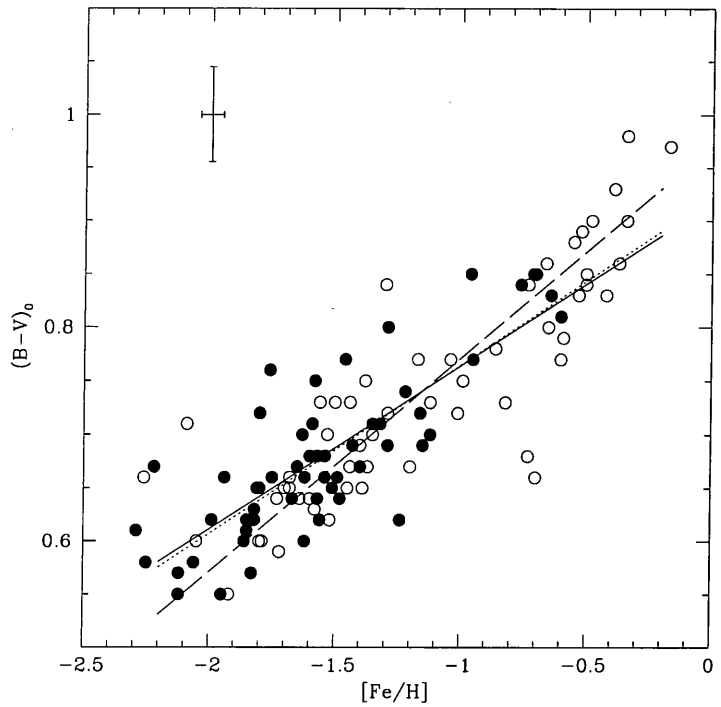

Figure 2.7: Relation between integrated $B - V$ colours and metallicity for Milky Way GCs. These data have been taken from from the McMaster database of Harris (1996). Filled circles indicate those clusters with $E_{B-V} \leq 0.25$. The dotted line represents a least–squares fit to these clusters, the solid line is a fit to the entire data. We also show the relation obtained by Couture, Harris, & Allwright (1990) (long dashed line).

We have de-reddened the $B - V$ colours using the E_{B-V} values given by Harris (1996). A linear least-squares fit to the entire sample of 113 GCs yields:

$$(B - V)_0 = 0.158 \times [\text{Fe/H}] + 0.922 \tag{2.1}$$

In order to assess the uncertainties arising from highly reddened clusters, we have also repeated the fit to GCs with $E_{B-V} \leq 0.25$ (filled circles in Figure 2.7). We obtain from the resulting 57 clusters:

$$(B - V)_0 = 0.153 \times [\text{Fe/H}] + 0.917 \tag{2.2}$$

The scatter in Equations 2.1 and 2.2 are 0.05 and 0.044 respectively. Since the two relations are functionally very similar, we adopt Equation 2.1 due to the factor of two larger sample size used in its derivation. Equation 2.1 is valid for -2.5 $\leq$ [Fe/H] $\leq$ 0, corresponding to $B - V$ colours of

$0.53 \leq (B-V) \leq 0.92$. Equation 2.1 is slightly flatter than that derived by Couture, Harris, & Allwright (1990):

$$(B-V)_0 = 0.2 \times [\mathrm{Fe/H}] + 0.971 \tag{2.3}$$

We predict somewhat higher metallicities for $B-V >$ =0.75, with a difference of $\sim$ 0.25 dex at $B-V = 0.92$, the red limit of our relation.

Excluding the reddest ($B-V$=1.8) cluster, the mean colour of the GCs in NGC 253 is $B-V$ = 0.76 $\pm$ 0.06 (where the uncertainty is the standard deviation on the mean of the colours). Using Equation 2.1, gives a mean metallicity for the clusters of [Fe/H]=-1.02 $\pm$ 0.39 dex. This compares favourably with the spectroscopic value of -1.23 $\pm$ 0.19 dex. Given the smaller formal uncertainties in the spectroscopic value, and the fact that the colours may be significantly affected by reddening, we adopt the spectroscopic value as the mean metallicity if our sample of NGC 253 GCs. Clearly, on the basis of one object little can be said about the metallicities on the NGC 55 globular clusters. Nevertheless, at *prima facae*, the colour of #53 in NGC 55 ($B-V$=0.76) corresponds to a metallicity of -1.02 dex.

2.5 Definition of a New Sample of Globular Clusters

The cluster samples selected by LA83a and LA83b are based on the visual inspection of photographic plates. Clearly such selection is prone to subjective errors and saturation effects. A more quantitative approach was taken by B86 by using electronographic plates, but as can be seen from Table 2.4, even this sample is contaminated by both foreground stars and background galaxies. In this section we explore the use of image parameters obtained by the COSMOS measuring machine (MacGillivray & Stobie 1984) in order to identify new samples of GCs around NGC 253 and NGC 55.

2.5.1 COSMOS Plate Scans

COSMOS is a powerful scanning machine, designed to digitize astronomical photographic plates in order to produce high-resolution pixel data (MacGillivray & Stobie 1984). The machine produces a raster map, by converting photographic plate-density into intensities via calibration 'spots' on the plate. Discrete objects in the scans are identified by applying a threshold at some percentage above the locally calculated sky level. Image parameters are then derived for each object on the

basis of its moments, up to the second order. The COSMOS image identification algorithm has since been extended to deal with very crowded fields and blended objects (Beard, MacGillivray, & Thanisch 1990).

AAT prime focus plates of the Sculptor group spirals, NGC 55 and NGC 253, were raster scanned with the COSMOS facility using the mapping mode, with a step size of 16 μm and a 16 μm spot size. The image area threshold was set to 10 pixels (plate scale 15.3 arcsec mm^{-1}), with all pixels above this threshold being grouped into discrete objects. We give details of the plates scanned in Table 2.8.

Table 2.8. Prime focus plates scanned using COSMOS

Plate	Object	Date	Exp. Time (min)	Emulsion	Filter
1739	NGC 253	20–10–79	80	IIIa–J	GG385
1740	NGC 55	20–10–79	90	IIIa–J	GG385

The COSMOS image analysis software was then run on each digitized frame to provide a list of objects with information on position, magnitude, orientation, axial ratio (major and minor axis lengths) and area. An area of approximately five pixels was removed around the perimeter of each scan which mainly contained noise and plate defects. We calibrated the COSMOS instrumental magnitudes using the photoelectric sequences of Hanes & Grieve (1982), and Alcaino & Liller (1984).[3] Alcaino & Liller (1984) give V magnitudes and colours for 24 stars down to V = 16.95 ($B - V$ = 0.59) in the field of NGC 55, and for 19 stars to V = 16.53 ($B - V$ = 0.74) in the vicinity of NGC 253. Those from Hanes & Grieve (1982) are somewhat brighter, in the range $9 \leq V \leq 14$ for the two galaxies. There are a total of ten overlaps between their photometric sequences, with six in the NGC 253 field and four in the NGC 55 field. Both give good agreement, with a mean B magnitude offset, $\Delta_B = 0.025$ mag, $\sigma = 0.06$ and $\Delta_B = 0.045$ mag, $\sigma = 0.03$ for NGC 253 and NGC 55 respectively. For calibration at the faint end, the cluster candidates reached down to $B \sim 21$, and a faint star ($B = 21.3$) from the New Luyten Two–Tenths catalogue (NLTT) (Warren et al. 1989) was also used for the calibration of plate J1739. [4] In Figure 2.8 we

[3] It should be noted for future reference that the star designated as V on their finding chart 38 for NGC 253 is tabulated as P in the paper.

[4] There is significant disagreement between Blecha's and Liller & Alcaino's photometry. In some instances the data differs by a full magnitude for the same object. This is seen in the COSMOS data, where Blecha's candidates are

show the best–fitting calibration curve for the COSMOS instrumental magnitudes for NGC 55. A least–squares fit to the data yields an rms of 0.2 mag. The photometric calibration for NGC 253 shown in Figure 2.9 shows greater scatter, with $\sigma = 0.5$ mag. The origin of this larger scatter in the NGC 253 plate is unknown, but is seen over the entire magnitude range.

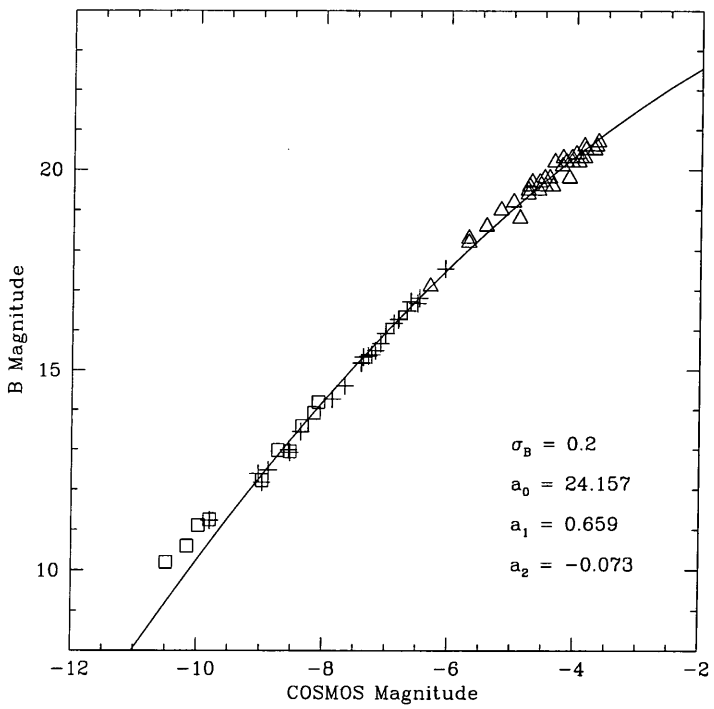

Figure 2.8: NGC 55: Correlation between COSMOS instrumental magnitudes and photometry of LA83a, Alcaino & Liller (1984) and Hanes & Grieve (1982). Alcaino & Liller's photometric stars are shown as crosses, Hanes & Grieve stars are open squares. Cluster candidates are shown as open triangles. A least–squares fit to the data gives a formal error in B of $\sigma = 0.2$ mag.

We have obtained an astrometric solution for the COSMOS scans so as to locate spectroscopically identified objects from this work within the COSMOS datasets. The typical astrometry plate residuals were of order $\sim 0\farcs3$.

2.5.2 A New Cluster Sample

We identify GC candidates from the COSMOS plate scans by their image moments; both on the basis of their ellipticity and residual image area. To place meaningful constraints on these image

systematically fainter. For internal consistency, only Liller & Alcaino's photometry was used for the calibration of the J1739 plate.

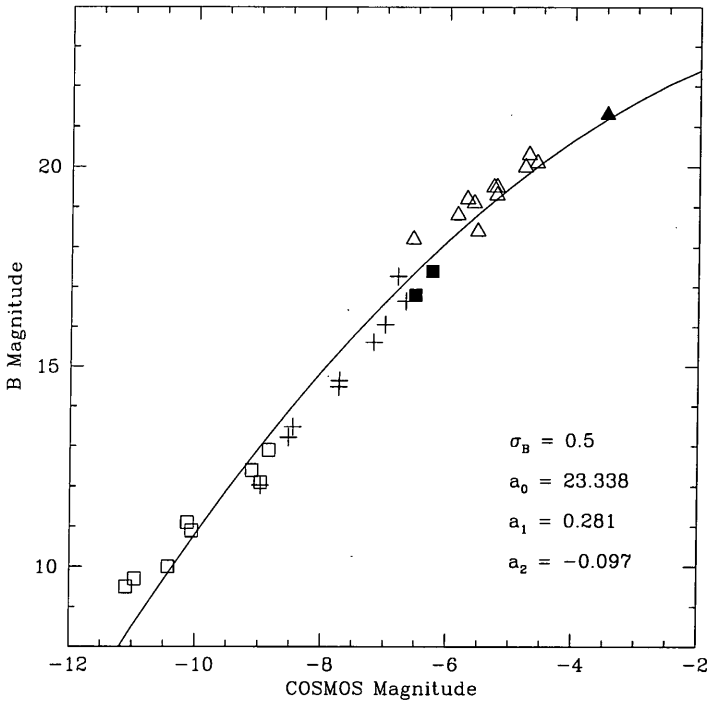

Figure 2.9: NGC 253: Correlation between COSMOS instrumental magnitudes and photometry of LA83b (open triangles), Alcaino & Liller (1984) (crosses) and Hanes & Grieve (1982) (open squares). Also plotted as a filled triangle is a faint star (B = 21.3) from the NLTT catalogue (Warren et al. 1989) and two additional stars obtained from the SIMBAD database (filled squares). A least–squares fit to the data gives a formal error in B of $\sigma = 0.5$ mag.

parameters, we assume that the 'classical' GCs in NGC 55 and NGC 253 have physical appearances similar to those in the Galaxy. This is not an unreasonable assumption, GCs in external galaxies are known to have half-light radii and ellipticities similar to Milky Way GCs (Ashman & Zepf 1998).

The ellipticity for each COSMOS object was derived from its measured image moments, where ellipticity is defined as $\epsilon = 1 - b/a$ (b and a are the measured semi–minor and semi–major axes respectively). For both plates, an ellipticity limit was set at approximately three times the rms stellar ellipticity, ($\epsilon \sim 0.30$) above which threshold objects were classified as being either truly elliptical or a blend of two or more objects (e.g. Harris et al. 1984). White & Shawl (1987) find a mean ellipticity of 0.93 ± 0.01 (i.e. 0.07 ± 0.01 in our definition of ellipticity) for the Milky Way GCs. We have set an ellipticity limit slightly higher than their maximum value of 0.75 (i.e. $\epsilon \sim 0.25$), and more in line with the range described by the LMC clusters of $0.05 \leq \epsilon \leq 0.3$ (Goodwin 1997). Our object ellipticity showed only a weak dependence on magnitude, in the sense that, at fainter magnitudes, the numbers of elliptical objects *marginally* increased. This was not a strong

trend, and fainter GCs should not be discriminated against in this scheme (the limits which define elliptical images increase towards fainter magnitudes).

A powerful diagnostic to test for the extended nature of the candidates is the measured COSMOS image area as a function of magnitude. In Figures 2.10 and 2.11 we show the logarithm of the image area (in pixels) against magnitude for COSMOS objects in the magnitude range $16 \leq B \leq 22$. The sharply defined sequence is the stellar locus arising from foreground stars. Extended objects show an excess of area for their magnitude, and are raised from this stellar sequence (Harris et al. 1984). Our spectroscopic candidates were located in the COSMOS data by searching for the appropriate right ascension and declination, with a 3-σ tolerance ($\sim 1''.0$). Where several objects were found in the same location, a comparison of the calibrated magnitudes distinguished between candidates in our sample and foreground/background objects. Da Costa & Graham (1982) identify three bright star clusters with $V \sim 17$ near the centre of NGC 55, one of which was returned in the COSMOS data and is indicated by a triangle in Figure 2.10. The two remaining clusters, along with a number of other cluster candidates failed to be found. These objects are all seen in projection close to the disks of the two galaxies, and were presumably lost in the bright local background. Also, it should be noted that whilst the spectroscopic sample went out to radii comparable with that of the plate scans, NGC 253 was slightly offset from the centre of the COSMOS field, and consequently some candidates fell outside the scanning limits (on the western side of the plate).

In order to quantify the excess in area shown by genuinely extended objects, and to differentiate between object types (stars, galaxies and GCs) a line was fit to the stellar sequence and a residual area, δA, for each object calculated. Figures 2.12 and 2.13 show the results of this exercise, where $\delta A = 0$ corresponds to the stellar locus. Several points are evident from these figures. The scatter in δA is somewhat greater in NGC 253 than in NGC 55, with its the stellar locus being less well constrained (reflecting perhaps the larger photometry residuals – see § 2.5.1). Those objects which lie on the stellar locus, which we have identified spectroscopically, all have radial velocities consistent with foreground stars, and appear point–like on Sky Survey images. The galaxies are located well above the stars, and follow a similar distribution for both fields, their residual areas increase strongly as a function of magnitude. The candidates which we have identified as GCs largely inhabit a parameter space *between* the stars and galaxies, although some overlap is apparent.

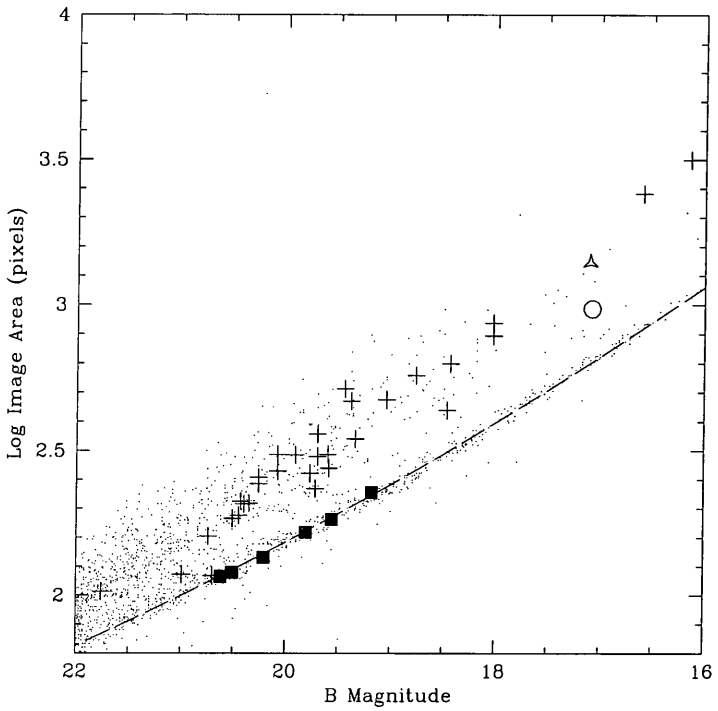

Figure 2.10: Log image area versus magnitude for objects in NGC 55. A subset of the COSMOS objects are plotted as points, confirmed galaxies are crosses and stars are represented by filled squares. The open triangle indicates cluster #1 of Da Costa & Graham (1982) and the position of the GC identified in this work is indicated by an open circle. The dashed line shows the fit applied to the stellar sequence.

In Figures 2.12 and 2.13 we plot the model predictions of Harris et al. (1984), scaled to the adopted distance of NGC 55 and NGC 253 (2.0 Mpc and 2.5 Mpc respectively). These models where created by applying the COSMOS algorithm to a set of model cluster images with a range of magnitudes and assume a King (King 1966) profile (see Equations 4.1 and 4.2 in Chapter 4). The models shown in Figures 2.12 and 2.13 have $r_t/r_c = 30$, although models with other concentration parameters ($r_t/r_c = 6 \sim 100$) show similar characteristics (Harris et al. 1984). The lines for model clusters with size = 1 possess core radii of 1.5 pc and tidal radii of 45 pc (0.″15 and 4.″6 respectively at 2 Mpc). Sizes 2 and 3 are correspondingly twice and three times as large. Six of the spectroscopically identified GCs in NGC 253 lie below the size = 3 model line, with the remaining three lying marginally above this. The apparent size of clusters on the sky will be sensitive to the assumed distance to the two galaxies, and as pointed out by Harris et al. (1984), each plate exhibits slightly different behaviour due to saturation effects and their individual isophotal thresholds (in fact Harris et al. indicate that magnitudes can be in error by as much 0.6 mag for the most extended GC candidates). The cluster of Da Costa & Graham

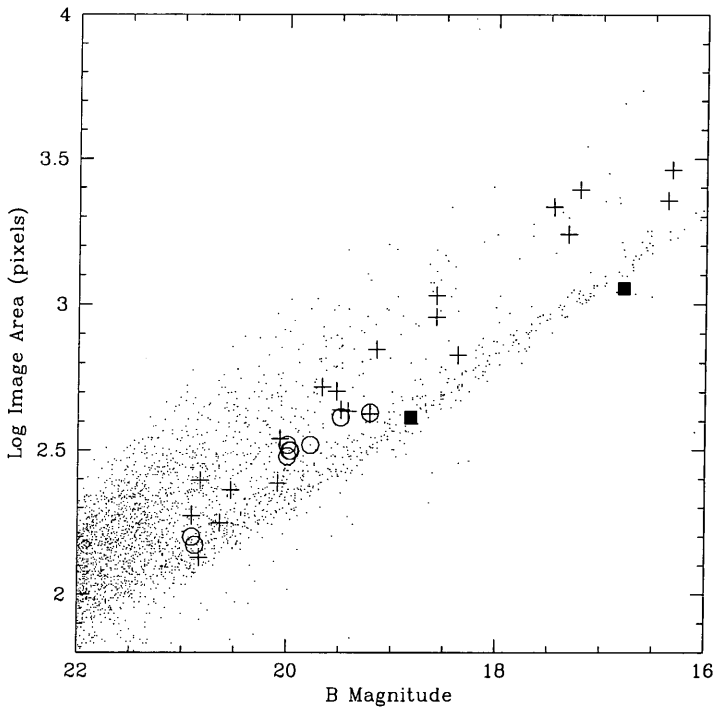

Figure 2.11: Log image area versus magnitude for objects in NGC 253. A subset of the COSMOS objects are plotted as points, confirmed galaxies are crosses, stars are represented by filled squares and the open circles indicate confirmed globular clusters.

(1982) shown in Figure 2.12 shows characteristics more like that of the galaxies than the other GCs, though DSS images of this object show an extremely bright and confused background which could possibly confuse the analysis software.[5]

The regions of parameter space which we expect contain GCs are delimited in Figures 2.12 and 2.13 by the long dashed lines. We have set the lower limit (above the stellar locus) to be 3 σ from the mean stellar area residual. The upper limit corresponds to size = 4 model clusters and was chosen so as to include as many cluster candidates as possible, whilst minimizing contamination from background galaxies. We define our new sample to lie within these limits. We note that the degree of crowding increases significantly at fainter magnitudes, therefore we have taken a magnitude cut at $B \sim 20.5$. As a final measure, we have visually examined images of each of the candidates for obvious stellar appearance or any structure indicative of a background galaxy. We identify 20 objects in total which appear distinctly 'un–cluster–like' and these were removed from

[5] There is little chance of a misidentification by Da Costa & Graham between their globular cluster and a background galaxy. They obtain a radial velocity for their cluster of $v_h = 106 \pm 8$ kms^{-1} and it is seen in projection against the stellar light of NGC 55.

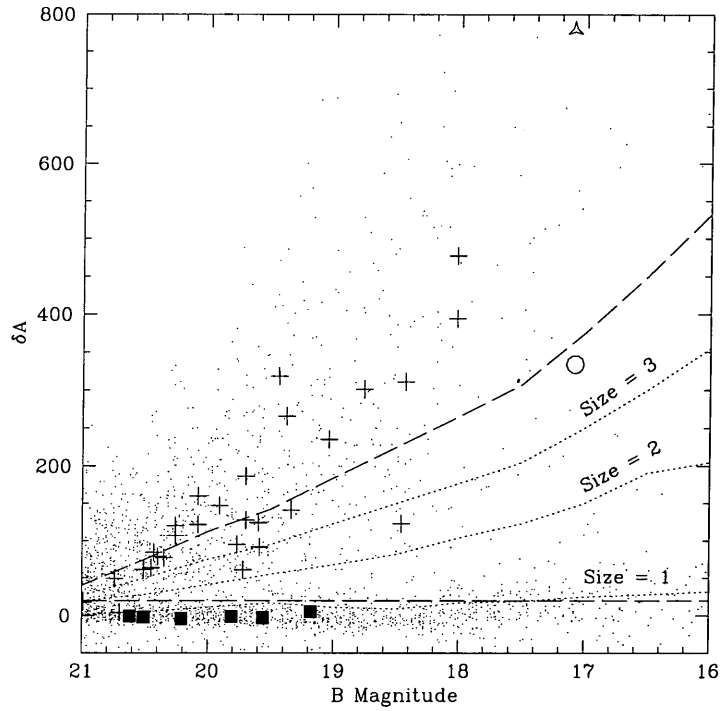

Figure 2.12: Area residuals of round candidates in NGC 55. The residual δA =0 corresponds to the stellar locus. Confirmed galaxies are shown as crosses, stars are indicated by filled squares. The probable GC is shown as an open circle. Dotted lines are the cluster models of Harris et al. (1984). The long dashed lines indicate the parameter space containing new globular cluster candidates.

the sample. From the initial datasets, 91 GC candidates have been identified in NGC 253 and 84 in NGC 55. In Table 2.9 we list the positions and approximate B magnitudes of the new cluster candidate samples.

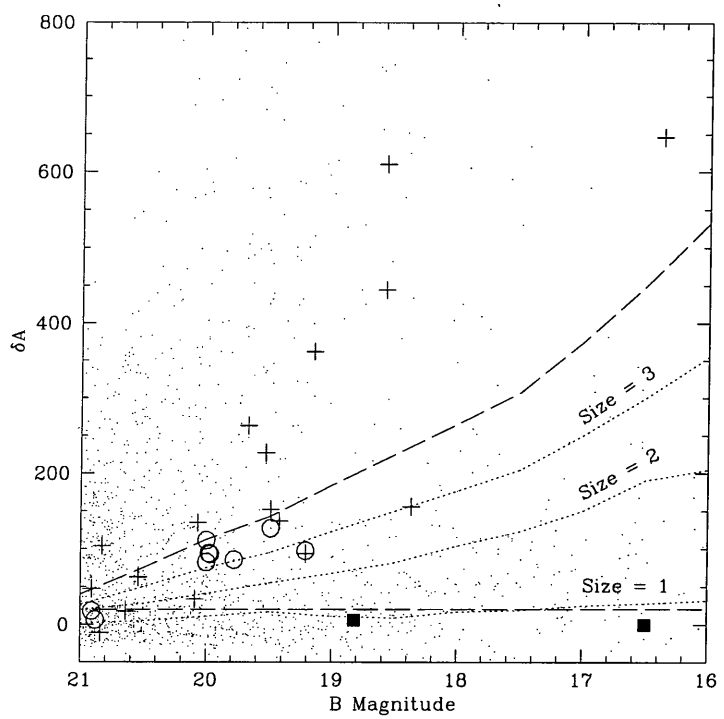

Figure 2.13: Residuals in area for objects in the NGC 253 field. Symbols are as for previous figure.

Table 2.9.: New globular cluster candidates in NGC 253 and NGC 55.

NGC 253				NGC 55			
ID	α(1950)	δ(1950)	B	ID	α(1950)	δ(1950)	B
1	0 44 7.68	-25 39 16.1	18.37	1	0 13 3.46	-39 38 55.7	18.69
2	0 46 44.19	-25 29 40.4	18.46	2	0 12 57.83	-39 26 3.6	18.70
3	0 46 59.32	-25 30 24.6	18.47	3	0 14 24.19	-39 15 25.7	18.72
4	0 43 54.34	-25 9 47.0	18.53	4	0 10 47.66	-39 37 41.6	18.72
5	0 44 26.32	-25 34 44.3	18.54	5	0 15 0.86	-39 35 45.1	18.86
6	0 47 1.08	-25 39 17.8	18.60	6	0 11 29.17	-39 19 43.2	18.87
7	0 46 54.30	-25 36 15.5	18.67	7	0 11 1.67	-39 53 41.0	18.87
8	0 44 8.25	-25 22 19.4	18.68	8	0 13 48.19	-39 14 29.4	18.91
9	0 44 47.79	-25 32 9.6	18.76	9	0 12 42.25	-39 1 49.5	18.93
10	0 46 13.33	-25 28 37.7	18.80	10	0 11 42.33	-39 25 8.1	19.03
11	0 45 17.67	-25 9 38.2	18.83	11	0 12 8.84	-39 25 59.1	19.08
12	0 46 33.06	-25 40 55.7	18.83	12	0 12 0.20	-39 28 45.6	19.12

continued from previous page

NGC 253				NGC 55			
ID	α(1950)	δ(1950)	B	ID	α(1950)	δ(1950)	B
13	0 43 45.23	-25 23 9.1	18.90	13	0 14 4.81	-39 23 47.1	19.14
14	0 43 47.97	-25 17 58.8	18.98	14	0 12 52.24	-39 42 50.1	19.14
15	0 46 37.88	-25 28 42.6	18.99	15	0 12 15.83	-39 44 26.2	19.14
16	0 44 42.51	-25 39 44.7	19.00	16	0 14 25.55	-39 33 18.0	19.17
17	0 44 39.09	-25 18 22.5	19.02	17	0 12 45.44	-39 44 12.0	19.17
18	0 45 29.49	-25 21 44.1	19.14	18	0 12 47.47	-39 10 42.2	19.19
19	0 46 39.13	-25 22 34.6	19.20	19	0 13 7.21	-39 57 19.7	19.19
20	0 46 29.39	-25 34 10.0	19.21	20	0 14 49.86	-39 20 0.3	19.22
21	0 44 47.55	-25 39 16.4	19.23	21	0 14 49.49	-39 35 7.6	19.22
22	0 46 52.64	-25 23 35.8	19.25	22	0 12 55.67	-39 46 29.9	19.26
23	0 43 54.16	-25 30 53.1	19.27	23	0 13 4.33	-39 43 43.7	19.30
24	0 43 40.58	-25 14 40.3	19.33	24	0 12 42.38	-39 6 13.5	19.32
25	0 43 43.70	-25 19 50.2	19.41	25	0 14 41.43	-39 35 14.1	19.33
26	0 44 2.69	-25 11 29.1	19.42	26	0 14 40.96	-39 23 13.0	19.34
27	0 44 24.04	-25 19 48.0	19.43	27	0 14 7.81	-39 14 38.9	19.37
28	0 45 8.48	-25 34 55.7	19.43	28	0 13 1.59	-39 52 22.8	19.40
29	0 44 47.84	-25 29 55.3	19.46	29	0 14 6.12	-39 28 15.2	19.42
30	0 46 18.62	-25 12 10.8	19.54	30	0 10 35.36	-39 19 12.2	19.44
31	0 46 7.82	-25 31 25.5	19.54	31	0 11 30.20	-39 24 56.6	19.44
32	0 45 20.82	-25 35 0.5	19.56	32	0 11 45.84	-39 27 33.7	19.49
33	0 44 36.24	-25 13 3.8	19.58	33	0 13 1.89	-39 31 30.6	19.51
34	0 46 27.09	-25 17 27.8	19.62	34	0 13 28.69	-39 40 53.4	19.52
35	0 43 56.76	-25 26 6.5	19.73	35	0 13 12.97	-39 48 35.3	19.52
36	0 46 20.53	-25 7 30.0	19.74	36	0 13 37.10	-39 41 1.9	19.53
37	0 44 26.05	-25 33 27.7	19.78	37	0 12 1.03	-39 38 13.4	19.56
38	0 44 23.19	-25 34 27.1	19.78	38	0 13 10.13	-39 29 22.5	19.59
39	0 45 5.08	-25 41 4.9	19.78	39	0 12 37.46	-39 40 27.5	19.59
40	0 45 26.88	-25 14 3.7	19.80	40	0 12 56.36	-39 11 5.5	19.61
41	0 46 38.15	-25 38 5.1	19.84	41	0 12 24.07	-39 21 38.4	19.66
42	0 45 17.95	-25 7 18.2	19.85	42	0 13 16.92	-39 30 21.8	19.69

continued from previous page

NGC 253				NGC 55			
ID	α(1950)	δ(1950)	B	ID	α(1950)	δ(1950)	B
43	0 44 21.09	-25 9 56.4	19.85	43	0 11 15.90	-39 41 46.8	19.72
44	0 44 13.97	-25 16 45.2	19.89	44	0 13 27.56	-39 31 8.2	19.74
45	0 46 11.34	-25 34 21.7	19.89	45	0 13 48.31	-39 32 42.0	19.77
46	0 43 36.63	-25 25 59.0	19.92	46	0 11 44.80	-39 52 46.7	19.77
47	0 45 37.20	-25 30 0.9	19.92	47	0 13 43.24	-39 16 23.9	19.82
48	0 45 31.88	-25 13 15.9	19.93	48	0 13 7.18	-39 30 30.2	19.82
49	0 46 22.68	-25 41 22.3	19.95	49	0 12 55.83	-39 54 42.5	19.86
50	0 44 36.63	-25 35 13.0	19.96	50	0 11 54.33	-39 6 26.1	19.87
51	0 45 36.56	-25 25 22.5	19.97	51	0 14 43.92	-39 30 53.4	19.90
52	0 43 2.99	-25 29 3.3	19.97	52	0 12 23.58	-39 26 38.9	19.95
53	0 46 20.52	-25 18 24.7	19.99	53	0 12 3.73	-39 42 27.3	19.98
54	0 45 32.61	-25 19 12.7	20.00	54	0 10 41.10	-39 15 33.7	19.99
55	0 45 7.70	-25 7 49.0	20.02	55	0 10 13.53	-39 21 36.1	19.99
56	0 46 30.20	-25 18 57.3	20.02	56	0 12 3.47	-39 46 56.0	20.04
57	0 43 40.49	-25 18 60.0	20.03	57	0 11 6.42	-39 36 20.8	20.09
58	0 44 12.65	-25 25 0.7	20.03	58	0 14 21.57	-39 39 0.1	20.14
59	0 45 50.94	-25 26 24.1	20.03	59	0 14 3.89	-39 40 26.1	20.14
60	0 45 20.69	-25 24 50.2	20.04	60	0 12 46.07	-39 46 11.6	20.16
61	0 45 32.76	-25 26 14.9	20.04	61	0 13 28.03	-39 34 34.8	20.17
62	0 45 3.07	-25 26 6.2	20.05	62	0 11 30.88	-39 6 5.7	20.20
63	0 44 36.71	-25 28 30.0	20.05	63	0 13 13.77	-39 54 20.3	20.20
64	0 43 14.65	-25 21 54.9	20.09	64	0 11 36.53	-39 45 59.4	20.21
65	0 45 4.34	-25 23 34.2	20.13	65	0 11 57.43	-39 28 54.7	20.22
66	0 45 37.23	-25 23 39.7	20.17	66	0 11 23.35	-39 55 17.1	20.23
67	0 44 40.80	-25 11 6.0	20.19	67	0 11 16.33	-39 20 21.0	20.25
68	0 45 37.02	-25 25 54.8	20.20	68	0 12 36.07	-39 31 8.1	20.25
69	0 44 32.62	-25 36 32.1	20.21	69	0 13 35.26	-39 16 50.7	20.26
70	0 45 34.90	-25 12 47.7	20.25	70	0 12 58.36	-39 6 24.0	20.27
71	0 44 55.68	-25 27 17.0	20.25	71	0 12 45.49	-39 32 5.2	20.22
72	0 44 4.62	-25 33 56.6	20.26	72	0 13 43.07	-39 0 34.6	20.30

continued from previous page

NGC 253				NGC 55			
ID	α(1950)	δ(1950)	B	ID	α(1950)	δ(1950)	B
73	0 46 32.61	-25 24 17.2	20.27	73	0 12 44.11	-39 5 14.9	20.35
74	0 44 41.69	-25 41 10.1	20.27	74	0 13 47.95	-39 21 47.3	20.37
75	0 47 2.19	-25 16 21.5	20.29	75	0 12 2.75	-39 29 46.9	20.38
76	0 45 24.03	-25 27 38.9	20.30	76	0 12 47.66	-39 32 1.9	20.40
77	0 45 33.33	-25 19 35.5	20.31	77	0 13 26.69	-39 51 25.4	20.40
78	0 46 56.06	-25 15 35.7	20.32	78	0 14 20.98	-39 39 19.8	20.43
79	0 46 19.62	-25 16 33.5	20.34	79	0 13 3.11	-39 23 17.3	20.45
80	0 46 14.77	-25 26 23.3	20.34	80	0 14 54.78	-39 38 33.2	20.46
81	0 46 25.46	-25 29 25.5	20.36	81	0 13 53.54	-39 14 38.0	20.48
82	0 46 20.15	-25 17 50.8	20.38	82	0 13 39.53	-39 35 53.9	20.48
83	0 44 28.43	-25 28 57.1	20.38	83	0 13 49.87	-39 10 44.9	20.49
84	0 43 22.61	-25 21 44.0	20.40	84	0 13 25.27	-39 52 10.6	20.49
85	0 44 36.96	-25 13 5.7	20.41				
86	0 44 31.90	-25 41 39.1	20.41				
87	0 44 25.59	-25 41 47.8	20.47				
88	0 44 50.77	-25 8 33.0	20.49				
89	0 43 29.80	-25 17 5.3	20.49				
90	0 45 45.57	-25 13 2.6	20.50				
91	0 45 1.99	-25 23 58.9	20.50				

We estimate the contamination in the new GC samples from background galaxies by scaling the relative numbers of spectroscopically identified objects within our defined parameter space. In the new NGC 253 sample, there are 7 GCs and 7 background galaxies (i.e. 50% contamination). If we assume that there are *no* foreground stars in the new cluster samples, then we expect to obtain $\sim$ 45 clusters in the new NGC 253 sample. In the case of NGC 55, there are 6 galaxies and one GC within the sample limits, giving an expected $\sim$ 14 GCs in our sample.

2.6 Correlations Between Spiral Galaxies and their GCS

2.6.1 Specific Frequencies

In § 1.4.1, we discussed the definition of specific frequency, a method of normalising the absolute number of globular clusters associated with a galaxy by its starlight. The specific frequencies of NGC 55 and NGC 253 may be calculated from an estimate of their total cluster populations. The turn-over in the Galactic GCLF occurs at M_V = -7.6, σ = 1.2 (Harris 1999).[6] At an adopted distance of 2.5 Mpc for NGC 253, this corresponds to B = 19.9. Therefore, our cluster candidate selection cut reaches some $\sim$ 0.6 magnitudes past the turnover in the GCLF. Under the assumption that 50% of our new sample are GCs, we therefore detect of 60 GCs belonging to NGC 253 in our COSMOS scans, which go out to galactocentric radii of $\sim$ 20 $'$(corresponding to $\sim$ 14 Kpc at 2.5 Mpc). Assuming a surface density profile for the *halo* GCs similar to that of the Galaxy, $\sigma \propto r^{-2.5}$, we estimate that $\sim$ 8 GCs may lie outside our scans. This yields a projected total GC population of 68 $\pm$ 18 for NGC 253. The uncertainties are the 26 percentile derived from a bootstrap procedure of our spectroscopically identified objects. Applying Equation 1.2 to NGC 253, with M_V = -20.0, yields a specific frequency, $S_N = 0.7 \pm 0.2$.

Following the same arguments for NGC 55, with $\sim$ 17% of our new sample being GCs, yields an expected total cluster population of approximately 24 $\pm$ 12, including 4 GCs which may be outside our scans. At an adopted distance of 2.0 Mpc, with M_V = -19.5, gives a specific frequency of 0.4 $\pm$ 0.2 for NGC 55.

In Table 2.10 we summarize the currently available data in the literature on the GCS of spiral galaxies. We see that the projected specific frequencies of NGC 55 and NGC 253 are consistent with galaxies of their luminosity and Hubble type. We note that, if we were to derive specific frequencies for these two galaxies from purely the bulge luminosity, as has been suggested in the past, we obtain S_N values of $\sim$ 5 (assuming that the bulge contributes $\sim$ 15% of the total light of the galaxies, Pence 1980). However, this is probably unjustified since at least some proportion of GCs in spiral galaxies appear to be kinematically associated with the disk component (e.g. Zinn 1985; Huchra, Kent, & Brodie 1991; Barmby et al. 2000).

The derived S_N for all the galaxies given in Table 2.10 are clearly sensitive not only to the total number of GCs in the galaxy, but also to its assumed distance (and hence, absolute magnitude).

---

[6] There is some evidence that the turn-over in the GCLF for spirals is $\sim$ 0.2 mag brighter than for elliptical galaxies (Harris 1999)

Table 2.10. Globular cluster systems of spirals. Metallicities given in parenthesis are non-spectroscopic.

Sources : 1) Ashman & Zepf (1998) 2) This Work 3) Sarajedini et al. (1998) 4) Perelmuter, Brodie, & Huchra (1995) 5) Harris (1991) 6) Brodie & Huchra (1991) 7) Bridges et al. (1997) 8) Fischer et al. (1990) 9) Bothun, Harris, & Hesser (1992) 10) Kissler-Patig et al. (1999) 11) Da Costa & Hatzidimitriou (1998) 12) Olsen et al. (1998) 13) Olszewski et al. (1991)

† uncertain.

Galaxy	Hubble Type	M_V	N_{GC}	S_N	log ($M/M_\odot$)	T	$[Fe/H]_{GCS}$	Reference
NGC 3109	Im	-16.5	20†	5.0 ± 2.0	...	...	...	5
SMC	Im	-16.9	1	0.2	9.06	1.06	-1.41 ± 0.10	11
LMC	Sm	-18.4	13	0.6 ± 0.2	9.66	3.04	-1.41 ± 0.18 (-1.8 ± 0.2)	2,12,13
M 33	Scd	-19.4	30†	0.5	10.36	1.50	-1.55 ± 0.37 (-1.25 ± 0.1)	3,6
NGC 55	Sb(s)m	-19.5	24 ± 12	0.4 ± 0.2	10.10	0.99	...	2
NGC 253	Sc	-20.0	68 ± 18	0.7 ± 0.2	10.7	1.40	-1.25 ± 0.19	2
NGC 7814	Sab	-20.4	498 ± 164	3.5 ± 1.1	10.95	5.85	...	9
NGC 2683	Sb	-20.8	310 ± 100	1.7 ± 0.5	11.11	2.63	...	5
M 81	Sab	-21.1	210 ± 30	0.7 ± 0.1	11.23	1.45	-1.48 ± 0.2	4
NGC 5907	Sc	-21.2	170 ± 41	0.56 ± 0.17	11.18	1.33	...	10
Milky Way	Sbc	-21.3	180 ± 20	0.5 ± 0.1	11.22	1.29	-1.40 ± 0.01	6
NGC 4565	Sb	-21.4	204 ± 38	0.56 ± 0.15	11.35	1.12	...	10
NGC 5170	Sb	-21.6	815 ± 320	1.8 ± 0.7	11.43	3.26	...	8
NGC 4569	Sab	-21.7	900 ± 300	1.9 ± 0.6	11.47	3.28	...	5
M 31	Sb	-21.8	450 ± 100	0.9 ± 0.2	11.51	1.61	-1.21 ± 0.02	1,6
NGC 4216	Sb	-21.8	620 ± 310	1.2 ± 0.6	11.51	2.14	...	5
NGC 4594	Sa	-22.2	1600 ± 800	2.0 ± 0.1	11.61	4.11	-0.80 ± 0.25	7

Specific frequency is perhaps not the best method of comparing numbers of GCs between galaxy types. As argued by Zepf & Ashman (1993), it does not account for varying mass-to-light ratios (i.e. varying stellar populations) between galaxy types. In an attempt to correct for this in a statistical sense, these authors define what is essentially a specific *mass* frequency, T, normalised to 10^9 $M_\odot$ thus:

$$T \equiv \frac{N_{GC}}{M_G/10^9\ M_\odot} \tag{2.4}$$

where M_G is the galaxy mass. The galaxian luminosity is converted to a mass by adopting a characteristic $\mathcal{M}/L_V$ ratio for each morphological type. We derive T values for the galaxies in Table 2.10 using the $\mathcal{M}/L_V$ ratios of Faber & Gallagher (1979) after Zepf & Ashman (1993). The $\mathcal{M}/L_V$ ratios for each morphological type are: Sa (5.4), Sab–Sb (6.1), Sbc–Sc (5.0), Scd–Sd (4.0) and Sdm–Irr (2.0) (Faber & Gallagher 1979). The uncertainties in T given in Table 2.10 are purely from uncertainties in the total globular populations of the galaxies, they do not account for errors in the galaxy magnitudes and conversion from $\mathcal{M}$ to L_V.

We plot the T values of the galaxies in Table 2.10 against normalised mass in Figure 2.14.

Whilst the systematic and statistical uncertainties are large in Figure 2.14 (certainly larger than the error bars given), the figure does indicate that the relative number of GCs varies between spiral types. The early-type spirals (Sa–Sb) seemingly have GCS twice as large as the later-types for their mass. This is comparable to the situation between early-type spirals and ellipticals, with the latter typically having T values a factor of 2–3 times higher (Ashman & Zepf 1998). The mean T values for the differing morphological types are $\overline{T}$(Sa–Sab) = 3.67, σ = 1.6, $\overline{T}$(Sb–Sbc) = 2.0, σ = 0.8, $\overline{T}$(Sc–Scd) = 1.41, σ=0.07 and $\overline{T}$(Sdm–Irr) = 1.69, σ = 1.0. The mean T value for *all* spiral types in Table 2.10 is 2.25 (σ = 1.30), whereas that for ellipticals is $\sim$ 5.

Investigating the correlations (or the lack thereof) between GCS and their host-galaxies clearly requires more data, particularly with regards to spiral galaxies.

2.6.2 Mean Metallicities

From the co-addition of their spectra, in § 2.4.2 we obtained a mean metallicity for the NGC 253 GCs of [Fe/H] = -1.23 $\pm$ 0.19 dex. To date, information upon the metallicities of the GCS of spirals is scarce. However, we find that the data which is available in the literature are consistent with the values found in this study. From *HST* colour-magnitude diagrams of 10 GCs in M 33 (Sc spiral), Sarajedini et al. (1998) derive a mean metallicity of [Fe/H] = -1.25 $\pm$ 0.1. This is

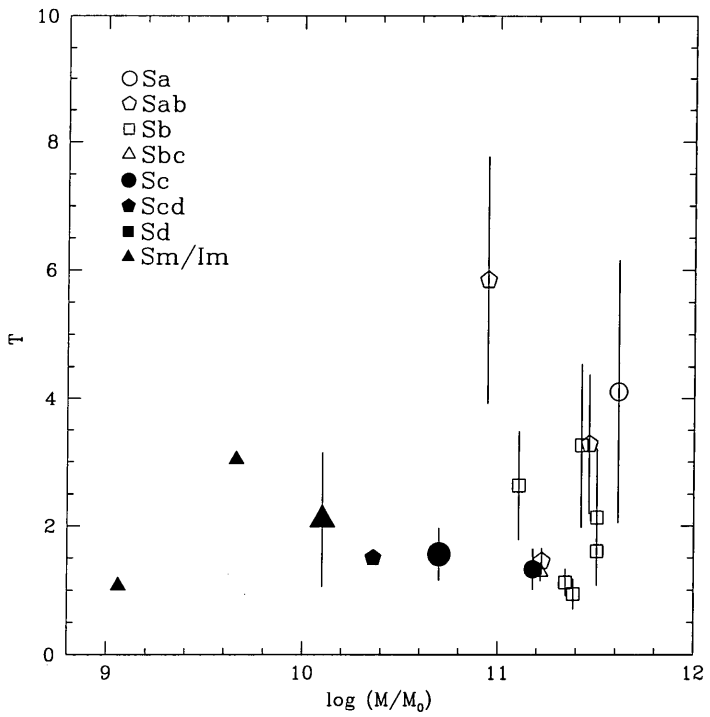

Figure 2.14: The specific mass frequency versus galaxy mass for spiral galaxies. Galaxy luminosities have been converted to mass estimates using the $\mathcal{M}/L_V$ ratios given by Faber & Gallagher (1979). The two larger symbols represent NGC 55 (triangle) and NGC 253 (circle).

consistent with the value obtained by Brodie & Huchra (1991) of [Fe/H] = -1.55 ± 0.37 from low-resolution spectroscopy of 22 clusters in M 33. In Chapter 4, we obtain a mean metallicity of [Fe/H] = -1.41 ± 0.18 from the integrated spectra of 8 globular clusters in the LMC. Similar to that found by Olsen et al. (1998) of [Fe/H] = -1.36 ± 0.15 from *HST* CMDs of five clusters in common. For earlier type spirals, the Galaxy (Sbc) and M 31 (Sb) cluster systems have mean metallicities of -1.40 ± 0.01 and -1.21 ± 0.02 respectively (Brodie & Huchra 1991). Perelmuter, Brodie, & Huchra (1995) find [Fe/H] = -1.48 ± 0.19 for globulars in M 81, the nearby bright Sab galaxy, whilst Bridges et al. (1997) obtain [Fe/H] = -0.80 ± 0.25 for the GCS of NGC 4594 (the Sombrero).

For elliptical galaxies, the mean metallicity of the GCS is known to correlate with host galaxy luminosity (e.g. Brodie & Huchra 1991; Zepf & Ashman 1993 ; Forbes, Brodie, & Grillmair 1997; Harris 1999; Forbes & Forte 2000). To look at this purely in the context of spiral galaxies, we plot the mean metallicity of the GCS against magnitude of the host galaxy in Figure 2.15. In order to impart some homogeneity into Figure 2.15, we only give metallicities which have been derived spectroscopically, thus avoiding the possible offsets between photometric systems. Furthermore,

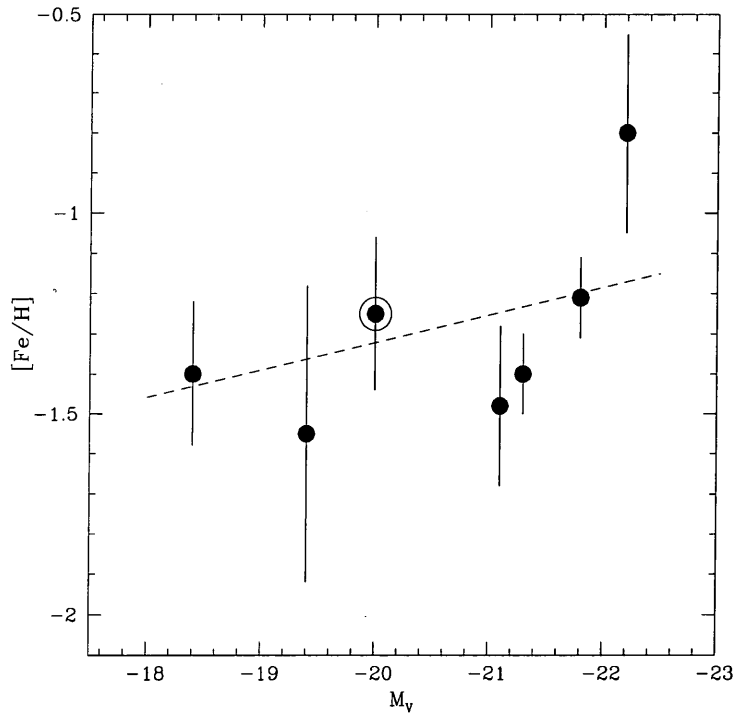

Figure 2.15: Relation between the mean metallicity of the globular cluster system and the luminosity for spiral galaxies. The position of NGC 253 is enclosed by an open circle. The dashed line is an (unweighted) least-squares fit to these data.

with the exception of the mean spectroscopic metallicity for the LMC (Chapter 4), *all* of the metallicities have been derived using the empirical calibrations and methodology of Brodie & Huchra (1990). Since these calibrations are based upon observations of Milky Way and M 31 GCs, the relative scale of [Fe/H] should be good, even if the absolute value is suspect. These data are listed in Table 2.10 in the previous section.

For the sake of clarity, we have not distinguished between spiral types in the figure. Bearing in mind the small number of data-points, we find evidence of a weak correlation between the metallicity of the GCS and the luminosity of the host galaxy. However, we also note that if we were to remove the most metal-rich GCS datapoint (NGC 4594) then this correlation will all but disappear.

From a least-squares fit to the data in Figure 2.15 we obtain:

$$\langle[\mathrm{Fe/H}]\rangle = -0.11 \times M_V - 3.54 \qquad (2.5)$$

with an rms about the fit of 0.19 dex. This relation is similar to that for elliptical galaxies (albeit somewhat flatter). But contrasts with the situation for giant ellipticals, which show little or no correlation between [Fe/H] and M_V (Harris 1999). However, as discussed by Forbes, Brodie, & Grillmair (1997), such a 'mean' GCS metallicity ignores the differing subpopulations of GCs within each galaxies' GCS. This is equally applicable to the GCS of spiral galaxies, which in the case of the Galaxy and M 31, exhibit broad or bimodal GC metallicity distributions.

2.7 Summary and Conclusions

On the basis of radial velocities and visual image examination, we have identified 14 GCs in the spiral galaxy NGC 253, and one possible GC belonging to NGC 55. All but two of the NGC 253 GCs have colours consistent with 'classical' old globulars. One cluster is very blue ($B-V$ = 0.19) and its spectrum shows strong Balmer absorption, possibly indicative of a young star cluster. The other is probably highly reddened ($B-V$ = 1.80), since it lies close to the disk of NGC 253.

We find that the GCS of NGC 253 has a mean velocity consistent with the systemic velocity of its parent galaxy, and has a velocity dispersion of 74 km s^{-1}. We measure line-strengths from the co-addition of the 14 cluster spectra, and obtain a mean metallicity for the NGC 253 GCS of [Fe/H] = -1.23 $\pm$ 0.19. This value is in agreement with that obtained from the $B-V$ colours of the NGC 253 globulars of [Fe/H] = -1.02 $\pm$ 0.39 dex, derived from a calibration to 113 Galactic globular clusters.

Using digitized plate scans combined with the spectroscopically identified stars, galaxies and GCs has allowed us to create new samples for the two galaxies which we expect will contain many new GCs. On the basis of the spectroscopic sample, we estimate the contamination in the new samples to be 50% and 83% for NGC 253 and NGC 55 respectively. From these values, we estimate the total GC populations of the galaxies to be 68 $\pm$ 18 for NGC 253 and 24 $\pm$ 12 for NGC 55. Adopting absolute V-band magnitudes of M_V = -20.0 and M_V = -19.5 for NGC 253 and NGC 55, yields specific frequencies of 0.7 $\pm$ 0.2 and 0.4 $\pm$ 0.2 for the two galaxies, consistent with galaxies of their luminosity and Hubble type.

Chapter 3

Spectroscopy of Globular Clusters in M 49

Abstract. We have obtained 87 new spectra for GCs associated with the giant Virgo elliptical NGC 4472 (M 49). Combined with previous studies, this yields a total dataset of 144 spectra for GCs in this galaxy, for which we have measured line-strengths and radial velocities. From analysis of their co-added line-strengths, we find that our sample of GCs in NGC 4472 span a metallicity range of approximately -1.6 $\leq$ [Fe/H] $\leq$ 0 dex. We find evidence of a radial metallicity gradient in the GCS which is steeper than that seen in the underlying starlight. Determination of the *absolute* ages of the GCs is uncertain, but based upon a calibration with Galactic GCs we find that the metal-poor (blue) population of GCs have an age of 14.5 $\pm$ 4 Gyr and the metal-rich (red) population are 13.8 $\pm$ 6 Gyr old. Monte Carlo simulations indicate that the GC populations present in these data are older than 6 Gyr at the 95% confidence level. Therefore, we find that within the uncertainties the GCs are old and coeval, implying that the bimodality seen in the broadband colours primarily reflects metallicity and not age differences. Analysis of the kinematics of the GCs has revealed that the blue and red GCs are dynamically distinct, strengthening previous findings. We find that the blue GCs have a velocity dispersion of σ = 356 $\pm$ 25 km s^{-1} and the red GCs have σ = 221 $\pm$ 22 km s^{-1}. We find evidence for moderate rotation ($\sim$100 km s^{-1}) in the blue clusters, and little or no rotation in the red GCs, for which we derive an upper limit of $(v/\sigma)_{\rm proj} < 0.34$ at 99% confidence. We obtain a mass profile for the GCs which is in good agreement with X-ray estimates. We find a steeply rising $\mathcal{M}/L$ ratio with radius, indicative of a massive dark matter halo surrounding this galaxy.

3.1 Introduction

It has become clear in recent years that subpopulations in extragalactic globular cluster systems are not uncommon. Indeed, since their first detection by Zepf & Ashman (1993) using the $B-I$ colour data of Couture, Harris, & Allwright (1991) for the giant elliptical NGC 4472 and $C-T_1$ colours for GCs in Centaurus A (Harris et al. 1992), the study of colour bimodality in GCS

has become a growth industry (e.g. Neilsen & Tsvetanov 1999; Gebhardt & Kissler-Patig 1999). It is now estimated that *at least* half of all early-type galaxies have bimodal GCS (Gebhardt & Kissler-Patig 1999). The presence of subpopulations of GCs points toward multiple and distinct epochs/mechanisms of GC formation. However, the origin of these subpopulations is unclear, as are their implications for the formation of their host galaxies.

To first order, the GCS colour distributions are thought to reflect the distribution of metallicity in the GC populations (Ashman & Zepf 1998). Therefore, multi-modal colour distributions are usually interpreted as multi-modal metallicity distributions of the GCS. However, despite almost a decade of research into the nature of these bimodal distributions, the process(es) by which they form are still unknown.

Since GCs in elliptical galaxies are generally thought to be old, their relative ages will not significantly affect their broadband colours owing to the well-known effect of age-metallicity degeneracy (e.g. Faber 1972; O'Connell 1976; Worthey 1994, henceforth W94). Therefore, any age information contained within the colour distributions of the GCS will be entangled within their intrinsic metallicity spread. One route to breaking this degeneracy is through the careful selection of spectroscopic indices, an approach which has successfully been applied to the integrated spectra of galaxies (e.g. González 1993; Davies, Sadler, & Peletier 1993; Fisher, Franx, & Illingworth 1995; Kuntschner 1998). Metallicities may be estimated from metal-sensitive features, and ages may be obtained from Balmer indices, which in principle measure the temperature (and hence age) of the main-sequence turnoff (MSTO) in a stellar population.

However, until recently, the task of obtaining spectra of GCs outside the Local Group has been truly an heroic undertaking. At the distance of Virgo $(m - M)_0 \simeq 31.0$, the very brightest GCs have $V \sim 20.0$. Many hours of integration time were required to obtain spectra of signal-to-noise high enough to measure accurate radial velocities, let alone line-strengths (e.g. Hanes & Brodie 1986; Mould et al. 1990; Brodie & Huchra 1991; Grillmair et al. 1994).

The latest generation of telescopes and instrumentation has revolutionized this field. High quality spectra of GCs have now been obtained in statistically significant numbers for the Virgo cD M 87 (Cohen & Rhyzov 1997; Cohen & Rhyzov 1998; Cohen 2000), NGC 4472 (Mould et al. 1990; Sharples et al. 1998 - henceforth S98) and the central cD of Fornax, NGC 1399 (Grillmair et al. 1994; Kissler-Patig et al. 1998).

In this Chapter, we present a continuation of the study of S98 who analyse the radial velocities of 57 GCs associated with the bright giant elliptical NGC 4472. We have obtained a further

171 spectra of GC candidates using the Multi–Object Spectrograph (MOS) at the 3.6-m Canada-France-Hawaii telescope (CFHT), 87 of which are new, *bona fide* GCs belonging to this galaxy.

The plan of this Chapter is as follows: In the remainder of this Introduction, we discuss the four currently favoured scenarios for the formation of GCs systems, and their resulting observational predictions. We then discuss the recent spectroscopic studies of the GCS of two cD galaxies, NGC 4486 (M 87) and NGC 1399, before looking in more detail at the case of NGC 4472, the target of our present study. In Section 3.2 we detail the observations, data reduction and measurement of radial velocities of our sample of NGC 4472 GCs. In Section 3.3 we discuss how we obtain line-strengths from the spectra, how we derive a realistic uncertainty from these data and present the final line-strength measurements. Then, in Section 3.4, we show how we measure ages and metallicities for the GCs using stellar population models and discussing our results. In Section 3.5 we look at the kinematics of the NGC 4472 GCs, and their implication for the dynamics of NGC 4472. We discuss our findings in the context of the formation of the GCS and NGC 4472 in Section 3.6, before presenting a summary of our conclusions in Section 3.7.

3.1.1 Formation Models for Globular Cluster Systems

There are currently four favoured models which attempt to explain the observed properties of GCS associated with bright ellipticals, and they may be summarized as follows :

- ***In situ* collapse:** in this picture, the material which goes to form the GCS is part of the collapsing material which will go on to eventually form the host galaxy. The galaxy stars and GCs form in two distinct phases, first producing a metal-poor component, and later (after a delay during which time significant enrichment occurs, perhaps due to the detonation of Type II SNe) giving rise to a second, enriched component (e.g. Forbes, Brodie, & Grillmair 1997; Harris, Poole, & Harris 1998).

- **Mergers of spiral galaxies:** the host elliptical is formed by the merging of spirals (e.g. Toomre 1977) and GCs are formed from the cold gas originating from the disks of these galaxies. The final GCS consists of a metal-poor component from the progenitor spirals, and a newly created metal-rich component (Ashman & Zepf 1992).

- **Accretion of dwarf galaxies:** the metal-rich clusters are native to the galaxy, whilst the metal-poor clusters are accreted through the disruption of dwarf galaxies (Cote, Marzke, & West

1998) which have their own GCs. Additionally, GCs may be formed during this process if the accreted dwarf galaxies are gas-rich (Hilker 1998).

- **Primordial GCs:** hierarchical models of structure formation predict that the Jeans mass just after recombination in the early universe is $\sim 10^6$ $M_\odot$. Such models predict that the first gravitationally bound objects will have a mass spectrum characteristic of GCs (Peebles & Dicke 1968). This scenario has since been re-addressed by various authors (Rosenblatt, Faber, & Blumenthal 1988; West 1993; Kissler-Patig, Forbes, & Minniti 1998; Burgarella, Kissler-Patig, & Buat 2000). The metal-poor clusters would condense out from Jeans-mass clumps, prior to the formation of the host galaxy. The metal-rich GCs would later form from enriched galaxian material.

Whilst all of the above models can lead to bimodal GCS metallicity distributions, in detail each of these scenarios has its difficulties, and perhaps no single model can account for *all* observed GCS. However, they do predict characteristics for the final GCS which are, in principle at least, observable. The *in situ* collapse model predicts that the metal-poor population will be older than the metal-rich population by 1–3 Gyr. The exact age difference between the populations depending upon the time-scale for the cooling and re-collapse of the baryonic matter during the hiatus in star formation. In such a scenario, GCs may be expected to follow predominantly radial orbits, although this is highly dependent upon the initial angular momentum of the collapsing proto-galaxy.

The merger model also predicts that the metal-poor clusters should be older than the metal-rich ones. However, this model implies that in some cases at least, the metal-rich component will be significantly younger than the metal-poor one if the hierarchical formation of structure is a true picture of galaxy formation, where some galaxies (and hence GCs) form late (see Chapter 5). Furthermore, the old clusters from the progenitor spirals are expected to be more spatially extended than the new clusters, with mean metallicities typical of the GCS of bright spirals. Kinematically, they may exhibit some preference for rotation over isotropy due to the efficient outward transport of angular momentum in mergers (Hernquist 1993).

The accretion model provides the only mechanism which can comfortably give rise to metal-poor GCs which are younger than the metal-rich ones. The metal-poor cluster are also expected to be more spatially extended than the metal-rich clusters, and may show a larger velocity dispersion, characteristic of the local dwarf population (Cote, Marzke, & West 1998). If GCs are *primordial*, then the most metal-poor GCs would be extremely old, indeed the oldest objects in the observable

universe. However, the characteristics of these GCs is not well constrained. Since GCs would need to form preferentially in areas of high density (i.e. galaxies and galaxy clusters), their spatial distribution and kinematics would be highly dependent upon the nature of the biasing invoked.

Unfortunately, none of these models make unique predictions for the final properties of the resultant GCS, and it is clear that many of these models are essentially very similar. Moreover, it is not clear that one model should necessarily exclude the others, and it is perhaps more reasonable for a combination of the above scenarios to be acting at the same time. However, detailed chemical and kinematical analysis of these GCS subpopulations will lead to strong constraints being placed upon the models, perhaps identifying one 'preferential' process for the creation of the observed GCS in bright elliptical galaxies.

3.1.2 Spectroscopy of Globular Clusters in Giant Ellipticals

In an important contribution, Cohen & Ryzhov (1997) obtained spectra for 205 GCs in the Virgo cD galaxy M 87. Using the Keck telescope they acquired what was at the time the largest spectroscopic sample of extragalactic GCs yet obtained for a single galaxy. These authors found that the red and blue cluster subpopulations were kinematically indistinct and that velocity dispersion of the cluster system rose from 270 $\mathrm{km\,s^{-1}}$ at r = 9 Kpc to 400 $\mathrm{km\,s^{-1}}$ at r = 40 Kpc, showing indications of continuing to rise at even larger radii. They also found evidence of rotation in the GCS, but only divided their sample into two radial bins ($< 180''$ and $> 180''$). These data were re-analysed by Kissler-Patig & Gebhardt (1998) with five updated velocities, who found that the the M 87 GCS exhibited a rotation of 300 ± 70 $\mathrm{km\,s^{-1}}$ beyond 3 r_e. They showed that the high velocity dispersion found by Cohen & Ryzhov (1997) was primarily driven by this rotation. Kissler-Patig & Gebhardt (1998) concluded on this basis that the most likely mechanism for producing this substantial rotation was via a major merger. These data have been recently supplemented by a further 16 spectra of GCs out $\sim 540''$ (Cohen 2000), which confirm these findings. Cohen, Blakeslee, & Ryzhov (1998) obtained line-strengths for a sub-sample of 150 GC spectra from the 1997 paper, selected on the basis of S/N. They found that the M 87 GCS spans a wide metallicity range, -2.0 < [Fe/H] < 0.1, with a mean metallicity of [Fe/H] = -0.95 and a metal-rich tail extending further than that of the Milky Way GCS. Measured from the Hβ index, they determined a mean age of the GCS using the W94 stellar population models of 13 Gyr, with a dispersion of 2 Gyr.

From a somewhat smaller sample, Kissler-Patig et al. (1998) obtained 5.6 Å resolution spectra of 21 GCs belonging to NGC 1399, the central cD galaxy of the Fornax cluster. They derived a mean metallicity of [Fe/H] = -0.8 dex for the GCS and found that the elemental abundances of the majority of the GCs do not differ from those observed in the Milky Way and M 31. Interestingly, two of their GCs stood out in that their metallic line indices were comparable to the diffuse stellar light of the host galaxy, perhaps implying that they may have formed from nearly solar metallicity gas in a different formation process from the bulk of the GCs (Kissler-Patig et al. 1998). They found that these clusters exhibited Hβ and Hγ indices incompatible (i.e. too high) with *any* age-metallicity combination of existing stellar population models.

Both NGC 4486 and NGC 1399 are giant cD galaxies which dominate the potential wells of their respective clusters (Virgo and Fornax). Whilst they are intrinsically very interesting, they are perhaps unrepresentative of luminous ellipticals in general. To date, the only other giant elliptical galaxy for which significant numbers of GC radial velocities have been obtained is NGC 4472, the brightest elliptical in the Virgo cluster.

3.1.3 NGC 4472

NGC 4472 (M 49) is the brightest galaxy in the Virgo cluster of galaxies, and lies $\sim 4°$ south of the central cD galaxy M 87. NGC 4472 (Hubble type E2/S0), plays host to some 6300 $\pm$ 1900 GCs (Geisler, Lee, & Kim 1996) which have been shown to possess a bimodal colour distribution (Zepf & Ashman 1993; Geisler, Lee, & Kim 1996). In Table 3.1 we list the basic data for this galaxy.

Being the brightest elliptical in the local universe, NGC 4472 and its GCS has been the subject of a number of studies. The first broad-band, multi-colour CCD study of its GCS was performed by Cohen (1988). Using the 5-m Hale telescope at Mount Palomar, she observed a field of some $\sim 9' \times 9'$ using Gunn-Thuan gri photometry. Of the 3183 point-sources she identified with $g \leq$ 25.0, she considered 291 likely GCs, amongst which she detected no significant colour gradient in the GCS. In 1991, Couture, Harris, & Allwright (1991) obtained somewhat deeper BVI data for this galaxy. Their field size of $\sim 2.8' \times 2.8'$ was significantly smaller than that of Cohen (1988) although so were their photometric errors, by a factor of ~ 2. From the $B - I$ colours of 70 GC candidates, they obtained a mean metallicity of [Fe/H] = -1.15 for the GCS, however their data showed some evidence for an internal scaling error, since the metallicities they derived from $B - I$, $B - V$ and $V - I$ differed significantly. These authors found a significant colour gradient

Table 3.1. Basic galaxy data for NGC 4472.

Sources: 1) de Vaucouleurs et al. (1991), 2) Sandage & Tammann (1981), 3) Davies, Sadler, & Peletier (1993), 4) Ferrarese et al. (1996), 5) Geisler, Lee, & Kim (1996)

Property	Value	Source
Right Ascension (1950.0)	$12^h27^m14.29^s$	1
Declination (1950.0)	08°00′02″	1
Type	E2/S0	1
B	9.33	1
$B-V$	0.96	1
$(m-M)_o$	31.04	4
M_V	-22.67	
N_{GC}	6300 ± 1900	5
S_N	5.6 ± 1.7	5
Effective radius (r_e)	99″	3
P.A.	162°	2
V_{helio}	961 km s^{-1}	2

in their data, in all their indices. Later, Ajhar, Blakeslee, & Tonry (1994) obtained KPNO 4-m and MDM 2.4-m VRI photometry for this galaxy, resulting in the identification of a total of 170 GC candidates. Ajhar, Blakeslee, & Tonry (1994) found evidence for a colour distribution broader than that expected for a Gaussian distribution, but their data was neither deep enough nor had the necessary metallicity sensitivity to identify finer substructure. In agreement with Cohen, they found *no* evidence of a colour gradient in their data. Until recently, the definitive ground-based study (indeed, the best dataset for *any* GCS in terms of sample size and completeness) was performed by Geisler, Lee, & Kim (1996) (henceforth GLK96) using Washington CT_1 photometry and covering a field of $16.4' \times 16.4'$ (see Figure 3.1). GLK96 obtained accurate $C-T_1$ colours (with mean internal photometric errors of $\sim$ 0.05 mag), which are twice as sensitive to metallicity as equivalent $B-V$ and $V-I$ colours (Geisler & Forte 1990), for 1800 GC candidates. They found a clearly bimodal colour distribution, with peaks at $C-T_1$ = 1.31 and 1.83, corresponding to metallicities of [Fe/H] $\sim$ -1.30 and -0.1 respectively. In addition, they found a radial gradient in the cluster system of -0.4Δ[Fe/H]/Δ log r, apparently driven by the fact that the blue, metal-poor clusters were more spatially extended than their red counterparts. Recently, Rhode & Zepf (2000)

have obtained BVR photometry of the NGC 4472 GCS using the wide-field Mosaic Imager at the KPNO 4-m telescope. By estimating their contamination from archival *HST* data and from the spectroscopy of S98, these authors detected $\sim$ 1500 GC candidates which show strong bimodality. By probing out to radii of $\sim 23'$, they found a colour gradient of the GCS within $8'$, which they also attributed to the varying spatial distribution of red and blue GCs. However, at radii $>8'$, they found no colour gradient.

In an effort extract age information about the GCS of NGC 4472, Puzia et al. (1999) used *HST* V, I photometry to determine both mean colours and turn-over magnitudes for the red and blue GCs. By assuming that the mean mass functions of the two subpopulations were similar, these authors found that the blue and red GCs are coeval within their uncertainties (which were $\pm$ 3 Gyr). They concluded that possibility of one population being half the age of the other was excluded at the 99% confidence level. Lee & Kim (2000) also analysed *HST* data for NGC 4472, using three datasets in common with the Puzia et al. (1999) study, and arrived at a somewhat different conclusion. Their study indicated that the red GCs are several Gyr *younger* than the blue GCs. This difference from the Puzia et al. (1999) study they attributed to a combination of a $\sim$ 30% larger sample size, greater areal coverage and increased completeness. However, (Lee & Kim 2000) included no discussion of uncertainties in their age estimates, leading to the conclusion that the subpopulations may still have been coeval within their errors.[1]

The first spectroscopic observations of the GCs of NGC 4472 were performed by Mould et al. (1990). These authors obtained low-resolution spectra ($\sim$ 5 Å) for 54 GC candidates based upon the photographic study of Strom et al. (1981). Unfortunately, their contamination was high and more than half of their sample turned out to be either foreground stars or background galaxies. For the 26 GCs which they did obtain spectra, they obtained a velocity dispersion of 340 $\pm$ 50 $\mathrm{km\,s^{-1}}$ and found a rotation in the clusters of amplitude 113 $\mathrm{km\,s^{-1}}$

Almost a decade later, S98 obtained spectra for 47 GCs associated with this galaxy. Including data for 10 GCs from the study of Mould et al. (1990), these authors found evidence for *kinematical* differences between the blue and red cluster populations. They showed that the red GCs possessed a velocity dispersion of 240 $\mathrm{km\,s^{-1}}$, whereas the blue clusters had σ = 320 $\mathrm{km\,s^{-1}}$. They found that the entire cluster system showed a rotation of 85 $\pm$ 35 $\mathrm{km\,s^{-1}}$ at the 88% con-

[1] A similar result was found by Kundu et al. (1999) for GCs in the inner regions of NGC 4486, also using *HST*. They found that the red GCs were 3–6 Gyr younger than their blue counterparts, with the magnitude of the age difference dependent upon the stellar evolutionary models they adopted

fidence level. They also found tentative signs of a higher level of rotation in the blue clusters, possibly giving rise to their higher velocity dispersion. The subpopulations present within the data-set of GLK96 were characterized by S98 with a double-Gaussian distribution using the KMM mixture-modelling test (Ashman, Bird, & Zepf 1994). S98 found that the most probable boundary between the metal-rich and metal-poor clusters was at $C - T_1$=1.625 ([Fe/H] $\sim$ -0.57). In the rest of this Chapter, we follow S98 and regard the *blue* clusters as having $C - T_1 \leq 1.625$ and the *red* clusters as having $C - T_1 > 1.625$. Due to the overlap in the blue and red subpopulations, and the photometric errors, not every GC will be correctly assigned to its true population. This effect will be most significant at $C - T_1 \sim 1.625$.

3.2 Spectroscopy of the NGC 4472 Globular Clusters

3.2.1 Observations

The data constituting our combined sample was obtained from two separate observing runs. Spectroscopic observations of 79 cluster candidates were taken with the Low-Dispersion Survey Spectrograph (LDSS) on the 4.2-m William Herschel Telescope (WHT) in April, 1994 (see S98 for further details of these observations and the data reduction). In May, 1998 we obtained spectra for a further 171 cluster candidates using MOS on the CFHT. The object selection in both studies was based on the Washington photometry of NGC 4472 GC candidates published by GLK96. Five multislit spectroscopic masks were prepared using the MOS software provided at the CFHT, though only four were actually used. Slits were cut using the LAMA machine, with typically 40 $\sim$ 45 objects per mask. One of the masks was centred on the nucleus of NGC 4472, with the other four being displaced by $\sim$ 5.'5 into the NE, NW, SE, and SW quadrants to obtain the best spatial coverage of the cluster system. Highest priority was given to candidates in the magnitude range $19.5 \leq V \leq 21.5$, although candidates were selected down to $V \sim 22.5$. Table 3.2 gives the details of the masks, listing the number of candidates per mask, along with the number of spectroscopically confirmed GCs, background galaxies and foreground stars.

We show in Figure 3.1 an image of NGC 4472 taken with the T_1 filter (top panel) and the same image after a smoothed image has been subtracted (bottom panel). We have marked the positions of the 134 GCs for which we have obtained radial velocities on this median-subtracted image.

We used the B600 grism for the CFHT observations, with a dispersion of 2.24 Å pix^{-1}. This produced spectra with an instrumental resolution of $\sim$ 5.5 Å (330 kms^{-1}) and a useful spectral

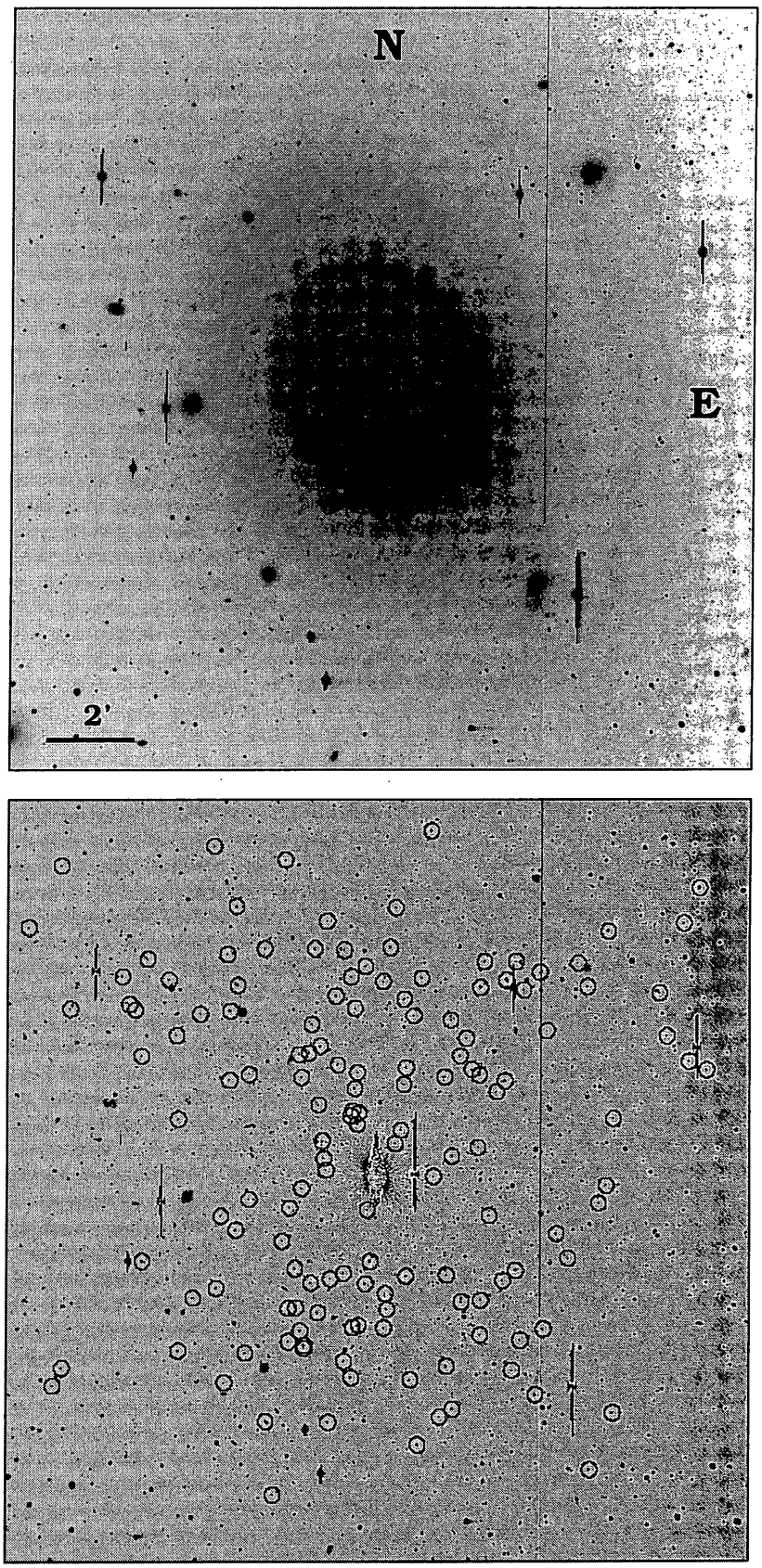

Figure 3.1: Top panel : Image of NGC 4472 in the T_1 filter. North is at the top and east is to the right, the field is $16'4''$ on a side. Bottom panel : Median-subtracted image of NGC 4472. The positions of the GCs for which we have obtained radial velocities are marked by circles (courtesy of D. Geisler).

Table 3.2. Details of the mask setup and spectroscopic completeness for the CFHT observations.

Mask #	RA (1950.0)	DEC (1950.0)	Objects/ Mask	Confirmed Globulars	Background Galaxies	Foreground Stars
Mask1	12 27 15.14	08 16 37.4	unused	unused	unused	unused
Mask2	12 27 01.69	08 12 36.3	47	22	4	2
Mask3	12 27 01.69	08 20 38.3	42	26	3	0
Mask4	12 27 27.06	08 20 38.4	42	31	3	2
Mask5	12 27 27.06	08 12 36.4	45	21	3	3

range of 3800 – 6500 Å. The detector was a STIS 2048^2 chip, with readout noise 9.3 e^-, noteworthy for its excellent performance in the blue (quantum efficiency $\sim$ 82 % at 4000 Å). We took flat field and bias frames at the beginning and end of each night, and the spectra were wavelength calibrated using frequent mercury arc exposures taken before and after the programme object frames. Table 3.3 lists the observational details for the CFHT run.

Table 3.3. Details of observations for CFHT run.

Dates	$16–19^{th}$ May, 1998
Telescope/Instrument	3.58m CFHT/MOS
Detector	2048^2 STIS-2
Dispersion (Resolution)	2.24 Å pix^{-1} (5.5 Å FWHM)
Wavelength Coverage	3800–6500 Å
Seeing	$< 1''$
Mean Airmass	1.1
Exposure times (NGC 4472)	6000s per mask

In order to calibrate radial velocities, we obtained long slit spectra for a number of radial velocity standard stars. In addition, we took integrated spectra of several Galactic GCs (GGCs) to aid in our metallicity calibration. The spatial extent of these GCs on the sky (mean core radii $\sim$ 40 arcsec) required us to synthesize an aperture in order to obtain a representative integrated spectrum. Therefore, we scanned the cores of the GCs over a typical range of $90''$, both in right ascension and declination. Combined with the WHT observations, this yielded high S/N spectra ($\sim$ 500 at 5000

Å) of five GGCs in the metallicity range -2.24 < [Fe/H] < -0.29 dex with one overlap, namely NGC 6356. We summarize our calibration objects observed in Table 3.4.

Table 3.4. Programme standard stars and Galactic GCs for radial velocity and metallicity calibration.
† Abundances from Zinn (1985), henceforth denoted $[Fe/H]_Z$

ID	Object	Spectral Type	$[Fe/H]\dagger_Z$
NGC 6341	GGC	F2	-2.24
NGC 7078	GGC	F3/4	-2.15
NGC 6205	GGC	F6	-1.65
NGC 6356	GGC	G3	-0.62
NGC 6553	GGC	G4	-0.29
HD 90861	Star	K2III	...
HD 102494	Star	G9IV	...
HD 112299	Star	F8V	...
HD 132737	Star	K0III	...
HD 171232	Star	G8III	...
HD 208906	Star	F8V-VI	...

3.2.2 Data Reduction

The majority of these data reduction was performed using the package DOSLIT in IRAF together with other standard tasks. The object frames were first trimmed and bias-subtracted, and any bad pixels were cleaned by interpolating across adjacent columns. An overscan correction was not applied since this portion of the STIS-2 chip was found to be highly variable across the CCD. The MOS multi-slit data takes the form of 40–45 spectra project onto the two dimensional image frame. The spectra are aligned along the dispersion axis, approximately parallel to the columns of the chip. The spatial position of each spectrum was located on the CCD, and traced along the dispersion axis. A low-order polynomial was fit to the sky across each pixel in the dispersion direction, and the sky was subtracted. The spectra where then summed along the slit, and multiple exposures combined to give the final spectrum for each object. We experimented with both optimal and standard subtraction, and found little difference between the two methods. The spectra were

wavelength-calibrated using mercury arcs which were obtained before and after each of the science exposures. Residuals from a 2^{nd}-order fit to these arcs were typically $\sim$ 0.1 Å.

We show examples of four GC spectra from our sample in Figure 3.2, arranged in order of their signal-to-noise ratios.

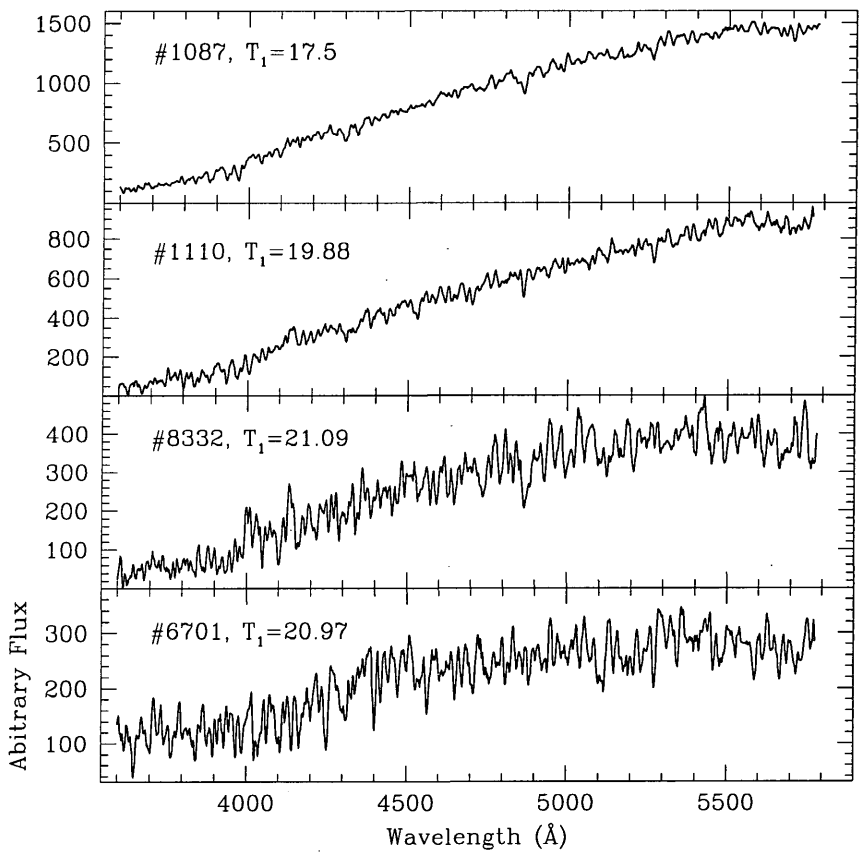

Figure 3.2: Four GC spectra of signal-to-noise ratios of approximately 25, 19, 10 and 6 (top to bottom). The spectra have been smoothed with a 3-pixel boxcar.

Figure 3.2 illustrates two points; (*i*) the raw counts in the spectra rapidly fall towards the blue. This occurs because our sensitivity decreases towards shorter wavelengths, coupled with the fact that GCs are (generally) old stellar populations, and (*ii*) the brighter objects do not always give rise to the spectra with the highest flux. Because this is multi-slit data, the same number of photons do not necessarily hit the detector for a given flux from the source (due to the changing position and size of the slits). Once extracted, the spectra we re-binned into units of log(λ) in order to determine their radial velocities via cross-correlation.

3.2.3 Radial Velocities

We have used the Fourier cross-correlation task FXCOR for measuring radial velocities from the spectra. The six velocity templates were de-redshifted by their literature values and then individually cross-correlated against each of the candidate cluster spectra. An 'r' value of 2.5 Tonry & Davis (1979) was set as the lower threshold for reliable measurement; below this value any velocities returned, however plausible, were removed from further analysis. The final velocities of the GCs were then taken to be the mean velocity weighted by the cross-correlation peak height of each template. A heliocentric correction was then applied to these velocities.

We list our final radial velocities for 144 GCs in Table 3.5. The sample comprises of the 57 GC velocities from combined sample of Mould et al. (1990) and S98, and a further 87 GC velocities from this work. The uncertainties in the table are those obtained from the cross-correlation task.

Table 3.5.: Velocities of GCs in NGC 4472.

† from GLK96. Sources : CFHT = this study, WHT = S98, Mould = Mould et al. (1990).

ID†	RA (1950.0)	DEC (1950.0)	T_1 † (mag)	$C-T_1$ † (mag)	[Fe/H]† (dex)	Rad ($''$)	Rad_{proj} ($''$)	V_{helio} km s^{-1}	Source
170	12 27 5.19	8 9 52.62	21.19	1.73	-0.3	437	347	1243 ± 69	CFHT
282	12 27 32.88	8 10 24.10	20.38	1.65	-0.5	464	444	751 ± 39	CFHT
463	12 27 17.87	8 10 55.48	19.93	1.59	-0.7	352	345	342 ± 27	CFHT
637	12 27 10.03	8 11 24.07	19.95	1.54	-0.8	329	282	814 ± 31	CFHT
647	12 27 4.56	8 11 25.41	21.15	1.34	-1.2	355	256	1101 ± 39	CFHT
676	12 27 19.80	8 11 30.50	20.72	1.46	-1.0	322	321	1304 ± 56	CFHT
714	12 27 34.88	8 11 35.35	20.32	1.55	-0.7	428	386	1061 ± 39	CFHT
744	12 27 20.91	8 11 40.22	19.73	1.38	-1.2	317	317	814 ± 29	CFHT
876	12 27 28.14	8 11 58.28	19.63	1.46	-1.0	347	333	1487 ± 24	CFHT
995	12 26 46.05	8 12 9.99	20.90	1.54	-0.8	510	128	828 ± 90	CFHT
1047	12 27 0.94	8 12 13.84	21.14	1.89	0.1	342	193	1083 ± 30	CFHT
1087	12 27 17.20	8 12 17.45	19.64	1.44	-1.0	269	264	1070 ± 29	CFHT
1110	12 27 12.04	8 12 20.28	19.88	1.37	-1.2	268	238	1626 ± 24	CFHT
1207	12 27 26.09	8 12 29.34	21.34	1.25	-1.5	304	294	739 ± 69	CFHT
1234	12 26 46.82	8 12 32.23	20.81	1.47	-0.9	489	111	1059 ± 64	CFHT
1255	12 27 20.37	8 12 34.38	19.71	1.35	-1.2	263	263	816 ± 66	CFHT
1315	12 27 11.39	8 12 40.92	20.68	1.42	-1.0	250	216	1370 ± 76	CFHT
1423	12 27 2.74	8 12 51.27	20.94	1.57	-0.7	296	166	1641 ± 29	CFHT
1448	12 26 56.90	8 12 54.23	20.79	1.34	-1.2	354	136	1353 ± 26	CFHT
1475	12 27 7.89	8 12 56.99	21.15	1.46	-1.0	251	184	1018 ± 37	CFHT
1518	12 27 7.89	8 13 0.59	19.25	1.85	0.0	248	181	1050 ± 36	WHT
1570	12 27 6.52	8 13 5.58	20.98	1.58	-0.7	253	170	1034 ± 61	CFHT
1587	12 27 26.80	8 13 7.25	21.16	1.12	-1.8	279	261	471 ± 75	CFHT
1650	12 27 23.30	8 13 13.56	20.85	1.95	0.2	245	239	1040 ± 55	CFHT
1712	12 27 7.54	8 13 18.95	20.36	1.34	-1.2	234	162	1144 ± 40	WHT
1731	12 27 28.81	8 13 21.12	20.71	1.82	-0.1	289	257	1294 ± 51	CFHT
1749	12 27 14.86	8 13 22.62	20.92	1.98	0.3	202	191	1407 ± 88	CFHT
1764	12 27 12.15	8 13 23.58	20.82	1.72	-0.3	206	179	855 ± 37	CFHT

continued from previous page

ID†	RA (1950.0)	DEC (1950.0)	T_1 † (mag)	$C-T_1$ † (mag)	[Fe/H]† (dex)	Rad $''$	Rad_{proj} $''$	V_{helio} km s^{-1}	Source
1798	12 27 12.65	8 13 25.92	20.69	1.98	0.3	202	178	811 ± 31	CFHT
1982	12 27 9.12	8 13 42.03	20.89	1.01	-2.0	203	147	648 ± 43	CFHT
2031	12 27 15.13	8 13 46.37	20.71	1.37	-1.2	178	170	1352 ± 65	Mould
2045	12 27 6.50	8 13 47.76	20.94	1.77	-0.2	217	129	857 ± 54	WHT
2060	12 27 7.15	8 13 48.33	20.62	1.29	-1.3	212	132	1108 ± 65	Mould
2140	12 27 21.65	8 13 55.45	20.45	1.80	-0.2	196	192	784 ± 31	CFHT
2163	12 27 23.34	8 13 57.68	20.15	2.01	0.3	208	197	402 ± 43	WHT
2195	12 26 58.16	8 14 0.81	21.33	1.14	-1.7	299	79	1241 ± 56	CFHT
2256	12 27 14.99	8 14 5.84	21.24	1.90	0.1	159	151	954 ± 28	CFHT
2341	12 27 0.22	8 14 12.97	20.76	1.91	0.1	267	77	1001 ± 68	WHT
2406	12 27 13.24	8 14 18.46	20.84	2.03	0.4	149	131	1244 ± 70	WHT
2420	12 27 8.45	8 14 19.32	20.95	2.08	0.5	175	108	763 ± 92	CFHT
2452	12 27 25.28	8 14 22.52	21.49	1.40	-1.1	209	183	1828 ± 81	CFHT
2482	12 27 10.16	8 14 24.68	21.58	2.08	0.5	157	111	767 ± 56	WHT
2528	12 27 16.79	8 14 28.28	20.34	1.46	-1.0	139	138	654 ± 65	Mould
2543	12 27 20.34	8 14 29.30	20.27	1.36	-1.2	157	153	1199 ± 48	WHT
2569	12 27 11.33	8 14 31.73	20.12	1.89	0.1	144	110	1056 ± 46	WHT
2634	12 27 7.09	8 14 37.95	19.70	1.56	-0.7	173	84	1014 ± 57	WHT
2753	12 27 13.65	8 14 47.02	20.88	1.19	-1.6	119	105	945 ± 100	CFHT
2759	12 26 53.73	8 14 47.31	19.97	1.31	-1.3	337	14	654 ± 92	CFHT
2817	12 27 30.93	8 14 50.60	21.05	1.50	-0.9	263	182	665 ± 47	CFHT
3150	12 27 5.95	8 15 12.16	21.40	1.79	-0.2	163	46	952 ± 42	WHT
3307	12 27 29.92	8 15 21.38	20.25	1.53	-0.8	237	148	1790 ± 65	Mould
3361	12 27 1.91	8 15 26.61	20.34	1.55	-0.7	210	14	1392 ± 33	CFHT
3628	12 27 0.59	8 15 43.97	21.22	1.90	0.1	222	-8	1008 ± 49	WHT
3635	12 27 24.04	8 15 44.45	20.86	1.34	-1.2	147	99	936 ± 94	CFHT
3757	12 27 13.40	8 15 51.81	21.02	1.82	-0.1	58	43	1220 ± 95	CFHT
3808	12 27 6.60	8 15 54.58	20.35	1.83	-0.1	134	9	832 ± 35	WHT
3909	12 27 33.58	8 16 0.40	21.43	1.36	-1.2	280	128	1253 ± 90	CFHT
3980	12 27 3.05	8 16 5.44	21.15	1.28	-1.4	182	-17	1112 ± 45	WHT

continued from previous page

ID†	RA (1950.0)	DEC (1950.0)	T_1 † (mag)	$C-T_1$ † (mag)	[Fe/H]† (dex)	Rad $''$	Rad_{proj} $''$	V_{helio} km s^{-1}	Source
4168	12 27 7.64	8 16 19.41	20.36	1.68	-0.4	112	-10	1384 ± 44	WHT
4210	12 27 34.25	8 16 22.93	20.53	1.62	-0.6	287	109	1910 ± 29	CFHT
4386	12 27 19.17	8 16 34.72	19.83	1.94	0.2	63	29	1197 ± 33	WHT
4513	12 27 9.78	8 16 42.77	20.10	1.85	0.0	78	-22	908 ± 80	WHT
4731	12 27 9.56	8 16 58.18	19.96	1.43	-1.0	82	-38	698 ± 57	WHT
4780	12 27 20.80	8 17 0.91	19.52	1.95	0.2	88	11	971 ± 45	WHT
4959	12 27 23.06	8 17 11.94	21.38	1.33	-1.3	123	11	1449 ± 44	WHT
5090	12 27 9.43	8 17 20.27	19.83	1.61	-0.6	90	-59	582 ± 46	WHT
5323	12 27 16.29	8 17 33.85	20.33	0.82	-2.5	53	-41	1263 ± 65	Mould
5456	12 27 12.490	8 17 41.40	19.26	1.39	-1.1	68	-66	737 ± 65	Mould
5561	12 26 56.85	8 17 48.30	20.82	1.39	-1.1	277	-144	903 ± 48	WHT
5564	12 27 34.86	8 17 48.46	21.26	1.37	-1.2	302	31	862 ± 19	CFHT
5629	12 27 11.90	8 17 52.27	21.09	1.36	-1.2	82	-79	522 ± 52	WHT
5707	12 27 12.63	8 17 55.85	21.47	1.44	-1.0	79	-78	1712 ± 30	CFHT
5750	12 27 12.08	8 17 58.85	21.50	1.47	-0.9	86	-84	1063 ± 89	CFHT
5856	12 27 9.09	8 18 6.40	21.03	1.13	-1.7	120	-105	1050 ± 84	CFHT
6108	12 27 24.66	8 18 22.75	21.49	1.42	-1.0	174	-49	913 ± 39	CFHT
6164	12 27 12.26	8 18 27.18	19.79	1.65	-0.5	110	-110	426 ± 30	WHT
6231	12 27 16.55	8 18 32.34	20.77	1.82	-0.1	110	-95	1046 ± 50	CFHT
6284	12 27 25.39	8 18 36.81	19.44	1.57	-0.7	191	-59	569 ± 54	WHT
6294	12 27 1.30	8 18 37.70	21.02	1.64	-0.5	233	-170	1034 ± 84	WHT
6344	12 27 7.59	8 18 41.28	20.89	2.01	0.3	160	-145	1220 ± 50	CFHT
6357	12 27 20.14	8 18 41.85	20.47	1.26	-1.4	140	-88	958 ± 29	CFHT
6388	12 27 23.15	8 18 44.48	20.18	1.36	-1.2	170	-76	1212 ± 24	CFHT
6394	12 27 3.03	8 18 45.02	21.40	1.42	-1.0	215	-170	760 ± 85	CFHT
6427	12 27 12.47	8 18 47.52	21.11	1.79	-0.2	128	-128	1141 ± 50	WHT
6476	12 27 43.03	8 18 50.23	20.94	2.23	0.9	435	9	966 ± 36	CFHT
6485	12 27 22.50	8 18 51.23	21.07	1.53	-0.8	168	-86	510 ± 82	CFHT
6520	12 27 16.76	8 18 53.55	20.06	1.86	0.0	131	-114	607 ± 57	WHT
6564	12 27 10.77	8 18 57.26	20.03	1.34	-1.2	147	-146	1077 ± 31	WHT

continued from previous page

ID†	RA (1950.0)	DEC (1950.0)	T_1 † (mag)	$C-T_1$ † (mag)	[Fe/H]† (dex)	Rad $''$	Rad_{proj} $''$	V_{helio} km s^{-1}	Source
6615	12 27 41.49	8 19 1.25	20.48	1.47	-0.9	416	-8	1923 ± 49	CFHT
6696	12 27 21.46	8 19 8.53	20.08	1.59	-0.6	173	-107	561 ± 23	CFHT
6701	12 26 53.65	8 19 8.64	20.97	2.00	0.3	348	-235	1092 ± 141	CFHT
6721	12 27 7.36	8 19 10.51	21.09	1.73	-0.3	185	-174	1180 ± 45	WHT
6748	12 27 8.24	8 19 12.40	20.21	1.53	-0.8	179	-172	817 ± 20	CFHT
6872	12 27 9.21	8 19 20.75	20.15	1.46	-1.0	178	-175	870 ± 41	WHT
6989	12 27 22.00	8 19 30.62	20.61	1.75	-0.3	196	-126	1009 ± 24	CFHT
7028	12 27 39.52	8 19 33.52	21.40	1.38	-1.1	401	-48	1548 ± 39	CFHT
7043	12 26 56.69	8 19 34.38	20.47	1.78	-0.2	321	-246	808 ± 67	CFHT
7095	12 27 29.05	8 19 39.76	21.43	1.56	-0.7	272	-102	1285 ± 80	CFHT
7197	12 27 8.44	8 19 48.23	20.94	1.50	-0.9	208	-205	782 ± 50	WHT
7281	12 27 20.64	8 19 53.81	21.43	1.25	-1.5	207	-154	389 ± 123	CFHT
7340	12 27 17.40	8 19 58.99	20.91	1.77	-0.2	197	-173	1067 ± 29	CFHT
7364	12 26 58.79	8 20 1.39	21.36	1.36	-1.2	312	-262	1522 ± 100	CFHT
7399	12 27 1.33	8 20 5.10	20.35	1.40	-1.1	285	-253	1005 ± 44	WHT
7430	12 26 53.05	8 20 6.46	20.76	1.41	-1.1	383	-292	862 ± 66	CFHT
7449	12 26 47.44	8 20 7.69	20.75	1.65	-0.5	457	-320	724 ± 65	CFHT
7458	12 27 12.24	8 20 8.65	20.75	1.84	-0.1	208	-207	807 ± 57	WHT
7531	12 26 52.55	8 20 13.48	19.71	2.07	0.5	393	-301	818 ± 72	CFHT
7616	12 27 16.55	8 20 20.19	21.35	1.49	-0.9	217	-198	600 ± 90	CFHT
7659	12 27 10.56	8 20 24.00	19.87	1.34	-1.2	229	-229	1520 ± 44	CFHT
7702	12 27 38.87	8 20 27.43	21.19	1.88	0.0	419	-102	1388 ± 58	CFHT
7746	12 27 27.01	8 20 31.49	21.29	1.42	-1.0	288	-160	712 ± 68	CFHT
7784	12 27 23.23	8 20 34.42	19.20	1.52	-0.8	260	-181	868 ± 51	WHT
7798	12 27 32.56	8 20 35.38	20.96	1.39	-1.1	348	-139	1340 ± 39	CFHT
7872	12 27 14.71	8 20 42.03	20.33	1.45	-1.0	237	-227	908 ± 77	CFHT
7886	12 26 55.98	8 20 43.76	20.62	1.58	-0.7	370	-315	1236 ± 33	CFHT
7889	12 27 25.49	8 20 43.50	18.85	1.58	-0.7	285	-179	614 ± 65	Mould
7894	12 27 1.99	8 20 37.28	21.61	1.73	-0.3	302	-281	730 ± 81	WHT
7914	12 27 18.07	8 20 46.44	21.20	1.33	-1.3	246	-216	1101 ± 29	CFHT

continued from previous page

ID†	RA (1950.0)	DEC (1950.0)	T_1 † (mag)	$C-T_1$ † (mag)	[Fe/H]† (dex)	Rad $''$	Rad_{proj} $''$	V_{helio} km s^{-1}	Source
7938	12 27 11.91	8 20 47.72	20.92	1.44	-1.0	247	-245	1251 ± 50	WHT
7945	12 26 51.93	8 20 48.19	19.79	1.59	-0.7	420	-337	651 ± 33	CFHT
8000	12 27 28.43	8 20 53.31	21.08	1.49	-0.9	319	-175	368 ± 40	CFHT
8090	12 27 13.14	8 21 0.92	20.51	1.46	-0.9	258	-252	903 ± 66	WHT
8143	12 27 31.74	8 21 4.72	20.96	1.52	-0.8	360	-170	672 ± 109	CFHT
8164	12 27 26.33	8 21 6.88	21.32	2.04	0.4	311	-197	738 ± 40	CFHT
8165	12 27 23.58	8 21 6.85	20.22	1.39	-1.1	291	-210	1027 ± 47	WHT
8210	12 26 54.15	8 21 10.08	20.43	1.32	-1.3	408	-348	576 ± 88	CFHT
8273	12 27 1.10	8 21 15.85	20.60	1.43	-1.0	341	-322	784 ± 90	CFHT
8332	12 27 11.29	8 21 21.13	21.09	1.40	-1.1	282	-280	1226 ± 100	CFHT
8353	12 27 8.71	8 21 22.83	20.03	1.98	0.3	293	-293	928 ± 40	WHT
8357	12 27 4.34	8 21 22.94	20.26	1.45	-1.0	320	-313	981 ± 61	CFHT
8384	12 27 15.30	8 21 24.44	21.39	1.41	-1.1	280	-265	768 ± 54	WHT
8596	12 27 34.37	8 21 44.56	19.73	1.31	-1.3	415	-196	888 ± 31	CFHT
8653	12 26 43.83	8 21 49.48	20.50	1.26	-1.4	554	-433	744 ± 44	CFHT
8712	12 27 40.99	8 21 54.70	20.93	1.49	-0.9	495	-175	817 ± 63	CFHT
8740	12 27 9.77	8 21 57.52	21.27	2.14	0.6	322	-321	913 ± 106	CFHT
8890	12 27 15.78	8 22 14.08	20.41	1.88	0.0	329	-309	870 ± 65	WHT
8919	12 27 1.83	8 22 15.97	19.87	1.45	-1.0	385	-376	1014 ± 65	CFHT
9145	12 27 42.37	8 22 39.12	19.79	1.76	-0.2	539	-211	973 ± 38	CFHT
9360	12 26 46.61	8 23 6.82	21.00	1.67	-0.5	569	-494	1191 ± 99	CFHT
9414	12 27 6.09	8 23 14.28	20.82	1.74	-0.3	411	-411	832 ± 40	CFHT
9527	12 26 59.87	8 23 31.95	20.91	1.58	-0.7	465	-457	941 ± 61	CFHT
9666	12 27 18.87	8 23 51.27	20.04	1.74	-0.3	430	-388	811 ± 71	CFHT
9991	12 27 26.39	8 14 35.49	19.41	1.27	-1.4	213	175	1040 ± 65	Mould
9992	12 27 15.80	8 17 16.74	19.99	1.48	-0.9	34	-27	641 ± 65	Mould

In addition to the formal errors returned by the cross-correlation task, one can make an estimate of the uncertainties from the overlap between common objects on different observing runs. Be-

tween the data from S98 and the CFHT sample there are a total of 13 overlaps, and we show the velocities for these clusters in common in Figure 3.3.

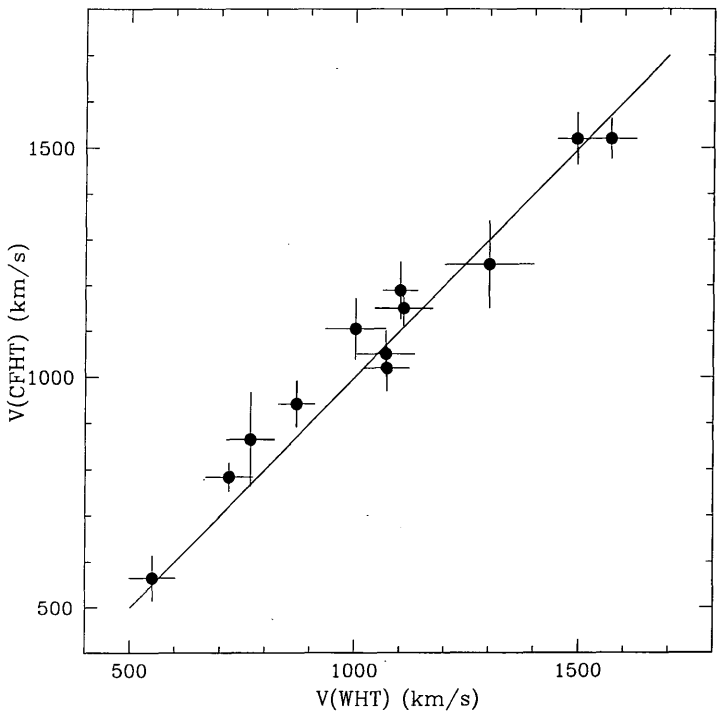

Figure 3.3: Repeat velocities between WHT and CFHT observations. The uncertainties on each velocity is the error returned from the cross-correlation task. The solid line is of unit slope.

The mean difference between the velocities is -17 $\mathrm{km\,s^{-1}}$ (WHT-CFHT), with an inferred velocity uncertainty for a single measurement of 78 $\mathrm{km\,s^{-1}}$. Some of this dispersion originates from the velocity difference in one cluster (#7340), for which we obtain V_{WHT}=1308 $\pm$ 124 $\mathrm{km\,s^{-1}}$ and V_{CFHT}=1067 $\pm$ 40 $\mathrm{km\,s^{-1}}$. By removing this cluster, we obtain σ = 50 $\mathrm{km\,s^{-1}}$, however the offset increases accordingly to -26 $\mathrm{km\,s^{-1}}$. To check whether these uncertainties from the cross-correlation task are reasonable, we obtain a χ^2 from the overlaps:

$$\chi^2 = \sum_{i=1}^{n} \frac{(v_{\mathrm{c}_i} - v_{\mathrm{w}_i})^2}{(\sigma_{\mathrm{c}_i}^2 + \sigma_{\mathrm{w}_i}^2)^{0.5}} \tag{3.1}$$

where v_{c} and v_{w} are the observed velocities of the clusters from the CFHT and WHT runs, and σ_{c} and σ_{w} are their respective errors obtained from the cross-correlation. For ν = 13 degrees of freedom, we obtain a reduced χ^2 of 0.83. A value of just under one indicates that we have marginally *overestimated* our uncertainties by $\sim$ 10% (e.g. Taylor 1982). Since this is a comfortable error margin, we retain these uncertainties.

Following Mould et al. (1990), we take a velocity range of $300 \leq V_{\rm h} \leq 2000$ km s^{-1} as being representative of GCs associated with NGC 4472, which has a heliocentric velocity of 961 km s^{-1} (Sandage & Tammann 1981). This is consistent with the mean velocity of our entire GC sample of 990 ± 26 kms^{-1}, which has a velocity dispersion of 314 kms^{-1}. For completeness, we list in Appendix A the 20 objects for which we obtained spectra and found them to be either foreground stars or background galaxies. We have achieved an 83% success rate in spectroscopically confirming our targets as GCs, higher than previous studies. This high success rate is largely due to selection of targets from high quality photometry, and bodes well for future spectroscopic programs (Zepf et al. 2000). Of the 171 targets observed in total during the CFHT run, we were unable to obtain reliable velocities for 51 of these spectra. The majority of these spectra had S/N too low for useful analysis, and were generally the very faintest GC candidates observed ($V \geq 22$). However, four pairs of spectra suffered from a combination of spectral curvature and their spatial proximity to one another. This lead to a total of eight spectra merging in the dispersion direction, and subsequently no useful radial velocity could be measured for them.

3.3 Line-Strengths of the Globular Clusters

3.3.1 Co-adding the Spectra

The quality of our individual spectra is adequate to obtain accurate radial velocities, but is insufficient for reliable line-strength analysis. Therefore, for any believable measurement of equivalent widths of absorption lines, a method of combining the spectra is required so as to improve their S/N ratio. Such an approach has been successfully implemented by a number of authors, where individual, low-S/N spectra have been *co-added* to create a higher S/N 'mean' spectrum (e.g. Bridges et al. 1997; Puzia et al. 2000).

Since the broadband colours of the GCs primarily reflect their metallicities (on the assumption that these are old stellar populations, $\tau \gtrsim 6$ Gyr), blue GCs should be metal-poor, and become progressively more metal-rich as they redden. We have therefore chosen to separate the clusters by colour and combine them on this basis; we have assigned the cluster spectra to bins by their $C - T_1$ colours, obtained from the photometry of GLK96. The key advantage of selecting the spectra on this basis is that we use an independent constraint to bin the clusters. The GC catalogue of GLK96 is bimodal in colour, and the subset of brightest GCs selected for spectroscopy from this catalogue were chosen so as to preserve this bimodality, albeit with reduced cluster numbers.

Figure 3.4 shows the sample of 860 cluster candidates from GLK96 (open histogram) and those for which radial velocities have been obtained and subsequently used in the metallicity analysis (shaded histogram).

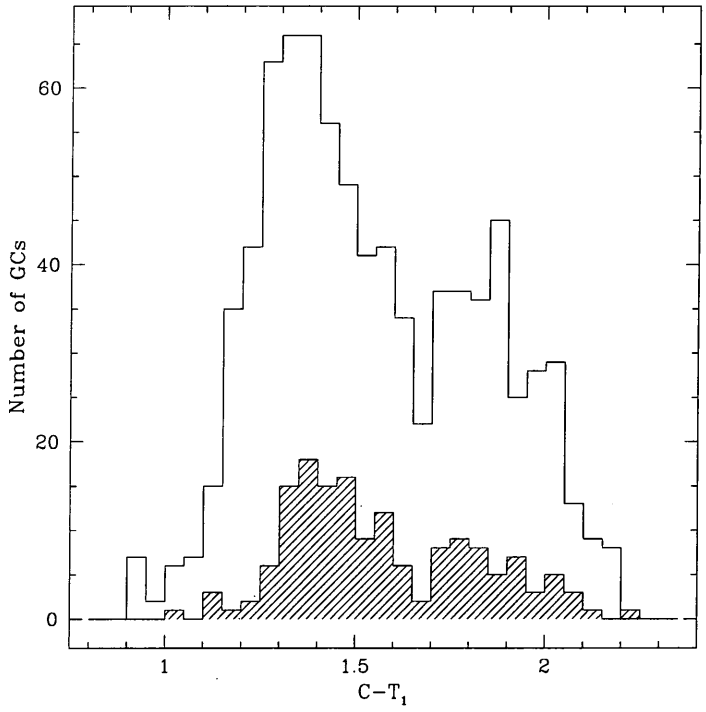

Figure 3.4: Colour distribution for GC candidates with $19.5 \leq V \leq 22.5$ and $0.5 < C - T_1 < 2.2$ from GLK96. The open histogram is for the full sample of 860 candidates; the shaded histogram is for the GCs for which we have radial velocities and have used in the metallicity analysis.

Owing to this bimodality in these data, creating bins of a fixed width in colour leads to significantly different numbers of spectra in each bin. Spectra resulting from such binning are not readily comparable since their signal-to-noise (S/N) varies as a function of the number of spectra per bin. The bins were therefore constructed by assigning approximately equal numbers of spectra to each bin, yielding final spectra of similar S/N, but with different widths in colour. In order to determine the number of spectra per bin acceptable for reliably measuring line-strengths, the following procedure was adopted. The spectral energy distributions (SEDs) of W94 (see § 3.4.2) at a fixed age and range of metallicities were degraded to the typical S/N of the NGC 4472 GC spectra. This was achieved by adding random noise to the spectra until they possessed a distribution in S/N equivalent to that of the NGC 4472 GC data. Subsequent spectra were then co-added and their line-strength indices measured (see § 3.3.2 for discussion of index measurements). This process

was reiterated until a sufficient number of realisations produced stable measurements in all indices, that were consistent with the indices measured for the original, un-degraded spectrum.

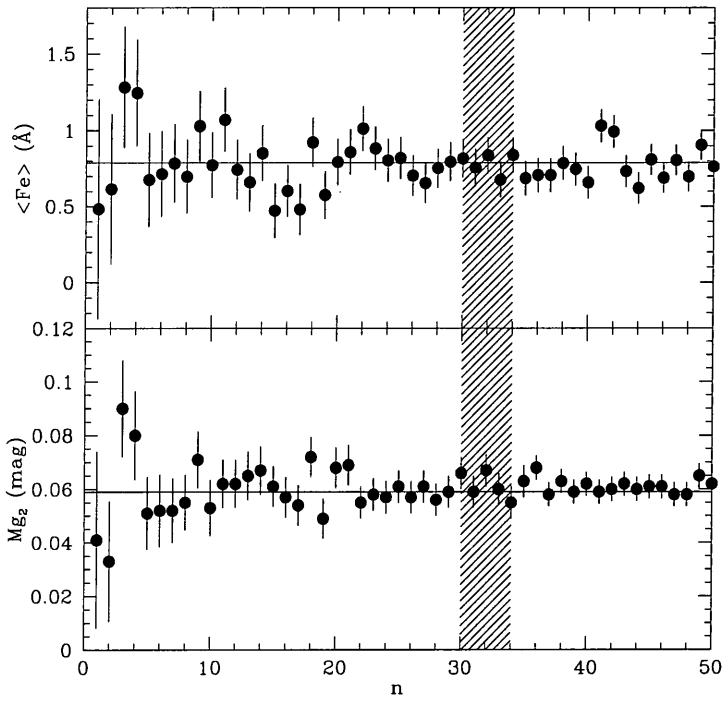

Figure 3.5: Line-strength measurements of ⟨Fe⟩ (top panel) and Mg_2 of the degraded and co-added SEDs of W94. Each set of realisations is represented by a filled circle, with its associated statistical error. The shaded region indicates the location where the line-strength measurements were found to be stable. The solid horizontal line in each panel indicates the value of the index measurement for the original SED. Note that ⟨Fe⟩ is measured in units of Angstroms, whereas Mg_2 is expressed as a magnitude.

An example of the results of this exercise is shown in Figure 3.5 for the ⟨Fe⟩[2] and Mg_2 indices. Each filled circle represents a set of n realisations, with their associated statistical errors, derived from the S/N of each spectrum obtained by summing over pixels along the slit within a fixed wavelength range ($\sim$ 4545 – 5500 Å) (see Equation 4.9 in Chapter 4). The shaded column indicates where the number of co-added spectra were found to be sufficient to produce a stable index measurement. In the case of Figure 3.5, the degraded SED is that predicted by the W94 models for a 17 Gyr stellar population with [Fe/H] = -1.7 dex. The indices measured from the co-added spectra (at n = 32) in Figure 3.5 are 0.065 $\pm$ 0.011 mag for Mg_2, and 0.85 $\pm$ 0.30 Å for ⟨Fe⟩, in excellent agreement with the models which predict 0.06 mag and 0.79 Å for ⟨Fe⟩ and

[2] ⟨Fe⟩ is defined as the mean of the Fe5270 and Fe5335 indices in Gonzaléz (1993).

Mg_2 respectively. We repeated this procedure for different index features, none of which showed any evidence of systematic effects.

As discussed in the introduction to this Chapter, we now have radial velocities for 144 GCs associated with NGC 4472. However 10 of these velocities came from the study of Mould et al. (1990), and were not available for this analysis. Furthermore, because these were spectra taken with a multislit spectrograph, the wavelength range of the spectrum of a particular object is dependent upon the position of the object in the telescope focal plane. Consequently, the reddest and bluest features analyzed were not present in all the spectra. Three spectra from the CFHT data possessed rather small wavelength ranges as a result of this, and were excluded from these analyses. This left a total of 131 GC spectra available for co-addition. Initially, four colour bins where selected, set by the number of spectra required per bin. The first (bluest) bin consisted of 35 spectra, whilst the remaining three each comprised of 32 spectra apiece. Prior to co-addition, the spectra were transferred to the rest-frame using their measured radial velocities. This procedure is essential for any measurement of line indices using fixed-wavelength bandpasses (e.g. Brodie & Huchra 1990).

3.3.2 Measuring the Line-Strength Indices

Numerous systems for measuring line-strengths in stellar populations exist, all with their respective merits and failings. However, the key features considered important in this study where the size and availability of the observational database, and the range of stellar models with which to calibrate these data. In this respect, the Lick system (Burstein et al. 1984; Faber et al. 1985; Gorgas et al. 1993; Trager et al. 1998) was our system of choice.

The absorption-line indices were measured in our co-added spectra following a prescription similar to that described in Brodie & Huchra (1990), using a FORTRAN programme LS1D (described in Chapter 4). Each index is fully described by two pseudocontinuum regions and one feature bandpass region.

For atomic lines, the equivalent width of a line is defined as:

$$EW = \int_{\lambda_1}^{\lambda_2} \left(1 - \frac{F_{I\lambda}}{F_{C\lambda}}\right) d\lambda \tag{3.2}$$

where λ_1,λ_2 are the wavelength limits of the passband, and $F_{I\lambda}$,$F_{C\lambda}$ are the flux per unit wavelength of the measured feature and the continuum respectively. Molecular line-strengths are similarly defined, but are measured in magnitudes:

$$I = -2.5 \log \left[\left(\frac{1}{\lambda_2 - \lambda_1} \right) \int_{\lambda_1}^{\lambda_2} \frac{F_{I\lambda}}{F_{C\lambda}} \, d\lambda \right] \tag{3.3}$$

The Lick index definitions which we have used are those given in Worthey et al. (1994) and Worthey & Ottaviani (1997), we list the bandpasses measured in this study in Table 3.6.

Table 3.6. The Lick/IDS indices measured in this study.

Index	Blue Continuum (Å)	Feature Bandpass (Å)	Red Continuum (Å)	Feature Width (Å)
CN_1 (mag)	4080.125 – 4117.625	4142.125 – 4177.125	4244.125 – 4284.125	35
CN_2 (mag)	4083.875 – 4096.375	4142.125 – 4177.125	4244.125 – 4284.125	35
G4300 (Å)	4266.375 – 4282.625	4281.375 – 4316.375	4318.875 – 4335.125	35
Hβ (Å)	4827.875 – 4847.875	4847.875 – 4876.625	4876.625 – 4891.625	28.75
Mg_1 (mag)	4895.125 – 4957.625	5069.125 – 5134.125	5301.125 – 5366.125	65
Mg_2 (mag)	4895.125 – 4957.625	5154.125 – 5196.625	5301.125 – 5366.125	42.5
Mg b (Å)	5142.625 – 5161.375	5160.125 – 5192.625	5191.375 – 5206.375	32.5
Fe5270 (Å)	5233.150 – 5248.150	5245.650 – 5285.650	5285.650 – 5318.150	40
Fe5335 (Å)	5304.625 – 5315.875	5312.125 – 5352.125	5353.375 – 5363.375	40
Hδ_A (Å)	4041.600 – 4079.750	4083.500 – 4122.250	4128.500 – 4161.000	38.75
Hγ_A (Å)	4283.500 – 4319.750	4319.750 – 4363.500	4367.250 – 4419.750	43.75

For comparison with the stellar population models of W94 (see § 3.4.2), we measured the indices within our co-added spectra as defined in Table 3.6. Figure 3.6 illustrates the locations of the majority of the feature bandpasses measured in this study, the regions of pseudocontinua are omitted for clarity. Note that the Mg_2 index (not shown in Figure 3.6), encompasses both Mg_1 and Mg b.

However, we also wish to use the empirical metallicity calibrations of Brodie & Huchra (1990). These authors obtained relations between the metallicity scale of Zinn (1985) and the line-strength indices of integrated spectra based upon observations of GCs in the Milky Way and M31. They

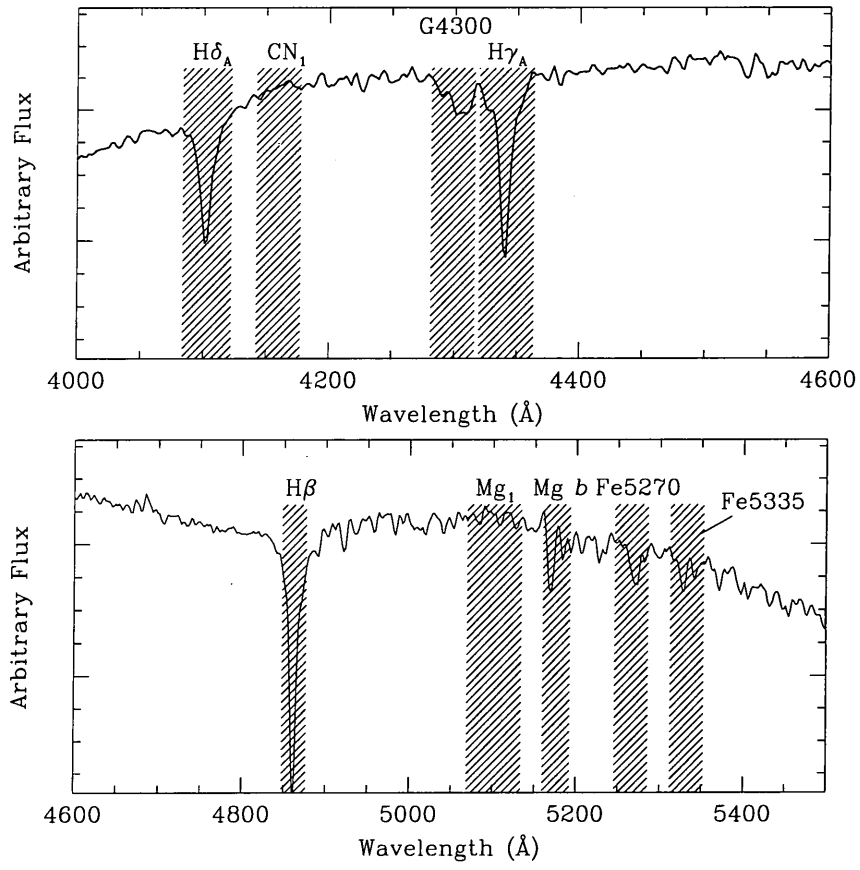

Figure 3.6: Location of the feature bandpasses measured in our data. Shaded regions show the width and position of the features, which are over-plotted on to the normalised spectrum of the metal-poor GC M15.

defined six indices which act as 'primary calibrators' for metallicity in old stellar populations, four of which fall within our useful wavelength range. These authors define indices which are similar to those of Lick, but generally differ slightly in continuum and feature placement (and nomenclature). We show the Brodie & Huchra (1990) index definitions we have measured in Table 3.7.

The Lick/IDS system is based upon a stellar library which is *not* flux-calibrated, but which was normalised by division with a quartz-iodide tungsten lamp (see Chapter 4 for a description of the Lick/IDS). Furthermore, its resolution (FWHM) varies as a function of wavelength. Our data have a fixed spectral resolution of $\sim$ 5.5 Å (FWHM) and have also not been flux-calibrated. Consequently, it is difficult to accurately transform our measurements on to the Lick System and care must be taken, particularly with regard to the continuum slope (e.g. Worthey & Ottaviani 1997; Cohen, Blakeslee, & Ryzhov 1998).

Table 3.7. Primary calibrators of Brodie & Huchra (199) measured in our co-added spectra.

Index	Blue Continuum (Å)	Feature Bandpass (Å)	Red Continuum (Å)	Feature Width (Å)
G Band (Å)	4268.25 – 4283.25	4283.25 – 4317.00	4320.75 – 4335.75	33.75
MgH (mag)	4897.00 – 4958.25	5071.00 – 5134.75	5303.00 – 5366.75	63.75
Mg2 (mag)	4897.00 – 4958.25	5156.00 – 5197.25	5303.00 – 5366.75	41.25
Fe52 (Å)	5235.50 – 5249.25	5248.00 – 5286.75	5288.00 – 5319.25	38.75

The first step in approximating to the Lick system was to convert the resolution of our data to that of the IDS. In Table 3.8 we reproduce the data given in table 8 of Worthey & Ottaviani (1997), illustrating the dependence of spectral resolution upon wavelength for the IDS. For our multislit data, the useful spectral range is 3800 Å – 5500 Å, covering a Lick resolution from approximately 11.5 Å to 8.4 Å.

Table 3.8. Dependence of spectral resolution on wavelength for the Lick/IDS.

Wavelength (Å)	Resolution (FWHM) (Å)
4000	11.5
4400	9.2
4900	8.4
5400	8.4
6000	9.8

The data given in Table 3.8 was interpolated to give a function relating wavelength to FWHM for the Lick/IDS. We then convolved our spectra with a Gaussian kernel whose width was given by:

$$\sigma(\lambda) = \frac{\sqrt{(\delta\Lambda_{\rm IDS}(\lambda)^2 - \delta\Lambda^2_{\rm N4472})}}{2.35 \times \text{Å pix}^{-1}} \tag{3.4}$$

where $\delta\Lambda_{\rm N4472}$ and $\delta\Lambda_{\rm IDS}(\lambda)$ correspond to the resolution (FWHM) of our data and that of the Lick/IDS respectively.

The indices of the un-broadened spectra were then compared to those of the Lick resolution spectra to investigate systematic differences between the two. The broader indices were largely unaffected, for example Mg_2, which has a feature width of 42.5 Å, was unchanged. However Mg *b*, a narrower index (feature width 32.5 Å) was systematically lower by approximately 0.14 Å when measured from the broadened spectra.

Our next consideration was the effect of the instrumental response curve upon the continuum slope of the indices. Unlike our analysis of the LMC clusters in Chapter 4, we do not have a range of Lick standard stars with which to calibrate each individual index onto the Lick/IDS system. Therefore, to calibrate onto the stellar population models of W94 we rely upon observations of GGCs (see § 3.4.2).

However, the continuum shape of an integrated spectrum is known to (sometimes significantly) effect its measured line-strength indices. Therefore, in order to characterize this effect, we have simulated the effect of varying the local spectral slope of each feature bandpass, by altering the global continuum shape of the spectra. A polynomial was fit to each of our co-added spectra, representing the full range of continuum shape in our data. This entire set of artificial 'response functions' were then added to a normalised standard spectrum and the indices of each were measured and the results compared. In Table 3.9 we show the effect upon the index measurements resulting from this variation in the continuum shape.

As Table 3.9 indicates, the majority of the features remain relatively stable. However the CN_1, CN_2 and Mg_1 features show large dispersion, and the significant differences between their mean and median values indicates highly skewed distributions. Clearly these features are very sensitive to small shifts in the slope of the local continuum and cannot be trusted in these current data. To a lesser extent, Mg_2 and $H\delta_A$ are also susceptible to changes in the continuum level. In recognition of this we have chosen to omit the CN_1, CN_2 and Mg_1 indices from further analysis, and bear in mind the behaviour Mg_2 and $H\delta_A$. We note that extreme care must be taken when measuring indices under the Lick system if the continuum has not been corrected to that of the IDS. This is especially true for the broader features.

Errors in the velocities of the individual spectra had no significant effect upon the line indices measured for our co-added spectra. Our uncertainties in the radial velocities velocities are typically 75 $\mathrm{km\,s^{-1}}$, translating to approximately half a pixel at the resolution of these data. Similarly, we have applied no correction for line broadening due to any *internal* velocity dispersion of the GCs.

Table 3.9. Effect of the continuum shape on index measurements of features. For comparison purposes, we have converted the molecular indices CN_1, CN_1, Mg_1 and Mg_2 into equivalent widths of absorption. In this case, the line-strength indices given are measured from the stellar spectrum of HD 102494, a G9 subdwarf.

Feature	Mean (Å)	Median (Å)	σ (Å)	Width (Å)
CN_1	0.193	0.289	0.42	35
CN_2	0.223	0.350	0.40	35
G4300	3.017	2.986	0.10	35
Hβ	0.808	0.801	0.02	28.75
Mg_1	0.358	0.297	0.54	65
Mg_2	2.396	2.322	0.20	42.5
Mg b	1.542	1.545	0.02	32.5
Fe5270	1.335	1.399	0.02	40
Fe5335	0.982	0.984	0.01	40
Hδ_A	-1.739	-1.694	0.19	38.75
Hγ_A	-3.016	-3.041	0.10	43.75

Internal stellar velocity dispersions of GCs are small, typically less than $\sim$ 10 kms^{-1} (Meylan & Heggie 1997)

3.3.3 Uncertainties in the Indices

The value of any line-strength measurement is dependent upon a suitable calculation of its associated uncertainty. For an old stellar population at roughly solar metallicity, an error as small as 0.2 Å in the Mg b index translates into an uncertainty of $\sim$ 0.2 dex in metallicity, and an uncertainty of 0.2 Å in the Hβ index corresponds to an error of $\sim$ 3 Gyr in age (W94). The main sources of uncertainty in our index measurements from the co-added spectra stem from systematics in the binning process and any intrinsic spread in the chemical composition of the GCs. The latter is inherent in these data; the spectra comprise of colour bins of a finite width which can be adjusted through alterations in this binning. The former stems from effects of the continuum slope, index placement, shot-noise in the spectra and uncertainties in the data reduction (e.g. sky-subtraction, wavelength calibration).

The total uncertainties may be best estimated through the use of a bootstrap technique, which takes into account the stochastic nature of co-adding individual, low S/N spectra.

The method we use here is quite straightforward: Each of our colour bins contain n spectra, and we assign each spectrum a number from 1 to n. A spectrum is selected randomly from the bin by its corresponding number and placed into a pool which holds the spectra to be co-added. This process is then repeated until the resulting pool contains n randomly selected spectra from the original bin. Each spectrum is selected *with replacement*, so the initial bin is never depleted and the new pool is likely to contain several repetitions of the same spectrum. The spectra contained within the pool are then co-added to produce a final composite spectrum, which then has its line indices measured. This description comprises one realisation and is repeated many times so as to produce many index measurements of the same feature. Typically 150 realisations were performed for each colour bin. We then take the final index value to be the mean of the distribution of measurements for each bin and its associated uncertainty as the standard deviation of this distribution. To assess the mean $C - T_1$ colour of the co-added spectra, we have also measured the flux-weighted colours for each bin. This is preferable over a magnitude weighting scheme, since the amount of light received through each slit on to the detector is not only a function of an individual GCS brightness, but also of its position in the slit.

Figure 3.7 shows representative co-added spectra for the four colour bins, which have the mean flux-weighted colours of $C - T_1$= 1.30, 1.44, 1.61 and 1.91 respectively. The spectra are representative, since our final index measurements are the mean derived from many such spectra. Metal lines clearly become progressively stronger with redder colours (e.g. Mg b feature at $\sim$ 5180 Å), whilst the Balmer lines weaken (e.g. Hβ at 4860 Å and Hγ at 4340 Å).

We have extensively tested the effects of altering the bin size for our GC data. We have varied n, the number of spectra per bin, and repeated the procedure described previously, determining the variance in the indices in each case. We show the dependence of σ upon n for our co-added spectra in Figure 3.8. The uncertainties in all of the indices behave in a similar fashion. There is a steep initial gain in accuracy as the S/N of the spectra increase, which slowly flattens at increasingly larger n. The uncertainties in the Mg_2 index are $\sim$ 0.1 Å greater than for the other indices, which we largely largely attribute to its sensitivity to variations in the continuum slope. Figure 3.8 indicates that we may expect an uncertainty in most of the indices of 0.3 Å – 0.4 Å and 0.5 Å (0.013 mag) in Mg_2 for $n \simeq 30$. The uncertainties in the indices will not asymptotically tend to zero for several reasons. Firstly, there is a fundamental limit set by the shape of the continuum

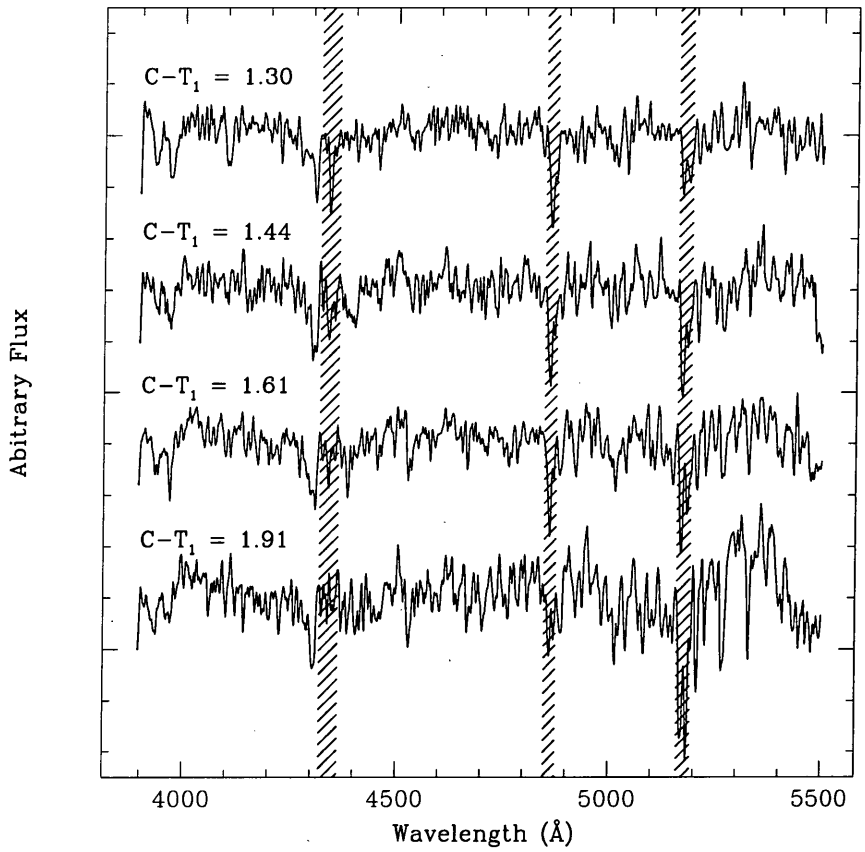

Figure 3.7: Representative co-added spectra of the NGC 4472 GCs obtained from the bootstrap procedure. The spectra become progressively redder from top to bottom. The mean colours in $C-T_1$ are 1.30, 1.44, 1.61 and 1.91 respectively. The positions of Hγ at 4340 Å, Hβ at 4860 Åand the Mg b feature at $\sim$ 5180 Å are indicated by the shaded columns. The spectra have been continuum-normalised by a fifth-order polynomial, and have been shifted in the y-axis for clarity.

of the co-added spectra (e.g. Table 3.9). Unless the continuum is removed in a consistent way, this will remain the principle contribution to the error budget. Moreover, as the bin size increases, so does the intrinsic spread of chemical abundance in the GCs. Assuming the $C - T_1$ colours of our spectroscopic sample accurately reflect the metallicities of the clusters, binning the *entire* sample will encompass a colour range of $0.82 \leq C - T_1 \leq 2.23$, corresponding to a metallicity range of $-2.46 \leq$ [Fe/H] ≤ 0.8 (Equation 3.5). By naively obtaining the mean of the sample, assuming a normal distribution, these colours have a standard deviation of $\sigma_{C-T_1} \sim 0.25$ mag, corresponding to an intrinsic metallicity dispersion of ~ 0.6 dex.

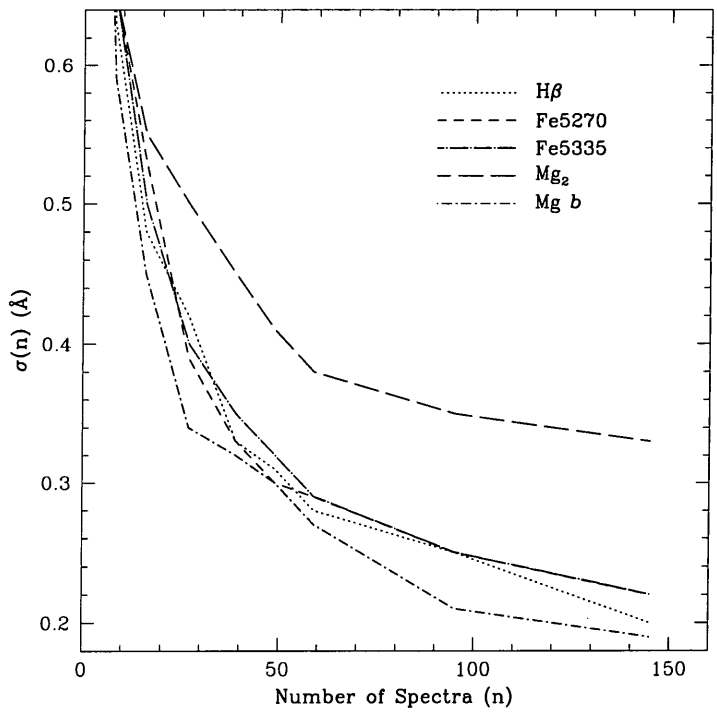

Figure 3.8: The dependence of the variance in the measured indices of the co-added spectra, upon the number of spectra per bin.

3.3.4 The Measured Indices

We list the final line-strength indices measured for the GC bins using the bandpass definitions of Worthey et al. (1994) and Worthey & Ottaviani (1997) in Table 3.10. The associated uncertainties in these indices, obtained from the bootstrap procedure, are tabulated in alternate rows. The uncertainties for the mean bin colour are taken to be the standard deviation of the distribution of the flux weighted $C - T_1$ colours, also from the bootstrap procedure. In column 3 of Table 3.10 we give the metallicities predicted by the mean $C - T_1$ colours, using the linear relation of Geisler & Forte (1990):

$$[\mathrm{Fe/H}] = 2.35 \times (C - T_1) - 4.39 \tag{3.5}$$

Equation 3.5 is based upon a calibration of 48 Galactic GCs using the photometry of Harris & Canterna (1977) and [Fe/H] values from Zinn (1985) and Armandroff (1988). The metallicity range spanned by the GGCs used in the calibration is -2.5 < [Fe/H] < -0.25 dex.

We also list our measurements for the Brodie & Huchra (1990) index definitions in Table 3.11, again our uncertainties in these indices are obtained from the bootstrap.

Table 3.10. Measured indices for our four colour bins of NGC 4472 GCs. Column 2 gives the flux weighted mean $C - T_1$ colour for the bin. The metallicity given in column 3 is derived from these colours using Equation. 3.5, the relation of Geisler & Forte (1990) and is henceforth denoted $[Fe/H]_{GF}$. Uncertainties derived from the bootstrap procedure are given in alternate rows.

Bin	C-T_1 (mag)	$[Fe/H]_{GF}$ (dex)	G4300 (Å)	Hβ (Å)	Mg_2 (mag)	Mg b (Å)	Fe5270 (Å)	Fe5335 (Å)	Hδ_A (Å)	Hγ_A (Å)
1	1.30	-1.34	2.030	2.452	0.072	1.648	1.573	1.093	2.497	0.374
...	$\pm$ 0.09	0.21	0.397	0.330	0.011	0.303	0.275	0.274	0.815	0.566
2	1.44	-1.00	3.590	1.956	0.114	2.287	1.778	0.942	-0.466	-1.607
...	$\pm$ 0.07	0.16	0.550	0.430	0.011	0.295	0.436	0.317	1.346	0.582
3	1.61	-0.61	4.017	1.630	0.126	2.115	1.706	1.432	0.018	-2.763
...	$\pm$ 0.06	0.14	0.469	0.244	0.008	0.206	0.289	0.179	0.896	0.753
4	1.91	0.10	6.417	1.225	0.240	4.347	3.195	2.770	-2.052	-6.354
...	$\pm$ 0.11	0.26	0.943	0.410	0.019	0.359	0.331	0.468	1.913	1.658

In order to derive metallicities from the indices given in Table 3.11, the equivalent widths were first converted into line-strength magnitudes :

$$I = -2.5 \log \left(1 - \frac{W_\lambda}{\lambda_2 - \lambda_1}\right) \tag{3.6}$$

where $\lambda_2 - \lambda_1$ is the width of the feature bandpass and W_λ is the measured equivalent width.

We then use the linear relations between the measured index and metallicity given in Brodie & Huchra (1990):

$$[Fe/H]_G = 11.415 \times (CH) - 2.455 \tag{3.7}$$

$$[Fe/H]_{MgH} = 20.578 \times (MgH) - 1.840 \tag{3.8}$$

$$[Fe/H]_{Mg2} = 9.921 \times (Mg2) - 2.212 \tag{3.9}$$

$$[Fe/H]_{Fe52} = 20.367 \times (HK) - 2.086 \tag{3.10}$$

We will use these metallicities for comparison with the predictions of the stellar population models and mean $C - T_1$ colours in § 3.4.

Table 3.11. Measured indices for our four colour bins of NGC 4472 GCs using the bandpass definitions of Brodie & Huchra (1990).

Bin	G Band (Å)	MgH (mag)	Mg2 (mag)	Fe52 (Å)	$\overline{[Fe/H]}$ (dex)
1	1.85	0.035	0.092	1.55	-1.35
...	± 0.39	0.009	0.011	0.28	0.18
2	3.49	0.037	0.135	1.72	-1.03
...	± 0.52	0.010	0.012	0.43	0.23
3	3.91	0.039	0.147	1.65	-0.97
...	± 0.46	0.006	0.008	0.29	0.16
4	6.75	0.111	0.260	3.58	0.30
...	± 0.80	0.012	0.018	0.34	0.27

3.4 Metallicities and Ages

3.4.1 Fiducial Globular Clusters

As a quantitative comparison, and in order to calibrate the stellar population models which we use for obtaining abundances and ages, we have obtained trailed, long-slit integrated spectra for five Galactic GCs (see Table 3.4). We give the Lick indices which we have measured for our sample of GGCs in Table 3.12. So as to increase the size of this dataset, we have supplemented this with data from Brodie & Huchra (1990) (17 GCs) and Cohen, Blakeslee, & Ryzhov (1998) (12 GCs). For the GGC metallicities given in Table 3.12, Zinn (1985) quotes a typical uncertainty in the metallicities of 0.15 dex. The uncertainties in the line-strengths given in Table 3.12 are derived purely from the S/N of the spectra, and are probably an underestimate for the highest S/N GGCs (e.g. NGC 6205 and NGC 7078).

In Figures 3.9 – 3.12 we plot our NGC 4472 data together with the combined sample of GGCs for which we have line-strength measurements. The linear fits in these figures which we have applied to our data are not physically motivated, but merely serve as a comparison to the GGCs.

Inspection of Figures 3.9 – 3.12 reveals several interesting points. As expected, the Hβ index increases with the decreasing strength of the more metallicity-sensitive lines and the co-added data of NGC 4472 GCs falls within the metallicity and age ranges of the GGCs. The metal-rich ends of these data coincide at approximately solar, but the GGCs extend out to somewhat lower

Table 3.12. Measured Lick/IDS indices for GGCs from the WHT and CFHT observing runs. Uncertainties are derived from the signal-to-noise of the spectra.

ID	Run	G4300 (Å)	Hβ (Å)	Mg_2 (mag)	Mg b (Å)	Fe5270 (Å)	Fe5335 (Å)	Hδ_A (Å)	Hγ_A (Å)	[Fe/H]$_Z$ (dex)
NGC 6341	WHT	0.83	2.63	0.013	0.56	0.47	0.34	3.94	2.37	-2.24
...	...	± 0.72	0.05	0.009	0.07	0.15	0.03	0.13	0.19	...
NGC 7078	CFHT	0.37	3.10	0.018	0.53	0.96	0.37	4.71	3.43	-2.15
...	...	± 0.06	0.03	0.002	0.04	0.04	0.04	0.07	0.06	...
NGC 6205	WHT	2.14	2.31	0.045	1.00	0.92	0.78	3.17	0.71	-1.65
...	...	± 0.82	0.08	0.003	0.12	0.02	0.05	0.13	0.13	...
NGC 6356	CFHT	4.98	1.73	0.151	3.13	1.80	1.61	-0.52	-3.79	-0.62
...	...	± 0.38	0.19	0.011	0.09	0.11	0.10	0.16	0.15	...
NGC 6356	WHT	4.72	1.57	0.174	3.16	1.94	1.49	0.08	-3.80	-0.62
...	...	± 0.20	0.17	0.012	0.08	0.11	0.12	0.10	0.09	...
NGC 6553	CFHT	5.08	1.55	0.244	4.11	3.13	2.38	-0.90	-5.59	-0.29
...	...	± 0.17	0.30	0.002	0.15	0.04	0.07	0.18	0.21	...

metallicities. The mean line of the NGC 4472 GCs traces that of the GGC distribution fairly closely. The index-index plots in Figure 3.11 and Figure 3.12 are in good agreement with each other, with no obvious evidence of systematic offsets between the different indices. Although there is only one overlap between the two observing runs, namely NGC 6356, the agreement is good in this case. Five of our GGCs are in common with the combined dataset of GGCs from and Cohen, Blakeslee, & Ryzhov (1998), and in most cases these data are in good agreement. However, our measurement of Hβ for NGC 7078 (M15) is $\sim$ +0.5 Å offset from the value measured by Cohen, Blakeslee, & Ryzhov (1998), and the reason for this is unclear. However, we do note that Cohen, Blakeslee, & Ryzhov (1998) quote no uncertainties for their observations of GGCs.

To summarize: we find that the reddest bin of our GCs has a similar metallicity to the most metal-rich GGCs. The bluest bin is significantly more metal-rich than the bluest GGCs. The line-strength indices of the clusters act together in the expected sense, metal-lines strengthen towards the red and the Balmer indices weaken. The co-added data are self-consistent within the boot-strapped uncertainties, which gives us confidence in our data and error estimates.

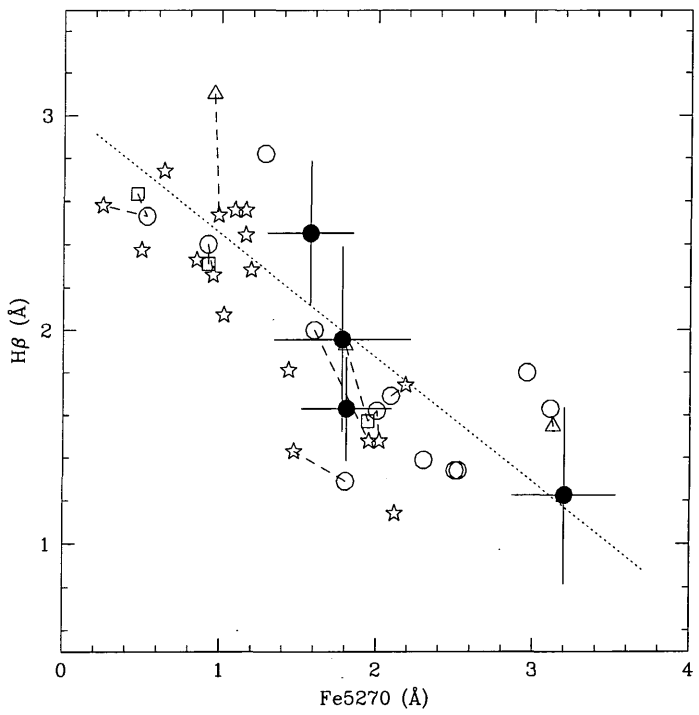

Figure 3.9: Hβ index as a function of Fe5270. Solid circles with error bars are the co-added NGC 4472 cluster data. Open symbols are Galactic GCs: CFHT - triangles, WHT - squares, circles indicate the data of Cohen, Blakeslee, & Ryzhov (1998) and stars represent data from Brodie & Huchra (1990). Dashed lines join GCs common between the datasets. The dotted line indicates the formal linear fit to our co-added NGC 4472 data.

3.4.2 The Worthey Models

In order to derive the metallicities and ages of the NGC 4472 GCs, we compare our data with single age, single metallicity stellar population models (SSPs). These model aggregates of coeval stars with homogeneous metal content, i.e. an idealised GC. The SSP models considered here are the on-line versions of W94 which can come in several flavours, and may be fine–tuned from the web-page of Dr. Worthey.[3] The finer details of these models, and those of Kurth, Fritze-v. Alvensleben, & Fricke (1999) are discussed in Chapter 4.

In this analysis, we restrict ourselves to the Worthey models which adopt a Salpeter initial mass function (α=-2.35) and assume a single, instantaneous burst of star formation. However, the grids used in this study differ from the original Worthey (1994) models in one important respect, which is in their treatment of the horizontal branches (HBs) for metal-poor GCs.

[3] http://astro.sau.edu/~worthey/

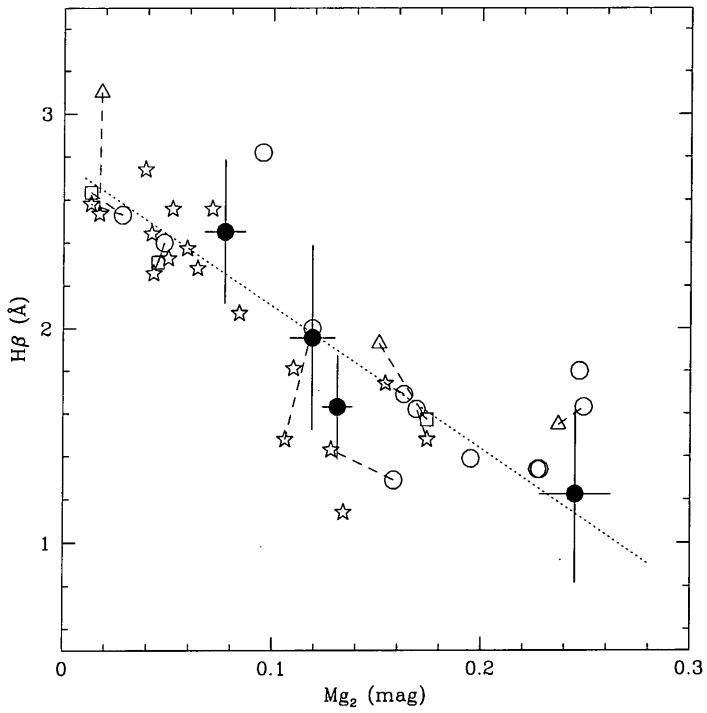

Figure 3.10: Hβ against Mg$_2$ for the NGC 4472 GCs. Symbols are the same as for Figure 3.9.

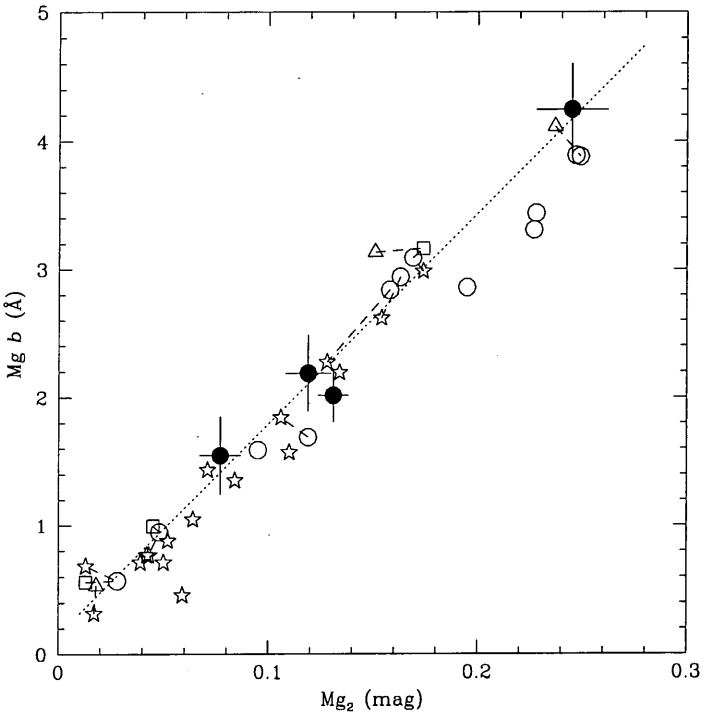

Figure 3.11: Mg b against Mg$_2$ for the NGC 4472 GCs. Symbols are the same as for Figure 3.9.

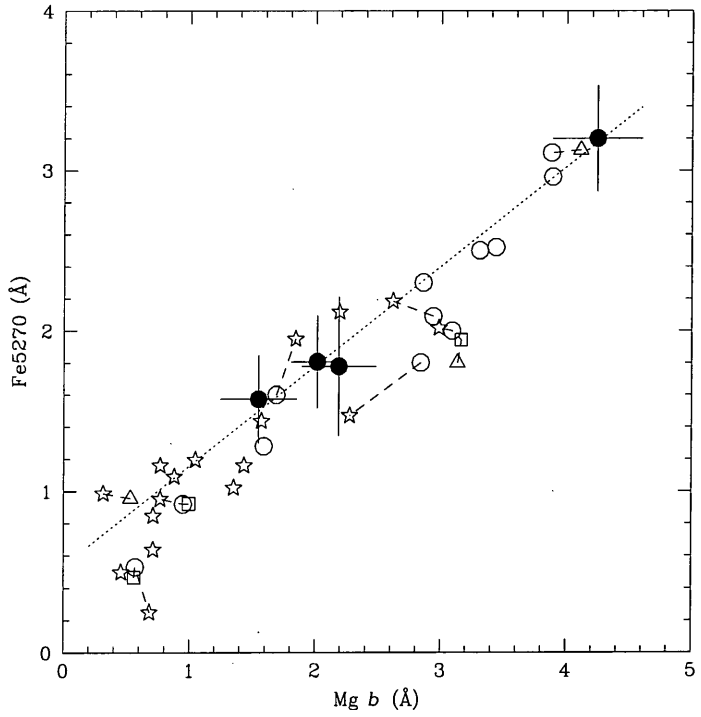

Figure 3.12: Fe5270 against Mg *b* for the NGC 4472 GCs. Symbols are the same as for Figure 3.9.

A number of SSP models (e.g. the original W94 models; Buzzoni 1995) operate under the assumption that the principle contribution to the absorption seen in the Balmer indices stems from the main sequence turn-off in the HR diagram. However, many workers have questioned the validity of this assumption, particularly with regards to the contribution from warm HB stars (e.g. Rabin 1983; Burstein et al. 1984; Fisher, Franx, & Illingworth 1995; Bressan, Chiosi, & Tantalo 1996; Jorgensen 1997; Lee, Yoon, & Lee 2000). The morphology of the HB in the W94 models now follows the observed behaviour of GGCs, in that they become more extended toward the blue for more metal-poor GCs, as opposed to assuming a red clump at the base of the HB irrespective of metallicity. The GGCs M3 and M92 were used as templates for this behaviour (e.g. Aaronson et al. 1973; Worthey 1993). This change has the effect of significantly increasing the predicted Hβ index, by upwards of 0.5 Å at [Fe/H] $\leq$ -0.5 dex. In Figure 3.13 we illustrate this effect and its importance with regard to the predicted ages for GCs, of which a substantial proportion have metallicities [Fe/H] $\leq$ -0.5 dex. A GC with a measured Fe5270 index of 1.5 Å and Hβ index of 2.4 Å would be assigned an age of $\sim$ 10 Gyr according to the old models, but is predicted to be $>$ 17 Gyr old by the models adopting the corrected HB morphology.

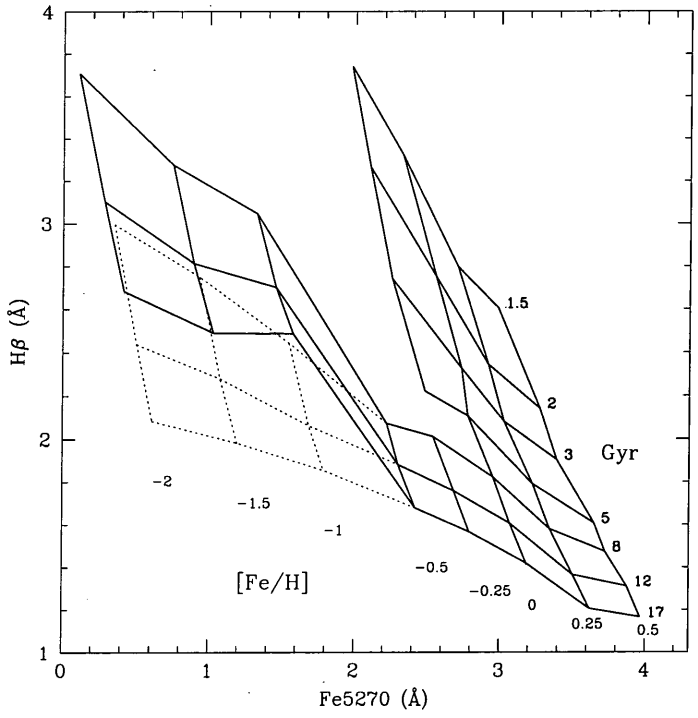

Figure 3.13: Effect of horizontal branch morphology on the Hβ–Fe5270 grid of the SSP models of W94. The horizontal scale indicates the positions of lines of isometallicity. The approximately horizontal grid lines represent isochrones ranging from 1.5 to 17 Gyr (read from top to bottom). Faint dotted lines indicate the predictions of the original models assuming a red clump at the MSTO, long dashed lines show the effect of including extended HBs following the observed behaviour of GGCs.

As a case in point, it is interesting to compare the Hβ indices of GGCs at the same metallicity, but with differing HB morphologies. One of our calibrating GGCs is M13 (NGC 6205), for which we have measured Hβ = 2.31 $\pm$ 0.08 Å, and has an extremely blue HB. Amongst the sample of Brodie et al. (1990) is the GGC NGC 7006, for which they obtain Hβ = 2.48 $\pm$ 0.3 Å, and has a HB ratio of less than unity (it has a greater number of HB stars redward of the RR Lyrae gap than blueward). Since both of these GGCs have Fe/H $\sim$ -1.65, one might expect NGC 6205 to have enhanced Hβ with respect to NGC 7006. However the fact that NGC 7006 has higher Hβ than NGC 6205 (bearing in mind the errors) would imply that HB morphology has little or no effect on Hβ, contrary to the predictions of SSP models accounting for this. Clearly a high quality and homogeneous data set is required to investigate whether the horizontal branch may affect the Balmer indices of GCs at the same metallicity. This assumption of a red clump in the original W94 models may possibly explain the findings of Cohen et al. (1998) for their spectroscopic sample of 150 GCs associated with M 87. They found that formally, their metal-rich GCs are *older* than the

metal-poor ones, perhaps the opposite of what one might expect. This new treatment of the HBs in the models predicts similar ages for their metal-rich and metal-poor GCs.

The W94 model grids cover a metallicity-age parameter space of -0.5 $\leq$ [Fe/H] $\leq$ 0.5 with isochrones of 1.5 $\leq$ τ $\leq$ 17 Gyr. To cover old, metal-poor populations, the models were subsequently extended to bracket -2.0 $\leq$ [Fe/H] $\leq$ 0.5 for ages 8 $\leq$ τ $\leq$ 17 Gyr. The degree of orthogonality in different index-index plots indicates the level of decoupling between age and metallicity in the models.

3.4.3 Metallicities of the Globular Clusters

We have chosen to calibrate the W94 SSP models using the indices measured for the combined sample of GGCs. The metallicities predicted by the models of W94 must first be placed on to the metallicity scale of our GGCs. We use the most widely used metallicity scale for GGCs, which is that of Zinn (1985). This scale is based upon a number of narrow-band photometric indices sensitive to the ultraviolet blanketing in the integrated light of the GC spectra. Whilst there is increasing evidence that this metallicity scale is non-linear (e.g. Carretta & Gratton 1997), we adopt it here since it remains self-consistent and the empirical calibrations of Brodie & Huchra (1990) are based upon this scale.

We first obtain metallicity on the W94 scale as a function of the Fe5270, Mg b and Mg_2 indices for our entire sample of GGCs. This is achieved via interpolation of the SSP grids, as described in Chapter 4. The newly assigned metallicities for the GCs are then compared to those of Zinn (1985) in order to derive a transformation from the W94 model metallicities to that of the Zinn (1985) metallicity scale. We have not used the G4300 and Fe5335 indices for the re-scaling of the models, since we have very few GGCs in our combined sample with measurements of these indices.

For the magnesium indices, we obtained the linear transformations:

$$[\mathrm{Fe/H}]_z = 0.631 \times [\mathrm{Fe/H}]_{\mathrm{Mg}\ b} - 0.349, \sigma = 0.19\ \mathrm{dex} \tag{3.11}$$

$$[\mathrm{Fe/H}]_z = 0.799 \times [\mathrm{Fe/H}]_{\mathrm{Mg_2}} - 0.230, \sigma = 0.16\ \mathrm{dex} \tag{3.12}$$

for Mg b and Mg_2 respectively.

We found that the Fe5270 index proved to be non-linear, and was better fit with a quadratic:

$$[\mathrm{Fe/H}]_z = -0.186 + 0.406 \times [\mathrm{Fe/H}]_{\mathrm{Fe}} - 0.393 \times [\mathrm{Fe/H}]^2_{\mathrm{Fe}} \quad (3.13)$$

with an rms of σ=0.2 dex.

We now derive metallicities from the model predictions for our co-added data using the mean[4] of the Fe5270, Mg b and Mg_2 indices, transformed on to the Zinn (1985) scale as described above; we do not use the Balmer lines in this determination. We have assigned weights to each index, corresponding to the inverse of the scatter from Equations 3.11 – 3.13.

In Table 3.13 we list the metallicities determined for our four mean GC spectra. We compare these metallicities with the mean of those predicted by the empirical calibrations of Brodie & Huchra (1990) and with those predicted by the mean $C - T_1$ colours using Equation 3.5.

We plot the metallicities derived using the different methods against their respective bins in Figure 3.14.

Table 3.13. Metallicities for our co-added NGC 4472 globular clusters derived using the W94 models (denoted $[\mathrm{Fe/H}]_{\mathrm{W}}$), the empirical calibrations of Brodie & Huchra (1990) (denoted $[\mathrm{Fe/H}]_{\mathrm{B}}$) and the $C - T_1$-[Fe/H] relation of Geisler & Forte (1990) (Equation 3.5). We give the weighted mean metallicity from the different methods in Column 5. Uncertainties in the metallicities are tabulated in alternate rows.

Bin	$[\mathrm{Fe/H}]_{\mathrm{W}}$	$[\mathrm{Fe/H}]_{\mathrm{B}}$	$[\mathrm{Fe/H}]_{\mathrm{GF}}$	$\overline{[\mathrm{Fe/H}]}$
1	-1.29	-1.3	-1.34	-1.31
...	$\pm$ 0.3	0.21	0.21	0.13
2	-0.91	-1.03	-1.00	-0.99
...	$\pm$ 0.35	0.31	0.16	0.13
3	-0.84	-0.97	-0.61	-0.78
...	$\pm$ 0.25	0.21	0.14	0.11
4	-0.27	0.30	0.10	0.05
...	$\pm$ 0.30	0.30	0.26	0.16

[4] Strictly speaking, the indices should be averaged *linearly*, whereas the commonly used metallicity indicator [Fe/H] is expressed as a logarithmic scale. However, the difference between the two was only at the level of $\sim$ 1%, significantly less than the measurement error.

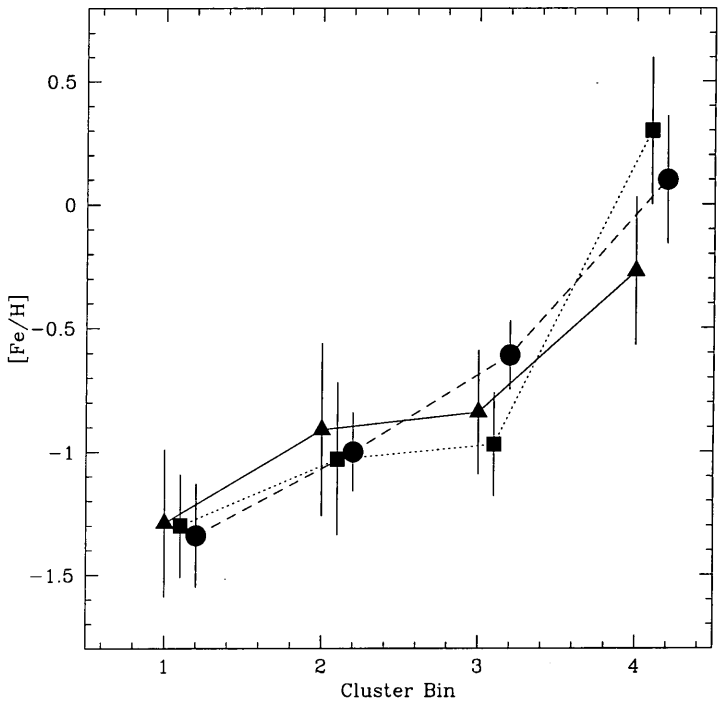

Figure 3.14: Comparison of metallicities for our NGC 4472 GCs derived from the W94 models (triangles connected by solid lines), the empirical calibrations of Brodie & Huchra (1990) (squares connected by dotted lines) and the colour-metallicity relation of Geisler & Forte (1990) (circles connected by dashed lines). The position of the bins for the Brodie & Huchra and Geisler & Forte-derived metallicities have been shifted slightly in the x-axis for display purposes.

We find that the metallicity predictions of the W94 models are consistent within the uncertainties with the primary calibrators of Brodie & Huchra (1990). However, formally the models predict that our reddest bin is $\sim$ 0.6 dex more metal-poor than the value derived from the Brodie & Huchra (1990) calibration. Kissler-Patig et al. (1998) indicate a similar phenomenon for metal-rich GCs in NGC 1399. They find that for $Mg_2 > 0.180$ mag, a linear extrapolation of the Brodie & Huchra (1990) calibrations differs noticeably from their metal-rich GCs. Applying the correction employed by Kissler-Patig et al. (1998) to our data assigns our reddest cluster bin [Fe/H] $\sim$ -0.2, thus bringing the metallicity into line with the model predictions. Furthermore, the metallicities derived from the flux-weighted Washington colours using Equation 3.5 compare well to the predictions of the Worthey (1994) models and those of Brodie & Huchra (1990). However, again they tend to give slightly higher metallicities for the reddest bin.

Our binned clusters have metallicities of approximately -1.6 $\leq$ [Fe/H] $\leq$ 0, which is the range covered by the most metal-rich two-thirds of the Milky Way GCs. Clearly this is truncated due

to the binning of the GCs; the colour distribution of our spectroscopic sample infers a metallicity range of -2.46 $\leq$ [Fe/H] $\leq$ 0.8 (Equation 3.5). However, we note that both the relations of Brodie & Huchra (1990) and Geisler & Forte (1990) are based upon observations of *Galactic* GCs. Neither of these calibrations included clusters at solar metallicities and therefore in this regime they are rather uncertain.[5] Our bluest and reddest cluster bins correspond approximately with the bimodal peaks of the NGC 4472 GC metallicity distribution at [Fe/H] $\sim$ -1.3 and -0.1 (GLK96).

The agreement between the metallicities predicted by the W94 models with those derived from the empirical calibration and flux-weighted colours is encouraging, and gives us confidence in the model predictions. Since we will use the SSP models in the age determination of the GCs, we assign the metallicities predicted by the models to our GC data as opposed to the mean metallicity given in Table 3.13.

3.4.4 Radial Gradients in the Globular Cluster System

From their sample of $\sim$ 1800 GCs, GLK96 found evidence of a radial gradient from their mean C-T_1 colours, in the sense that the clusters became bluer with increasing radius. The colour gradient they measured corresponds to Δ[Fe/H]/Δlog $r \simeq$ -0.4 dex/log (arcsec), with an rms of $\sim$ 0.2 dex. This gradient they primarily attributed to the varying spatial concentration of the blue and red cluster populations, in the sense that the ratio of blue to red GCs increased as a function of galactocentric radius. Moreover, they found that the mean colours of the red GCs were similar to that of the spheroid light, whilst the colours of the metal-poor population were bluer than the galaxy light by $\sim$ 0.5 mag at all radii.

We now investigate how the line-strengths of the NGC 4472 GCs behave as a function of their projected radius from the centre of NGC 4472. We first separate our GC data into four radial bins, and measure their mean line-strength indices. Our spectroscopic sample spans a range of galactocentric radii of $65'' \leq r \leq 569''$ ($0.5 \leq r_e \leq 6$), where $r_e = 99''$, the effective radius of NGC 4472 (Davies, Sadler, & Peletier 1993). To investigate whether any detected radial gradient in our spectra originates from a varying spatial distribution in the GC subpopulations, we fix the ratio of blue:red GCs for each bin. Since the global ratio of blue to red GCs in this study is $\sim$ 2:1,

[5] The Milky Way GCS perhaps extends to solar abundances. The most metal-rich Galactic GC known is Liller 1, which has approximately solar metallicity (Davidge 2000). However, this cluster is at an extremely low Galactic latitude where both reddening and contamination from Galactic bulge stars is high.

the number of red GCs per bin effectively sets our limiting bin size. In Figure 3.15 we plot ⟨Fe⟩, Mg_2 and Hβ measured for our data against the logarithm of their mean galactocentric radii.

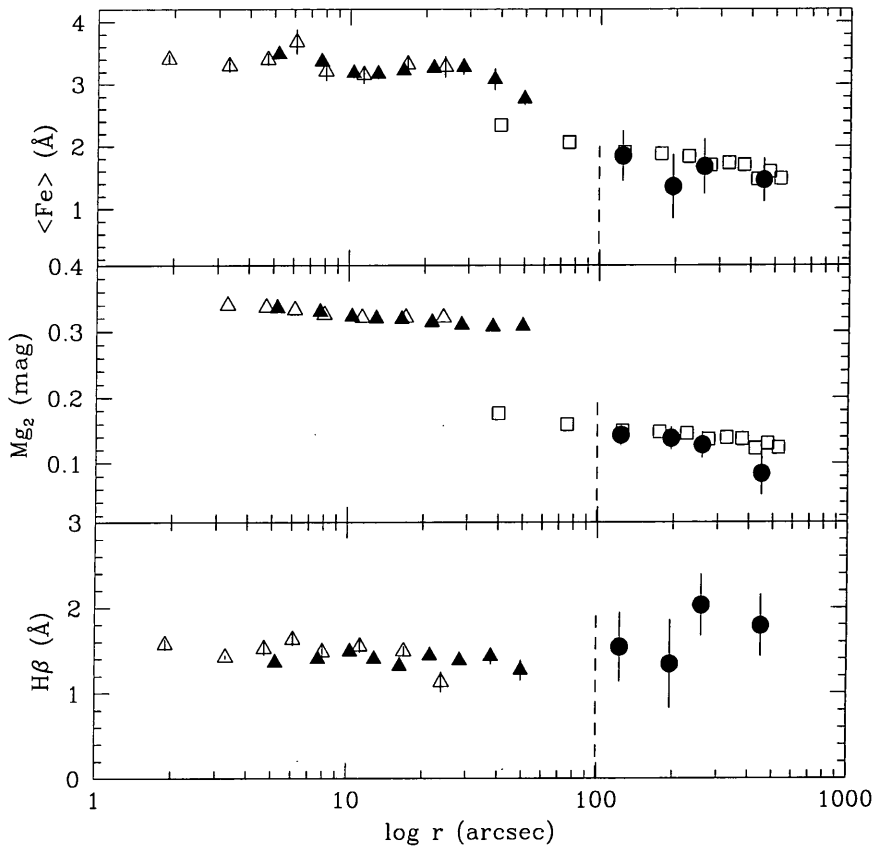

Figure 3.15: The behaviour of the ⟨Fe⟩, Mg_2 and Hβ indices (upper, middle and lower panels respectively) with the logarithm of the projected galactocentric radius. Solid circles represent our co-added NGC 4472 GCs with their respective boot-strapped uncertainties. The open squares are the predicted index values for NGC 4472 GCs from the photometry of GLK96 (see text). We also plot the nuclear data of Davies, Sadler, & Peletier (1993), both for the Cryogenic camera (solid triangles) and the Texas Instruments CCD (open triangles). The dashed line indicates the effective radius of NGC 4472 ($r_e \sim 99$ arcsec).

We also show in Figure 3.15 line-strengths of the spheroid light of NGC 4472, taken from Davies, Sadler, & Peletier (1993), who have measured the Mg_2, ⟨Fe⟩ and Hβ indices out to $\sim 0.5\ r_e$ for this galaxy.

In an effort to link the radial ranges covered by our data with that of Davies, Sadler, & Peletier (1993) more completely, we have converted the $C - T_1$ colours of the radially binned NGC 4472 GCs from GLK96 to 'line-strength indices' using Equation 3.5 and the empirical calibrations of Brodie & Huchra (1990). For clarity we have omitted the error bars on the converted photometry,

but typically the uncertainty in $\langle$Fe$\rangle$ is $\sim$ 0.4 Å and in Mg_2 is $\sim$ 0.03 mag. The conversion from $C-T_1$ to $\langle$Fe$\rangle$ is not a direct one, since Brodie & Huchra (1990) calibrated Fe5270 with metallicity, as opposed to the mean of the Fe5270 and Fe5335 indices. We have applied a correction of 0.3 Å to convert the Fe5270 prediction to $\langle$Fe$\rangle$. We have not performed this conversion for Hβ, since there is no such relation for this index (indeed, Hβ is anti-correlated with metallicity).

The converted GC colour data of GLK96 is in good agreement with our $\langle$Fe$\rangle$ line-strengths at all radii. A shift of $\sim$ 0.5 dex in $\langle$Fe$\rangle$ (corresponding to removing the blue GCs) would make these data coincide (in terms of line-strengths) with that of the nuclear measurements. The metal-rich GCs appear to have similar iron abundances to the spheroid light. However, the situation for Mg_2 appears somewhat different. Again, our data are consistent with the indices predicted by the GC photometry of GLK96, however, the GCs are offset downwards from the spheroid data of Davies, Sadler, & Peletier (1993) by $\sim$ -0.10 mag at the same radius. Assuming that the data of GLK96 traces the behaviour of the GCs inwards to 0.5 r_e, then even after applying an additive shift of 0.05 mag (for the metal-rich GCs), there is still a difference of $\sim$ 0.05 mag between the GCs and spheroid light. The fact that the data of GLK96 is also offset from the spheroid data of Davies, Sadler, & Peletier (1993) simply reflects the fact that both the metallicity relations of Brodie & Huchra (1990) and Geisler & Forte (1990) were calibrated with Galactic GCs, which do not show magnesium enrichment at the levels seen for giant ellipticals (e.g. see R. Gratton in Martinez-Roger, Perez-Fournon, & Sanchez 1999; Henry & Worthey 1999).

It is evident that there is a metallicity gradient in Mg_2 and $\langle$Fe$\rangle$, they clearly weaken with increasing galactocentric radius. We see no significant trend of changing flux in the spectra with radius, which could possibly introduce an artificial radial gradient. Applying a weighted linear fit to the $\langle$Fe$\rangle$ and Mg_2 indices, we obtain Δ[Fe/H]/Δ log r = -0.30 $\pm$ 0.21 dex for $\langle$Fe$\rangle$ and Δ[Fe/H]/Δ log r = -0.94 $\pm$ 0.31 for Mg_2. The steep gradient seen in Mg_2 is primarily driven by the outermost radial bin (which has the largest uncertainties). Removing this point from the fit yields a gradient of Δ[Fe/H]/Δ log r = -0.45 $\pm$ 0.19 dex. Both of these values are consistent with the mean gradient found by GLK96 of Δ[Fe/H]/Δ log r = -0.4 $\pm$ 0.2 dex, and the global mean gradient found for GCS of Δ[Fe/H]/Δ log r = -0.5 dex (Ashman & Zepf 1998). By comparison, the gradient from the spheroid data of Davies, Sadler, & Peletier (1993) is Δ[Fe/H]/Δ log r = -0.20 $\pm$ 0.10 dex, similar to the value found by Kim, Lee, & Geisler (2000) using Washington photometry (for $r \leq$ 180 arcsec).

Interestingly, the Hβ index shows *no* sign of a negative gradient, indeed if anything it marginally increases with log r. Again, this is similar behaviour to that of the spheroid light. Davies, Sadler, & Peletier (1993) concluded that the flat or rising profiles seen in their data arose from increasing Hβ emission towards the galaxy centre. However, emission is not expected in the NGC 4472 GCs, or at least not at a detectable level since they are old stellar systems with little or no gas (Ashman & Zepf 1998). Therefore the presence on a *positive* gradient of Hβ in the GCs would point toward either an age effect (Faber, Worthey, & Gonzales 1992), or perhaps more likely a metallicity effect.

To investigate how the red and blue GCs behave individually, and to directly compare the spheroid light with the GC subpopulations, we have binned our GCs into a blue and red population, taking the colour cut to be $C - T_1 = 1.625$. We have further split each of these bins by radius into two equal components and measured there line-strengths. We show our results in Figure 3.16.

The Mg_2 and $\langle Fe \rangle$ indices decrease with increasing galactocentric radius for *both* the red and blue GC subpopulations. We find that the radial gradients of the clusters from spectroscopy are twice as steep as those determined from the photometric data. However, the significance of this, particularly for the red GCs (for which $n \sim 23$) is marginal. Measured in $\langle Fe \rangle$, the innermost red cluster bin is comparable to the spheroid light from Davies, Sadler, & Peletier (1993), whereas the Mg_2 index of this bin is some 0.05 mag lower. In the middle panel of Figure 3.16, we plot a vector corresponding to the maximum correction expected for [Mg/Fe] overabundant ratios seen in the brightest elliptical galaxies, of which NGC 4472 is known to be affected (Worthey, Faber, & Gonzalez 1992; Henry & Worthey 1999; Kobayashi & Arimoto 1999). If we apply this maximum correction ($\sim$0.05 mag) to the Mg_2 index of the GCs, then these data become consistent with the spheroid data of Davies, Sadler, & Peletier (1993). Since the $\langle Fe \rangle$ index of the GCs is consistent with that of the spheroid light with no correction, we tentatively conclude that the GCs in NGC 4472 show no sign of non-solar [Mg/Fe] ratios, a point we return to in § 3.4.5. The Hβ indices act in the opposite sense to $\langle Fe \rangle$ and Mg_2, and again we see that the gradient is larger for the red GCs.

3.4.5 Cluster Ages

We now turn to the problem of deriving mean ages for our GCs using the W94 models. Our primary age indicator for these data is the Hβ index, therefore the uncertainties in this index will reflect heavily on our age estimates for the GCs. In order to calibrate the W94 models, we rely upon our combined dataset of GGCs. We have chosen to adopt a canonical age for the GGCs

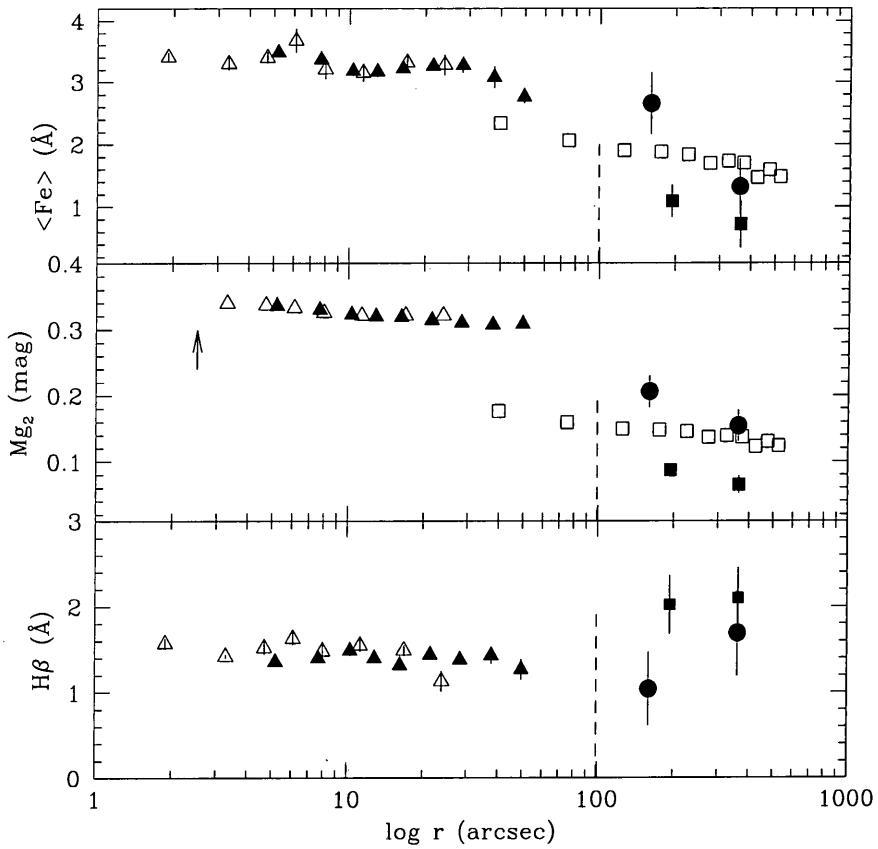

Figure 3.16: The behaviour of the ⟨Fe⟩, Mg_2 and Hβ indices with the logarithm of their galactocentric radius for the two subpopulations of GCs. Solid circles represent the red ($C - T_1 \geq 1.625$) GCs, solid squares represent the blue GCs. The triangles denote the nuclear data of Davies, Sadler, & Peletier (1993), both for the Cryogenic camera (solid) and the Texas Instruments CCD (open triangles). The dashed line indicates the effective radius of NGC 4472. The arrow in the middle (Mg_2) panel shows the maximum corrective vector for [Mg/Fe] overabundance taken from Henry & Worthey (1999).

of 12 Gyr. This age for the GGCs is consistent with recent work using the latest HIPPARCOS parallaxes (Carretta et al. 2000) and is also convenient since this isochrone is directly modelled (i.e. not interpolated) in the W94 models. We fit the 12 Gyr line of the models to the Hβ index of the GGCs using a χ^2 procedure. The shift implied in Hβ is then applied to our NGC 4472 GC data. This correction to the models is typically $\sim$ -0.4 Å, and is effectively a zero-point calibration. Without this shift, nearly *all* the GGCs would be predicted to have ages $\geq$ 18 Gyr.

In Figures 3.17 – 3.20, we compare our data to the corrected models. Each of the figures consist of two panels: the upper panel over-plots the SSP grids of W94 on to our co-added data (filled

circles with boot-strapped uncertainties), the lower panel compares the combined sample of GGCs to these same models.

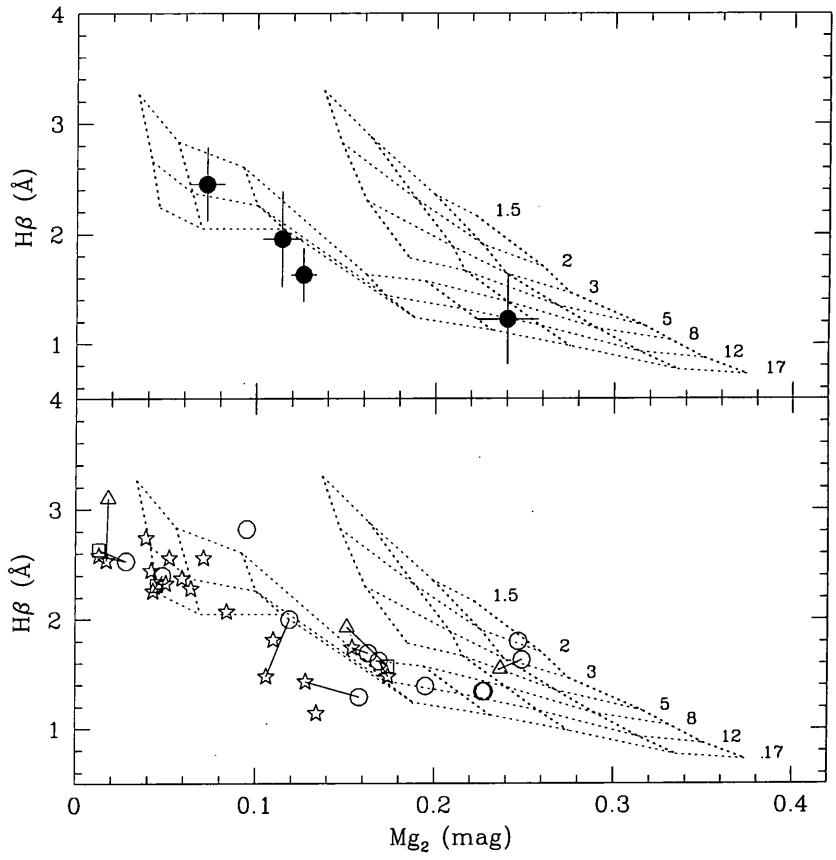

Figure 3.17: Predictions of the Worthey (1994) models for these data. Top panel : co-added NGC 4472 globular clusters are represented by filled circles with boot-strapped error bars. Lower panel : data for the combined sample of Galactic GCs. Open circles : GGCs from Cohen et al. (1998), open stars : GGCs from Brodie & Huchra (1990), open triangles represent the CFHT data and squares indicate the WHT data. Dotted lines connect the same GGCs between different datasets. The scale on the right-hand side of the grids gives age predictions of the models ranging from 1.5 – 17 Gyr.

On the whole, we find that the models give a good reproduction of the behaviour of our data, both for the co-added NGC 4472 GCs and the GGCs. The Balmer indices track the isochrones of the models fairly closely, across two decades in metallicity. The new modelling of the cluster HBs shows strikingly similar behaviour to that of our three most metal-poor cluster bins. It is apparent that there are small shifts between different metal indices, but these are typically 0.2 Å and within the boot-strapped uncertainties.

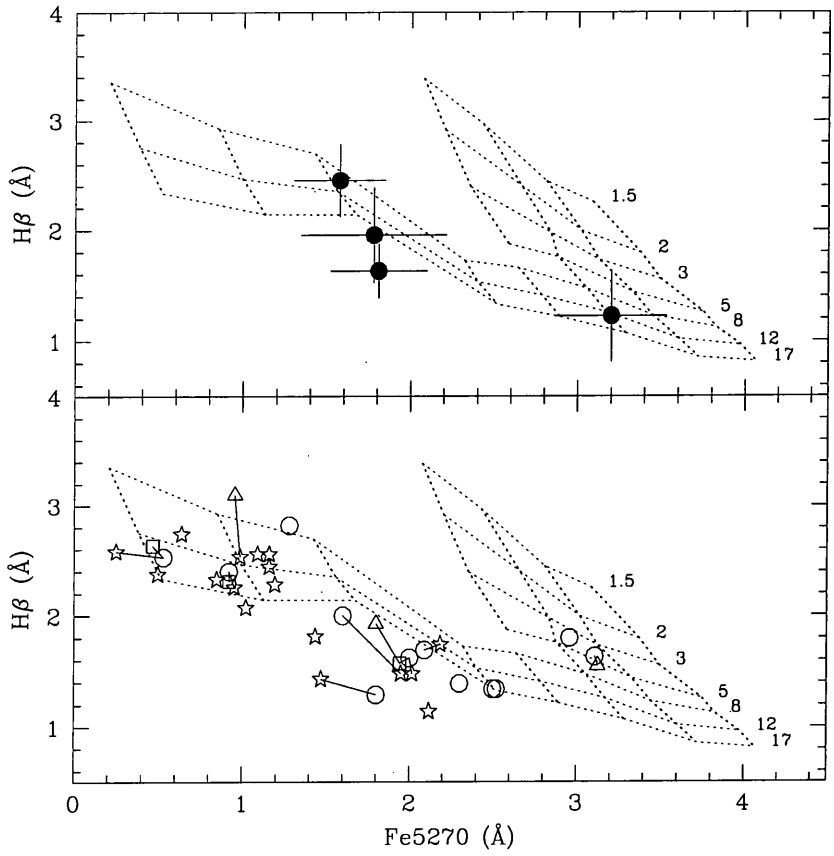

Figure 3.18: Hβ index against Fe5270. Symbols are the same as for Fig 3.17.

In Figure 3.20 we plot Fe5270 against Mg_2 for our data and the combined sample of GGCs. For comparison, we also plot the nuclear data of Davies et al. (1993), which we have placed into three radial bins. The spheroid data of Davies et al. (1993) is clearly offset from the models, which is usually interpreted as an Mg_2 overabundance (Davies et al. 1993). Unlike the stellar spheroid light, the NGC 4472 GCs show no evidence of Mg_2 enhancement over iron. This is consistent with the discussion of radial gradients in § 3.4.4.

We have already derived metallicities for the GGCs and NGC 4472 GCs, and effectively calculate age as a function of this metallicity since the Hβ (age) lines of the models are calculated with respect to the metal indices. We have determined the ages for the NGC 4472 GCs using the isochrones of the W94 models predicted for the Fe5270, Mg_2, Mg b and Hβ indices along with their respective uncertainties. We then take the final ages for the co-added GCs to be the mean age derived from these indices, which we list in Table 3.14 in addition to our final metallicities (predicted from the W94 models) for each bin. Considering the large uncertainties, it is clear from

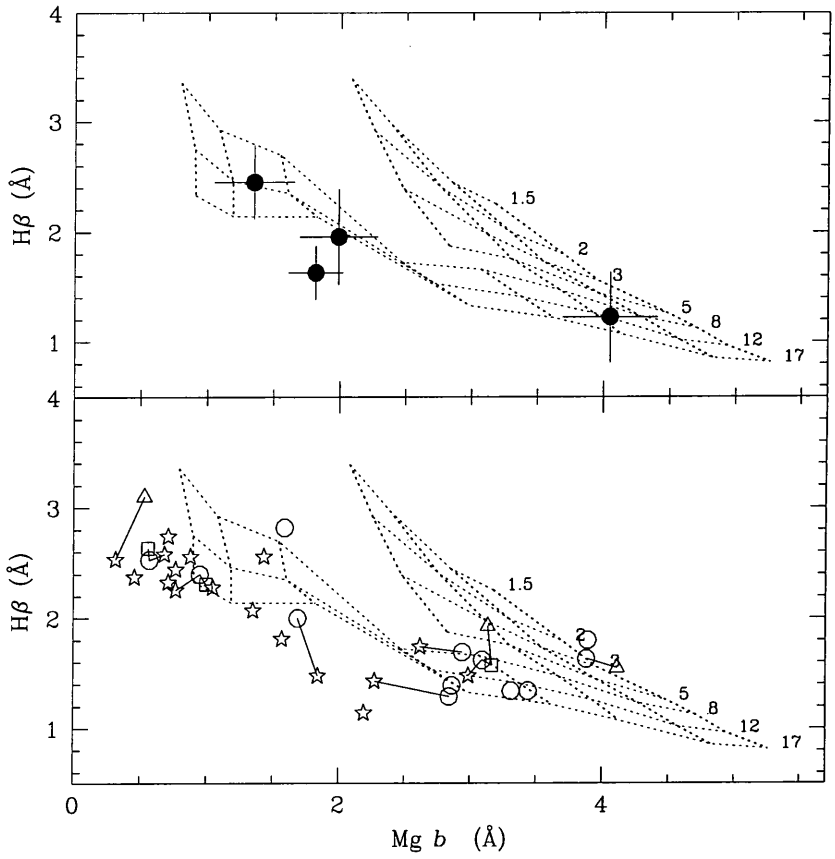

Figure 3.19: Hβ index versus Mg *b*. Symbols are the same as for Fig 3.17.

Table 3.14 that there is no evidence of a substantially younger population of GCs present in our data. However, the most metal-rich and metal poor bins do appear to be younger than the two intermediate ones. This is likely an artefact of the W94 models at metallicities -1.0 < [Fe/H] < -0.5, the regime were HB morphology starts to play a rôle. The switch to M3 morphology happens below [Fe/H] = -0.95 and the switch to M92 morphology happens below [Fe/H] =-1.55. This change does not occur as a smoothly varying function of metallicity, and therefore may be predicting too sharp a rise in the Hβ index. Moreover, the models also predict too old an age for the GGCs at these metallicities. Since the 12 Gyr age isochrone of the models is fit to the GGCs, this may have the effect of inducing too large a shift in Hβ and therefore predicting younger ages in the co-added data. We find that the mean age of the four bins is 14 $\pm$ 6 Gyr, consistent with our canonical age adopted for the GGCs of 12 Gyr, and identical to that derived by Cohen, Blakeslee, & Ryzhov (1998) of 13 $\pm$ 2 Gyr for their sample of M 87 GCs.

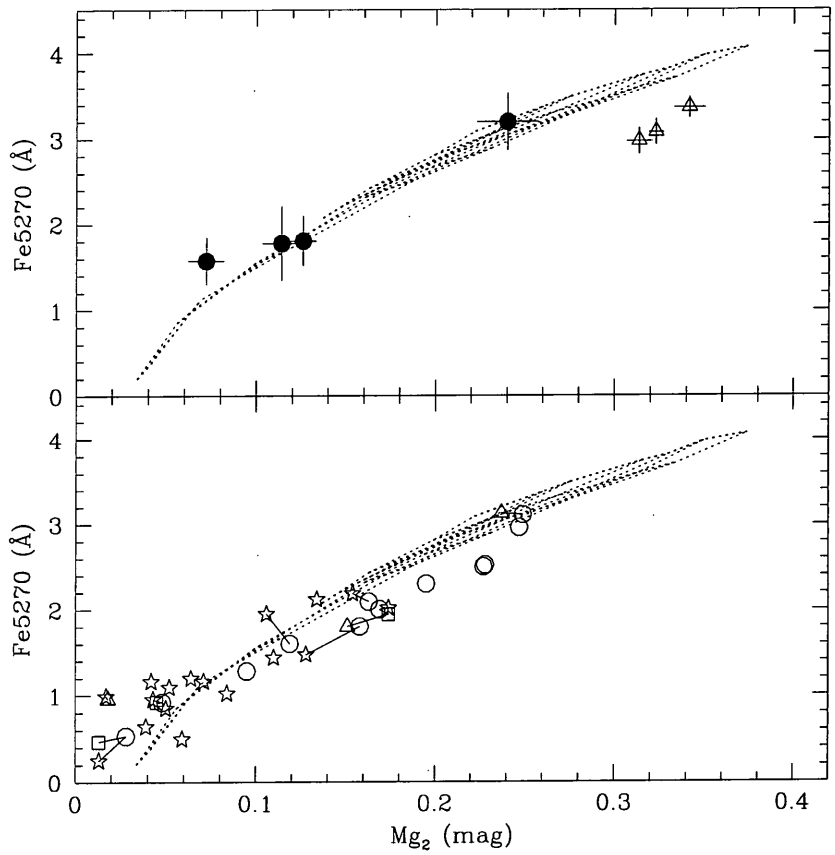

Figure 3.20: Symbols same as Fig 3.17. We have also included the spheroid data of Davies et al. (1993) which we have binned in radius (open triangles, top panel). The age scale of the models has been omitted for clarity.

Table 3.14. The final ages and metallicities for our co-added data, derived from the stellar population models of W94. The ages in Column 3 are the mean of those predicted by the Hβ index as a function of Fe5270, Mg b and Mg$_2$.

Bin	[Fe/H]$_Z$ (dex)	Mean Age (Gyr)
1	-1.29 $\pm$ 0.30	$10.7\,^{+6}_{-5}$
2	-0.91 $\pm$ 0.35	$15.3\,^{+8}_{-5}$
3	-0.84 $\pm$ 0.25	$18.5\,^{+4}_{-5}$
4	-0.27 $\pm$ 0.30	$11.3\,^{+8}_{-9}$

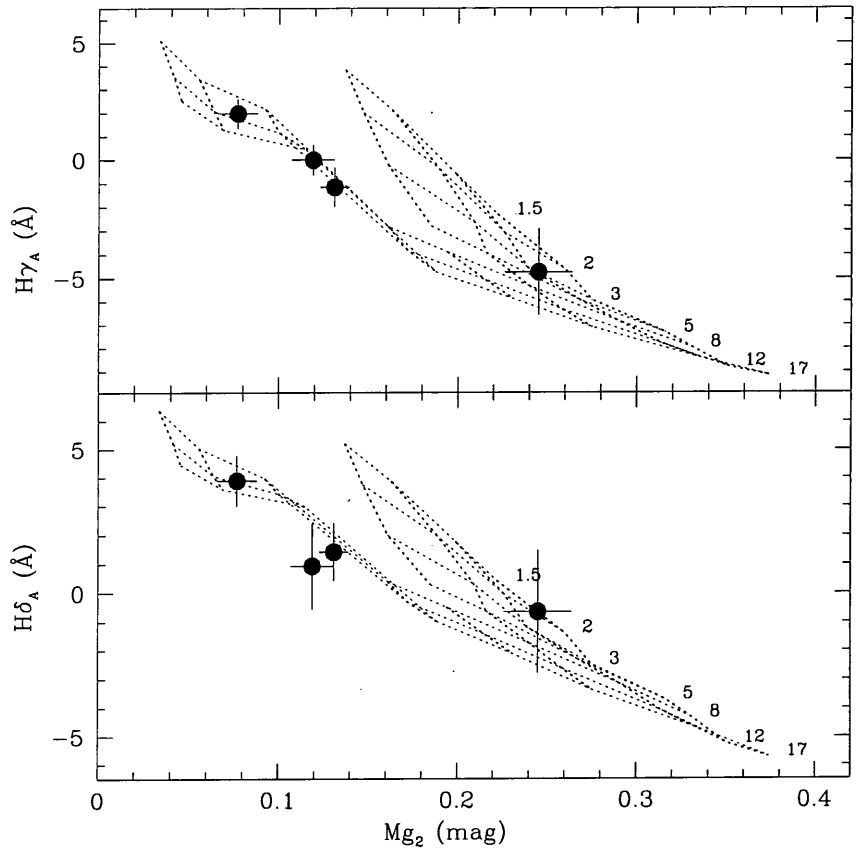

Figure 3.21: The Worthey (1994) model predictions for our two other age indicators. Top panel: $H\gamma_A$ versus Mg_2, bottom panel: $H\delta_A$ versus Mg_2. The Galactic globular clusters are not shown since we have very few measurements of the higher-order Balmer lines for these data.

We have also measured two other primarily age-sensitive indices, namely $H\gamma_A$ and $H\delta_A$, which we show in Figure 3.21. Both these indices exhibit similar behaviour to $H\beta$ measured for the GCs, but with indications that the most metal-rich bin is somewhat younger than the others. However, not only is the correction of the models to these data more uncertain (since we have few GGCs for which there are $H\gamma_A$ and $H\delta_A$ measurements), but also the *relative* uncertainties in these indices are somewhat larger, since the W94 grids for these indices show less orthogonality than for the $H\beta$ index (i.e. $H\gamma_A$ and $H\delta_A$ are less sensitive to age). We therefore do not derive ages for the GCs from these higher-order Balmer lines.

In order to reduce the uncertainties in the indices (especially $H\beta$), but at the expense of losing our baseline in metallicity, we now bin our sample of NGC 4472 GCs into one metal-poor GC population and one metal-rich population. We take the dividing line between the populations as $C - T_1 = 1.625$, obtained from the KMM mixture-modelling test (Ashman, Bird, & Zepf 1994)

applied to the full NGC 4472 GC data of GLK96. Again we co-add these data and measure the Lick/IDS indices using the bootstrap procedure described in § 3.3.3. Our metal-poor and metal-rich bins contain 85 and 46 spectra respectively, with flux weighted colours of $C - T_1 = 1.40 \pm 0.05$ and $C - T_1 = 1.8 \pm 0.07$, corresponding to metallicities of [Fe/H] = -1.10 ± 0.11 and [Fe/H] = -0.16 ± 0.16 using Equation 3.5. We plot Mg b, Fe5270 and Mg_2 against Hβ for these two bins in Figure 3.22, as before the models have been normalised to the canonical ages adopted for the GGCs.

From these indices, we obtain a mean age of 14.5 ± 4 Gyr for the metal-poor bin and 13.8 ± 6 Gyr for the metal-rich bin. The smaller uncertainties in the metal-poor bin correspond to the larger numbers of blue GC spectra available for co-addition (for $40 \leq n \leq 100$ the uncertainty in the index goes as $\sigma \simeq n^{-0.3}$).

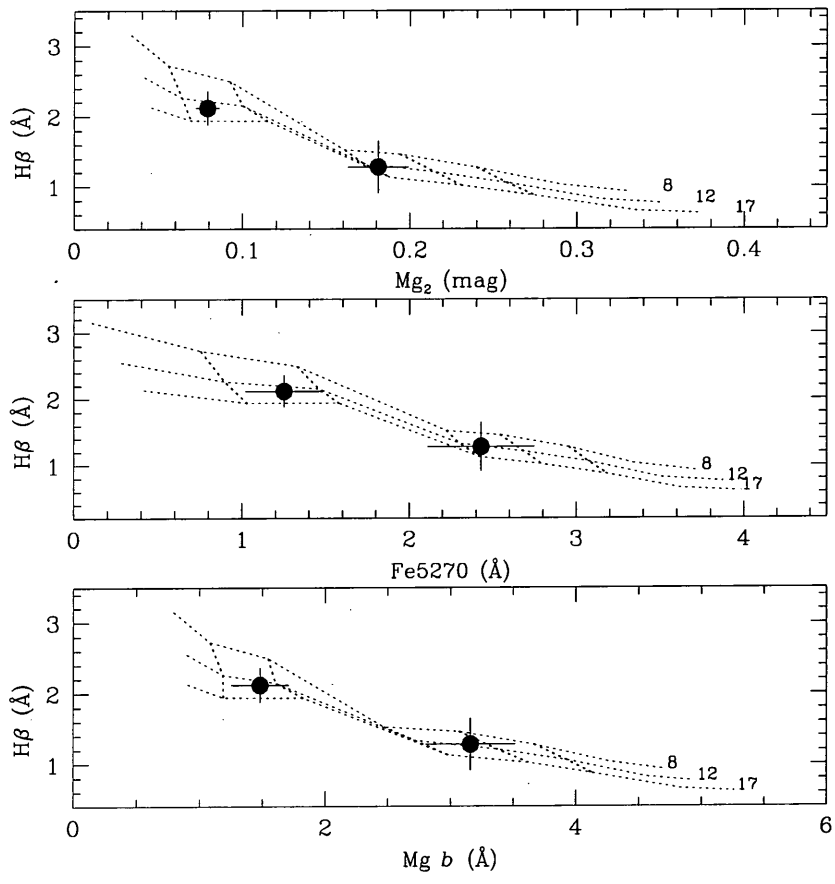

Figure 3.22: Age predictions of the Worthey (1994) models for the Hβ index versus Mg_2, Fe5270 and Mg b for our metal-poor and metal-rich bins of NGC 4472 GCs. We show only the $\tau \geq 8$ Gyr isochrones for clarity.

As a check for systematic errors in our age results, we perform Monte Carlo simulations on the W94 model SEDs predicted for the ages and metallicities of our metal-poor and metal-rich GC bins. We obtain SEDs corresponding to the indices measured for each bin and then artificially degrade them following a procedure similar to that described in § 3.3.3. We generate the same number of realisations as there are spectra in each of our red and blue bins. We then measure the ages of the co-added artificial spectra, again using the W94 model grids. We find that each of our cluster bins is older than 6 Gyr at the 95 % confidence level, and older than 3 Gyr at the 98.5 % confidence level.

From HST V and I data, Puzia et al. (1999) concluded that the blue and red GCs in NGC 4472 are coeval within their uncertainties, finding an age difference between the two populations of -0.6 $\pm$ 3 Gyr. Using three datasets in common with Puzia et al. (1999), Lee & Kim (2000) conclude that the *red* GCs are younger than the blue GCs by 3–6 Gyr, but in their analyses give no discussion of their uncertainties.

Our findings that the blue and red GCs of NGC 4472 are old and coeval within the uncertainties are not inconsistent with either of the above two studies, but do not rely upon any assumption about the underlying mass distributions of the GC populations.

3.5 Kinematics of the Cluster System

3.5.1 Velocity Dispersions

We now turn to the kinematics of our sample of NGC 4472 GCs. The majority of the analysis in § 3.5.2 and § 3.5.3 was performed by Steve Zepf, and is described in detail in Zepf et al. (2000).

One of our principle objectives in obtaining a larger sample of radial velocities for the NGC 4472 GCs, was to compare and contrast the kinematics of the red and blue GC subpopulations. From 57 velocities, S98 found evidence for the spatially extended blue GCs having a higher velocity dispersion than the red GCs at the 86% confidence level. Such a kinematical difference, if real, points towards differing physical origins of the cluster subpopulations, implied by their differing colour distributions. To investigate this, we begin by showing in Figure 3.23 the spatial and velocity distributions of our full sample of 144 GCs.

Figure 3.23 indicates that the velocity dispersion of the GCs shows some evidence of falling with galactocentric radius, and no clear signs of rotation can be seen. It also serves to illustrate the point that we can usefully probe the kinematics of this galaxy out to several effective radii (the effective

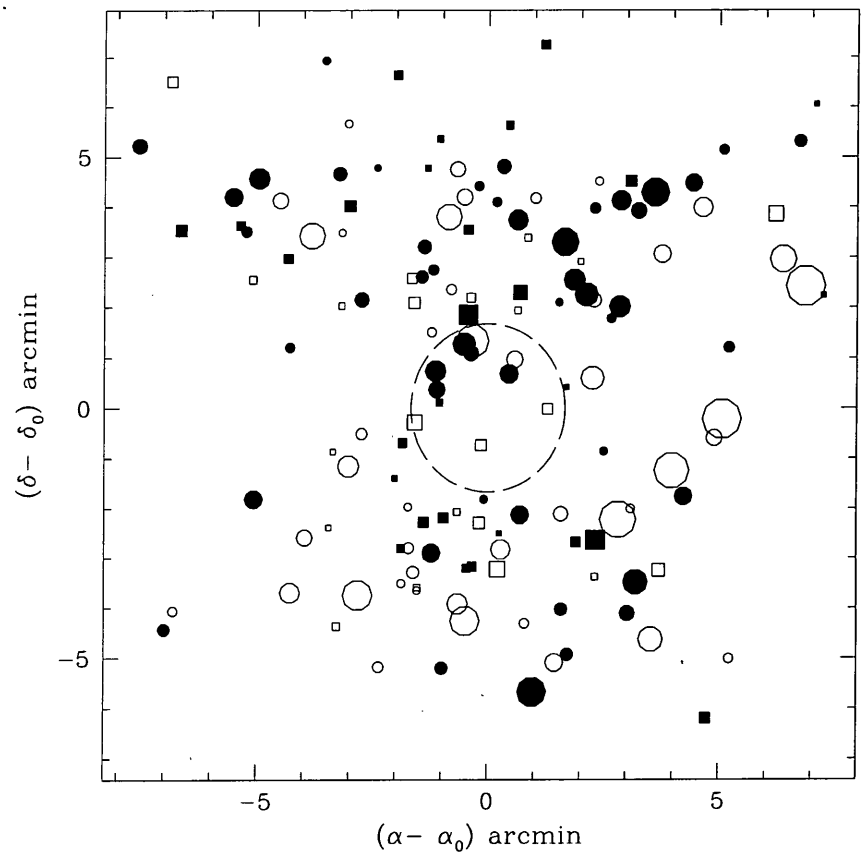

Figure 3.23: Velocity and spatial distributions of our sample of NGC 4472 GCs. The red ($C - T_1 > 1.625$) GCs are shown as squares, the blue GCs are shown as circles. Symbol size indicates the magnitude of the cluster velocity difference from the systemic velocity of NGC 4472. In this scheme, filled symbols indicate a negative velocity with respect to the galaxy. The dashed circle indicates the effective radius of NGC 4472. The origin of the co-ordinate system is the centre of NGC 4472 at α=12^{h}27^{m}14^s, δ=08°16′36″ (1950.0).

radius of NGC 4472 is shown by the dashed circle in Figure 3.23, the current limit of kinematical studies of the galaxies' integrated light). Four blue GCs (right from centre in Figure 3.23) have very similar velocities, significantly higher than the majority of the cluster system. This perhaps points to a velocity subsystem amongst the blue clusters, however, little can be quantitatively said upon the basis of four objects.

In Figure 3.24, we compare the velocity histograms of the blue and red clusters. The figure clearly shows that the velocity dispersion of the blue GCs is significantly higher than that of their red counterparts. To test the significance of this difference, we have applied an F-test to these data. This statistical test checks the validity of the assumption that two populations have identical standard deviations. We find that the F-test rejects this assumption at the $> 99\%$ confidence level;

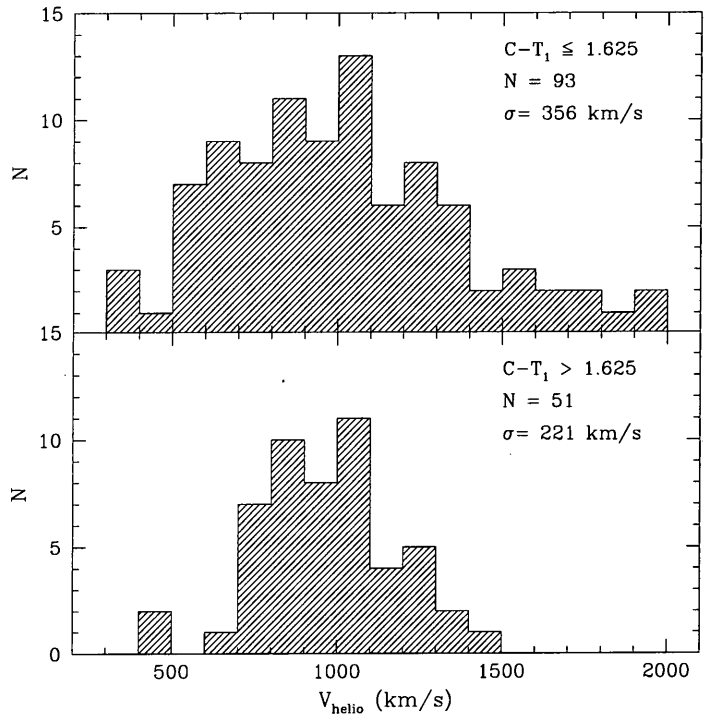

Figure 3.24: Velocity histograms for the blue (top panel) and red globular cluster subpopulations.

the red and blue clusters are kinematically distinct, with the blue clusters forming a dynamically 'hotter' system. We find that the blue GCs possess a velocity dispersion $\sigma_{\rm blue} = 356 \pm 25$ km s^{-1} and the red GCS have $\sigma_{\rm red} = 221 \pm 22$ km s^{-1}. These uncertainties in the dispersions come from a boot-strapping of the individual velocities.

In addition to looking at the global velocity dispersion of our sample, we have sufficient sampling to look at radial variations in the GC velocity dispersion. The spatial distribution of the GCs in our sample is such that they span radii of $0.5 \leq r_{\rm e} \leq 6$, effectively bridging the gap between the stellar light of NGC 4472 and the surrounding cluster potential. Since each cluster has its own discrete radial velocity and spatial location, a method of averaging is required in order to obtain velocity dispersion as a function of r. For our purposes we have simply radially binned the GCs in r. Whilst binning is sensitive to both bin-size and placement, since we only want to examine the general behaviour of the velocity dispersion of the GCs with respect to the dynamical subsystems of the galaxy and cluster, it will suffice. In the next Section, we show a slightly more sophisticated treatment of the radial variation in the GCs velocity dispersions. We show in Figure 3.25 the velocity dispersion of the GC subpopulations as a function of radius from the centre of NGC 4472. We compare these data with velocity dispersion measurements of the stellar

light of NGC 4472 (Fisher, Franx, & Illingworth 1995). We have also taken velocities for 54 galaxies within 100″of NGC 4472 with $V \leq 3000\,\mathrm{km\,s^{-1}}$ from the NASA extragalactic database (NED). These have been radially binned and their velocity dispersions calculated.

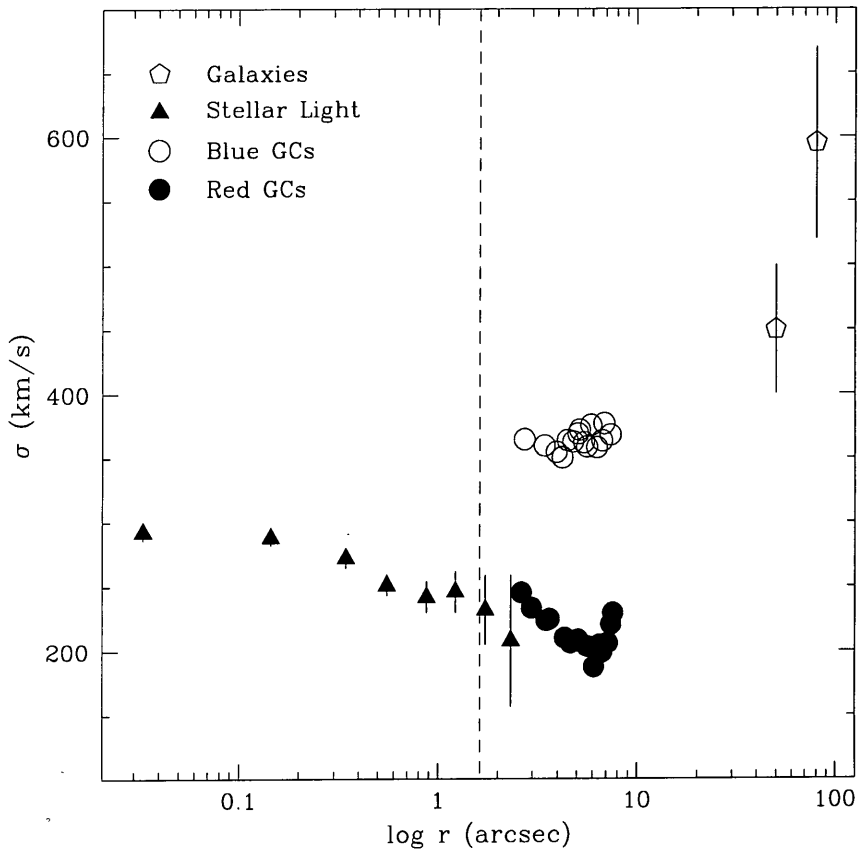

Figure 3.25: Velocity dispersion of the blue and red GCs as a function of galactocentric radius. Solid circles represent the red GCs, open circles represent the blue GCs. We also show data for the stellar light of NGC 4472 from Fisher, Franx, & Illingworth 1995 (solid triangles) and radially binned dispersion for satellite galaxies within the NGC 4472 potential (open pentagons), taken from the NED database. The dotted line indicates the effective radius of NGC 4472. The GC data is correlated in the radial direction, the bin-width used is 75″ yielding approximately 30 GCs per bin.

Figure 3.25 shows the clear delineation in velocity dispersion between the blue and red GCs. Moreover, the red GCs appear to kinematically associated with the stellar light, showing a slowly falling dispersion profile with log r. In contrast, the blue GCs seemingly trace a transition between the potential of the galaxy, and that of the NGC 4472 subcluster. Such an interpretation is tempting, the possibility that the blue GCs are kinematically similar to that of the surrounding cluster (note that the x-axis of Figure 3.25 is plotted in log r; the separation between the GCs and the NGC 4472 satellites is $\sim 50'$) lends some support for idea that the blue GCs may have been

accreted from the field (e.g. Cote, Marzke, & West 1998). However, the velocity dispersion of the blue GCs slowly declines with radius, and shows marginal evidence for an increasing rate of decline at the largest radii (see § 3.5.2), perhaps contrary to the expected rise if they were truly associated with the subcluster potential.

3.5.2 Rotation in the Cluster System

An important constraint in testing galaxy formation models in the context of their GCS, is the level of rotation imparted to the GCS. Both models of *in situ* dissipational collapse (e.g. Forbes, Brodie, & Grillmair 1997) and major mergers (Ashman & Zepf 1992) may lead to rotation in one or both of the GC subpopulations, as angular momentum is conserved during these processes. Moreover, models whereby the blue GCs are accreted from dwarf galaxies, such as proposed by Cote, Marzke, & West (1998) predict that the metal-poor clusters would tend to isotropy, and their velocity dispersions may reflect that of the surrounding subcluster and dwarf population.

The most straightforward way to look for rotation in the GCs is to plot their velocities as a function of projected galactocentric radius along the major axis of the galaxy. A least-squares fit to these data should then, in principle, reveal any rotation in the sample. However, as pointed out by S98, this assumes that this rotation is aligned with that of the galaxy, which may not necessarily be the case if the galaxy has recently undergone some form of dynamical interaction (e.g. a major merger).

Therefore, we look for rotation in the clusters by applying a non-linear fit:

$$V(r) = V_{\rm rot} sin(\theta - \theta_o) + V_o \tag{3.14}$$

where V_o is the mean velocity of the population, $V_{\rm rot}$ is the amplitude of the rotation and θ_o is the position angle of the line of nodes of the rotation. Equation 3.14 determines the best-fitting flat rotation-curve, $V_{\rm rot}$ and θ_o are left as free parameters. We list the results from our fits to Equation 3.14 in Table 3.15. We see no evidence for significant rotation in the red GCs, and evidence for modest rotation in the blue GCs, and hence the entire GC sample (which is dominated by the blue fraction). Interestingly, the position angles of the best-fit solutions ($\sim 180°$) are similar to the position angle of NGC 4472 itself, at 162° (Sandage & Tammann 1981). We have performed Monte Carlo simulations of the rotation solutions in order to test the significance of these results. By fixing the position angles of the clusters, but drawing their velocities from a randomly distributed sample, we find that only 16% of the realisations yield a rotation amplitude

as large as that observed in our true sample. We have also employed Monte Carlo simulations to place upper limits on the rotation of the GCs. This is achieved by creating samples of clusters of fixed size and velocity dispersion, but with randomized rotational velocities. We define the 99% confidence level at the point at which 99% of the randomized samples yield a rotation larger than that observed. From this procedure, we obtain an upper limit on the rotation of the entire sample of 120 $\mathrm{km\,s^{-1}}$ at 99% confidence. At the same confidence level, we obtain upper limits of 200 $\mathrm{km\,s^{-1}}$ and 75 $\mathrm{km\,s^{-1}}$ for the blue and red GC subpopulations respectively.

Table 3.15. Kinematical data for the NGC 4472 GCs.

Population	N	V_o ($\mathrm{km\,s^{-1}}$)	σ ($\mathrm{km\,s^{-1}}$)	$V_{\rm rot}$ ($\mathrm{km\,s^{-1}}$)	θ_o (deg)	$V_{\rm max}$ ($\mathrm{km\,s^{-1}}$)	$(v/\sigma)_{\rm proj}$
All GCs	144	1018 ± 26	315 ± 33	69	181	< 130	< 0.41
Blue GCs	93	1059 ± 37	356 ± 25	101	177	< 200	< 0.56
Red GCs	51	940 ± 31	221 ± 22	15	180	< 75	< 0.34

A common method of characterizing the degree of rotation in a dynamical system, is to look at the ratio of mean streaming motion, v, to random motion, σ, i.e. v/σ. Specifically, galaxies are characterized by their maximal rotation velocity and average velocity dispersion at the galaxy centre. In this case, we determine the projected (i.e. observed) values for maximum rotation and mean velocity dispersion, $(v/\sigma)_{\rm proj}$. From our previously derived upper limit on the rotation velocity of the red GCs, we find $(v/\sigma)_{\rm proj} < 0.34$ at the 99% confidence level. This value is very low; the metal-rich thick-disk GCs of the Milky Way have $(v/\sigma)_{\rm proj} > 1$ (Ashman & Zepf 1998). Moreover, by adopting an ellipticity of 0.2 for the red GCs (e.g. Lee, Kim, & Geisler 1998; Rhode & Zepf 2000), one would expect a rotationally flattened system to possess $(v/\sigma)_{\rm proj} \sim 0.4$ (Binney & Merrifield 1998).

To look at the radial variations of velocity dispersion and rotation in the GCs in more detail, it is necessary to smooth these data. As discussed in § 3.5.1, binning these data in radius is not an ideal way of looking at radial trends in these data. Therefore, we have smoothed these data with a Gaussian kernel of width $\sigma = 100''$. Such a broad smoothing allows us to assess general trends in these data, without producing large fluctuations due to our finite sampling. This kernel width corresponds to approximately 2–3 independent radial bins. We show the rotational velocity and velocity dispersion of the GCs as a function of radius in Figure 3.26.

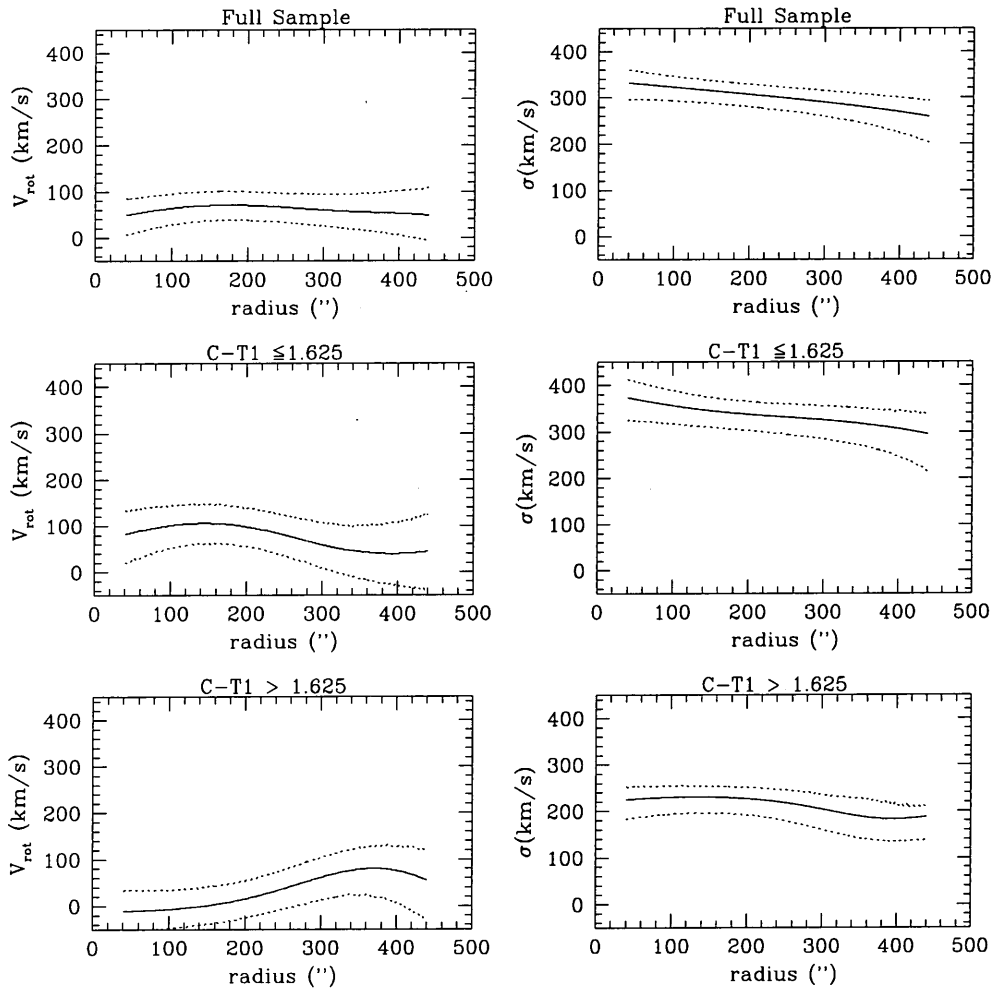

Figure 3.26: The radial variation of the rotation (left panels) and velocity dispersion of the NGC 4472 GCs. The top panel shows the full sample, the middle and bottom panels show the blue and red GC subpopulations respectively. The dotted lines indicate 1 σ uncertainties from boot-strapping. As is the case for Figure 3.25, the points are not independent in the radial direction.

The velocity dispersions of these data show the general trend of declining with radius, both for the entire sample and for the red and blue GCs respectively. There is slight evidence for an increase in the decline of the velocity dispersion at $r \sim 400''$, however the significance of this is only at the 1 σ level. A slowly declining velocity dispersion of the NGC 4472 GCs contrasts with that of the M 87 GCS. Over the same radial range, Cohen (2000) finds that the velocity dispersion of the M 87 GCs continues to rise with increasing r, reaching a value of 450 $\mathrm{km\,s^{-1}}$ at $\sim 400''$.

3.5.3 Mass of NGC 4472

Having obtained a velocity dispersion profile of the GCs, we may derive an estimate of the mass distribution of NGC 4472 using the observed $R^{1/4}$ density profile of the GCs (Rhode & Zepf 2000) and making some assumption about the anisotropy of the system. We obtain $M(r)$ by applying the Jeans equation to our data (e.g. Hartwick & Sargent 1978;Binney & Tremaine 1987), here given in terms of observable quantities (Hartwick & Sargent 1978):

$$M(r) = \frac{r\langle v_r^2 \rangle}{G} \left[-\frac{d \ln v_c}{d \ln r} - \frac{d \ln \langle v_r^2 \rangle}{d \ln r} + (\lambda - 2) + \frac{\bar{v}_{\rm rot}^2}{\langle v_r^2 \rangle} \right] \tag{3.15}$$

where v_r is the radial component towards the galaxy centre, $v_c(r)$ is the observed density distribution and $\bar{v}_{\rm rot}(r)$ is the mean streaming velocity in the θ direction. Assuming spherical symmetry (GCS systems are roughly spherical e.g. Lee, Kim, & Geisler 1998) and isotropic orbits (λ = 2) for the GCS, implies $\langle v_r \rangle^2 = \sigma_{\rm GC}$, our observed velocity dispersion.

We show in Figure 3.27 the results of the application of Equation 3.15 as a function of radius. The scale on the top of the plot assumes a distance modulus of $(m - M)_o$ = 31.04 to NGC 4472 (Ferrarese et al. 1996), in this scheme 1′corresponds to approximately 5 kpc. ls

We have compared our derived masses with X-ray mass estimates from *ROSAT* data assuming hydrostatic equilibrium (Irwin & Sarazin 1996). We find that the agreement between the two different methods is good, implying that our above assumptions are reasonable and the assumption of hydrostatic equilibrium for the X-ray isophotes is basically correct. The rising mass profile in Figure 3.27 indicates that the $\mathcal{M}/L$ ratio of NGC 4472 is a factor of $\sim$ 5 greater at radii of 30 kpc than it is near the centre of this galaxy. We therefore conclude that there is strong dynamical evidence of a massive dark halo surrounding NGC 4472.

3.6 Discussion

In this Section, we discuss the implications of the results of this study. We first look at the results of the chemical and kinematical analyses separately, before trying to construct a coherent picture for the formation of the NGC 4472 GCS.

3.6.1 Results of the Line-Strength Analysis

Our analysis has revealed that the NGC 4472 GC subpopulations are coeval within our measurement errors and old, and are separated by $\sim$ 1.0 dex in metallicity. We find that the NGC 4472

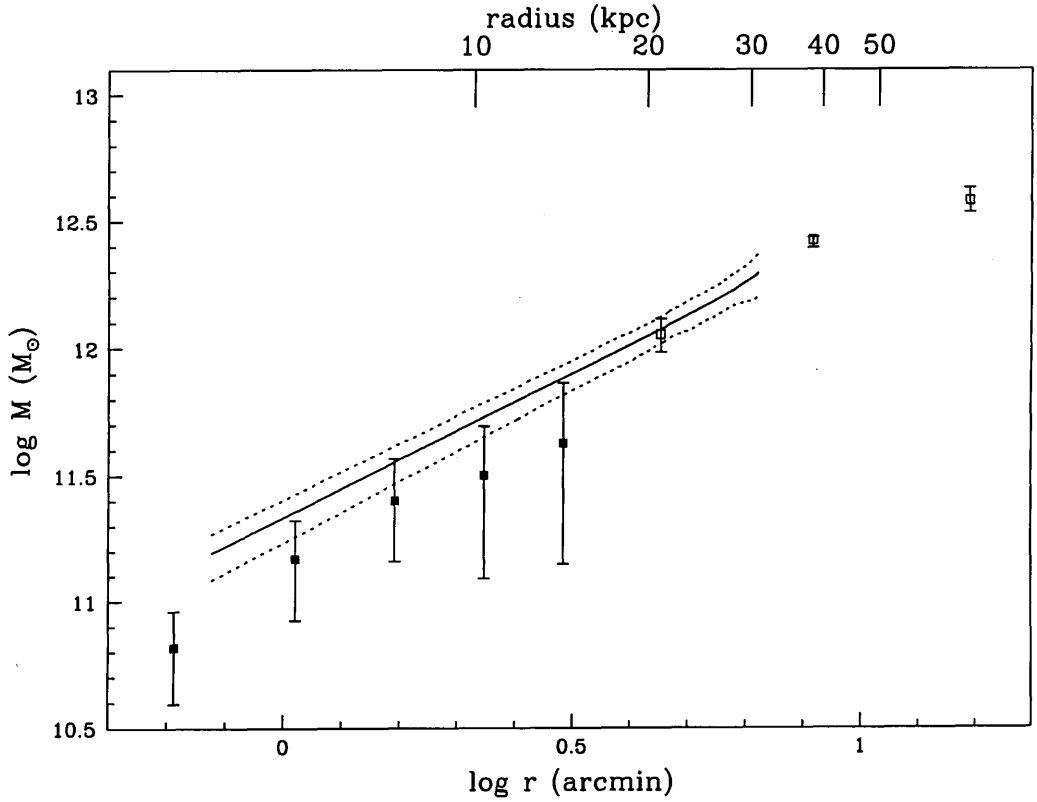

Figure 3.27: Mass profile of NGC 4472, derived from the velocity dispersions of the GC sample. The solid line is the best fit to these data, the dotted line represent our 1-σ uncertainties. The squares represent masses obtained from *ROSAT* observations (Irwin & Sarazin 1996). The open symbols include an uncertainty in the mass derivation due to the fact that the X-ray isophotes become irregular at $r > 4'$, indicating that the hot gas may not be in hydrostatic equilibrium.

GCS exhibits a radial metallicity gradient steeper than the underlying halo light of the galaxy, with the red and blue GCs both showing evidence of this behaviour. We see no evidence for [α/Fe] enhancement in the metal-rich GCs, at the level observed for the stellar light of NGC 4472.

The GC populations of NGC 4472 clearly formed from gas with significantly different levels (perhaps histories) of enrichment, but at roughly similar times. Whilst our spectroscopic estimates do not place strong constraints upon the age differences of the red and blue clusters, and are clearly model-dependent, they are consistent with the findings of Puzia et al. (1999) without assuming a constant mass distribution for the GCs.

The presence of a strong radial metallicity gradient in the GCs would imply a largely dissipative formation mechanism, which classically points towards some form of monolithic protogalactic collapse (e.g. Eggen, Lynden-Bell, & Sandage 1962), or modified multiphase collapse model (e.g. Forbes, Brodie, & Grillmair 1997). A gradient of Δ[Fe/H]/Δ log $r \simeq$ -0.4 for the GCs is well within the predictions of theoretical models of the formation of spheroids. For example, the dissipative models of Larson (1974) predict Δ[Fe/H]/Δ log r = -1.0, whilst those of Carlberg (1984) range from -0.5 to 0.0. The presence of such a gradient is supported by the fact that the red GCs clearly must have undergone some level of dissipation, since they are more spatially concentrated than the blue GCs (GLK96) and the massive dark matter halo of NGC 4472.

In terms of abundance ratios, the enhancement seen in [Mg/Fe] in massive ellipticals is generally attributed to different levels of enrichment from Type Ia supernovae (SNe), which largely contribute Fe, and Type II SNe, which produce Mg and Fe in roughly equal quantities. If the NGC 4472 GCs truly possess [Mg/Fe] $\simeq$ 0, then this would imply that their formation was decoupled at some level from that of the spheroid light. Whether differing degrees of Type Ia/Type II SNe enrichment indicates different star formation time-scales, a variable binary fraction or a variable IMF is uncertain. But certainly determining whether the [α/Fe] ratios in GCs are truly enhanced with respect to solar, and whether there are variations *between* different cluster subpopulations will place strong constraints on their formation.

3.6.2 Results of the Kinematical Analysis

Perhaps the principle result from analysing the kinematics of the NGC 4472 GCS, is to strengthen the previous findings of S98, in that the red and blue GCs are kinematically different. This kinematical distinction, coupled with their chemical differences, implies that the red and blue GCs do indeed form two separate populations of GCs, a fact which was previously only *inferred* from their bimodal colour distribution.

We find some evidence of moderate rotation in the blue GCs, and find little or no rotation in the red GC population. This result for the red GCs is seemingly contrary to indications that they must have formed in a preferentially dissipational process. The fact that the red GCs have a velocity dispersion very similar to the stellar light of NGC 4472, whilst the blue GCs have significantly higher dispersion, suggests that the red GCs are more closely associated with the underlying galaxy light than their blue counterparts. This is perhaps not a surprising result, the position of the red peak of GCS is known to correlate with the luminosity of the host galaxy, whereas the blue peak

shows little or no such correlation (e.g. Brodie & Huchra 1991; Zepf & Ashman 1993; Forbes, Brodie, & Grillmair 1997; Harris 1999).

The velocity dispersion of GCs slowly declines with radius, indicating that the GCs follow the potential of their host galaxy rather than the surrounding cluster. Under the assumption of isotropy, we find a rising $\mathcal{M}/L$ ratio indicating the presence of a massive dark halo extending out to at least ~ 30 kpc, the limit of our data. The findings of Rhode & Zepf (2000), in that the GCS of NGC 4472 extends out to 3 times these radii, indicates that the GCS will provide important dynamical information out to $\sim 10\, r_e$ for this galaxy.

3.6.3 Formation of the NGC 4472 GCS

In an attempt to construct a likely picture for the formation of the NGC 4472 GCS, one may envision a χ^2 fit of the currently favoured models to the observational data. However, one is faced with the fact that such an exercise would yield no best fit solution to these data. The models are currently not specific enough in their observational predictions, and the data does not offer strong enough constraints for the models.

The ages of the GCs in NGC 4472 are comparable to the ages of the Milky Way GCs, indicating that they are old and must have formed at high redshift ($z > 1$). The chemical, kinematical and spatial similarities between the red GCs and the halo light of NGC 4472 indicate that they formed under a similar process, and perhaps at similar times. The spatial distribution, and if real, the radial gradient in the red GCs points toward significant dissipation during their formation, as is the perhaps case for NGC 4472 itself (e.g. Davies, Sadler, & Peletier 1993; Kobayashi & Arimoto 1999). However, the absence of rotation in the red GCs indicates that they could not have formed in a purely dissipational collapse, a problem for models of *in situ* formation, which predict the collapse and hence conservation of angular momentum of the proto-galaxy (e.g. Forbes, Brodie, & Grillmair 1997). A major merger may remove significant angular momentum from the red GCs outwards (Hernquist 1993), but this would then require that the spatially extended blue GCs to be imparted with significant rotation, which is seemingly not the case. If the blue GCs were truly associated with the surrounding NGC 4472 subcluster, this would point strongly to a high level of accretion for these GCs (e.g. Cote, Marzke, & West 1998). However, not only does the velocity dispersion of the blue GCs slowly decline with radius, but also there appears to be no significant population of blue clusters at larger galactocentric distances (Rhode & Zepf 2000).

In summary, none of the currently in vogue models for GCS formation, *in situ* collapse, spiral-spiral mergers, accretion of dwarf galaxies or GCs of primordial origin, satisfactorily fit the entire range of observations of the NGC 4472 GCS by themselves. It is perhaps closer to the truth that a combination of some or all of these processes have lead to the currently observed GCS of this galaxy.

3.7 Summary and Conclusions

We have obtained 87 new spectra of GCs associated with the giant elliptical NGC 4472. These data, combined with the spectroscopic study of S98 yields a total dataset of 144 GCs. We have analysed the line-strengths and kinematics of these GCs and find:

- The NGC 4472 GCs span a spectroscopic metallicity range of -1.6 $\leq$ [Fe/H] $\leq$ 0 dex. This range is consistent with that derived from broad-band colours.
- There appears to be a radial metallicity in the NGC 4472 GCS which is not an artefact of the changing spatial distribution of the red and blue GCs. This gradient is steeper than that seen in the underlying starlight of the galaxy.
- We find that blue and red GCs are coeval within our uncertainties. The blue GCs are 14.5 $\pm$ 4 Gyr old, and the red GCs have an age of 13.8 $\pm$ 6 Gyr. Both populations are older than 6 Gyr at the 95% confidence level. We therefore conclude that the bimodality in the colours of the NGC 4472 GCS principly reflect metallicity and not age differences.
- The spatially extended blue GCs have significantly higher velocity dispersion than the more concentrated red GCs. We find that the subpopulations are kinematically distinct at $>$ 99 % confidence. The kinematics of the red GCs are more closely related to the stellar light of NGC 4472 than the blue GCs, which seemingly have more in common with the velocity dispersion of the NGC 4472 subcluster.
- We find evidence for moderate rotation in the blue clusters, and little or no rotation in the red clusters. From Monte Carlo simulations, we place an upper-limit upon the rotation of the red clusters of $(v/\sigma)_{\rm proj} < 0.34$ at the 99% confidence level.
- We find that the mass distribution derived from the GCs is in good agreement with estimates obtained from X-ray observations, indicating that to first order our assumptions about the dynamical properties of the GCs are correct. We find that the $\mathcal{M}/L$ ratio of the galaxy

continues to rise out to $\sim$ 30 kpc. At these radii the $\mathcal{M}/L$ ratio is a factor of $\sim$ 5 greater than in the central regions of NGC 4472, implying the presence of a massive dark matter halo around this galaxy.

Chapter 4

Star Clusters in the LMC

Abstract. In this Chapter we present high signal-to-noise spectra for 64 star clusters in the Large Magellanic Cloud using the FLAIR spectrograph at the UK Schmidt. The clusters have been placed onto the Lick/IDS system in order to test the calibration of the age-metallicity predictions derived from Simple Stellar Population (SSP) models which use the Lick/IDS fitting functions. Many of the star clusters fall within the parameter space (i.e. young, metal-poor) which is unconstrained by the models of Worthey, therefore we use the SSP models of Kurth, which cover the nearly the entire range of metallicity and age for the clusters. We find that the model predictions are in good agreement with literature metallicity values, although in the mean our integrated spectra tend to predict slightly higher metallicities ($\sim$ + 0.15 dex). This offset is primarily driven by the most metal-poor (globular) clusters, which have metallicities 0.1–0.3 dex higher than the values derived from *HST* Colour-Magnitude diagrams. The ages of the clusters also compare favourably with those derived from Colour-Magnitude diagrams, however, for the younger clusters we systematically derive older ages, by $\sim$ 0.7 Gyr. We confirm previous findings of an age-gap in the LMC clusters between 3–4 $< \tau <$ 9–15 Gyr, with a corresponding metallicity gap at -1.2 $\leq$ [Fe/H] $\leq$ -0.8. We obtain an age–metallicity relation for the clusters which is in good agreement with that of the LMC field stars. We confirm the status of the *bona fide* LMC GCs, in that they present late-type spectra and are old and metal-poor.

4.1 Introduction

With the exception of the Sagittarius dwarf galaxy, the Magellanic Clouds (MC) are the nearest known galaxies to the Milky Way, and harbour significant populations of star clusters. Both the Large Magellanic Cloud (LMC) and Small Magellanic Cloud (SMC) are gas-rich dwarf irregulars (Hubble-types Sm and Im 'peculiar' respectively), and lie within the orbits of the most distant Galactic GCs.

The LMC is estimated to harbour more than 2000 star clusters (Olszewski, Suntzeff, & Mateo 1996), and the Small Cloud somewhere in the region of 500–600 (Bica & Schmitt 1995). The

clusters in the Clouds cover a broad spectrum of age and metallicity, from the youngest (often termed 'populous') clusters which are typically 10 Myr old (e.g. NGC 2100), to those of GC age (e.g. NGC 1754). Due to their proximity (LMC $\sim$ 53 kpc; SMC $\sim$ 60 kpc; Olszewski, Suntzeff, & Mateo 1996), the Clouds provide a unique opportunity for comparing the integrated light of their stellar populations with Colour-Magnitude Diagrams (CMDs) and spectroscopy of individual stars. It is this ability to compare the integrated properties of the star clusters, covering such a span of age and metallicity, with other observational methods which is the key motivation behind this present study.

The plan of this Chapter is as follows: in the remainder of this section, we introduce the principle physical characteristics of the LMC, briefly review past observations of the LMC star clusters, and discuss previous observational techniques employed to derive ages and metallicities for the clusters. Next, in Section 4.2, we describe our sample selection and observations performed for this present study. In Section 4.3 we describe the reduction steps required for our fibre spectra, before we turn to obtaining radial velocities of the clusters in Section 4.4. We then proceed to describe our line-strength measurements and correction to the spectroscopic system in Section 4.5. We describe the stellar population models we use in this study in Section 4.6, before testing our model calibration and deriving ages and metallicities for the clusters. In Section 4.7 we compare our derived ages and metallicities to those in the literature, and then proceed to look at the age–metallicity relation of the LMC clusters. Finally, we present a summary and our conclusions from this study in Section 4.8.

4.1.1 The Large Cloud

The LMC presents a planar structure, tilted at an angle of somewhere in the region of 27 degrees (de Vaucouleurs & Freeman 1972) to 45 degrees (Alvarez, Aparici, & May 1987), with a prominent off-centre bar, a nucleus and irregular spiral arms. It has a total mass of 3.8×10^9 $M_\odot$, with a neutral gas mass comprising of some 15% (5×10^8 $M_\odot$) of this total (Kim 1998). Figure 4.1 shows an *R* band CCD image of the LMC, taken with the 'parking lot' camera[1], kindly supplied by G. Bothun. The field size of the image is $\sim 6 \times 10$ degrees, and clearly shows the bar feature and the 30 Doradus region (to the left, and slightly above the main bar). In Table 4.1, we list the basic data for this galaxy.

[1] Yes, the observations were made from a parking lot at Las Campanas

Table 4.1. Basic galaxy data for the Large Magellanic Cloud.
Sources: 1) de Vaucouleurs et al. (1991), 2) Olsen et al. (1998), 3) Olszewski et al. (1991)
4) Bothun & Thompson (1988).

Property	Value	Source
Right Ascension (1950.0)	$05^h24^m00.1^s$	1
Declination (1950.0)	$-69°48'00''$	1
Type	Sm	1
B	0.9	1
$B-V$	0.54	1
M_B	-17.9	1
N_{GC}	13	2,3
S_N	0.6 ± 0.2	2,3
Effective radius (r_e)	3°	4
P.A.	170°	2
V_{helio}	278 $km\,s^{-1}$	1

Surface photometry indicates that the LMC has a half-light radius of $\sim$ 3 deg, with a characteristic scale length of 1.7 deg (Bothun & Thompson 1988). The angular extent on the sky of the known LMC cluster system is in excess of 10 deg, and therefore extends out to at least six scale lengths of the galaxy (Olszewski et al. 1991).

4.1.2 A Potted History of the Large Cloud Clusters

Historically, the study of the Magellanic Cloud clusters has caused much confusion, and still continues to present a rich source for debate and investigation. The initial findings by Thackeray, that the most luminous stars in the LMC cluster NGC 1866 were very blue, and that it contained Cepheid variables, led Baade (1951) to conclude that the LMC was composed entirely of a 'pure' population I system. He contended that galaxies either consisted entirely of old, metal-poor stars (population II) or younger, solar-type stars (population I), with no cross-over between the systems. Baade's idealised concept of population I and population II systems was further bolstered by Thackeray's discovery that the Sculptor dwarf contained RR Lyrae variables (i.e. population II stars), whilst both Baade (1951) and Shapley (1951) posited that the Magellanic Clouds contained none. So it was against a sceptical climate that Thackeray and Wesslink announced that they

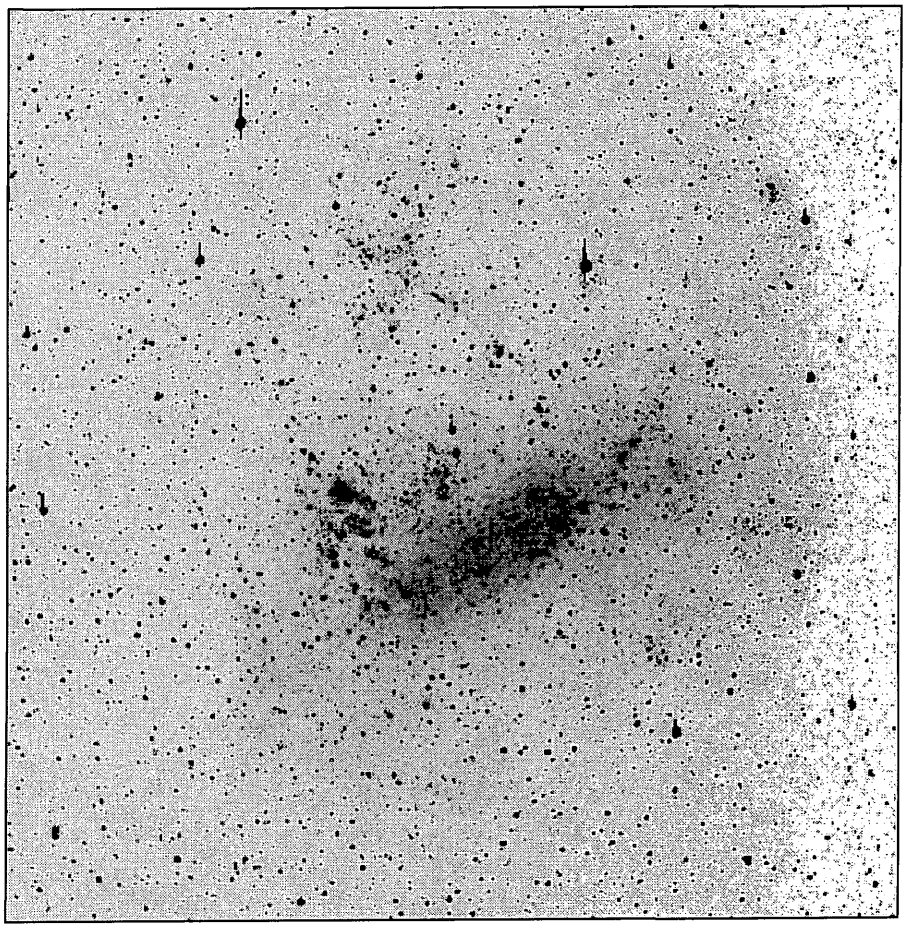

Figure 4.1: An *R* band image of the Large Magellanic Cloud. The field size is approximately 6 × 10 degrees, with north at the top and east to the left. The bar region and 30 Doradus complex (a giant HII region, north and to the east of the bar) can be clearly seen. The observations where performed in a parking lot with an 85 mm $\mathcal{F}$/2.0 Nikon camera and off-the-shelf RCA CCD. (Image kindly supplied by G. Bothun).

had found RR Lyraes in the Clouds by going somewhat deeper than the previous studies. This realisation that the Clouds harboured multiple stellar populations, both in the form of field stars and star clusters, lead to the true recognition of the Clouds' importance for the study of stellar populations.[2] Indeed, in 1956, Shapley commented *"the Magellanic Clouds serve as a gateway to the Metagalaxy—to the outer and overall aggregate of galaxies"* (see Shapley 1957).

[2] Another significant result of these studies was to put the extragalactic distance ladder on a truly quantitative footing, with the Magellanic Clouds being the first 'rung' (with debate over the exact distance to the LMC still ongoing, even in the era of post *HIPPARCOS* parallaxes e.g. Feast & Catchpole 1997; McNamara 1997; Kaluzny et al. 1998).

4.1.3 Integrated Techniques

The proximity of the Clouds has lead to the application of several observational techniques to investigate the nature of their stellar populations. An extensive classification of the Cloud clusters was performed by Searle, Wilkinson, & Bagnuolo (1980). These authors devised a two-dimensional classification scheme using integrated Gunn-Thuan photometry for 61 Cloud clusters, and showed that they primarily form an age sequence in the *Q(ugr)-Q(vgr)* diagram, with metallicity becoming increasingly important for the oldest clusters.

They assigned SWB types I–VII to the clusters, with I representing the highest metallicity, young, blue clusters through to VII, old and metal-poor clusters—essentially Milky Way GC analogues.[3] Later, Frenk & Fall (1982) showed that the same sequence was apparent in the 'equivalent' *(U-B)* vs *(B-V)* diagram if the reddening affect of dust is negligible, which they termed E-SWB. This classification had the great advantage that it was based upon a specific photometric system. Subsequently, there have been numerous efforts to derive an age-etallicity relation (AMR) for the clusters from their integrated *UBV* colours, from the catalogues of van den Bergh (1981) (Elson & Fall 1988; Chiosi, Bertelli, & Bressan 1988) and more recently from the integrated *UBV* photometry of Bica et al. (1991) (e.g. Girardi & Bica 1993; Girardi et al. 1995).

In conjunction with studies using integrated photometry, a number of workers have focused upon the information which may be derived from the integrated spectra of the Cloud clusters. Perhaps the first study was performed by Cannon (1929), who identified the integrated spectra of 8 Cloud clusters as being A-type, a much earlier spectral type than any GCs within the Galaxy. Mayall (1946), reviewed the work of Cannon (1929) and showed that this classification (previously applied to Galactic GCs) was unsuitable, since it relied upon the spectral shape as one key criterion, before the extinction effects of dust, and its influence upon continuum shape, were recognised. The first quantitative data upon the old Cloud clusters was obtained by Danziger (1973), who created a classification based upon metal-line strength. However, this classification was unsuccessful because he failed to realise that the spectra may be ordered by *Balmer*-line strength, and not solely metal-line strength (which is a smooth, but non-monotonic relationship—e.g. SWB 1980). Rabin (1982) obtained integrated spectra for what he termed 'red' star clusters and found that these red clusters had significantly enhanced Balmer absorption lines with respect to their Galactic counterparts. This lead him to conclude that few (if any) of his sample were of comparable age.

[3] The SWB-types used in this study are those defined by Bica, Claria, & Dottori (1992), extended to include SWB 0, indicative of very young clusters.

Rabin made extensive use of what became known as the hydrogen metals diagnostic diagram (HMD), a classification plane for star clusters with Balmer-line strength on one axis and metal-line strength on the other. By constructing stellar population models using stellar evolutionary tracks, he quantitatively demonstrated that the strength of the Balmer lines in his integrated spectra were strongly dependent upon the clusters' age. An example of such a HMD, essentially an early version of the stellar population model grid (e.g. Worthey 1994; Vazdekis et al. 1996), is shown in Figure 4.2. This grid, constructed by Manduca and presented by Searle (1984), improved upon and extended the work by Rabin (1982).

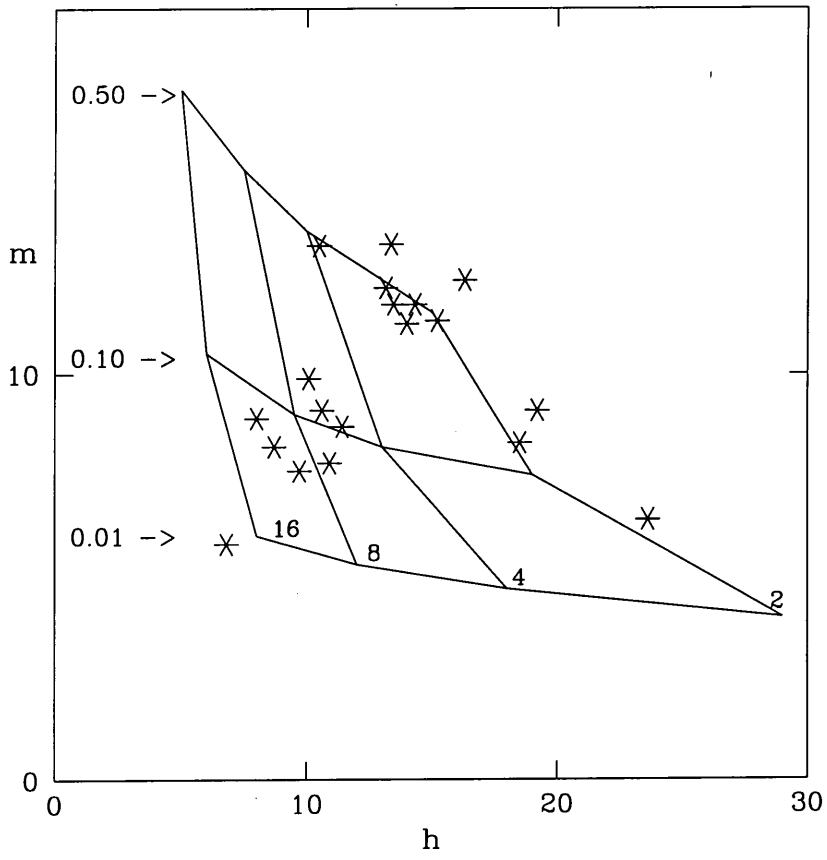

Figure 4.2: Classification of the Hydrogen Metal Diagram for a sample of star clusters in the LMC, taken from Searle (1984), using the grids of Manduca. Horizontal grid lines are metallicity in solar units, vertical lines are isochrones in Gyr.

The clusters appear to form an 'S' shape tilted upon its side, a characteristic of the SWB classification, however in this case the physical origin of this shape becomes clearer. This quantitative

attempt at age and metallicity classification from integrated spectra, indicated the usefulness of such an approach and the diagnostic nature of such a diagram.

4.1.4 Individual Stellar Studies

Colour-magnitude diagrams have long been a key observational tool for probing stellar populations, since they reflect their physical properties, such as age, mass and chemical composition.

CMDs were first constructed for LMC clusters by Arp (1961) and later by Gascoigne (1962,1966). These authors demonstrated that whilst some of the CMDs exhibited what appeared to be old stellar populations, many resembled CMDs of open clusters, with many appearing very young indeed and having no known counterparts in the Galaxy.

There are now several recent examples in the literature of CMDs for young (1–3 Gyr) LMC clusters (Olszewski 1988; Geisler et al. 1997) and old (>10 Gyr) clusters (Hesser, McClure, & Harris 1984; Walker 1990). Geisler et al. (1997) obtained CMDs of 25 candidate 'old' clusters using Washington system photometry, and concluded that most were in fact young clusters. However, these ground-based studies are restricted to uncrowded regions of the Cloud, and with an expected main-sequence turn-off at $V\sim$ 23.0 for an old population, are challenging. Like so many other areas of astronomy, the field has been revolutionized with the advent of *HST*. Its excellent resolving power has allowed CMDs of Cloud clusters to be obtained which are several magnitudes fainter than the turn-off, even in the crowded regions of the bar of the LMC. Olsen et al. (1998) derived CMDs in the F555W and F814W filters for the LMC clusters NGC 1754, NGC 1835, NGC 1898, NGC 1916, NGC 2005 and NGC 2019, all located in regions of high stellar density. They found that all the clusters have well-developed horizontal branches and have ages consistent with those of Galactic GCs. [4] Similar studies have also been carried out for the clusters NGC 1466, NGC 2257 and Hodge 11 (Johnson & Bolte 1996), which have somewhat larger projected distances from the LMC bar. Whilst CMDs derived in such a manner are extremely powerful, such studies do not lead to 'definitive' ages for the clusters and are not infallible. As pointed out by Olsen et al. (1998), the CMD age indicators are metallicity dependent, therefore uncertainties in the CMD-derived abundances translate to uncertainties in age. Indeed, taking spectroscopic abundances for the clusters yielded somewhat younger ages ($\sim$ 2 Gyr) for the clusters in the Olsen et al. (1998) study.

[4] With the exception of NGC 1916, which they found to have substantial differential reddening across the cluster, precluding accurate age determinations.

In terms of spectroscopy of individual stars in the clusters, there have been relatively few studies (e.g. Cowley & Hartwick 1982). Perhaps the most extensive programme to date is that by Olszewski et al. (1991), who obtained spectra for some 80 cluster giants. They derived abundances from the Ca II triplet ($\lambda \sim 8500$ Å) and velocities accurate to $\pm$ 5 km s^{-1} for clusters in the Large Cloud. They found a mean metallicity for the old clusters of $\langle$[Fe/H]$\rangle$ = -1.80, somewhat more metal-poor than the mean value of the entire Milky Way GCS, but similar to that of its halo clusters (Ashman & Zepf 1998).

As a result of these analyses, a fascinating picture of the cluster AMR has emerged. The LMC appears to possess old GCs ($\tau > 10$ Gyr), and young clusters ($\tau < 3$–4 Gyr) but no clusters intermediate to these ages (with the possible exception being the distant cluster ESO 121 SC-03, Da Costa 1991). This age gap has a corresponding metallicity gap, whereby the young clusters are, in the mean, $\sim$ 1.2 dex more metal-rich than the old clusters. In contrast, the situation for the field stars seems to be radically different, with evidence of differing star formation histories within the Large Cloud. Butcher (1977) concluded that from signs of a discontinuity in the luminosity function of the main sequence from ground-based studies, most of the LMC stars were formed 3–5 Gyr ago. Studies by Bertelli et al. (1992), Westerlund, Linde, & Lynga (1995) and Vallenari et al. (1996) indicate that the LMC field stars possess a small component of old stars, but in the main are either young or have intermediate ages. In addition, Bertelli et al. (1992) concluded that the star formation rate (SFR) of the LMC has remained at a relatively low level for most of its lifetime, but suddenly increased by up to a factor of $\sim$ 10 in its SFR in the past few Gyr, yielding essentially a bimodal age distribution similar to that seen in the LMC clusters. Similarly, a constant SFR over approximately a period of 10 Gyr is found by Geha et al. (1998) for outer disk fields of the LMC using *HST*. They find a significantly higher rate than that found by Bertelli et al. (1992), and also find evidence of a recent increase of star formation, in this case by a factor of $\sim$ 3. Elson, Gilmore, & Santiago (1997) present *HST* observations of the bar regions of the LMC, and obtain similar results, but also show evidence of a period of star formation 1–2 Gyr ago not seen in the outer disk. Clearly the star formation in the LMC is somewhat more complex than would appear to be the case for the LMC star clusters. The issue of whether the star clusters in the LMC do not reflect the field star formation history of the LMC, or whether the absence of 4–12 Gyr clusters indicates some form of (perhaps contrived) preferential destruction of the intermediate-age clusters is still moot.

4.2 Obtaining Spectra of the Star Clusters

In this section, we describe the selection and distribution of the cluster sample. We then proceed to give details of the spectroscopic system used for obtaining the cluster spectra, and finally the observations themselves.

4.2.1 Sample Selection for Spectroscopy

The proximity and spatial extent of the Cloud clusters presents an interesting challenge to the observer, both in obtaining integrated spectra representative of each clusters' stellar population, and in obtaining spectra of a representative sample of the cluster system. As will be described shortly, the observations were performed with the Fibre-Linked Array-Image Reformatter (FLAIR) system (Parker & Watson 1995), a multi-object fibre spectroscopy system at the AAO's 1.2-metre UK Schmidt Telescope (UKST). This system has two principle advantages over other systems for obtaining spectra of the Cloud clusters: the availability of large (6.7 $''$) fibres and the large field of view of the Schmidt telescope. The large fibre size allows for a representative sample of the cluster light into the spectrograph, whilst minimizing the contaminating flux contribution from the surrounding field. This avoids the necessity of having to trail long-slit spectra over spatially extended objects and thereby increasing the probability of contamination from foreground stars (e.g. Searle 1984). The Schmidt photographic plates possess a useful field area of 40 deg^2, with a radius of the unvignetted field of 2.7 deg. The FLAIR fibres are attached to copies of these plates, and so in principle can cover a huge area of sky. In practice however, constraints upon fibre positioning and fibre length yield a slightly smaller, though still significant usable field. This field size, coupled with multiple fibres (40 $\sim$ 100 depending upon the FLAIR configuration) yields a high degree of multiplexing, whilst keeping to a minimum the required number of changes in the field configuration. Perhaps the key disadvantage of this approach is a restriction upon the size and morphology of clusters for which representative integrated spectra can be obtained. As the concentration of the cluster falls (or as its spatial extent increases), the fibre samples a smaller fraction of stars within the cluster, leading to possible stochastic effects (e.g. Chiosi, Bertelli, & Bressan 1988).

Our sample of star clusters were drawn from the catalogue of Bica et al. (1999), who give accurate co-ordinates, blue-visual magnitudes, sizes and shapes for over 6000 bodies in the Large Cloud. The initial 1808 objects identified by Bica et al. (1999) as star clusters were cross-correlated with the earlier catalogue of Bica et al. (1996) to yield SWB types for 504 candidates.

This was subsequently condensed down to a manageable number of observable targets on the basis of the following criteria:

- **Position** the FLAIR fibre field is restricted to one photographic Schmidt plate, covering 40 deg^2, therefore objects must be within this field (chosen to be centred upon the bar of the LMC). Clusters were assigned a higher weight if they were in uncrowded regions.
- **SWB type** the sample was selected to contain similar numbers of all types (with some emphasis upon obtaining targets with SWB type VII—GC analogues).
- **Previous Studies** an effort was made to include as many clusters with CMD and/or spectroscopically derived ages and metallicities as possible.
- **Brightness** brighter clusters were preferentially chosen to obtain the maximum S/N, and to minimize the possible stochastic contributions from a few bright giants.
- **Appearance** clusters were selected to be compact and clearly visible against the background galaxy since they had to be marked-up by eye on the Schmidt plates. A key point was that they must have a core radius of order of the entrance aperture of the fibre in order to minimize the sky contribution.

In Figures 4.3 & 4.4 we show the spatial distribution of our final sample of 180 clusters, in addition to the 64 clusters for which we have obtained reliable spectra. It should be noted that Figures 4.3 & 4.4 do not give a true indication of the distribution of the whole population of clusters in the LMC as a function of age. Not only is the sample biased in the sense that the brighter clusters were generally chosen, but we also preferentially selected clusters in less dense/crowded regions. The true distribution follows a general trend of increasing spatial distribution of the clusters as one goes to later SWB types (Bica et al. 1999). In Figure 4.5 we show the location of our sample of star clusters in the $U-B$, $B-V$ (i.e. E-SWB) plane. The two-dimensional nature of the classification is evident, as is the fact that we have obtained a reasonable distribution of SWB types in our spectroscopic sample. Figure 4.6 shows DSS images of LMC star clusters in our sample, representing SWB types 0–VII. The concentrated nature of the cluster cores, and each cluster's spatial extent on the sky (each image is 120 $\times$ 120 arcseconds) is evident.

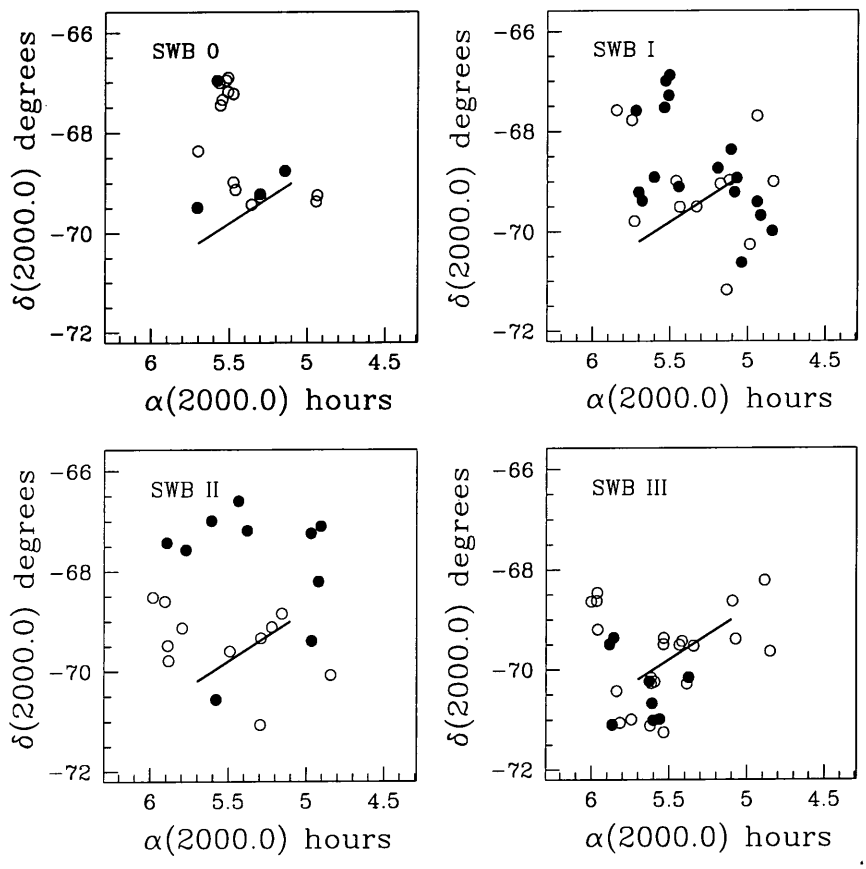

Figure 4.3: Spatial distribution of our final sample star clusters in the LMC. Open circles indicate candidate clusters from our final sample, solid circles indicate clusters for which we have obtained spectra. The clusters have been separated on the basis of SWB type, here we show types 0–III. The solid line represents the position and orientation of the LMC bar,

4.2.2 The FLAIR System

The FLAIR system is unique in that it allows multi-object spectroscopy of astronomical objects over a wide (40 deg^2) field. The method of locating targets and positioning the fibres is somewhat unusual, so we discuss this procedure in some detail.

From our final sample of 180 star clusters, finding charts were constructed at the same plate-scale of the UKST (67.14 $''$/mm). A thin, transparent film copy centred on the bar of the LMC, α =05 23.6, δ =-69 45, (2000 epoch) was created based upon UKST R-band IIIa-F plates at the Royal Observatory, Edinburgh. The positions of the clusters were then located and marked onto this transparent copy by overlaying it onto the finding chart, and visually registering the positions of a number of bright stars. Fibres were then positioned over each marked object and secured

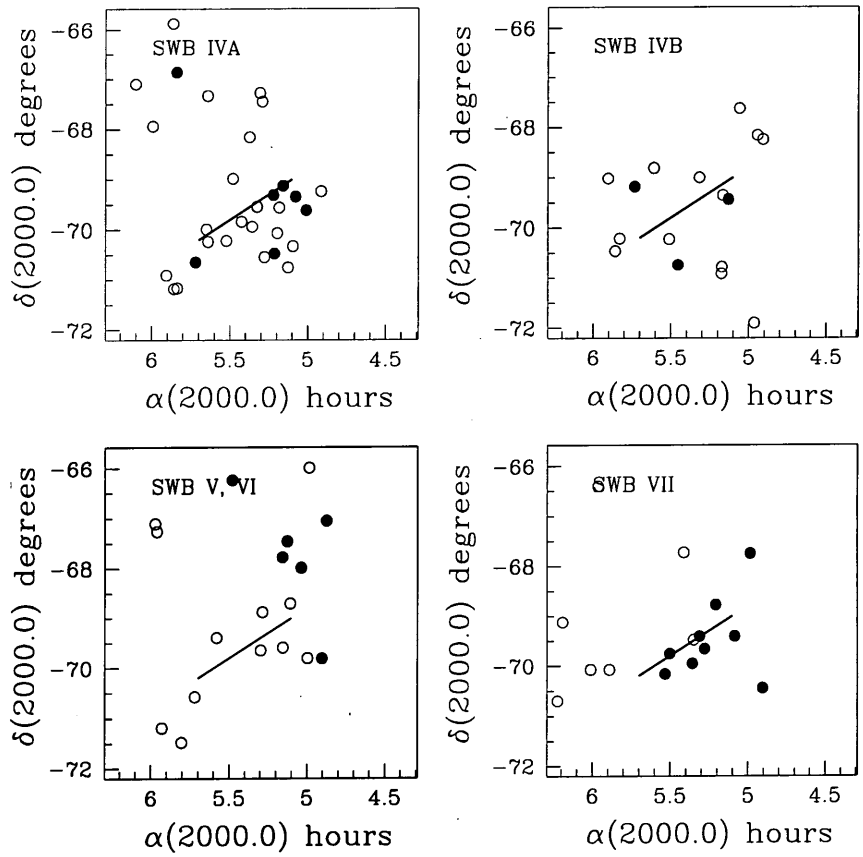

Figure 4.4: Spatial distribution of SWB types IVA–VII, symbols as for previous figure.

to the copy plate by way of strong magnets attached to each fibre ferrule using a pair of pliers. The FLAIR fibres end in a 2 mm, 90 degree prism, and actually lie parallel to the copy plate. Accurate positioning is achieved by back-illuminating the fibres, and placing the fibres over the targets on the plate by means of a CCTV camera. We estimate that a positioning accuracy of $< 1.0''$ was achieved. A complication in plate preparation was the fact that the fibre numbers fed to the spectrograph do not correspond to the ferrule numbers located over the targets on the copy plate. Therefore, at the time of fibring-up, a look-up table was generated to register the ferrules with their corresponding fibres, and hence targets. In addition to the object fibres, a number of fibres were reserved to measure the contribution from the sky background, an issue we return to in § 4.2.3.

Finally, a fiducial fibre-bundle was positioned by the telescope operator[5] for field acquisition and guiding. The copy plates were generally marked and fibred-up the day before the observations,

[5] Malcolm Hartley, who did a great job in the face of large technical difficulties.

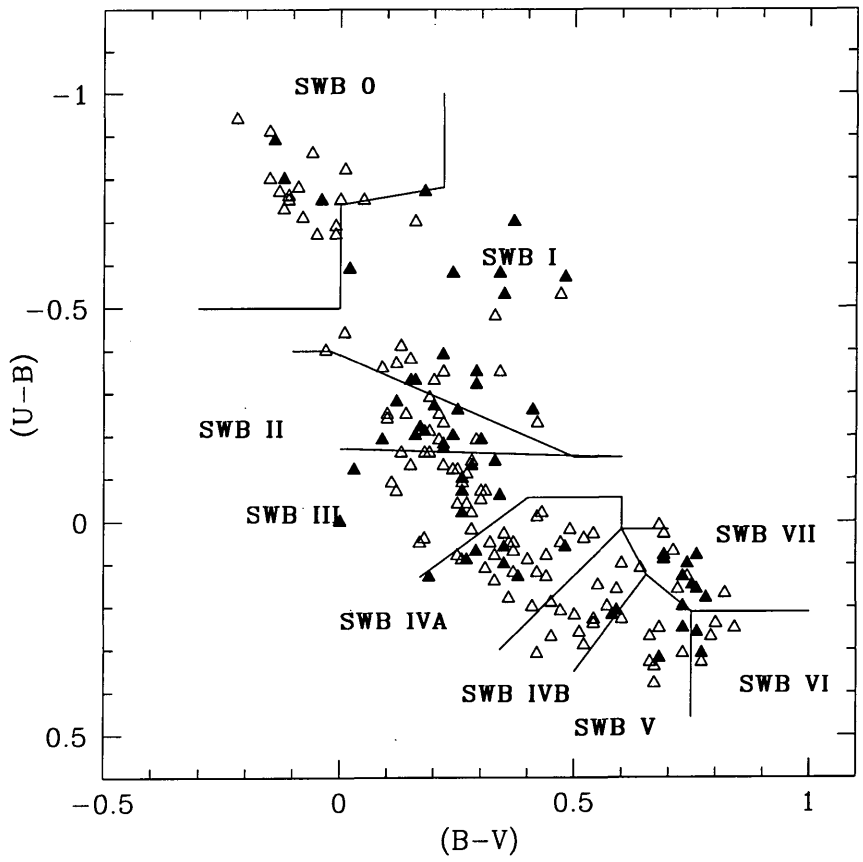

Figure 4.5: SWB classification of our final sample of star clusters. Open triangles represent our final sample for spectroscopy, filled triangles are clusters for which we have obtained spectra. The positions of each SWB type are marked on the $U-B$, $B-V$ plane with solid lines and were defined somewhat arbitrarily (see Searle, Wilkinson, & Bagnuolo 1980; Frenk & Fall 1982).

with the availability of two plate holders meaning that if necessary, one field could be observed whilst the other was being prepared.

There are two main FLAIR configurations available to the observer at the UKST, with several subsidiary options. Plate holders 14/5 and 14/6 allow for large (100 μm) fibres with 92 and 73 fibres per field respectively, and are primarily intended for observing galaxies ($B < 17.5$) and bright stars ($B < 16$). Smaller (55 μm) fibres are also available on the 14/6 plate holder which were originally intended for faint point-sources, since they accept in a factor of ~ 3 less background (though these are generally not used due to unforseen problems in the small diameter fibres—see Parker & Watson 1995). We opted to use the larger diameter fibres since they are well-suited to the sizes of our candidate star clusters.

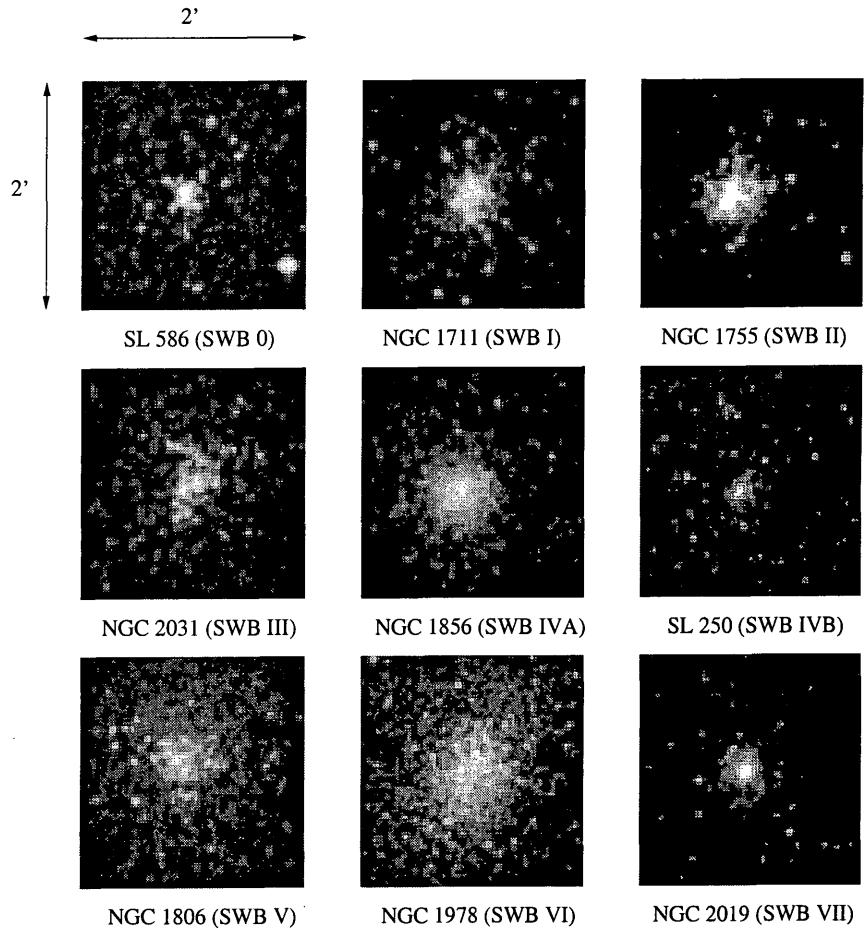

Figure 4.6: Representative images of the LMC star clusters in our spectroscopic sample, showing SWB types 0–VII. The images are 120″× 120″ on a side, taken from the Digital Sky Survey.

In order to calculate the effective magnitudes through the fibres, we assume that the clusters follow a King (1966) profile with a core radius, r_c, defined as:

$$r_c = \sqrt{\frac{9}{4\pi G \rho_0 \beta}} \tag{4.1}$$

and with a concentration parameter given by:

$$c \equiv log(r_t/r_c) \tag{4.2}$$

where ρ_0 is the central density, β is a constant and r_t is the tidal radius of the cluster.

Adopting a mean concentration of c = 2.5 (Harris 1996), yields typical core radii of $\sim$ 1 pc. Only a small fraction of star clusters in the LMC are true GCs, but since we preferentially chose compact systems, we consider this a reasonable assumption. At an adopted distance of 53 kpc for

the Large Cloud (Olszewski, Suntzeff, & Mateo 1996), star clusters with core radii of $r_c \sim 1$–2 pc correspond to angular diameters on the sky of ~ 4–8 $''$.

Our cluster sample has integrated magnitudes in the range $9.54 \leq V \leq 13.26$, with a median of $V = 11.4$ mag. We expect one core radius to supply ~ 5 % of this flux down the fibres, yielding effective magnitudes through the 6.7 $''$ fibres of $12.8 \leq V \leq 16.5$, with a median effective magnitude of $V = 14.6$ mag. It was decided at the time of the observations that such bright magnitudes may lead to significant cross-contamination of adjacent fibres, especially where faint and bright objects occur next to each other. Therefore, alternate fibres were blanked-off to reduce this possibility. These magnitudes imply that the contribution from the background will only be significant for the faintest clusters. Bothun & Thompson (1988) find a nominal central surface brightness for the LMC of $B \simeq 21.5$ mag arcsec^{-2}. Assuming that *all* this light is transmitted down the fibres, which have an effective aperture of ~ 35 arcsec^2, we find that the flux contribution of the background down the fibres will be $V \sim 17.2$ mag. This implies that for the brightest clusters, the background will contribute ~ 0.02 % to the total flux, whereas at $V = 16.5$, this contribution will be of order 50 %. Strictly speaking, the adopted central surface brightness for these calculations is only applicable to clusters in the bar of the LMC, therefore this estimate of the background contribution is an upper limit.

Plate holder 14/5 possesses a total of 92 fibres. Excluding one which was broken and six which were allocated as sky fibres, left a total of 39 fibres per field for target clusters.

An important emphasis of this study was to obtain a realistic treatment of errors in our measured line-strengths, therefore at the expense of decreased star clusters observed, we reserved 12 fibres across our fields for repeat observations. When the fields were re-configured, repeat objects were observed using different fibres, allowing us to estimate our repeatability (and any residual effects of fibre-to-fibre response on our results).

4.2.3 Estimating the Sky Contribution

The LMC presents a particularly difficult environment for accurate sky-subtraction. The background it presents to the observer varies on scales of a few arcsec to a few degrees, making both local and global estimation of the sky contribution extremely difficult. Since fibre spectroscopy usually employs one of two methods of sky subtraction, and the FLAIR system is no exception, there were two principle methods available to us:

In *simultaneous sky exposures*, several object fibres are reserved for use as sky fibres. These fibres are positioned evenly over the field in order to obtain a representative sample of sky. This is generally most effective when the background of the field is essentially uniform (i.e. the main contribution to counts are diffuse astronomical sources and the atmospheric background). The alternative to this is taking *separate sky fields*, where before and/or after the science exposures are taken, the entire field is offset by fixed amount. Each object spectrum then has its corresponding local sky spectrum subtracted using the same fibre.

Due to the varying background of the LMC, neither of these techniques were particularly ideal for accurate sky-subtraction of our star cluster spectra. However, it became clear that the method using separate sky fields would have serious shortcomings, since there was no guarantee that the offset sky fibres would not fall onto a region of high background or on to a bright star (indeed, in the dense bar regions this would be highly probable). We therefore opted to obtain sky exposures simultaneously with the science frames using dedicated sky fibres, but to treat them in a slightly different manner than is usual.

From the R band image of Bothun & Thompson (1988), we calculated approximate isophotal contours in the LMC. In Figure 4.7 we plot the isophotes of the LMC, and indicate the positions of our star clusters and sky fibres. We determined where the surface brightness of the LMC fell to $B \simeq 23$ mag arcsec^{-2}, comparable to that of the 'true'sky level. This, in conjunction with visual inspection of the Schmidt plates, allowed us to place three fibres in areas of low stellar density, effectively sampling the underlying sky counts. The median sky value was then subtracted from the object spectra (see § 4.3.8). The remaining three fibres were placed in proximity to isophotes indicating higher surfaces brightnesses, in order to try and estimate the flux contribution from these regions. The flux measured down each of these fibres provided an indication of the sky contribution at that particular surface brightness level. Using the isophotal contours, these sky levels were scaled to the positions of the clusters and subtracted. Note that the positioning of the fibres was only approximate, since at the time of the observations it proved difficult to overlay the isophotal contours onto the copy plate.

4.2.4 Observations

The observations of the star clusters in the LMC were carried out over the nights of the 3–7th November 1999, using FLAIR at the UKST.

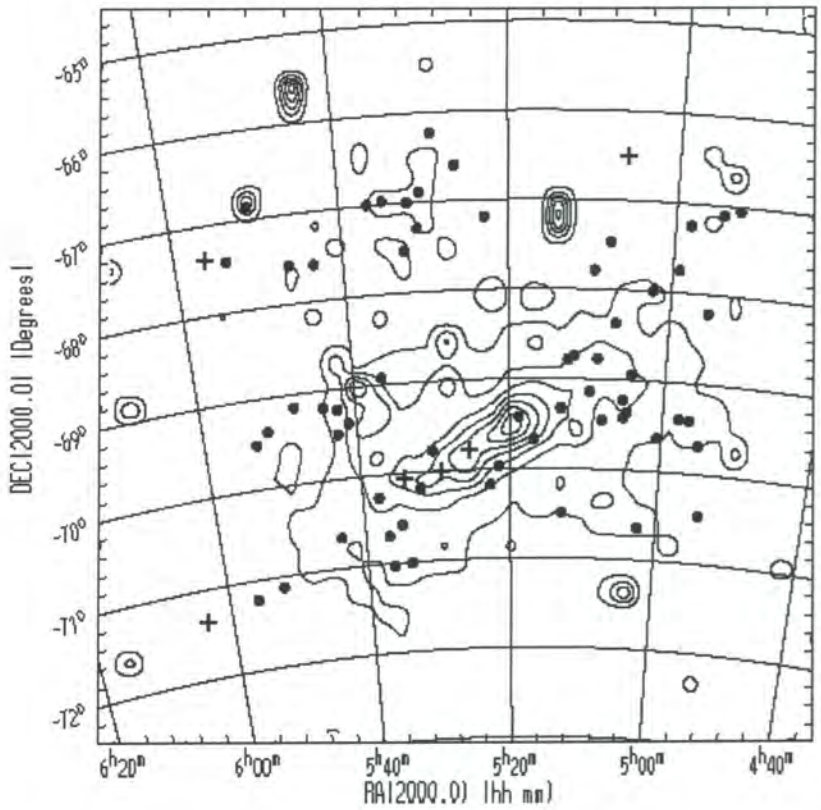

Figure 4.7: Isophotal contours calculated for the LMC from the R band image of Bothun & Thompson (1988). The nominal central surface brightness of the galaxy is $B \sim 21.5$ mag arcsec^{-2}, the isophotal contours are plotted in steps of approximately 0.25 mag. The positions of the sky fibres are indicated by crosses, and filled circles represent the star clusters for which we have obtained spectra. In this figure, North is up and East is to the left.

The general set-up of the FLAIR system for these observations is given in Table 4.2. At the beginning and end of each night, multiple bias-frames were taken in order to correct for large-scale variations on the EEV chip. To correct for differences in fibre-to-fibre response, dome flats and twilight frames were obtained. Mercury-Cadmium-Helium (HgCdHe) arcs were taken for wavelength calibration of our final spectra, these were obtained before and after each target field was observed to check for flexure or systematic shifts in the spectrograph (this proved unnecessary, the FLAIR spectrograph is mounted on the floor and is very stable.)

We opted for the 600V grism used in the first order, with an instrumental resolution of $\sim$ 2.6 Å pixel^{-1}. This yielded a useful spectral range of 4000–5500 Å, encompassing the majority of the Lick indices (see Trager 1997). Gaussian profile fits to 12 HgCdHe arc-lines allowed us to determine a Full-Width-Half-Maximum (FWHM) resolution of the spectra of 6.5 Å, with a dispersion between the 12 measurements of 0.2 Å.

In Table 4.3 we list our observations of LMC star clusters, giving exposure times for each plate configuration. Our initial goal was to observe two fields (i.e. two plate configurations) of LMC clusters and two fields of SMC clusters. However, due to mechanical problems at the UKST[6] only the two LMC fields were actually obtained. The seemingly uneven balance in exposure times between fields 1 & 2, shown in Table 4.3, are largely due to this mechanical problem. As a result of observing the two LMC fields with plate 14/5, we observed a total of 78 star clusters. Of these 78 clusters, 66 were unique identifications, since twelve clusters were common to both fields to provide a measure of our repeatability.

Table 4.2. The instrumental setup for spectroscopy.

Telescope	1.2-metre UK Schmidt
Instrument	FLAIR spectrograph
Dates	3–7 November 1999
Spectral range	4000–5500 Å
Grating	600 V
Dispersion	2.62 Å pixel^{-1}
Resolution (FWHM)	$\sim$ 6.7 Å
Detector	EEV CCD02-06 (400 $\times$ 578 pixels)
Underscan	11 pixels
Overscan	4 pixels
Gain	1.0 e$^-$ ADU^{-1}
Readout noise	11 e$^-$ (rms)
Seeing	2–3 $''$

During the observations, the typical seeing was 2–3 $''$. Perhaps surprisingly, this relatively poor seeing proved not to be a hindrance, since the cluster light was smeared by the atmospheric seeing

[6] The RA fine-positioner failed, as did the auto-guider later!

Table 4.3. Log of observations for the two plate configurations.

Field	RA(2000)	DEC(2000)	Clusters Obs.	No. of Sky Fibres	Exp. Time (s)
LMC Field 1	05 23.6	-69 45	39	6	17100
LMC Field 2	05 23.6	-69 45	39	6	6300

disk to a diameter of comparable size to the fibres. In addition to our target clusters, we observed a total of 14 standard stars. We obtained spectra for 11 stars to calibrate our line-strength indices onto the Lick/IDS system, and 3 radial velocity standards. We intended to observe more than 20 Lick standard stars, however the previously mentioned technical difficulties prevented this (we return to this point in § 4.5.4). We list all the observations of our standard stars in Table 4.4, with their associated spectral types (from the SIMBAD database) in addition to their rõle in our analyses. For completeness, we also include their literature radial velocities and metallicities where available. In Table 4.5 we list the positions, colours and magnitudes for the 64 star clusters for which we have reliable spectra. In addition, we give heliocentric radial velocities for the clusters, as described in § 4.4.2. Where there is more than one observation of the same cluster, the weighted mean velocity is taken.

Table 4.4. Log of observations for Lick/IDS and radial velocity standard stars.

ID	Alt. ID	Spectral Type	V_r	[Fe/H]	comment
HD 693	HR 33	F5 V	+14.4	–	radial velocity standard
HD 1461	HR 72	G0 V	-10.7	-0.33	Lick standard
HD 4128	HR 188	K0 III	+13.0	–	radial velocity standard
HD 4307	HR 203	G2 V	-12.8	-0.52	Lick standard
HD 4628	HR 222	K2 V	-12.6	–	Lick standard
HD 4656	HR 224	K4 IIIb	+32.3	-0.07	Lick standard
HD 6203	HR 296	K0 III	+15.3	-0.48	Lick standard
HD 10700	HR 509	G8 V	-16.4	-0.37	Lick standard
HD 14802	HR 695	G2 V	+18.4	-0.17	Lick standard
HD 17491	HR 832	M5 III	-14.0	–	Lick standard
HD 22484	HR 1101	F9 IV-V	+27.6	0.02	Lick standard
HD 22879	–	F9 V	+114.2	-0.85	Lick standard
HD 23249	HR 1136	K0 IV	-6.1	0.02	Lick standard
HD 203638	HR 8183	K0 III	+22.0	–	radial velocity standard

Table 4.5.: Data for our observed star clusters. Columns are : (1) identification .1= field 1, .2=field 2, (2) heliocentric velocity, (3) velocity error, (4) right ascension, (5) declination, (6) apparent diameter, (7) integrated V magnitude, (8) $U-B$ colour, (9) $B-V$ colour, (10) SWB type, (11) alternate identification.

Sources: [1] this work, [2] from Bica et al. (1999) ,[3] from Bica et al. (1996)

SL=Shapley & Lindsay (1963),H=Hodge (1960),KMHK=Kontizas et al. (1990),ESO=Lauberts (1982),HS=Hodge & Sexton (1966), H88=Hodge (1988),BRHT=Bhatia et al. (1991)

ID	V_h^1	V_{err}^1	RA(2000.0)[2]	DEC(2000.0)[2]	D [2]	V^3	$U-B^3$	$B-V^3$	SWB type[3]	Alt. Name[2]
	km s^{-1}	km s^{-1}			(arcsec)	(mag)	(mag)	(mag)		
BRHT 14b.2	319	73	05 32 20	-67 31 40	0.80	12.02	-0.70	0.37	I	KMHK1040
KMHK 1019.2	389	100	05 31 50	-66 59 49	0.70	11.49	-0.57	0.48	I	...
M-OB 4.2	368	100	05 40 49	-69 22 46	0.85	11.69	-0.53	0.35	I	H88-308
NGC 1711.1	267	107	04 50 37	-69 59 06	3.50	10.11	-0.37	0.12	I	SL 55
NGC 1718.1	280	71	04 52 25	-67 03 05	1.80	12.25	0.26	0.76	VI	SL 65
NGC 1735.2	323	105	04 54 20	-67 06 01	1.80	10.76	-0.28	0.12	II	SL 86
NGC 1751.1	313	61	04 54 12	-69 48 25	1.60	11.73	0.00	0.00	V	SL 89
NGC 1754.1	283	52	04 54 17	-70 26 29	1.60	11.57	0.15	0.75	VII	SL 91
NGC 1755.1	326	88	04 55 14	-68 12 17	2.20	9.85	-0.20	0.16	II	SL 99
NGC 1767.2	317	110	04 56 27	-69 24 12	1.30	10.61	-0.58	0.24	I	SL 120
NGC 1774.2	282	116	04 58 06	-67 14 32	1.70	10.76	-0.27	0.20	II	SL 141

continued from previous page

ID	V_h^1	V_{err}^1	RA(2000.0)[2]	DEC(2000.0)[2]	D [2]	V^3	$U-B^3$	$B-V^3$	SWB type[3]	Alt. Name[2]
	km s^{-1}	km s^{-1}			(arcsec)	(mag)	(mag)	(mag)		
NGC 1782.2	286	97	04 57 51	-69 23 35	1.20	10.50	-0.26	0.25	II	SL 140
NGC 1786.1	271	56	04 59 06	-67 44 42	2.00	10.88	0.10	0.74	VII	SL 149
NGC 1801.1	289	136	05 00 34	-69 36 50	2.20	12.16	0.09	0.27	IVA	SL 170
NGC 1806.1	246	63	05 02 11	-67 59 17	2.50	11.10	0.31	0.73	V	SL 184
NGC 1815.2	294	155	05 02 27	-70 37 15	1.20	12.41	-0.59	0.02	I	SL 189
NGC 1825.2	247	92	05 04 19	-68 55 35	1.00	12.04	-0.26	0.41	I	SL 202
NGC 1830.2	324	113	05 04 39	-69 20 37	1.30	12.56	0.13	0.19	IVA	...
NGC 1834.2	270	116	05 05 12	-69 12 27	0.95	11.82	-0.32	0.29	I	ESO56SC60
NGC 1835.1	227	49	05 05 05	-69 24 14	2.30	10.17	0.13	0.73	VII	SL 215
NGC 1846.1	314	66	05 07 34	-67 27 36	3.80	11.31	0.31	0.77	VI	SL 243
NGC 1852.1	303	49	05 09 23	-67 46 42	1.90	12.01	0.25	0.73	V	SL 246
NGC 1856.2	265	89	05 09 29	-69 07 39	2.70	10.06	0.10	0.35	IVA	SL 271
NGC 1863.2	330	111	05 11 39	-68 43 48	1.40	10.98	-0.33	0.16	I	SL 299
NGC 1865.1	265	100	05 12 25	-68 46 23	1.40	12.91	0.08	0.69	VII	SL 307
NGC 1872.2	273	131	05 13 11	-69 18 43	1.70	11.04	0.06	0.35	IVA	SL 318
NGC 1878.1	251	94	05 12 49	-70 28 18	1.10	12.94	0.07	0.29	IVA	SL 316
NGC 1898.2	254	61	05 16 42	-69 39 22	1.60	11.86	0.08	0.76	VII	SL 350
NGC 1916.2	374	89	05 18 39	-69 24 24	2.10	10.38	0.18	0.78	VII	SL 361

continued from previous page

ID	V_h^1	V_{err}^1	RA(2000.0)[2]	DEC(2000.0)[2]	D [2]	V^3	$U-B^3$	$B-V^3$	SWB type[3]	Alt. Name[2]
	km s^{-1}	km s^{-1}			(arcsec)	(mag)	(mag)	(mag)		
NGC 1939.1	296	72	05 21 25	-69 56 59	1.40	11.78	0.09	0.69	VII	SL 414
NGC 1940.1	316	70	05 22 43	-67 11 10	1.20	11.91	-0.19	0.30	II	SL 427
NGC 1943.1	276	65	05 22 29	-70 09 17	1.10	11.88	-0.17	0.27	II	SL 430
NGC 1951.1	342	112	05 26 05	-66 35 50	1.70	10.58	-0.19	0.09	II	SL 464
NGC 1967.1	312	65	05 26 43	-69 06 05	0.95	10.83	-0.75	0.05	I	SL 478
NGC 1978.1	318	40	05 28 45	-66 14 10	4.00	10.70	0.25	0.78	VI	SL 501
NGC 1987.1	322	87	05 27 17	-70 44 08	1.70	12.08	0.23	0.54	IVB	SL 486
NGC 2002.1	367	65	05 30 21	-66 53 02	1.90	10.10	-0.58	0.34	I	SL 517
NGC 2004.2	328	88	05 30 40	-67 17 13	3.00	9.60	-0.71	0.13	I	SL 523
NGC 2005.2	279	65	05 30 09	-69 45 08	1.60	11.57	0.20	0.73	VII	SL 518
NGC 2019.2	294	74	05 31 56	-70 09 34	1.50	10.86	0.16	0.76	VII	SL 554
NGC 2031.2	269	116	05 33 41	-70 59 12	3.30	10.83	-0.07	0.26	III	SL 577
NGC 2038.2	248	74	05 34 41	-70 33 39	1.60	11.92	-0.21	0.18	II	SL 590
NGC 2041.1	310	77	05 36 28	-66 59 26	2.60	10.36	-0.17	0.22	II	SL 605
NGC 2051.1	258	84	05 36 07	-71 00 42	1.50	11.69	-0.06	0.34	III	SL 608
NGC 2056.1	303	104	05 36 34	-70 40 18	1.50	11.77	-0.12	0.03	III	SL 611
NGC 2065.2	280	79	05 37 37	-70 14 09	2.30	11.24	-0.10	0.26	III	SL 626
NGC 2100.2	388	161	05 42 08	-69 12 42	2.50	9.60	-0.56	0.16	I	SL 662

continued from previous page

ID	V_h^1	V_{err}^1	RA(2000.0)[2]	DEC(2000.0)[2]	D [2]	V[3]	$U-B$[3]	$B-V$[3]	SWB type[3]	Alt. Name[2]
	km s^{-1}	km s^{-1}			(arcsec)	(mag)	(mag)	(mag)		
NGC 2102.2	314	145	05 42 20	-69 29 17	0.85	11.44	-0.75	-0.04	0	SL 665
NGC 2107.1	312	101	05 43 11	-70 38 26	1.70	11.51	0.13	0.38	IVA	SL 679
NGC 2108.1	276	65	05 43 56	-69 10 50	1.80	12.32	0.22	0.58	IVB	SL 686
NGC 2127.1	280	78	05 51 22	-69 21 39	1.50	11.64	-0.14	0.33	III	SL 751
NGC 2134.1	269	100	05 51 56	-71 05 51	2.80	11.05	-0.02	0.26	III	SL 760
NGC 2135.1	285	131	05 53 35	-67 25 40	1.50	12.05	-0.22	0.17	II	SL 765
NGC 2136.1	314	100	05 52 59	-69 29 33	2.80	10.54	-0.13	0.28	III	SL 762
Rob 1.2	259	100	05 08 39	-68 45 32	0.50	11.23	-0.89	-0.14	0	NGC 1850A
SL 106.2	313	142	04 55 06	-69 40 26	1.70	11.28	-0.33	0.15	I	...
SL 230.1	377	98	05 06 33	-68 21 48	1.40	11.34	-0.35	0.29	I	...
SL 250.1	325	80	05 07 50	-69 26 06	1.00	13.15	0.21	0.59	IVB	...
SL 360.2	506	154	05 18 12	-69 13 11	1.10	9.54	-0.91	-0.15	0	...
SL 586.2	359	101	05 34 43	-66 57 45	1.50	11.17	-0.80	-0.12	0	ESO86SC12
SL 601.2	364	120	05 36 10	-68 54 42	0.95	11.81	-0.77	0.18	I	KMHK1130
SL 675.1	343	67	05 43 16	-67 35 22	0.95	12.01	-0.39	0.22	I	...
SL 709.1	307	76	05 46 15	-67 34 06	1.10	11.47	-0.18	0.22	II	HS426
SL 741.1	307	118	05 50 25	-66 51 41	1.40	13.26	0.06	0.48	IVA	HS426

4.3 Standard Data Reduction

In this section, we outline the various steps for calibrating and extracting the multi-fibre spectra. In the following discussion, we define *data frame* as a generic term applying to all data and the *science frame* as the data frame of the star cluster spectra. The term *aperture* refers to the 2-dimensional extraction window corresponding to each fibre. The majority of these data reduction was performed using IRAF.

4.3.1 The Overscan Correction

In order to prevent negative counts being fed to the analogue-to-digital converter, a bias-level is supplied by the CCD controller to the detector. Information about this level is retained on one side of the chip by the overscan region, and must be removed from all the data frames. Using the CCDPROC task, the overscan was averaged along the readout direction to produce an overscan vector, and a smooth function was then fit to this vector. At each line this function was evaluated and subtracted from the columns in the data frame. Once this correction was performed, the data frames were trimmed to remove the overscan region, in addition to first and last few rows of the data which generally contain no useful information.

4.3.2 Bias Frames

To remove any residual structure in the electronic bias of the detector, zero-second exposures called *bias frames* were subtracted from the science frames. So that they were not dominated by the readout noise of the CCD, typically $\sim$ 50 bias frames were taken for each science image and combined using the ZEROCOMBINE task. The resulting average 'master bias' was then subtracted from the science frames.

4.3.3 Flat Fields

Flat-fielding is a crucial stage in the data reduction process, especially so for fibre spectra. A flat field is essentially an image of uniform intensity distribution, required to determine the relative efficiency of individual fibres with respect to each other and correct for vignetting along the spectrograph slit. Flat fields were obtained by taking exposures of an illuminated, uniform white board attached to the dome (i.e. dome flats), in addition to observations of the twilight sky. The latter is usually preferred since it generally produces a more uniform light distribution, and it

is these 'twilights' which were used in the data reduction. Additionally, twilight frames are important for correcting the fibre-to-fibre spectral response, since the shape of the sky spectrum is assumed to be uniform across the entire field. Multiple flat fields were taken and combined using the FLATCOMBINE task. In this case, the exposure time was non-zero so an 'average sigma clipping' rejection algorithm was employed to remove cosmic rays from the 'master flat'. Often, flat field corrections are performed at this stage by simply dividing the science frames by the two-dimensional master flat. However, we chose to perform the response correction by division of each extracted object spectrum by its corresponding flat field spectrum, since this seemed to yield a somewhat better fibre-to-fibre response correction.

4.3.4 Arc Frames

For wavelength calibration Mercury-Cadmium (HgCd) and Helium (He) arcs were obtained before and after each observation by brief exposures to comparison lamps. Specifically, these are low-pressure gas discharge lamps which produce sharp emission lines of precisely known wavelength. In principle, the emission line should be a δ-function, in practice it has a width reflecting the instrumental resolution of the spectrograph. The arcs were co-added to create a composite HgCdHe arc, yielding 12 prominent lines distributed fairly evenly across the useful spectral range (4000–5500 Å). Evidence for large-scale shifts in the 'before' and 'after' arc frames was not evident from comparisons of slices through the arc frame images. During the spectral extraction, any small shifts were dealt with by interpolating between the arcs on the basis of their Julian date of observation.

4.3.5 Preparing the Science Frames

Prior to extraction and calibration of the object spectra, bad columns in the data must be dealt with, cosmic rays removed, and individual science frames of the same field combined. The science frames were individually examined to check for bad columns, areas where charge becomes trapped and fails to readout correctly. Typically 2–3 bad columns were identified in each frame, and were corrected by linearly interpolating across adjacent columns. It became apparent that several bad columns were grouped adjacent to each other for many of the science frames, these fell in the $\sim$ 4950 Å region, and consequently affected one of our measured line-indices (see § 4.5.4). The IMCOMBINE task was used for median combining the science frames, and simultaneously dealt with cosmic ray events via the CRREJECT parameter. This technique of cosmic ray rejection is

based upon known detector noise parameters, and was found to work remarkably well, even with just two science frames.

4.3.6 Tracing and Extraction of the Spectra

Prior to the extraction of the spectra into a 1-dimensional format, the position and width of the individual apertures must be defined. This characterization of the apertures was performed interactively, since automatic aperture identification is not always particularly reliable. Figure 4.8 shows a cross-section image of one of our master flats—these were used as references for the aperture definitions since they possess many counts and are clearly identifiable. The aperture widths were automatically resized to approximately 10 % of the peak height of each profile, thus giving uniform relative aperture sizes.

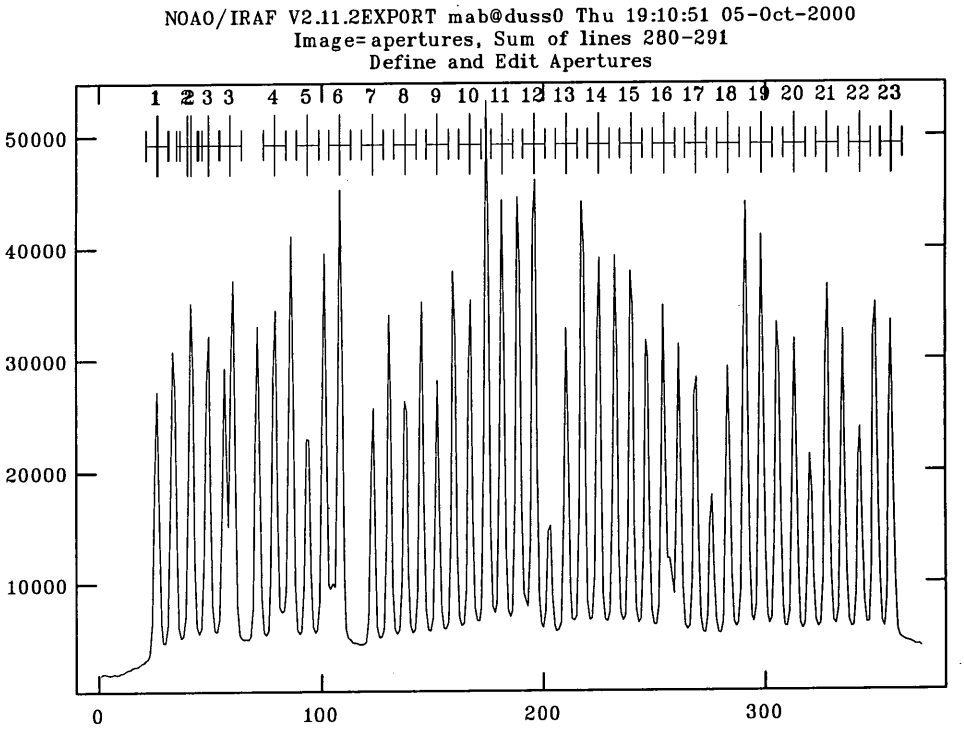

Figure 4.8: Slice across a flat field, showing the position and width of the apertures in the fibre data. For clarity, we have only shown alternate aperture definitions. Since alternate fibres were blanked off, the aperture spacing is a factor of two greater than would normally be the case. The gap between aperture #3 and aperture #4 arises from two broken fibres.

Each aperture was then traced at a series of points along the dispersion axis of the science frame, achieved by fitting a low-order polynomial to the spectra. Even assuming an exact one-to-

one correspondence between a column on the CCD and the spatial axis of the aperture, this tracing is required for each aperture for several reasons: (*i*) diffraction gratings are not always perfectly aligned in their holders and consequently are not always perfectly aligned with the CCD, (*ii*) the camera optics may introduce distortions along the spatial axis of the aperture, and (*ii*) differential atmospheric refraction will shift the positions of the blue and red ends by differing amounts.

Each trace was visually inspected since occasionally the trace would fail and jump to an adjacent spectrum (though not often, because bright flat fields were used as references) usually due to extremely strong absorption in the spectrum (e.g. arising from the Balmer lines). In general, the rms of the polynomial fit to the spectra was < 0.1 pixels. The spectra were then extracted by relocating each trace upon the centre of the aperture definition, and then summing across the aperture at each point along the dispersion. The flat field and arc-line spectra were extracted concurrently with the object spectra, using the same trace-fitting functions. A common extraction method is "optimal" or "variance" extraction, whereby account is taken of the noise and gain characteristics of the CCD, giving higher weight to more central, high S/N pixels (e.g. Horne 1986; Robertson 1986). Although this can often lead to improved extraction (especially for fainter spectra), it was not used in this case since the spectral profile of the EEV CCD used for FLAIR is under-sampled.

At this stage, the flat field corrections were performed. The pixel-to-pixel variations in the detector were dealt with as well as the differences in throughput between the fibres. The extracted flat fields spectra were averaged together and a smooth function fit. This function was then divided back into the individual flat-field spectra to maintain the pixel responses, but remove the basic shape of the spectrum. A response normalisation function for the fibres was calculated from the extracted flats, by calculating the total counts in each fibre. Assuming that the illumination down each of the fibres is uniform, this gives a direct measure of the relative throughput of the fibres. The total counts through each fibre were then multiplied into the flat field spectrum, making the throughput of each fibre the same. Finally, the flat field spectra were normalised by the mean counts of all the fibres in order to preserve the average number of counts in the object frames, after division by the response spectra.

4.3.7 Wavelength Calibration

Each spectrum essentially maps intensity with spatial position along the central locus of the spectrum. The curvature and misalignments usually present between the spectrum and the detector mean that these spatial positions do not have a one to one relationship with individual pixels in the

CCD. Therefore the spectra must be wavelength calibrated to obtain the correct relation between spatial position, $\mathcal{F}(x, y)$, and wavelength, $\mathcal{F}(\lambda)$. The first step in the wavelength calibration process was to identify the wavelength of the lines in one fibre arc-line spectrum. This was consequently used to create a reference dispersion function (relating pixel spatial position to wavelength) which could then be employed to automatically derive dispersion solutions for the remaining apertures. We show a typical HgCdHe arc in Figure 4.9.

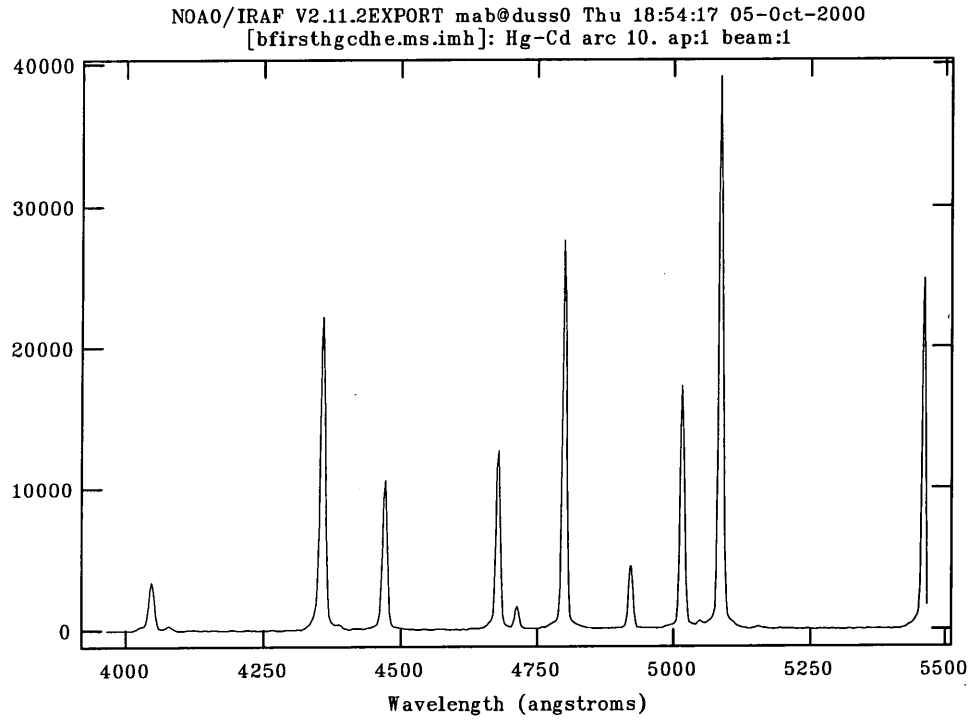

Figure 4.9: Example of a Mercury-Cadmium-Helium (HgCdHe) calibration arc. In this example, a dispersion function has been applied to the arc to show the wavelength position of the lines. The FWHM of the lines is $\sim$ 6.5 Å.

With the help of Mercury-Cadmium and Helium line maps, the lines were identified and marked with their corresponding laboratory wavelengths. A low-order (2–3) polynomial was then fit to the identified lines to produce the pixel-to-wavelength relation. Emission features in the remaining arc spectra were then automatically re-identified from a line list, though in each case these were visually checked for erroneous line identifications. The rms in the fit to the 12 arc features was typically $\sim$ 0.1 Å.

As a final step in the wavelength calibration, the spectra were rebinned onto a linear wavelength scale.

4.3.8 Sky Subtraction

The final, but perhaps the most crucial step in these data reduction, was *sky subtraction.* The flat-fielded and wavelength calibrated spectra consist (hopefully) of photons from the target clusters, and some contribution from the surrounding sky. Even though our sample of star clusters were specifically chosen to match the entrance aperture of the fibres, to obtain the 'true' spectrum of the clusters, the contribution from the sky must be determined and removed. For the interested reader, Wyse & Gilmore (1992) give an excellent treatment of the entire (and large) subject.

As mentioned in § 4.2.3, three of the sky fibres were placed over specific regions of low stellar density, where the surface brightness of the LMC becomes comparable with the true sky level. For each science frame, the sky spectra were median combined to create a representative sky spectrum, with a sigma-clipping algorithm employed to remove any possible cosmic rays. Even though the median value is generally robust against outliers, since only three fibres were allocated to sample the sky background, each sky spectrum was visually examined to check for spurious spectra (e.g. any sky fibres which happened to fall upon a bright star, nebula emission etc.). This median sky was then subtracted from all the object spectra.

4.3.9 Combining the Spectra

The final step in these data reductions were to combine common spectra in order to achieve the maximum S/N for each cluster. The spectra were combined in two ways; they were summed (i.e. simply co-added) and median combined. The spectra were summed in order to obtain an accurate measure of the total number of counts in each spectrum. This then allowed the S/N of each spectrum to be determined, primarily for the calculation of Poisson errors. For the measurement of line-strengths, the spectra were median combined to remove noisy pixels arising from events such as cosmic rays.

4.4 Radial Velocities of the Clusters

The main goal of this study was to measure line-strength indices for the LMC star clusters. However, we have also determined velocities for the clusters to an accuracy of ~ 100 km s^{-1}. Although the resolution of our spectra are not well suited for accurate radial velocities (c.f. Freeman, Illingworth, & Oemler 1983; Olszewski et al. 1991), in this section we discuss the velocity determination of the clusters since these are required to correct the spectra to the rest-frame.

4.4.1 Characterizing the Spectra

Prior to measuring the radial velocities of the star clusters, the general characteristics of these data were noted. Of the 78 star cluster spectra obtained, 75 useable spectra were extracted. Two were failed extractions (NGC 2118 in field #1 and NGC 1951 in field #2) due to a broken fibre not evident at the time of the observations. NGC 1951 was one of the 12 clusters common to both fields, therefore reducing our number of repeat spectra to eleven. In addition, one cluster (SL 788) presented what appeared to be a sky spectrum. We can only conclude that during the observations, the fibre was knocked out of position (which is not impossible since the fibres are held in place by magnetic buttons).

In Figures 4.10– 4.12 we show spectra representative of each SWB type. The spectra have been continuum-normalised and smoothed with a 5-pixel boxcar filter. The majority of the spectra show extremely strong Balmer lines—a well known characteristic of the LMC clusters (Rabin 1982). Clusters with SWB types VI & VII present what appear to be late-type spectra, comparable to those obtained from Galactic GCs. A number of the spectra show strong emission, which is largely confined to clusters of SWB types 0 & I.

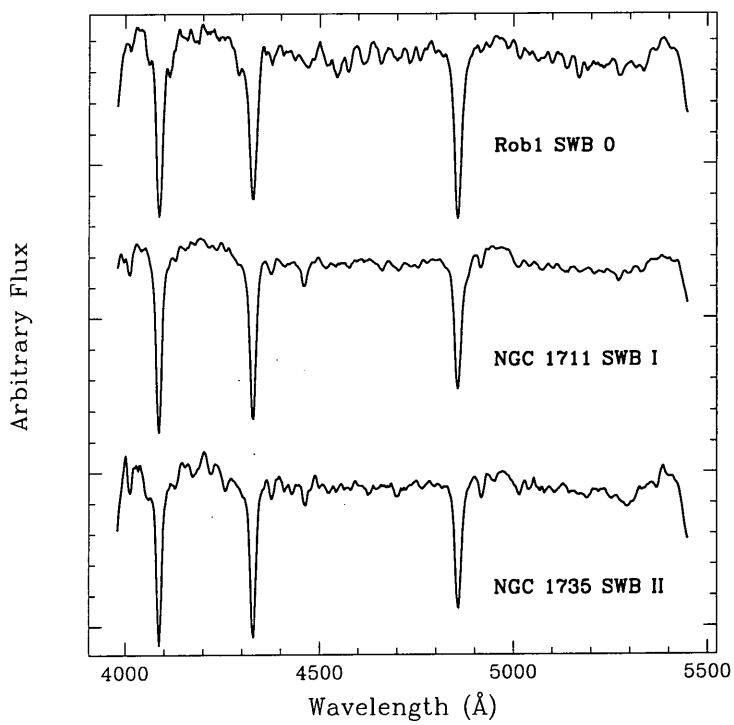

Figure 4.10: Example spectra of clusters with SWB types 0–II. The spectra have been continuum-normalised and smoothed with a 5-pixel boxcar filter. The principle feature of the spectra are the exceedingly strong Balmer lines.

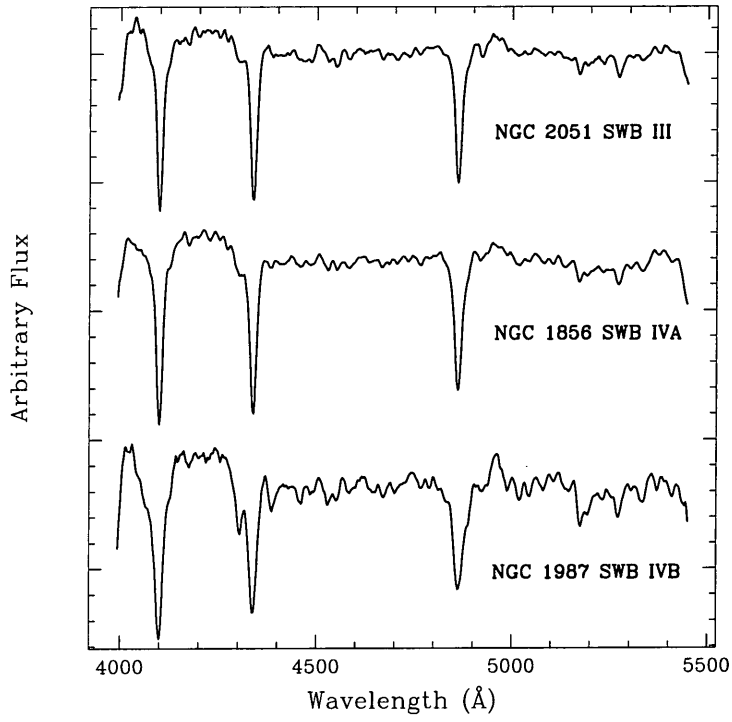

Figure 4.11: Example spectra of clusters with SWB types III, IVA and IVB.

We calculate the signal-to-noise of our spectra using:

$$S/N = \frac{F_{\rm source}}{\sqrt{(F_{\rm source} + F_{\rm sky} + r^2)}} \tag{4.3}$$

where $F_{\rm source}$ and $F_{\rm sky}$ are the counts pixel^{-1} from the source and sky respectively (in ADU) and r is the readout noise of the EEV CCD (11 e$^-$).

We have achieved a typical S/N for the spectra of $\sim$ 100 pixel^{-1} measured just redward of 5000 Å. The poorest quality spectrum is that of NGC 2031, for which we obtain a S/N $\sim$ 25. One of our 'best' spectra is that of the bright cluster NGC 1755 ($V = 9.85$), with a S/N $\sim$ 350.

4.4.2 Velocities

To measure the velocities of the clusters, we have cross-correlated the spectra with template stars of known velocity (e.g. Tonry & Davis 1979).

To use this technique, the spectra are first rebinned into channels of equal width in 'log wavelength'. This is done so that the Doppler shift is equal for all channels. The spectra are then Fourier filtered to remove small-scale (large wavenumber) variations (i.e. noise smaller than the

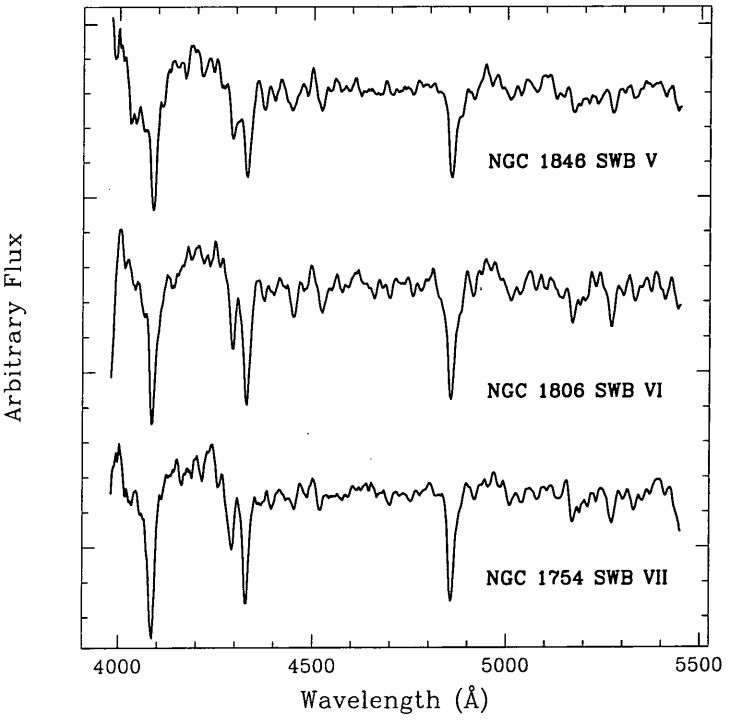

Figure 4.12: Example spectra of clusters with SWB types V–VII.

scale of the spectral features) and large scale (small wavenumber) variations such as those arising from changes in the spectral shape/instrumental response. The spectra are then convolved with templates of similar spectral type in order to create a correlation function. The maxima in this function should then indicate where the object best fits the template. If the velocity of the template is known, then the velocity of the object may be derived.

We have obtained high S/N spectra of three radial velocity standards (Table 4.4) to act as templates for the cross-correlation. In addition to these known standards, we opted to use the stars selected for the purposes of line-index calibration (also given in Table 4.4) since the catalogue velocities of these stars are also well known. The standard stars were first 'Doppler corrected' onto the rest frame by cross-correlation with model spectra of the same spectral type (kindly supplied by A. Vazdekis). These model Spectral Energy Distributions (SEDs) are calculated at a higher resolution than our data (1.8 Å FWHM, as opposed to 6.5 Å), and prior to cross-correlation were smoothed to the resolution of our data (see § 4.5.1). The SEDs are calculated at the rest frame, therefore the derived velocities from the cross-correlation reflect the true velocities of the standard stars (after heliocentric correction). The velocities of the standard stars were found to be in excellent agreement with the literature values (SIMBAD database). Each of these standards were

then cross-correlated with the star cluster spectra. For each template– cluster combination, the correlation function was examined to check for template mismatch or any other obvious problems. As previously mentioned, a number of the clusters showed evidence of emission in their spectra. For the purpose of cross-correlation, we interpolated across these emission lines. In principle, measuring the position of the emission lines would give velocities to a somewhat higher precision than from the cross-correlation. However, although the clusters showing emission are nearly all of SWB type 0 & I ($\tau < 10^8$ yr), we cannot be certain that this emission is not from ionized nebular regions in the Large Cloud itself (e.g. Morgan, Watson, & Parker 1992). These measured radial velocities would reflect that of the of the excited gas as opposed to the velocity of the cluster. In principle, this leads to a robust technique for determining whether the emission is internal or external to the cluster. One may compare the radial velocity of the cluster (from absorption lines) to that determined from the emission lines. However, our resolution is insufficient to adequately delineate the two (see § 4.6.3).

Our final velocities for each cluster were taken to be the mean of the individual velocities, weighted by their reciprocal uncertainty returned by the FXCOR task. The final heliocentric velocities for the clusters and their respective uncertainties are given in columns 2 & 3 of Table 4.5.

In Figure 4.13, we show the velocities for the eleven common clusters between our two LMC fields.

We find the standard deviation of the velocities to be $\sigma_v = 40$ km s^{-1}, with an offset of + 5.2 km s^{-1} between fields 1 and 2. The scatter in these data would indicate that the formal uncertainties from the FXCOR task slightly overestimate the true velocity error. However, regardless of this we determine the final uncertainty, σ_T , in the velocities to be the quadrature sum of the uncertainty from the FXCOR task and that from the rms of our repeatability, $\sigma_v^2 = \sigma_{rms}^2 + \sigma_{FXCOR}^2$. We find a mean velocity for the entire cluster sample of $V_h = 300 \pm 5$ km s^{-1}, where the uncertainty is given by $\sigma/\sqrt{n}$. This compares favourably with the optical recession velocity of the LMC of $V_h = 277 \pm 19$ km s^{-1}, and that measured from H I observations of $V_h = 324 \pm 10$ km s^{-1} (de Vaucouleurs et al. 1991).

As indicated at the beginning of this section, the principle reason for measuring the velocities of the clusters was so that we may correct the spectra to the rest-frame for measuring line-strengths. Therefore, each cluster was de-redshifted by its respective radial velocity. This shift was typically 5 Å ($\sim$ 2 pixels at the resolution of these data).

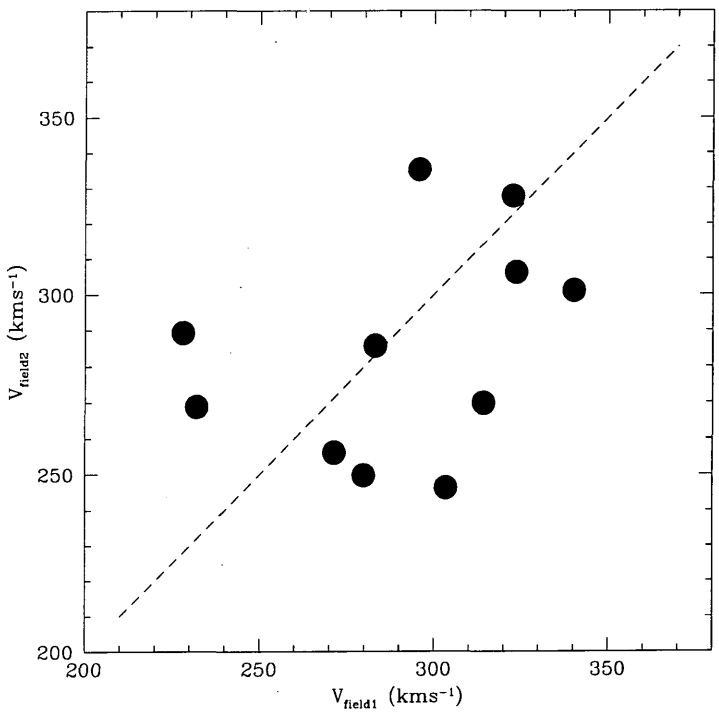

Figure 4.13: Velocities of clusters common between the two fields. The standard deviation between the measurements is $\sigma_{\rm rms} = 40$ km s^{-1}.

4.5 Line-Strengths of the LMC Clusters

In this section, we turn our attention to the measurement of the line-strength indices of the LMC star clusters. We begin by briefly describing the Lick/IDS system (Robinson & Wampler 1972), the spectral line-index system we have chosen to adopt for this study. We then discuss the procedure for both measuring the clusters' line-strengths and determining their uncertainties. Finally, we show how we calibrate these measurements onto the LICK/IDS system.

4.5.1 The Lick/IDS System

Comprehensive discussions of the Lick/IDS absorption-line index system, the derived absorption-line index fitting functions and observations of stars, galaxies and GCs have been given in a series of papers by the Lick group (Burstein et al. 1984; Faber et al. 1985; Burstein, Faber, & Gonzalez 1986; Gorgas et al. 1993; Worthey 1994; Trager et al. 1998). Here, we simply present a summary of the Lick/IDS stellar library and absorption-line index system.

The Lick/IDS system is now in the third decade of its attempt to understand the stellar populations of early-type galaxies. The entire Lick library now comprises of absorption line-strengths for 38 GCs, 381 galaxies and 460 stars. Derived from more than 7400 spectra, this makes it perhaps the largest homogeneous database of its kind. The Lick System defines a total of 25 indices, which are either primarily metallicity sensitive (the majority), or primarily age sensitive (e.g. the Balmer lines, Hβ, Hγ & Hδ, and to a lesser extent G4300).

The spectra were all obtained with the 3-metre Shane Telescope at the Lick Observatory (hence the Lick system), using the Cassegrain Image Dissector Scanner (IDS) spectrograph. The spectra have a wavelength-dependent resolution (FWHM) of 8–10 Å (increasing at both the blue and red ends), and cover a spectral region of 4000–6400 Å. The spectra were not flux-calibrated, but were 'normalised' by division with a quartz-iodide tungsten lamp. The behaviour of the line-strength indices with time was characterized and calibrated by nightly observations of K-giant standard stars. The wavelength calibration of the system turned out to be not particularly stable, with shifts of $\pm$ 3.0 Å often occurring during one observation due to flexure, and the influence of 'stray' magnetic fields. These non-negligible shifts were removed by the cross-correlation of each index with features of well-determined wavelength (e.g. Worthey et al. 1994).

In addition to its homogeneity, an important aspect of the Lick/IDS system is that it is supported by an ever-increasing number of stellar population models (e.g. Worthey 1994; see § 4.6.1). The Lick/IDS system allows observers to measure well-defined line-strength indices for a given stellar population, calibrate them onto a common system, and then compare these measurements with a variety of models in order to derive ages and metallicities for the population.

4.5.2 Measuring the Indices

We have described in the detail the definition and measurement of the Lick indices in Chapter 3, and show the bandpass definitions of the majority of the indices in Table 3.6. In summary: the absorption-line indices are composed of three bandpasses, two 'pseudo-continuum' bandpasses and one feature bandpass. The mean flux level of the pseudo-continuua are determined, and a straight line is drawn through their midpoints. The area below this 'continuum line' and within the wavelength region of the blue and red sidebands of feature bandpass is then integrated to yield a (pseudo) equivalent width (EW). Atomic features are measured in Angstroms, whilst molecular features are expressed as magnitudes.[7] We measure the indices using the Lick/IDS bandpass

[7] A hang-over from prehistory.

definitions with a FORTRAN programme LS1D.[8] This programme takes as its input a list of index definitions and a one-dimensional IRAF spectrum, and outputs measured equivalent widths (or line-strength magnitudes) and Poisson uncertainties (based upon the S/N of the spectra and known characteristics of the detector). We show in Figure 4.14, the Lick/IDS definition of one absorption-line index, namely Hβ.

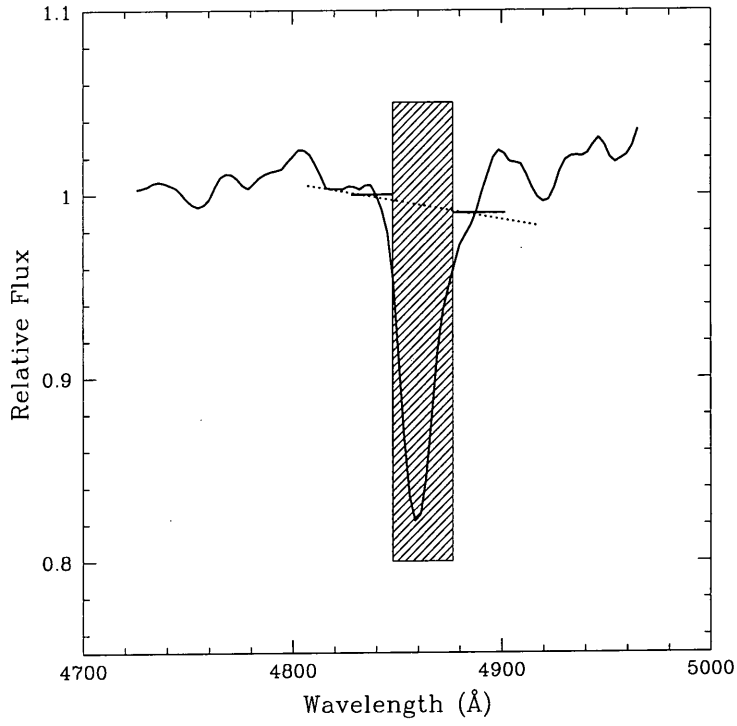

Figure 4.14: Lick/IDS absorption-line index definition of Hβ (centred upon 4861 Å). The portion of the spectrum is that from NGC 1754. The shaded column denotes the position of the feature bandpass, the two horizontal lines blueward and redward of this, connected by the dotted line, show the positions of the pseudo-continuua.

4.5.3 Estimation of Errors in the Indices

As discussed at length by Cardiel et al. (1998), a thorough treatment of error propagation throughout the entire data reduction process perhaps yields the best estimate of uncertainties in line-strength measurements. Analytic formulae for the calculation of uncertainties are certainly important, not only for constructing a realistic error budget, but also for gaining *insight* into the sources of error in the data reduction and analysis process. As is highlighted by Cardiel et al. (1998), by

[8] Kindly provided by Harald Kuntschner

rigorously implementing a parallel-processed error map, one can identify the primary sources of error, and even avoid unnecessary data reduction steps (a tenant which should never be ignored). However, performing such an 'error-tracing' is not always possible. Such an error propagation procedure was not undertaken for two reasons: (*i*) IRAF as yet possess no comprehensive facilities for doing this and (*ii*) every telescope and its respective instrumentation has its own quirks and idiosyncrasies (e.g. the IDS), and sources of error (random and systematic) are not always so readily apparent.

Here, we have elected to derive our total uncertainty in the measured indices from two sources. We use Poisson statistics to determine the photon error (shot-noise) in our data, coupled with duplicate observations to assess the repeatability of our measurements.

We follow the procedure of Rich (1988) in calculating the uncertainties from our S/N and sampling.

The equivalent width of a line is given by the difference between the continuum and feature:

$$W_\lambda(\mathring{A}) = \int_{\lambda_1}^{\lambda_2} \left(1 - \frac{I(\lambda)}{I_c(\lambda)}\right) d\lambda \tag{4.4}$$

where $I(\lambda)$ and $I_c(\lambda)$ are the contributions from the source and continuum respectively, and λ_1, λ_2 are the blue and red wavelength limits of the feature. Since CCD spectra are digital, this is better written as a summation:

$$W = \sum_{i=1}^{n} \left(\frac{I(\lambda)_i}{I_c(\lambda)_i}\right) \Delta\lambda_i \tag{4.5}$$

with

$$\Delta\lambda_i = \frac{\lambda_2 - \lambda_1}{n} \tag{4.6}$$

where n is the number of channels of the bandpass. The uncertainty in the measured equivalent width arises from a combination of Poisson statistics and error in the continuum placement. We assume that the readout noise of the CCD is negligible for these data.

From Poisson statistics, the uncertainty in measuring N counts is simply:

$$\sigma_N^2 = N \tag{4.7}$$

and the uncertainty in placing a continuum point is given by:

$$\sigma_c = \sqrt{\frac{N \text{ counts}}{n \text{ channels}}} \tag{4.8}$$

Here, N counts corresponds to the total counts in the feature (both positive and negative) and n channels is our sampling in the spectrum. Assuming that the errors are *uncorrelated*, we add in quadrature, giving a resultant uncertainty in the measured equivalent width, σ_W:

$$\sigma_W = \frac{\Delta\lambda N}{\bar{c}} \left[\left(\frac{\sigma_{\bar{c}}}{\bar{c}} \right)^2 + \frac{1}{N} \right]^{1/2} \tag{4.9}$$

where $\bar{c}$ is the mean continuum of the bandpass (i.e. the central continuum point as shown in Figure. 4.14).

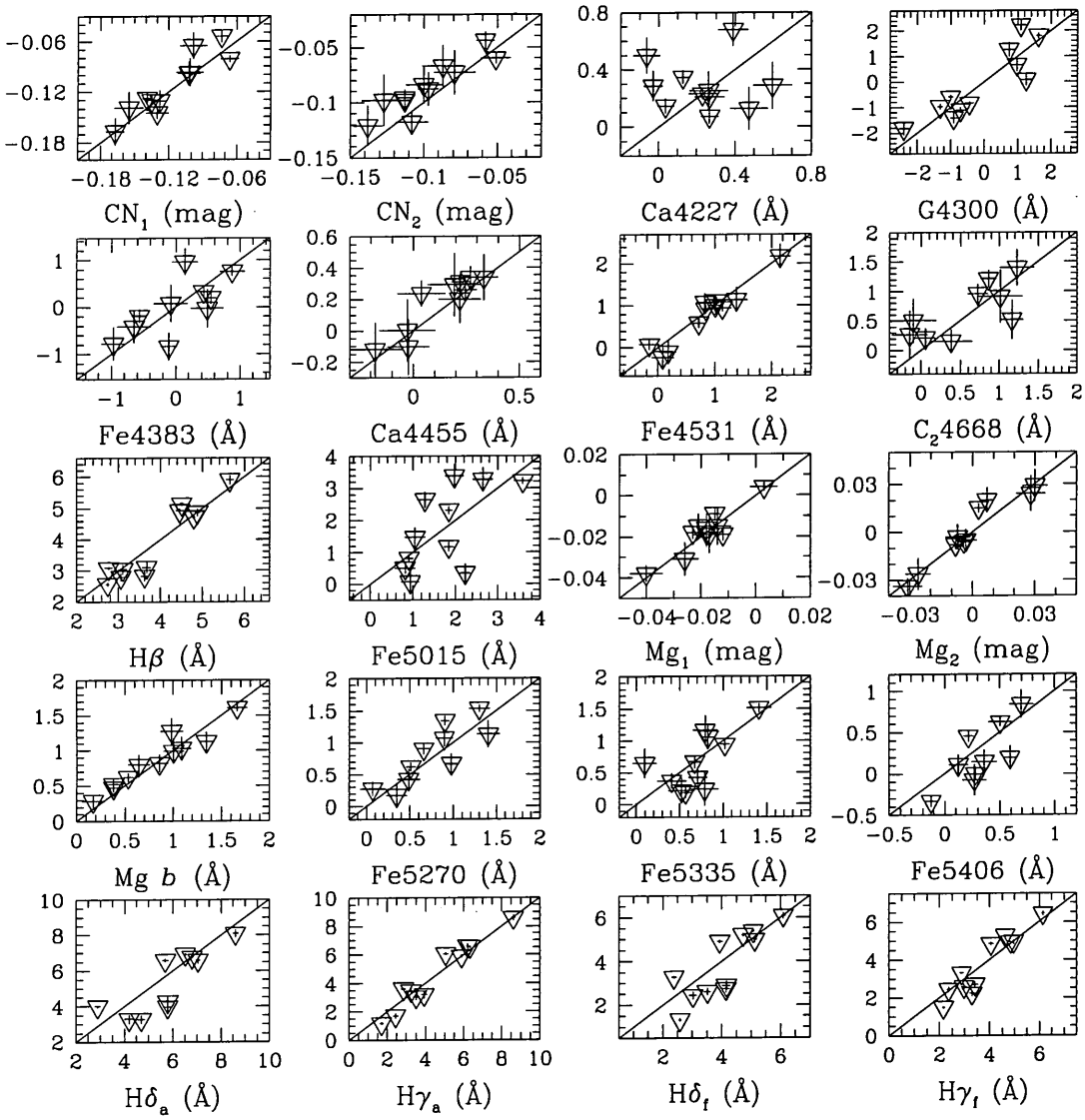

Figure 4.15: Repeatability of our index measurements for common clusters, the straight line represents unit slope. Uncertainties are derived from our Poisson errors.

To assess our repeatability, we have duplicated observations of eleven star clusters, over different nights, taking care to use *different* fibres for each cluster. The star clusters chosen for duplicate observations were: NGC 1754, NGC 1786, NGC 1801, NGC 1846, NGC 1852, NGC 1939, NGC 2004, NGC 2031, NGC 2041, NGC 2127 and NGC 2136. These clusters were selected to cover a wide range in colour ($\delta(B-V) \simeq 0.5$) and brightness (V= 9.60 $\sim$ 12.20), thereby assessing our ability to reproduce measurements of spectra with differing spectral energy distributions.

We measure the Lick/IDS indices for each cluster, and obtain the rms between measurements, $\sigma_{\rm rms}$, from a straight linear regression. We then define the uncertainty for each index as being the standard deviation on the mean of the measurements, $\sigma_{\rm I} = \sigma_{\rm rms}/\sqrt{n-1}$. In Figure 4.15, we show our ability to reproduce our index measurements. We list our repeatability in Table 4.6, giving the mean offset between measurements (*field1-field2*), the rms of the regression ($\sigma_{\rm rms}$) and the correlation coefficient, r, for each index. Inspection of Figure 4.15 and Table 4.6 indicates that our repeatability for the indices is somewhat variable, from excellent (e.g. Fe4531, $\sigma_{\rm I} = 0.06$ Å, r=0.96) to poor (e.g. Fe5015, $\sigma_{\rm I} = 0.30$ Å, r=0.63). Indeed, Ca4227 is actually anti-correlated, with r=-0.081 Å ! However, the majority of the Lick/IDS indices do show good correlation with $r \geq 0.7$, giving $\geq$ 98.4 % probability that the points are linearly correlated for $N = 11$ (Taylor 1982). The unsatisfactory agreement for the Fe5015 index is not particularly surprising. The adjacent bad columns mentioned in § 4.3.5 affected a region of width $\sim$ 8 Å, right in the centre of the blue Fe5015 continuum definition. Our poor repeatability of Ca4227 and Ca4455 perhaps may be attributed to the narrow nature of their bandpass definitions. The Ca4227 feature is 12.5 Å ($\sim$5 pixels) wide, and its blue-red continuum endpoints bracket only 40 Å ($\sim$ 15 pixels). Ca4455 is not much wider, with its feature and continuum definitions covering 22.5 Å and 46.25 Å (8 and 17 pixels) respectively. As indicated by Tripicco & Bell (1995), both Ca4227 and Ca4455 are very sensitive to bandpass placement, in addition to Ca4227 being quite sensitive to spectral resolution. We also note that the H$\delta_{\rm A}$ and H$\delta_{\rm F}$ indices have non-negligible offsets between repeat measurements of 0.539 Å and 0.265 Å respectively (see also § 4.6.5).

Having obtained both the statistical error due to the S/N of our spectra, and a measure of our repeatability for each index, we may combine the two to yield a total error, $\sigma_{\rm T}$, which is then:

$$\sigma_{\rm T}^2 = \sigma_{\rm W}^2 + \sigma_{\rm I}^2 \tag{4.10}$$

It is interesting to compare the typical Poisson uncertainties in our data, with the fundamental limit of being able reproduce our fibre-based observations.

Table 4.6. Our Repeatability of each Lick/IDS index.

Index	Offset	$\sigma_{\rm rms}$	r
CN_1 (mag)	-0.0054	0.0136	0.917
CN_2 (mag)	-0.0142	0.0189	0.655
Ca4227 (Å)	-0.052	0.166	-0.081
G4300 (Å)	-0.036	0.613	0.882
Fe4383 (Å)	-0.018	0.381	0.722
Ca4455 (Å)	0.021	0.270	0.544
Fe4531 (Å)	0.052	0.190	0.957
$C_2$4668 (Å)	-0.214	0.578	0.666
Hβ (Å)	0.118	0.453	0.931
Fe5015 (Å)	-0.005	0.932	0.631
Mg_1 (mag)	-0.0006	0.0040	0.920
Mg_2 (mag)	-0.0087	0.0108	0.942
Mg b (Å)	-0.102	0.223	0.799
Fe5270 (Å)	-0.139	0.333	0.838
Fe5335 (Å)	0.036	0.317	0.660
Fe5406 (Å)	0.183	0.335	0.726
H$\delta_{\rm A}$ (Å)	0.539	0.986	0.858
H$\gamma_{\rm A}$ (Å)	-0.004	0.528	0.971
H$\delta_{\rm F}$ (Å)	0.265	0.822	0.830
H$\gamma_{\rm F}$ (Å)	0.048	0.510	0.942

For this purpose, we have selected the integrated spectra of three clusters which we have classified as high, medium and low S/N : NGC 1711 (S/N $\sim$ 340), NGC 1718 (S/N $\sim$ 90) and NGC 2031 (S/N $\sim$ 25). Using Equation (4.9) we calculate the Poisson error for three Lick/IDS indices (Hβ, Fe5270 and Mg_1) and compare them to their corresponding $\sigma_{\rm I}$ values. We show the results of this exercise in Table 4.7.

Perhaps unsurprisingly, for the highest S/N spectra, $\sigma_{\rm I}$ dominates the Poisson uncertainties of the line-indices. Indeed, for spectra with S/N $\geq$ 200, the $\sigma_{\rm W}$ term becomes negligible and our uncertainties are essentially dictated by our repeatability of the line-strength index. For the noisiest spectra (S/N $\sim$ 25), $\sigma_{\rm W} > \sigma_{\rm I}$, indicating that the $\sigma_{\rm W}$ term is the dominant contribution to the entire

Table 4.7. Comparison of errors derived from Poisson statistics and our repeatability.

Cluster	S/N	σ_W(Hβ)	σ_W(Fe5270)	σ_W(Mg$_1$)
NGC 1711	340	0.033 (Å)	0.046 (Å)	0.002 (mag)
NGC 1718	90	0.136 (Å)	0.166 (Å)	0.007 (mag)
NGC 2031	25	0.330(Å)	0.398 (Å)	0.017 (mag)
σ_I	–	0.142 (Å)	0.110 (Å)	0.001 (mag)

error budget. Using Equation (4.10) we may calculate the total uncertainty, σ_T in the indices. As an illustration; for the three clusters in Table 4.7, the total uncertainties in the Fe5270 index are : σ_T = 0.12 Å, 0.20 Å and 0.41 Å for NGC 1711, NGC 1718 and NGC 2031 respectively.

In Table 4.8 we show our measurements of 20 Lick/IDS indices for 64 LMC star clusters. For the 11 clusters which have two separate observations, we take the weighted mean of each index as our final index measurement. The uncertainties given in Table 4.8 are those derived purely from Poisson uncertainties.

Table 4.8.: Lick/IDS indices obtained for our sample of LMC clusters. Uncertainties calculated using Equation 4.9 are tabulated on alternate rows.

Cluster	CN_1	CN_2	Ca4227	G4300	Fe4383	Ca4455	Fe4531	C4668	Hβ	Fe5015	Mg_1	Mg_2	Mg b	Fe5270	Fe5335	Fe5406	Hδ_A	Hγ_A	Hδ_F	Hγ_F
–	(mag)	(mag)	(Å)	(Å)	(Å)	(Å)	(Å)	(Å)	(Å)	(Å)	(mag)	(mag)	(Å)	(Å)	(Å)	(Å)	(Å)	(Å)	(Å)	(Å)
BRHT 14b	-0.042	-0.035	0.011	-0.527	-0.267	0.070	-0.045	-0.017	1.239	0.293	-0.040	-0.042	0.300	0.141	0.097	-0.204	1.320	2.199	1.237	1.781
....	± 0.003	0.003	0.023	0.042	0.061	0.031	0.049	0.073	0.028	0.064	0.001	0.002	0.031	0.036	0.043	0.034	0.044	0.038	0.031	0.024
KMHK 1019	-0.174	-0.153	0.200	0.043	-1.188	1.390	0.253	4.647	5.566	3.436	-0.001	-0.004	-0.567	1.155	1.993	0.706	7.603	6.067	5.414	4.950
....	± 0.021	0.025	0.179	0.339	0.510	0.246	0.405	0.584	0.220	0.544	0.014	0.016	0.295	0.326	0.373	0.305	0.288	0.288	0.200	0.176
M-OB 4	-0.091	-0.077	0.142	-0.829	1.193	1.152	0.388	2.028	1.943	1.615	-0.015	0.016	0.699	0.621	1.041	0.345	3.073	2.305	2.380	2.230
....	± 0.008	0.009	0.066	0.122	0.166	0.083	0.131	0.192	0.073	0.164	0.004	0.005	0.080	0.090	0.104	0.082	0.127	0.106	0.089	0.067
f NGC 1711	-0.136	-0.107	0.061	-1.388	0.088	0.533	0.397	0.121	4.336	0.653	-0.026	-0.037	0.086	0.305	0.178	0.011	6.202	6.085	4.948	4.874
....	± 0.003	0.004	0.028	0.053	0.074	0.038	0.059	0.090	0.033	0.080	0.002	0.002	0.040	0.046	0.054	0.043	0.048	0.043	0.033	0.026
NGC 1718	-0.120	-0.098	-0.033	1.682	0.179	-0.133	0.566	0.617	3.205	1.638	-0.011	0.020	0.616	0.867	1.497	0.829	5.688	3.558	4.461	4.088
....	± 0.018	0.020	0.141	0.245	0.346	0.174	0.258	0.372	0.136	0.306	0.007	0.008	0.148	0.166	0.188	0.146	0.264	0.221	0.182	0.133
NGC 1735	-0.130	-0.107	0.283	-1.546	-0.263	0.369	0.157	0.345	4.112	0.385	-0.033	-0.031	0.214	0.024	-0.510	-0.039	5.024	5.314	3.985	4.323
....	± 0.007	0.008	0.059	0.116	0.161	0.082	0.129	0.196	0.071	0.175	0.004	0.005	0.086	0.101	0.121	0.093	0.104	0.094	0.072	0.058
NGC 1751	-0.121	-0.123	0.858	2.295	1.608	-0.045	1.165	2.883	5.062	3.590	-0.004	0.042	1.215	1.444	0.931	0.347	5.808	3.482	4.580	4.528
....	± 0.019	0.022	0.146	0.270	0.383	0.200	0.289	0.413	0.146	0.334	0.008	0.009	0.163	0.180	0.211	0.166	0.281	0.251	0.193	0.147
NGC 1754	-0.103	-0.100	0.387	1.084	0.133	0.216	0.825	-0.228	3.053	1.280	-0.021	-0.003	1.053	0.890	0.695	0.021	4.690	2.435	3.500	2.357
....	± 0.010	0.012	0.080	0.143	0.202	0.101	0.150	0.222	0.078	0.179	0.004	0.005	0.084	0.096	0.112	0.087	0.157	0.130	0.109	0.082
NGC 1755	-0.135	-0.103	0.141	-1.196	0.306	0.312	0.638	0.690	5.047	1.351	-0.029	-0.018	0.410	0.673	0.413	-0.074	6.679	6.148	5.093	5.062
....	± 0.003	0.004	0.026	0.049	0.068	0.035	0.054	0.081	0.029	0.071	0.002	0.002	0.035	0.041	0.048	0.038	0.043	0.040	0.029	0.024
NGC 1767	-0.103	-0.085	-0.059	-1.248	0.717	0.834	0.084	0.122	3.496	0.574	-0.034	-0.039	0.177	0.282	-0.174	-0.249	4.530	4.384	3.705	3.717
....	± 0.005	0.005	0.039	0.073	0.102	0.052	0.083	0.127	0.047	0.114	0.003	0.003	0.056	0.066	0.079	0.062	0.069	0.062	0.048	0.038
NGC 1774	-0.134	-0.093	0.092	-1.653	-0.309	0.233	0.520	-0.164	5.732	0.787	-0.040	-0.046	0.180	0.247	0.180	-0.348	6.777	6.867	5.412	5.458
....	± 0.006	0.007	0.048	0.093	0.129	0.066	0.103	0.158	0.055	0.141	0.003	0.004	0.070	0.082	0.097	0.077	0.080	0.073	0.054	0.044

continued from previous page

Cluster	CN_1 (mag)	CN_2 (mag)	Ca4227 (Å)	G4300 (Å)	Fe4383 (Å)	Ca4455 (Å)	Fe4531 (Å)	C4668 (Å)	Hβ (Å)	Fe5015 (Å)	Mg_1 (mag)	Mg_2 (mag)	Mg *b* (Å)	Fe5270 (Å)	Fe5335 (Å)	Fe5406 (Å)	Hδ_A (Å)	Hγ_A (Å)	Hδ_F (Å)	Hγ_F (Å)
NGC 1782	-0.108	-0.078	-0.131	-1.385	0.111	0.080	0.279	0.199	4.474	0.843	-0.026	-0.032	0.181	0.231	0.185	-0.285	5.131	5.431	4.392	4.669
....	± 0.005	0.006	0.041	0.077	0.108	0.056	0.087	0.133	0.048	0.119	0.003	0.003	0.059	0.068	0.081	0.064	0.069	0.063	0.047	0.038
NGC 1786	-0.073	-0.058	0.264	1.616	0.423	0.243	0.843	0.057	2.735	0.904	-0.023	-0.008	0.532	0.509	0.564	-0.129	3.401	1.704	2.576	2.154
....	± 0.005	0.006	0.045	0.078	0.112	0.056	0.085	0.125	0.045	0.102	0.002	0.003	0.048	0.054	0.063	0.049	0.081	0.073	0.057	0.046
NGC 1801	-0.167	-0.138	-0.063	-2.385	-0.977	-0.019	0.275	0.138	5.634	0.931	-0.026	-0.026	0.090	0.340	0.099	-0.685	8.594	8.607	6.072	6.126
....	± 0.008	0.010	0.070	0.139	0.191	0.096	0.148	0.227	0.081	0.203	0.005	0.006	0.101	0.117	0.139	0.111	0.113	0.104	0.078	0.063
NGC 1806	-0.078	-0.052	0.132	1.119	0.272	0.566	1.775	1.584	3.170	2.810	0.011	0.042	0.868	1.669	0.733	0.846	4.722	3.784	3.282	3.24
....	± 0.010	0.012	0.084	0.148	0.208	0.103	0.151	0.225	0.084	0.187	0.004	0.005	0.092	0.101	0.119	0.091	0.154	0.131	0.109	0.082
NGC 1815	-0.142	-0.122	-0.162	-1.531	-0.111	0.189	0.157	1.965	3.426	0.104	-0.034	-0.043	0.241	0.169	0.033	-0.361	6.483	5.474	4.459	4.507
....	± 0.011	0.013	0.094	0.178	0.253	0.131	0.204	0.308	0.119	0.290	0.007	0.008	0.143	0.168	0.200	0.159	0.151	0.146	0.106	0.089
NGC 1825	-0.109	-0.081	-0.088	0.388	-0.179	0.125	1.651	0.484	2.687	3.763	0.002	0.021	1.423	1.344	0.416	0.348	3.838	3.337	2.587	2.731
....	± 0.014	0.016	0.114	0.201	0.288	0.145	0.213	0.324	0.123	0.271	0.007	0.008	0.134	0.154	0.183	0.142	0.214	0.178	0.152	0.112
NGC 1830	-0.186	-0.152	0.300	-1.976	-1.463	-0.803	1.292	1.119	4.893	1.245	-0.041	-0.008	0.592	0.653	0.311	-0.385	7.672	7.263	5.080	5.233
....	± 0.020	0.024	0.162	0.322	0.435	0.220	0.313	0.474	0.170	0.407	0.009	0.011	0.196	0.222	0.264	0.208	0.286	0.245	0.205	0.152
NGC 1834	-0.086	-0.070	-0.109	-1.291	-0.718	0.703	-0.121	1.664	2.672	1.519	-0.028	-0.007	0.216	0.966	0.816	0.567	3.198	5.217	2.426	3.584
....	± 0.014	0.016	0.115	0.212	0.290	0.141	0.221	0.317	0.120	0.273	0.006	0.008	0.136	0.154	0.181	0.139	0.218	0.171	0.153	0.108
NGC 1835	-0.085	-0.065	0.103	1.597	0.462	0.126	0.920	0.563	2.711	1.725	-0.016	0.004	0.759	0.688	0.425	-0.099	3.542	1.598	2.719	2.288
....	± 0.009	0.011	0.078	0.135	0.190	0.096	0.142	0.207	0.075	0.167	0.004	0.005	0.079	0.090	0.105	0.080	0.146	0.125	0.102	0.078
NGC 1846	-0.155	-0.129	0.580	0.817	0.486	0.170	2.098	0.535	3.612	1.946	-0.015	0.030	1.017	0.586	0.771	0.255	5.791	3.693	4.150	3.269
....	± 0.013	0.015	0.104	0.191	0.256	0.127	0.180	0.272	0.097	0.222	0.005	0.006	0.107	0.123	0.141	0.110	0.206	0.165	0.145	0.102
NGC 1852	-0.101	-0.080	0.469	0.968	-0.080	-0.027	1.386	1.001	3.663	2.630	-0.007	0.028	0.976	1.394	0.777	0.260	5.783	3.522	4.127	3.287
....	± 0.012	0.014	0.100	0.185	0.262	0.132	0.193	0.289	0.106	0.241	0.006	0.007	0.118	0.133	0.156	0.121	0.176	0.164	0.123	0.102

continued from previous page

Cluster	CN_1 (mag)	CN_2 (mag)	Ca4227 (Å)	G4300 (Å)	Fe4383 (Å)	Ca4455 (Å)	Fe4531 (Å)	C4668 (Å)	Hβ (Å)	Fe5015 (Å)	Mg_1 (mag)	Mg_2 (mag)	Mg b (Å)	Fe5270 (Å)	Fe5335 (Å)	Fe5406 (Å)	Hδ_A (Å)	Hγ_A (Å)	Hδ_F (Å)	Hγ_F (Å)
NGC 1856	-0.184	-0.140	0.238	-1.512	0.019	0.034	0.822	0.840	6.016	1.762	-0.018	0.004	0.828	0.680	0.811	0.229	9.146	8.303	6.594	6.453
....	± 0.006	0.007	0.048	0.094	0.127	0.065	0.098	0.147	0.051	0.125	0.003	0.003	0.061	0.070	0.081	0.063	0.077	0.072	0.053	0.043
NGC 1863	-0.156	-0.129	0.128	-1.885	-0.619	0.432	-0.093	-0.347	5.279	0.328	-0.031	-0.028	0.094	-0.157	0.095	-0.108	7.090	7.098	5.209	5.323
....	± 0.007	0.008	0.057	0.113	0.160	0.082	0.130	0.202	0.073	0.187	0.004	0.005	0.094	0.111	0.131	0.103	0.092	0.089	0.063	0.055
NGC 1865	-0.203	-0.185	0.266	-0.538	-0.206	0.001	0.895	0.154	5.446	1.038	-0.008	0.024	1.167	0.541	0.582	-0.504	9.919	7.288	6.211	5.757
....	± 0.014	0.017	0.119	0.228	0.321	0.163	0.241	0.367	0.130	0.323	0.008	0.009	0.156	0.183	0.212	0.168	0.188	0.184	0.134	0.111
NGC 1872	-0.180	-0.150	-0.045	-1.750	-0.412	0.192	0.519	0.191	5.209	-0.061	-0.030	-0.005	0.823	0.539	-0.123	-0.126	8.966	8.406	6.171	5.976
....	± 0.013	0.015	0.109	0.212	0.287	0.144	0.220	0.333	0.119	0.297	0.007	0.008	0.143	0.166	0.199	0.157	0.177	0.161	0.124	0.099
NGC 1878	-0.197	-0.152	0.181	-1.086	-1.052	-0.063	1.661	0.373	5.764	1.565	-0.021	0.002	0.637	0.547	0.861	0.275	10.50	8.414	7.218	6.233
....	± 0.009	0.010	0.071	0.137	0.186	0.093	0.135	0.205	0.070	0.172	0.004	0.005	0.083	0.094	0.109	0.085	0.114	0.104	0.079	0.063
NGC 1898	-0.053	-0.028	0.346	2.569	0.674	1.152	1.510	1.383	2.131	1.389	0.005	0.025	1.351	0.867	1.589	0.492	0.548	0.166	2.530	2.03
....	± 0.021	0.024	0.168	0.289	0.422	0.204	0.311	0.444	0.161	0.352	0.008	0.009	0.161	0.181	0.205	0.16	0.338	0.286	0.220	0.174
NGC 1916	-0.096	-0.090	-0.104	0.824	0.512	0.034	1.160	0.799	2.184	1.269	-0.024	-0.014	0.432	0.575	0.373	-0.163	4.361	2.802	3.039	2.685
....	± 0.010	0.011	0.083	0.146	0.207	0.105	0.156	0.231	0.086	0.190	0.004	0.005	0.091	0.102	0.120	0.093	0.144	0.132	0.102	0.082
NGC 1939	-0.098	-0.087	0.257	1.244	-0.655	-0.174	0.089	-0.106	3.093	1.044	-0.018	-0.007	0.638	0.490	0.517	0.349	4.199	3.244	3.011	2.97
....	± 0.012	0.014	0.100	0.178	0.259	0.131	0.196	0.288	0.104	0.239	0.006	0.006	0.114	0.130	0.151	0.115	0.180	0.160	0.127	0.100
NGC 1940	-0.126	-0.092	0.224	-0.943	0.683	0.526	1.107	1.107	4.863	2.490	-0.010	0.026	0.787	1.038	1.114	0.323	7.049	6.017	5.187	5.106
....	± 0.005	0.006	0.045	0.086	0.118	0.060	0.092	0.139	0.050	0.120	0.003	0.003	0.060	0.068	0.078	0.062	0.073	0.070	0.051	0.042
NGC 1943	-0.072	-0.085	0.481	-1.555	-1.230	-0.405	0.427	1.681	2.009	0.354	0.017	0.032	0.700	0.134	0.645	-0.178	1.444	3.899	0.855	2.561
....	± 0.014	0.016	0.110	0.217	0.306	0.157	0.231	0.346	0.137	0.317	0.008	0.009	0.156	0.181	0.208	0.165	0.221	0.180	0.157	0.115
NGC 1951	-0.091	-0.072	-0.051	-1.364	0.207	0.509	0.095	0.144	3.406	0.661	-0.031	-0.047	0.040	0.274	0.081	-0.353	4.116	4.254	3.545	3.511
....	± 0.004	0.004	0.030	0.056	0.078	0.039	0.062	0.094	0.035	0.083	0.002	0.002	0.041	0.048	0.057	0.045	0.053	0.047	0.036	0.029

continued from previous page

Cluster	CN_1 (mag)	CN_2 (mag)	Ca4227 (Å)	G4300 (Å)	Fe4383 (Å)	Ca4455 (Å)	Fe4531 (Å)	C4668 (Å)	Hβ (Å)	Fe5015 (Å)	Mg_1 (mag)	Mg_2 (mag)	Mg b (Å)	Fe5270 (Å)	Fe5335 (Å)	Fe5406 (Å)	Hδ_A (Å)	Hγ_A (Å)	Hδ_F (Å)	Hγ_F (Å)
NGC 1967	-0.144	-0.131	0.455	-2.440	0.179	0.626	0.413	-0.838	3.990	1.188	-0.03	-0.042	0.145	0.437	0.740	-0.244	6.027	5.533	4.738	4.065
....	± 0.013	0.015	0.105	0.212	0.284	0.144	0.226	0.350	0.127	0.305	0.007	0.008	0.151	0.174	0.205	0.163	0.184	0.167	0.125	0.104
NGC 1978	-0.085	-0.081	0.520	2.681	1.396	0.402	2.565	3.397	3.128	3.180	0.029	0.071	1.338	1.582	1.209	0.223	3.013	0.992	2.266	1.938
....	± 0.011	0.013	0.088	0.152	0.210	0.105	0.148	0.215	0.079	0.173	0.004	0.005	0.084	0.092	0.107	0.084	0.180	0.145	0.127	0.090
NGC 1987	-0.183	-0.165	0.122	0.086	0.685	0.194	1.654	2.224	3.851	2.869	-0.017	0.051	1.575	1.151	0.630	0.272	8.046	5.882	5.153	4.603
....	± 0.011	0.013	0.092	0.173	0.233	0.119	0.175	0.260	0.097	0.217	0.005	0.006	0.106	0.122	0.143	0.111	0.155	0.143	0.111	0.088
NGC 2002	-0.104	-0.093	0.073	-1.128	0.173	0.847	0.169	1.166	3.072	1.031	-0.023	-0.011	0.496	0.281	0.250	-0.004	4.503	4.457	3.488	3.592
....	± 0.004	0.005	0.038	0.072	0.103	0.052	0.084	0.127	0.049	0.116	0.003	0.003	0.058	0.068	0.080	0.062	0.065	0.061	0.045	0.038
NGC 2004	-0.081	-0.058	0.225	-0.843	0.746	0.877	0.930	2.369	3.076	3.194	0.004	0.082	1.603	1.517	1.487	0.613	4.002	3.602	3.267	3.299
....	± 0.004	0.005	0.036	0.069	0.097	0.049	0.077	0.116	0.044	0.102	0.002	0.003	0.050	0.056	0.064	0.051	0.062	0.059	0.043	0.036
NGC 2005	-0.092	-0.058	0.233	0.869	1.143	0.369	0.927	-1.503	3.167	1.344	-0.027	-0.005	0.743	0.613	0.797	-0.093	4.133	2.483	3.146	2.711
....	± 0.016	0.019	0.137	0.248	0.344	0.176	0.266	0.411	0.143	0.329	0.008	0.009	0.156	0.178	0.206	0.163	0.240	0.225	0.168	0.139
NGC 2019	-0.082	-0.060	0.462	0.827	0.157	0.028	1.560	1.053	2.471	1.199	-0.028	0.005	0.601	0.985	0.400	0.336	2.825	2.494	2.425	2.207
....	± 0.014	0.016	0.111	0.200	0.283	0.143	0.210	0.316	0.116	0.262	0.006	0.007	0.125	0.140	0.166	0.128	0.210	0.181	0.145	0.114
NGC 2031	-0.145	-0.119	0.206	-1.121	-0.382	0.241	0.072	0.158	4.910	0.502	-0.032	-0.035	0.288	0.271	0.360	-0.734	6.576	6.050	4.885	4.825
....	± 0.007	0.009	0.059	0.115	0.163	0.083	0.130	0.199	0.072	0.181	0.004	0.005	0.090	0.105	0.125	0.102	0.105	0.093	0.072	0.057
NGC 2038	-0.119	-0.089	0.334	-0.216	-0.087	0.323	1.350	1.446	4.413	1.865	-0.012	0.008	0.629	1.136	1.005	0.229	5.766	4.990	4.144	4.269
....	± 0.008	0.010	0.067	0.126	0.177	0.090	0.134	0.202	0.074	0.176	0.004	0.005	0.087	0.099	0.116	0.092	0.120	0.106	0.084	0.065
NGC 2041	-0.139	-0.113	0.127	-1.016	0.527	0.219	1.024	0.857	4.785	1.833	-0.015	0.003	0.385	0.894	1.008	0.208	6.795	5.880	5.052	4.825
....	± 0.004	0.005	0.033	0.062	0.084	0.043	0.065	0.098	0.035	0.085	0.002	0.002	0.043	0.048	0.056	0.044	0.058	0.050	0.040	0.030
NGC 2051	-0.141	-0.101	-0.003	-1.229	-0.056	0.093	1.163	0.555	5.410	1.445	-0.022	-0.004	0.517	0.819	0.459	0.004	7.815	7.138	5.596	5.802
....	± 0.006	0.007	0.049	0.093	0.127	0.065	0.098	0.149	0.052	0.128	0.003	0.004	0.063	0.072	0.085	0.066	0.079	0.073	0.055	0.044

continued from previous page

Cluster	CN_1 (mag)	CN_2 (mag)	Ca4227 (Å)	G4300 (Å)	Fe4383 (Å)	Ca4455 (Å)	Fe4531 (Å)	C4668 (Å)	Hβ (Å)	Fe5015 (Å)	Mg_1 (mag)	Mg_2 (mag)	Mg *b* (Å)	Fe5270 (Å)	Fe5335 (Å)	Fe5406 (Å)	Hδ_A (Å)	Hγ_A (Å)	Hδ_F (Å)	Hγ_F (Å)
NGC 2056	-0.176	-0.149	0.056	-1.715	-0.391	0.202	0.492	0.435	5.840	1.191	-0.031	-0.023	0.699	0.567	0.673	-0.321	8.487	7.692	6.094	5.738
....	± 0.007	0.008	0.058	0.113	0.153	0.078	0.119	0.180	0.063	0.158	0.004	0.004	0.077	0.090	0.106	0.085	0.100	0.087	0.069	0.053
NGC 2065	-0.121	-0.091	0.258	-0.733	-0.408	0.266	1.101	1.000	4.191	1.602	-0.041	-0.023	0.223	0.300	0.685	0.352	5.498	5.465	4.28	4.325
....	± 0.011	0.013	0.088	0.167	0.233	0.117	0.177	0.265	0.097	0.229	0.005	0.006	0.114	0.131	0.152	0.119	0.162	0.137	0.112	0.085
NGC 2100	-0.076	-0.071	0.074	-0.711	0.825	0.511	0.323	0.348	1.668	0.061	-0.039	-0.044	0.222	-0.163	0.142	-0.481	3.011	2.909	2.472	2.464
....	± 0.007	0.008	0.060	0.109	0.151	0.077	0.120	0.181	0.069	0.158	0.004	0.004	0.076	0.089	0.105	0.084	0.113	0.095	0.079	0.060
NGC 2102	-0.124	-0.101	0.078	-0.816	0.260	0.380	0.224	-0.675	4.857	0.511	-0.081	-0.073	-0.707	1.084	1.223	1.005	5.600	5.369	4.155	4.203
....	± 0.019	0.023	0.160	0.305	0.427	0.218	0.346	0.526	0.188	0.469	0.011	0.013	0.237	0.265	0.317	0.244	0.281	0.254	0.195	0.157
NGC 2107	-0.179	-0.154	0.292	-1.405	-0.367	0.175	1.103	-0.699	5.589	0.843	-0.018	-0.006	0.467	0.815	0.756	-0.152	9.215	7.779	6.500	5.935
....	± 0.009	0.010	0.069	0.136	0.183	0.092	0.136	0.211	0.072	0.177	0.004	0.005	0.086	0.098	0.115	0.091	0.120	0.104	0.083	0.063
NGC 2108	-0.143	-0.131	0.890	1.174	-0.391	-0.382	2.961	1.365	3.768	1.401	0.000	0.038	0.785	1.409	2.230	0.566	6.572	6.638	4.468	5.038
....	± 0.018	0.020	0.131	0.248	0.341	0.170	0.232	0.348	0.125	0.281	0.007	0.008	0.134	0.147	0.165	0.131	0.270	0.205	0.191	0.126
NGC 2127	-0.128	-0.098	-0.030	-0.926	-0.108	0.330	1.006	1.163	4.872	2.212	-0.008	0.007	0.345	0.972	0.810	0.586	7.047	6.198	5.106	4.940
....	± 0.006	0.007	0.049	0.092	0.127	0.064	0.097	0.145	0.052	0.124	0.003	0.003	0.062	0.069	0.081	0.062	0.081	0.074	0.056	0.045
NGC 2134	-0.191	-0.147	0.149	-1.669	-0.209	0.218	0.430	0.265	6.459	1.184	-0.023	-0.006	0.691	0.491	0.674	0.026	8.929	8.285	6.371	6.237
....	± 0.006	0.007	0.050	0.098	0.135	0.068	0.105	0.159	0.054	0.138	0.003	0.004	0.068	0.078	0.091	0.072	0.083	0.075	0.057	0.046
NGC 2135	-0.137	-0.106	0.213	-2.290	-0.250	0.038	-0.145	-0.760	5.58	-0.294	-0.022	-0.030	0.063	0.219	0.396	-0.485	7.262	7.659	5.222	5.814
....	± 0.009	0.010	0.072	0.145	0.198	0.102	0.160	0.245	0.087	0.225	0.005	0.006	0.111	0.130	0.153	0.122	0.120	0.111	0.083	0.067
NGC 2136	-0.135	-0.113	0.038	-1.323	-0.572	0.269	0.718	0.719	4.496	1.830	-0.012	-0.004	0.282	0.657	0.661	0.275	6.512	6.330	4.704	4.616
....	± 0.005	0.006	0.043	0.081	0.113	0.057	0.086	0.130	0.047	0.113	0 .003	0.003	0.056	0.064	0.075	0.058	0.074	0.065	0.051	0.040
Rob 1	-0.147	-0.107	0.023	-1.205	0.096	0.004	1.248	-1.086	6.394	-0.035	-0.038	-0.029	0.588	0.089	0.283	-0.100	7.263	6.743	5.246	5.234
....	± 0.010	0.011	0.080	0.154	0.212	0.110	0.166	0.260	0.087	0.228	0.005	0.006	0.109	0.129	0.152	0.119	0.130	0.123	0.091	0.075

continued from previous page

Cluster	CN_1 (mag)	CN_2 (mag)	Ca4227 (Å)	G4300 (Å)	Fe4383 (Å)	Ca4455 (Å)	Fe4531 (Å)	C4668 (Å)	Hβ (Å)	Fe5015 (Å)	Mg_1 (mag)	Mg_2 (mag)	Mg *b* (Å)	Fe5270 (Å)	Fe5335 (Å)	Fe5406 (Å)	Hδ_A (Å)	Hγ_A (Å)	Hδ_F (Å)	Hγ_F (Å)
SL 106	-0.117	-0.091	-0.016	-1.500	-0.272	0.691	0.220	0.151	3.463	0.699	-0.029	-0.040	0.005	0.287	0.094	-0.333	5.535	5.697	4.279	4.372
....	± 0.009	0.011	0.076	0.147	0.208	0.105	0.167	0.257	0.096	0.231	0.005	0.006	0.115	0.132	0.158	0.126	0.129	0.120	0.089	0.074
SL 230	-0.095	-0.087	-0.025	-1.612	0.639	0.116	0.685	2.498	3.898	2.103	-0.006	0.024	0.889	0.683	0.361	0.651	5.379	5.327	4.266	4.793
....	± 0.013	0.015	0.106	0.199	0.266	0.138	0.207	0.300	0.112	0.266	0.006	0.008	0.132	0.153	0.179	0.138	0.197	0.160	0.135	0.096
SL 250	-0.127	-0.092	0.206	-0.530	-1.330	-0.111	1.088	0.705	4.163	2.722	-0.022	0.015	0.692	1.052	0.482	-0.118	7.398	6.592	5.058	4.586
....	± 0.011	0.013	0.088	0.167	0.238	0.118	0.173	0.260	0.097	0.223	0.005	0.006	0.112	0.127	0.151	0.118	0.152	0.135	0.107	0.085
SL 360	-0.075	-0.080	-0.286	-1.658	-0.662	0.307	0.080	0.917	2.468	2.300	-0.026	-0.049	0.457	1.169	0.197	0.326	0.776	3.877	1.130	2.187
....	± 0.020	0.024	0.173	0.320	0.456	0.228	0.359	0.537	0.204	0.471	0.011	0.013	0.233	0.269	0.327	0.254	0.320	0.269	0.220	0.175
SL 586	-0.093	-0.079	-0.056	-0.986	0.115	0.599	0.088	0.924	2.645	0.638	-0.035	-0.050	-0.011	-0.061	-0.171	-0.625	3.578	3.218	2.926	2.719
....	± 0.003	0.003	0.024	0.044	0.063	0.032	0.051	0.077	0.029	0.070	0.002	0.002	0.035	0.041	0.049	0.040	0.045	0.038	0.031	0.024
SL 601	-0.101	-0.092	-0.105	-0.909	0.029	0.784	0.487	1.385	1.881	1.143	-0.023	-0.011	0.261	0.556	0.272	-0.166	3.061	2.473	2.055	1.767
....	± 0.011	0.014	0.098	0.184	0.264	0.135	0.213	0.324	0.127	0.291	0.007	0.008	0.143	0.163	0.194	0.153	0.173	0.162	0.122	0.103
SL 675	-0.094	-0.067	0.347	-0.923	1.212	0.844	0.507	1.922	4.147	2.799	0.010	0.037	0.906	0.938	1.328	0.855	5.505	4.391	4.089	3.83
....	± 0.007	0.008	0.057	0.109	0.149	0.076	0.119	0.176	0.064	0.151	0.004	0.004	0.075	0.085	0.097	0.076	0.103	0.092	0.072	0.057
SL 709	-0.114	-0.088	0.260	-0.234	1.887	0.302	1.070	-0.572	5.221	1.388	-0.039	-0.025	0.513	0.622	0.637	-0.205	5.377	4.803	4.240	4.840
....	± 0.004	0.005	0.033	0.061	0.082	0.043	0.066	0.100	0.034	0.084	0.002	0.002	0.041	0.048	0.056	0.044	0.058	0.052	0.040	0.031
SL 741	-0.221	-0.205	-0.181	-1.048	2.169	0.514	-0.070	1.384	5.335	1.404	-0.077	-0.051	0.274	-0.695	-0.957	-0.881	8.687	6.893	5.134	6.330
....	± 0.019	0.022	0.150	0.279	0.363	0.191	0.301	0.445	0.163	0.393	0.009	0.011	0.195	0.233	0.281	0.223	0.270	0.223	0.197	0.131

Measurements of Lick/IDS indices for clusters in common with our sample are scarce, however de Freitas Pacheco, Barbuy, & Idiart (1998) measure Lick/IDS indices for one common cluster, NGC 1978. These authors obtain Hβ = 3.01 $\pm$ 0.2 Å, Fe5270 = 1.81 $\pm$ 0.23 Å, Fe5335 = 1.44 $\pm$ 0.34 Å and Mg_2 = 0.109 $\pm$ 0.006 mag, after correcting to the Lick/IDS system. For this cluster, after applying our Lick/IDS offsets (see next section) we obtain: Hβ=3.18 $\pm$ 0.16 Å, Fe5270=1.77 $\pm$ 0.14 Å, Fe5335=1.54 $\pm$ 0.15 Å and Mg_2=0.151 $\pm$ 0.006 mag. With the exception of Mg_2 all these indices are in good agreement. The difference of 0.04 mag in Mg_2 probably arises from continuum slope differences (the data of de Freitas Pacheco, Barbuy, & Idiart was flux- calibrated).

4.5.4 Correcting to the Lick/IDS System

In order to use the SSP models based upon the fitting-functions of Worthey (1994) our spectra must be placed onto the Lick/IDS system. Whilst there is no 'text book' upon how this should be done, there are several examples in the literature on how this may be typically achieved (Worthey & Ottaviani 1997; Kuntschner 1998). We follow the basic methodology described by Kuntschner (1998).

The first correction to be applied to our data is a resolution broadening correction. The IDS resolution changes as a function of wavelength. Worthey & Ottaviani (1997) showed that the FWHM of the IDS varies from $\sim$ 11.5 Å in the blue ($\sim$ 4000 Å), reaches a minimum at 4900 Å of 8.4 Å, and then degrades again to $\sim$ 9.8 Å at 6000 Å. As discussed in § 4.2.4, our spectra have a resolution of $\sim$ 6.5 Å, which is constant with wavelength. To reproduce the resolution characteristics of the IDS, we convolved our spectra with a Gaussian kernel (see Equation 3.4 in Chapter 3), with a width which varies as a function of wavelength. Due to the λ^2 dependence of the width of the kernel, we were particularly careful to obtain an accurate value for the resolution of our data. As a simple consistency check, we ran the Gaussian convolution programme upon our arc-lines and measured the widths of the resulting profiles. These were found to be in excellent agreement with the wavelengths given in table 4 of Worthey & Ottaviani (1997).

Having removed the instrumental response from our spectra, and broadened them to the IDS resolution, only small, systematic offsets should remain between our spectra and that of 'identical' IDS spectra. Perhaps the best method of determining and removing these shifts is through observations of many stars which have been observed by the Lick group. Comparing index measurements for a number of common stars should reveal any systematic offsets, which may then be applied to our data. For this purpose, we have obtained spectra of 11 Lick standard stars

(see § 4.2.4 and Table 4.4). We measured the Lick/IDS indices for these stars, and compare them to the index values in the Lick stellar library. In Figure 4.16, we compare our measurements to those of the Lick/IDS *after* removal of the the mean offset between the systems. A number of measurements were clearly several standard deviations away from the mean values of the offsets. In this situation, one is faced with the dilemma of either leaving the measurement in, at the risk of undue weight being applied to this single point, or removing the point which is, perhaps, a somewhat questionable procedure. In consideration of this, we have applied an iterative 3-sigma clipping algorithm to the measured indices. Points three standard deviations away from the mean were removed, and the mean was recalculated. This process was reiterated until no more points were removed. In any event, for any single index, no more than one star was removed.

We take the uncertainty in the offsets to be $\sigma_s/\sqrt{n-1}$, where σ_s is the mean standard deviation of the stars with respect to their offsets, and n is the number of stars considered. We list the systematic offsets with respect to the Lick/IDS system, and uncertainties in this offset for each index in Table 4.9.

We compare our offsets with those derived by Kuntschner & Davies (1998), from observations at the 3.9-metre Anglo-Australian Telescope (AAT) from 13 Lick stars, and those obtained using the Michigan-Dartmouth-MIT (MDM) telescope (Worthey & Ottaviani 1997) (10 Lick stars). In general, the offsets in the indices obtained from our data are similar to those given by Kuntschner & Davies (1998) and Worthey & Ottaviani (1997). The widest bands (e.g. CN_1, CN_2, Mg_1 and Mg_2), which we expected to be most affected by continuum differences, show offsets of comparable magnitude to the MDM data, though the offsets for Mg_1 and Mg_2 are substantially larger than those of Kuntschner & Davies (1998). Whilst there is no *a priori* reason to expect similar offsets (since each observing system has its own peculiar characteristics), the comparisons are nevertheless reassuring. The Fe5015, Ca4227 and Ca4455 indices again show themselves to be problematical, with offsets of 0.8 Å, 0.5 Å and 0.6 Å respectively. Fe5015 and Ca4227 also show large residual scatter of 0.32 Å and 0.17 Å respectively. Due to these large offsets from the standard stars, and our inability to reproduce these indices accurately (see § 4.5.3) we have chosen to exclude Fe5015, Ca4227 and Ca4455 from further analysis. The Mg b feature also shows a substantial offset ($\sim$ 0.6 Å), although the reason for this was not immediately apparent.

It is perhaps this part of the calibration onto the Lick/IDS system which carries with it the largest uncertainty. In principle, the stars observed should have the same or similar metallicity range and spectral type as the target objects being corrected. Line-blanketing in stellar spectra

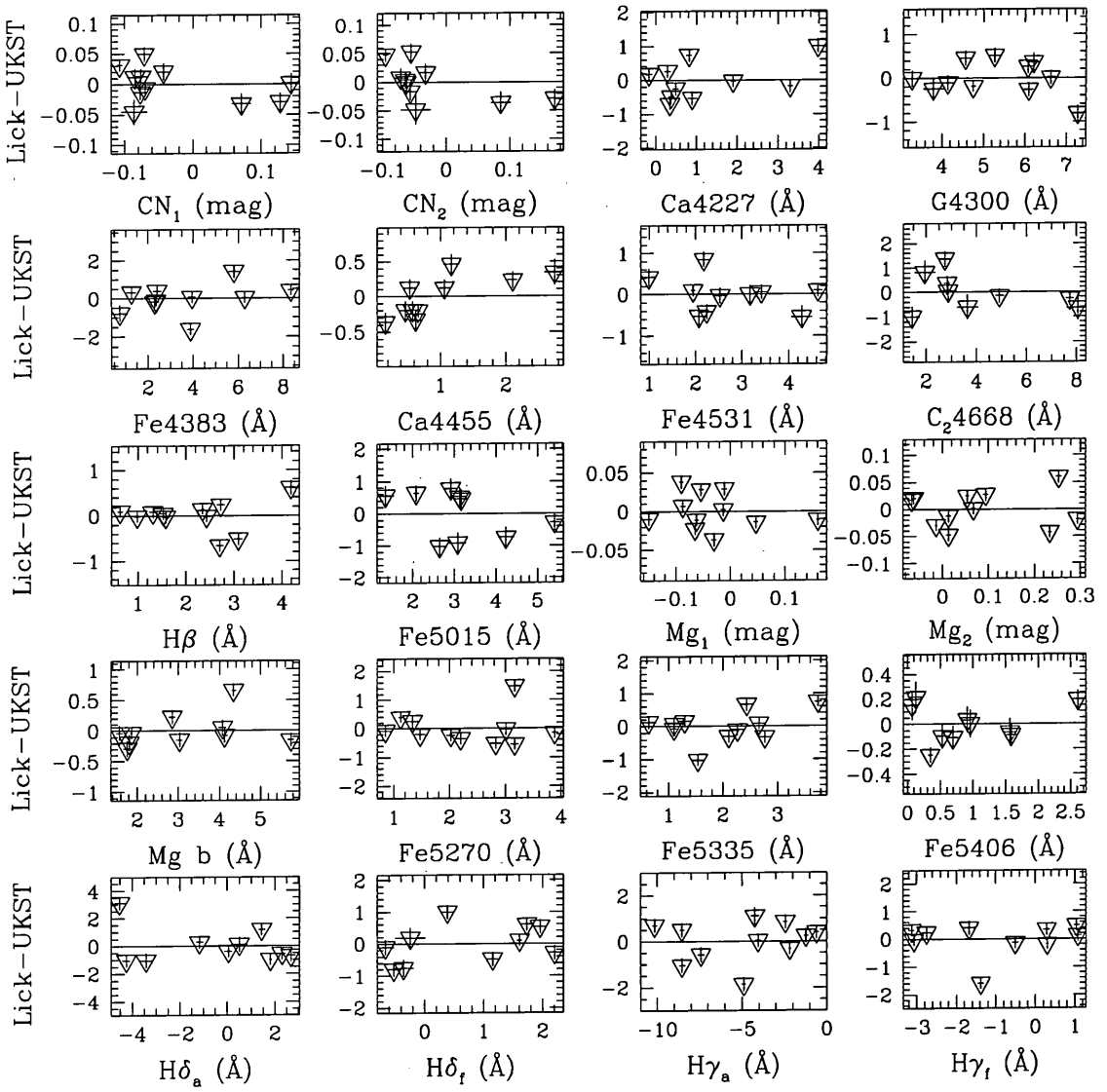

Figure 4.16: Comparison between FLAIR and Lick/IDS for 20 indices measured for eleven LICK/IDS standard stars, *after* removal of the systematic offset.

has the effect of suppressing the true continuum which, in turn, affects the measurement of line-indices. As indicated in the introduction to this Chapter, the majority of star clusters observed in the LMC have sub-solar metallicities. Well-determined metallicities range from [Fe/H] = -0.12 (NGC 1850A; Jasniewicz & Thevenin 1994), to M 92-type values of [Fe/H] = -2.3 (NGC 1841; Walker 1990). We have obtained spectra for Lick/IDS standards in the metallicity range -0.85 $\leq$ Fe/H $\leq$ 0.02, and therefore have only partially covered the metallicity range of the LMC star clusters. This unfortunate situation has arisen for three principle reasons:

Table 4.9. Systematic offsets in indices between Lick/IDS and [1]UKST (this work), [2]AAT (Kuntschner & Davies 1998), [3]MDM (Worthey & Ottaviani 1997). Where available, formal uncertainties in the offsets are given.

Index	Lick-UKST [1]	Lick-AAT [2]	Lick-MDM[3]
CN_1 (mag)	+0.004 ± 0.004	.....	-0.007
CN_2 (mag)	+0.019 ± 0.005	.....	-0.002
Ca4227 (Å)	+0.47 ± 0.17	.....	-0.16
G4300 (Å)	+0.06 ± 0.19	+0.21 ± 0.09	-0.09
Fe4383 (Å)	+0.36 ± 0.12	+0.60 ± 0.13	+0.01
Ca4455 (Å)	+0.62 ± 0.10	+0.37 ± 0.06	+0.22
Fe4531 (Å)	+0.40 ± 0.06	+0.00 ± 0.10	+0.15
$C_2$4668 (Å)	-0.10 ± 0.18	-0.19 ± 0.17	-0.13
Hβ (Å)	+0.05 ± 0.14	-0.05 ± 0.04	-0.01
Fe5015 (Å)	+0.81 ± 0.32	+0.00 ± 0.08	+0.26
Mg_1 (mag)	+0.04 ± 0.001	+0.003 ± 0.002	+0.043
Mg_2 (mag)	+0.08 ± 0.003	+0.023 ± 0.003	+0.049
Mg b (Å)	+0.60 ± 0.07	+0.15 ± 0.09	+0.01
Fe5270 (Å)	+0.19 ± 0.11	+0.07 ± 0.05	-0.01
Fe5335 (Å)	+0.33 ± 0.10	+0.00 ± 0.08	-0.05
Fe5406 (Å)	+0.35 ± 0.11	+0.00 ± 0.04	-0.04
Hδ_A (Å)	-0.48 ± 0.31 Å	.....	-0.41
Hγ_A (Å)	-0.24 ± 0.17 Å	+0.45 ± 0.28	-0.18
Hδ_F (Å)	-0.30 ± 0.26 Å	.....	-0.41
Hγ_F (Å)	-0.05 ± 0.16 Å	+0.00 ± 0.14	+0.03

- The majority of stars in the solar neighbourhood have solar abundances (e.g. Edvardsson et al. 1993), and this equally applies to the majority of Lick standard stars.
- The majority of Lick stars are northern hemisphere objects, the UKST is a southern hemisphere telescope.
- We were unable to observe our full set of programme stars, due to problems at the telescope.

However, as we shall see in the next section, the offsets given in Table 4.9 are to first order at least, generally correct.

4.6 Testing the SSP Models

In this section, we investigate the age and metallicity predictions of stellar population models for the LMC star clusters.

First, we discuss the SSP models we have chosen to use in deriving ages and metallicities from our integrated spectra. We then look at our ability to calibrate our data onto the model (Lick/IDS) system, and the effects of emission within our sample. Finally we obtain ages and metallicities for our sample of clusters and compare these predictions with those in the literature, which are derived from colour-magnitude diagrams and/or spectroscopy of giant stars.

4.6.1 Stellar Population Models

The synthesis of integrated spectral indices may be approached in several different ways. One technique is to adopt an entirely theoretical approach, whereby the total light contribution of each stellar evolutionary stage, and the behaviour of the spectral indices (as a function of temperature, surface gravity and metallicity), are calculated from physical theory (e.g. Tantalo et al. 1996). The former is derived from theoretical isochrones, the latter from spectral synthesis and stellar atmosphere models. This method is advantageous in that it is free from observational constraints (such as the lack of metal-poor stars in the solar neighbourhood), but is hampered both by its *lack* of observational constraints and modelling uncertainties. An opposite approach is to create models in an entirely empirical manner. Instead of theoretical isochrones, flux contributions are derived from observed CMDs, instead of spectral synthesis and stellar atmosphere models, the behaviour of the spectral indices are characterized using fitting-functions to real spectra (e.g. Idiart & Pacheco 1995). This circumvents uncertainties in the input physics, but is necessarily dependent upon what can be locally observed. Observational biases and gaps in the input stellar database may hamper this technique. A third method is essentially a compromise between these two approaches, either indices are derived theoretically and the light contributions empirically (e.g. Barbuy 1994), or *vice versa* (e.g. Worthey 1994).

We have chosen to look at two models constructed by employing this last approach, namely the models of Worthey (1994) (henceforth W94) and Kurth, Fritze-v. Alvensleben, & Fricke (1999) (henceforth KFF99).

We have selected this seemingly arbitrary choice models for several reasons:

- We have used the W94 models in Chapter 3, and found them to give reasonable predictions for old, metal-poor stellar populations (e.g. GCs)
- Both models use the polynomial fitting functions of W94, derived from the Lick/IDS library.
- The models of KFF99 cover a greater age-metallicity parameter space than those of W94.

The general construction of both these models is essentially very similar, and we have discussed the W94 models in Chapter 3. However, here we summarize the procedure for creating a single stellar population model, and highlight the principle differences between the two models.

An initial mass function (IMF) is assumed, describing the precise distribution of stellar masses for a coeval population of stars.

This may be expressed:

$$\phi(m)dm \propto m^{-(1+x)}dm \tag{4.11}$$

with an exponent, x = 1.35 commonly adopted (Salpeter IMF).

A theoretical isochrone for a given age and metallicity is then binned into discrete units of mass. For each bin along the isochrone, the adopted IMF translates directly into a number of stars of known temperature ($T_{\rm eff}$), (log) surface gravity (log g) and metallicity ([Fe/H]). Each 'star' bin is assigned a corresponding normalised stellar flux, obtained via the interpolation of a grid of fluxes:

$$\int_{\lambda_1}^{\lambda_2} F_\lambda d\lambda = 1 L_\odot \tag{4.12}$$

This flux is multiplied by the number of stars per bin, weighted by their individual luminosities, and the total integrated flux of the stellar population is then obtained by summation over all star bins. Broadband colours may then be calculated from the total flux by integrating under the appropriate filter transmission function, or alternatively, from the fluxes of the individual stars. To obtain line-strength indices, the integrated flux for each bin is used to determine the position of the pseudocontinuum within a defined bandpass. An observationally-derived polynomial fitting-function, a function of each stars' effective temperature, gravity and metallicity, $\mathcal{F}(T_{\rm eff}$, log g, [Fe/H]) then predicts the absorption in each bin. By weighting the indices by the monochromatic luminosity of each bin, and summing over all bins for the entire isochrone, yields the index value for the stellar population. Reiterating this process for isochrones of differing ages and metallicities then predicts line-strength indices for different stellar populations.

Both the W94 and KFF99 models assume a single burst of star formation, where the entire stellar population is created in the first, single time-step. This may be a reasonable assumption for star clusters, but is clearly not the case for larger stellar aggregates (e.g. galaxies). However, the star formation history of *any* stellar system can be described by the superposition of many such models with differing ages and metallicities (Kurth, Fritze-v. Alvensleben, & Fricke 1999). With the indices of a composite stellar population determined, one may then proceed to map a two-dimensional age–metallicity grid by plotting an age-sensitive index against a metallicity-sensitive one. In principle, measuring the correct choice of indices for a stellar population and plotting them on such a grid will yield the age and metallicity of the population.

The differences between the W94 and KFF99 models arise from their input physics, and differing numerical method. The models of W94 use a compilation of VandenBerg isochrones (Vandenberg 1985; Vandenberg & Bell 1985; Vandenberg & Laskarides 1987) and revised Yale isochrones (Green, Demarque, & King 1987). The fluxes used are almost entirely theoretical, from those of Kurucz (e.g. Kurucz 1979). The KFF99 models make use of the more recent Padova tracks (see Fagotto et al. 1994, and references therein). For fluxes, they use the homogenized library of Lejeune, Cuisinier, & Buser (1997,1998), constructed from the fluxes of Kurucz (e.g. Kurucz 1979), Bessell & Scholz (1989) and Fluks et al. (1994). Both the W94 and KFF99 models use solar abundance ratios, since the polynomial fitting-functions are based on observations of stars in the solar neighbourhood (i.e. scaled-solar).

The numerical method of constructing the models differ in their approach to using the theoretical isochrones. When the W94 models were constructed, there existed no set of isochrones satisfactorily covering all metallicities and all stages of stellar evolution. Therefore, the models were extrapolated to cover some of the parameter space unavailable through these isochrones. Even so, a large region of parameter space (young and metal-poor, $\tau < 8$ Gyr and [Fe/H] < -0.5) is unconstrained. Moreover, theoretical calculations for the evolution of stars are only available for discrete masses. A method is required to obtain a smooth continuation in composite stellar populations. W94 dealt with this issue by interpolating between tracks, however this possibly produces artificial and unphysical evolutionary states. The KFF99 models bypass this problem entirely by using a Monte-Carlo approach, developed extensively by Loxen (1997). Instead of interpolating isochrones, they create a large grid of stellar masses and ages over a series of time-steps. Each grid is randomly generated (i.e. Monte-Carlo), with each grid-cell corresponding to a 'pseudo-star'. These 'pseudo-stars' are then assigned a weighting factor which is derived from

the adopted IMF (i.e. Salpeter) and SFR at that particular grid-cell. The total flux from the entire population is then calculated, again yielding indices using the W94 fitting-functions.

KFF99 compare their SSP models with those of W94, Bruzual & Charlot (1996) (see Leitherer et al. 1996), Vazdekis et al. (1996) and Tantalo et al. (1996;1998). For their *B-V* colours, they generally find good agreement with all the models, although those of Vazdekis et al. (1996) are always slightly bluer. In terms of line-strengths, all the models use the fitting-functions of W94, with the exception of those of Tantalo, Chiosi, & Bressan (1998) who use the empirical calibrations of Borges et al. (1995). Again, agreement is good in most cases. However, the Mg_2 indices of KFF99 are some 0.02 mag lower than those of both Bruzual & Charlot (1996) and Vazdekis et al. (1996) for old ages, and those of Tantalo, Chiosi, & Bressan (1998) are lower than all the other models, probably due in part to the different fitting-functions used. All the above models (apart from those of W94) use the Padova isochrones.

We compare the W94 and KFF99 models grids for the Fe5270–Hβ indices in Figure 4.17, which illustrates the differences in age-metallicity parameter space covered by these two models. The W94 models cover an age range of $1.5 \leq \tau \leq 17$ Gyr and metallicity range of -0.25 $\leq$ [Fe/H] $\leq$ 0.5 dex, in addition to bracketing the -2.0 $\leq$ [Fe/H] $\leq$ -0.25 metallicity range for old stellar populations ($8 \leq \tau \leq 17$ Gyr). The models of KFF99 cover a somewhat larger (although slightly younger and more metal-poor) region of parameter space, with an age range of $0.5 \leq \tau \leq 16$ Gyr[9] and a metallicity range of -2.26 $\leq$ [Fe/H] $\leq$ 0.44 dex. Both models predict similar evolution of the Hβ index with metallicity; Hβ line-strength *decreases* with increasing metallicity for a given age. Also, both models predict that Hβ *increases* with younger ages for a given metallicity. Moreover, the KFF99 models indicate that for $\tau \leq 2.0$ Gyr, Hβ increases strongly as one goes to much younger ages for the stellar population. This arises due to the fact that strength of the Hβ line is a strong function of temperature (e.g. Tripicco & Bell 1995), and the temperature of the main-sequence turn-off (MSTO) is a measure of the age of a stellar population (for younger ages, the MSTO gets hotter).

Figure 4.17 shows the age and metallicity predictions of two indices (namely Fe5270 and Hβ) for the two models. However, the W94 models predict a total of 24 line-strength indices, of which 9 are also modelled by KFF99. Of these indices we have measured Hβ, Fe5270, Fe5335, Mg_1, Mg_2 and Mg *b* (NaD, TiO_1 and TiO_2 are too red for our spectra). We do not perform a

[9] An important point to note is that the fitting functions of W94 were designed for stellar populations older than 1 Gyr. Therefore, one must be cautious in employing the model indices to interpret spectra of clusters younger than this.

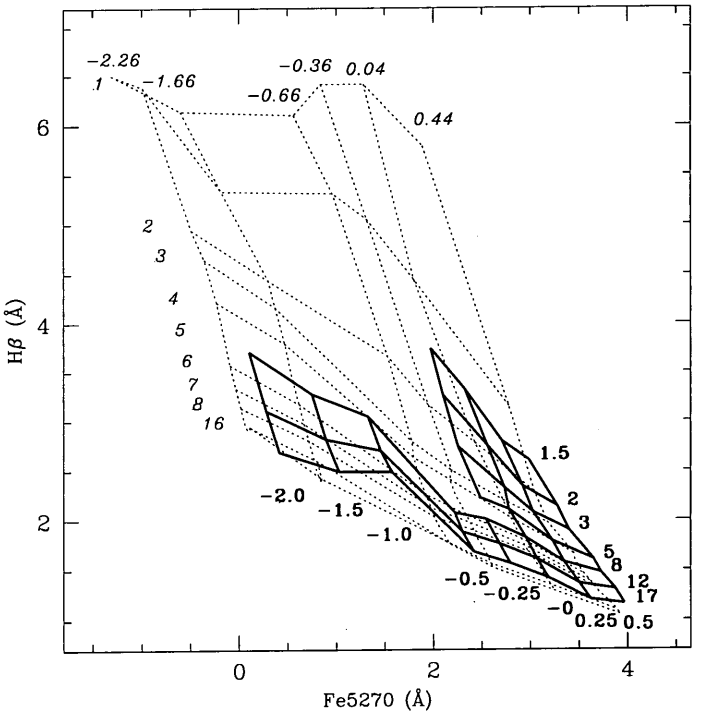

Figure 4.17: Comparison of the SSP model grids of W94 and KFF99 for the Fe5270 and Hβ indices. The thick solid lines indicate the parameter space covered by the W94 models. The fainter, dashed lines indicate the region covered by the KFF99 models. The KFF99 model 9–16 Gyr isochrones have been omitted for the sake of clarity. The age and metallicity scales for the W94 models are given in bold type to the right bottom of the plot, those of KFF99 are given to the left and top of the grids. Ages are in Gyr and metallicities are given in units of dex.

detailed comparison of the W94 and KFF99 models, since this has already been partly addressed by KFF99. However for completeness we do briefly re-compare the relevant indices. As indicated by KFF99, we find that most indices are in good agreement with the W94 models. However, we do note that the predictions for the Hβ index differ significantly. At all times, for a given age and metallicity, the KFF99 models predict lower values for Hβ than those of W94. At solar metallicity, the mean difference (H$\beta_{\rm KFF99}$ - H$\beta_{\rm W94}$) is merely $\sim$ -0.065 Å, however at lower metallicities the difference becomes much more pronounced. For [Fe/H] = -1.0, we find that the offset between the models (for 8–17 Gyr isochrones) is -0.5 Å. In other words, a star cluster with [Fe/H] = -1.0 and predicted to have an age of 17 Gyr on the basis of Hβ using the W94 models, would only be $\sim$ 8 Gyr using the KFF99 models.

The most significant difference between the models that we note is the behaviour of Hβ for old ages and low metallicities. For $\tau > 10$ Gyr and [Fe/H] $\leq$ -0.66, the Hβ index becomes *degenerate* in the KFF99 models; these models no longer predict a unique solution for age and metallicity.

This behaviour, not reproduced by the models of W94, can also be seen in the SSP models of Vazdekis et al. (1996) and arises due to the flux contribution from blue HB stars as discussed in Chapter 1.

The original W94 models did not address this issue, horizontal branch stars were assumed to populate a red clump at the beginning of the horizontal branch. These models were subsequently modified in an empirical manner, so that the horizontal branch morphology follows the observed behaviour of Galactic GCs, in that they become more extended toward the blue for more metal-poor GCs (see Figure 3.13 in Chapter 3 for a comparison of the W94 grids with different assumptions for horizontal branch morphology).

The KFF99 models deal with this phenomenon in a somewhat more quantitative manner by estimating the amount of mass-loss on the red giant branch (thereby affecting the colours of the horizontal branch stars) and employ Reimers' mass-loss relation (Reimers 1975):

$$\dot{M} = 1.27 \cdot 10^{-5} \cdot \eta M^{-1} L^{1.5} T_{\rm eff}^{-2} \tag{4.13}$$

were η is an empirical fitting factor, and is dependent upon horizontal branch morphology. For the KFF99 models considered here, η=0.35, somewhat lower than Lee, Yoon, & Lee (2000) who adopt η=0.65 in their population models.

Not only does this 'degeneracy' in Hβ, caused by horizontal branch morphology, have implications for the use of this index in age-dating old stellar populations, but it also has important practical consequences (see § 4.6.5).

4.6.2 The Model Calibration

Before we can derive the ages and metallicities for the clusters using SSP models based upon the Lick/IDS stellar library (Worthey 1994), it is important to check that we have been able to adequately place our data onto this system. For this purpose, in § 4.5.4 we broadened our spectra to the resolution of the Lick/IDS and then proceeded to determine the linear offsets in our data by observing a number of stars also observed by the Lick group. These offsets (given in Table 4.9) are an additive constant, which we have applied to our line-strength indices. To check our calibration, we compare Lick/IDS indices in our data which measure similar chemical species (or are at least influenced by these same elements e.g. Tripicco & Bell 1995). By plotting these indices against each other onto SSP grids, which are effectively degenerate in age and metallicity, we can look for evidence of any systematic offsets in these data. In Figures 4.18– 4.20 we show our data compared

to the W94 grids for the Fe4531, Fe5406, Fe5270 and Fe5335 indices (iron dominant), Hβ, Hγ_A, Hγ_F and Hδ_A indices (hydrogen dominant) and Mg_1, Mg_2, and Mg b (magnesium dominant).

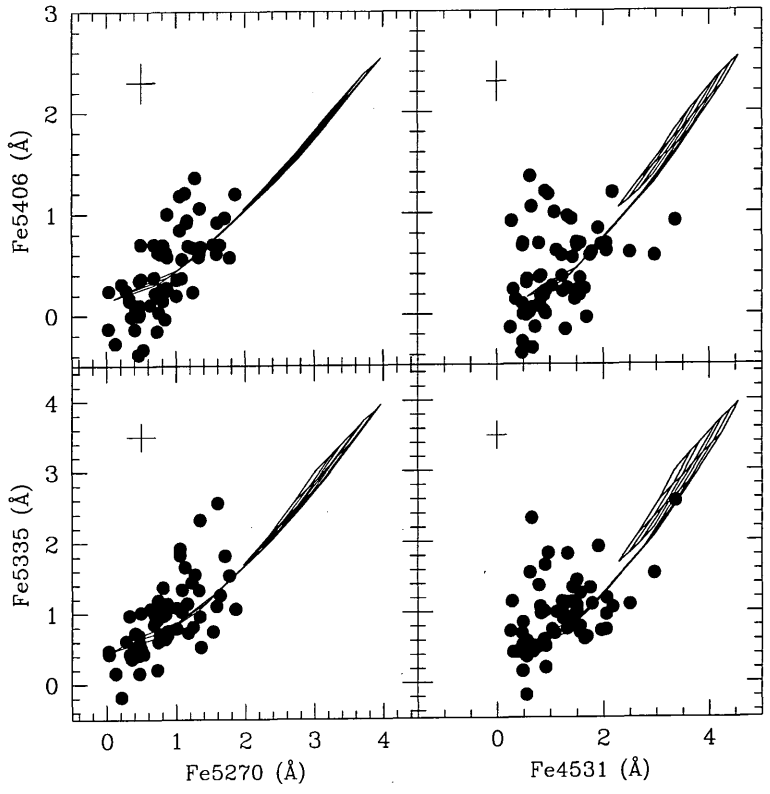

Figure 4.18: Index-index plots for the Fe4531, Fe5406, Fe5270 and Fe5335 indices measured from our data, compared to the model grids of W94. The error bar in the upper left shows the mean total error (σ_T) for the index.

Iron Indices: the scatter in the clusters appears in agreement with our observational uncertainties. The loci of these data are consistent with the loci of the models, indicating that no significant offsets are present. The scatter for Fe4531 seems to be larger than for the other iron indices, even though the formal error on this index is smaller. The Fe4531 index is actually dominated by Ti abundance (Tripicco & Bell 1995) rather than iron, which may be partly the reason for this behaviour. We note that the LMC clusters generally populate the low metallicity region of the models.

Balmer Lines: inspection of Figure 4.19 indicates that there are some inconsistencies between the LMC clusters and the models for the indices which measure the Balmer absorption lines:

The Hδ_A–Hγ_F plot (upper right panel) also shows what appears to be a systematic offset from the W94 grid. From Figure 4.19 it is not obvious which index (or both) is inconsistent with the

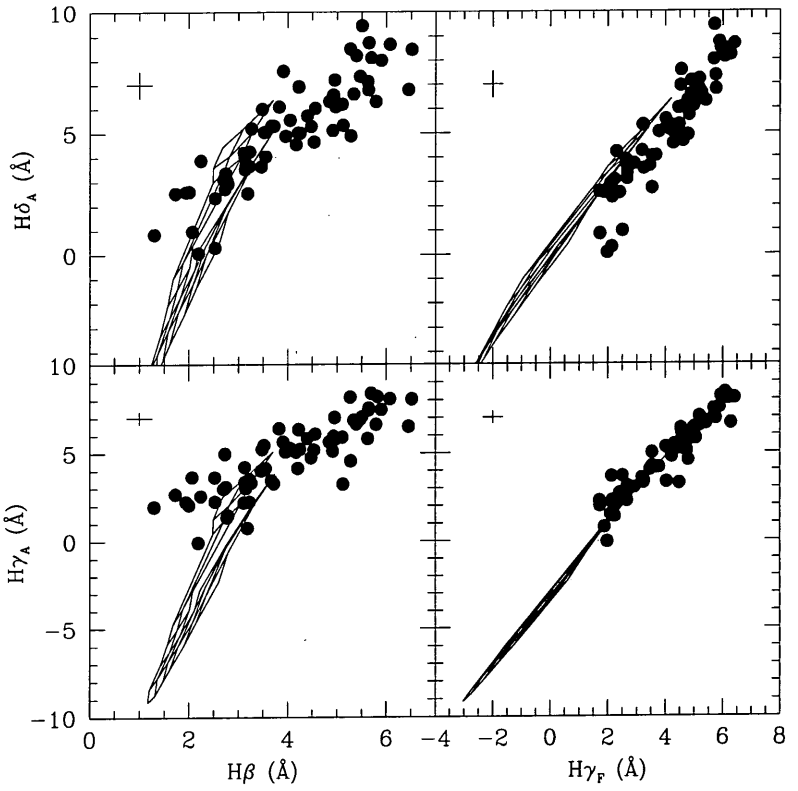

Figure 4.19: Index-index plots for Hβ, $H\gamma_A$, $H\gamma_F$ and $H\delta_A$ compared to SSP models of W94.

models. However, a detailed comparison of the Hδ, Hγ and Hβ indices leads us to believe that it is the Hδ index which is systematically offset from the models. Moreover, this applies to *both* $H\delta_A$ and $H\delta_F$ and is perhaps an artefact from the large offsets seen between repeat observations for Hδ in § 4.5.3. The magnitude of the offset in Hδ is $\sim$ -1.0 Å from Hβ and Hγ, which we add to this index for the purposes of searching for emission in the clusters (§ 4.6.3).

Compared to the $H\delta_A$– $H\gamma_F$ plot (upper right panel) and $H\gamma_A$–$H\gamma_F$ plot (lower right panel) of Figure 4.19, the scatter in Hβ seems significantly larger than the observational errors. Moreover, Hβ appears to follow a somewhat flatter relation than that which is predicted by the SSP models. Two effects conspire to create this situation:

- The age sensitivity of the Hβ index. As can be see in the lower and upper left panels of Figure 4.19, the SSP grids are not entirely degenerate, indicating a different degree of age–metallicity sensitivity between the Hβ, Hδ and Hγ indices. Worthey & Ottaviani (1997) construct and compare a metallicity sensitivity parameter from their model predictions for each of these indices, d log (age)/d log Z. This parameter indicates the age change necessary to

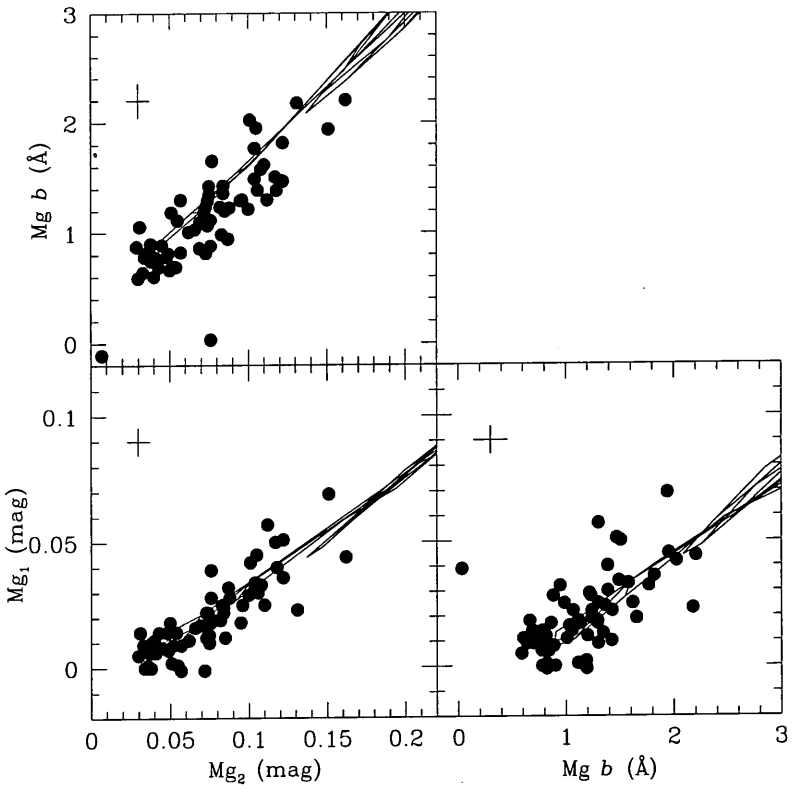

Figure 4.20: Index-index plots for Mg_1, Mg_2 and Mg b indices. Note that Mg_1 and Mg_2 are measured in magnitudes, whereas Mg b is in Angstroms.

counteract any metallicity change for a fixed index value (with lower values indicating a higher sensitivity to age than metallicity). They show (see table 7 of Worthey & Ottaviani 1997) that Hβ is the most age sensitive (d log (age)/d log Z = 0.6), followed by Hγ_F (d log (age)/d log Z =0.8), Hδ_F (d log (age)/d log Z =0.9), Hγ_A (d log (age)/d log Z =1.0) and finally Hδ_A (d log (age)/d log Z =1.1). This would indicate that at least *some* of the scatter in the left-hand panels of Figure 4.19 arises due to an intrinsic age spread in the LMC clusters.

- Emission in the spectra. As has already been noted in § 4.4.1, a number of the LMC clusters show strong emission. This has the effect of 'filling-in' absorption lines, thereby yielding a lower equivalent width of the index than would otherwise be the case if no emission were present. This effect is most noticeable for Hβ, since of the hydrogen indices we have measured, Hβ is most strongly affected (Osterbrock 1989). This emission is manifest in the left-hand panels of Figure 4.19 by the almost linear extension of Hβ from 6.5 $\sim$ 1.0 Å. We investigate the effects of emission further in § 4.6.3.

Magnesium Indices: the agreement between these indices and the models is good (Figure 4.20). Again the scatter appears consistent with the observational uncertainties. There appears to be a small offset between Mg_2 and Mg b (upper left panel). However, this is artificial. The models here are not entirely degenerate, and many of the LMC cluster occupy a region not covered by the W94 models. Much better agreement is achieved by plotting these same data onto the KFF99 models.

4.6.3 Emission in the Clusters

The existence of optical emission-line objects in the LMC has been known for sometime, identified largely on the basis of wide-field Hα objective-prism surveys (e.g. Henize, Aller, & Doherty 1953; Lindsay & Mullan 1963; Lucke 1974). Bica et al. (1999) identify a total of 1199 'emission-line related' objects from their compiled catalogue of LMC clusters and associations.

Emission lines in the optical are generally formed by the excitation of interstellar gas due to the presence of an ionizing radiation source. Much of the nebular emission seen in the LMC arises due to photoionization from the UV flux produced by stars more massive than $\sim 10\ M_\odot$; and this is certainly the primary emission mechanism in very young LMC star clusters. The lifetimes of such massive stars are $\leq 10^7$ yr, after which time they no longer act as a significant radiation source. Once this source of ionizing radiation vanishes, the emission region quickly follows. Therefore, the presence of such emission is often indicative of recent star formation.[10] (e.g. Copetti, Pastoriza, & Dottori 1986)

Optical nebular emission lines are dominated by forbidden metal lines such as those which arise from Nitrogen, Oxygen and Sulphur. These forbidden transitions occur in environments of low gas-density, where ions are within a few $kT \sim 1$ eV of their ground state configuration. It is precisely this 'forbiddeness' of transition which precludes the possibility of these ground-state transitions giving rise to absorption at these wavelengths (Osterbrock 1989). Some of the strongest lines in optical spectra originate from doubly-ionized [OIII], occurring at λ4959 and λ5007 (Figure 4.21). The other principle contributer to optical emission are lines from the Balmer series. These are recombination lines, which arise from the creation of hydrogen atoms via the capture of electrons by free protons. These hydrogen atoms then cascade down down to their

[10] Emission lines are also produced via shock-heating (e.g. supernovae), Active Galactic Nuclei (AGN) and evolved stars (post-Asymptotic Giant Branch (AGB) stars or Planetary Nebulae). However, certainly for the case of young star clusters, these processes are less important.

ground states, resulting in a characteristic release of energy. Lines of this Balmer series include Hα at λ6562.8, Hβ (λ4861.3), Hγ (λ4340.5) and Hδ (λ4101.7).

The superposition of this Balmer-line emission onto Balmer Lick/IDS indices has the effect of 'filling-in' these absorption lines. This effect can be clearly seen for the Hβ index in 4.21 (lower panel). This filling-in of the lines reduces their measured line-strengths, which, on the SSP grid, has the effect of artificially ageing the emission-affected clusters (e.g. González 1993; Kuntschner 1998). A more subtle effect of emission is to alter the position of the continuum side-bands of the Lick/IDS indices, again affecting measured line-strengths.

In Figure 4.21 we show two examples of strong emission in the LMC clusters NGC 1943 (SWB type II) and NGC 1967 (SWB I). The presence of emission in our LMC cluster spectra is a result of either one or both of the following: (*i*) emission which is intrinsic to the cluster or (*ii*) a superposition of nebular emission onto the absorption spectrum of the cluster. Both the clusters in Figure 4.21 are perhaps young enough for hot stars to still exist upon their main-sequences, implying that much of their observed emission may originate from within the cluster itself. However, the *strength* of emission seen in the older cluster NGC 1943, is perhaps indicative of a strong contribution from HII regions.[11]

There are several methods of correcting for emission in optical spectra, generally employed to correct for the filling in of the Balmer absorption lines. Perhaps the simplest technique is to attempt to fit an assumed profile (e.g. a Gaussian) to the affected line. However this assumes that (*i*) the absorption line is strong with a known profile and (*ii*) the emission is weak enough to leave an appreciable proportion of the absorption line visible, in order to estimate the width of the profile. This technique is inappropriate for unresolved lines, or where the continuum is effected. A more sophisticated approach, although along similar lines, is to create an absorption-line template from a known emission- free source (e.g. a galaxy or star cluster) and checking this template subtraction *a posteriori* with other emission lines (Goudfrooij & Emsellem 1996). Such an approach proved impractical for the LMC clusters, since the range of appropriate templates (either observed or theoretical) was not available.

Another route to detecting (and thereby correcting for) the filling in of the Hβ absorption line, is to estimate the contribution (i.e. the equivalent width) of the Hβ emission line, via comparison with other emission lines. This has been successfully achieved by Barbaro & Poggianti (1997). These authors found a tight correlation between Hβ and [OII]λ3727 using the galaxy data

[11] Both of these clusters are within 0.5 degrees of the LMC bar.

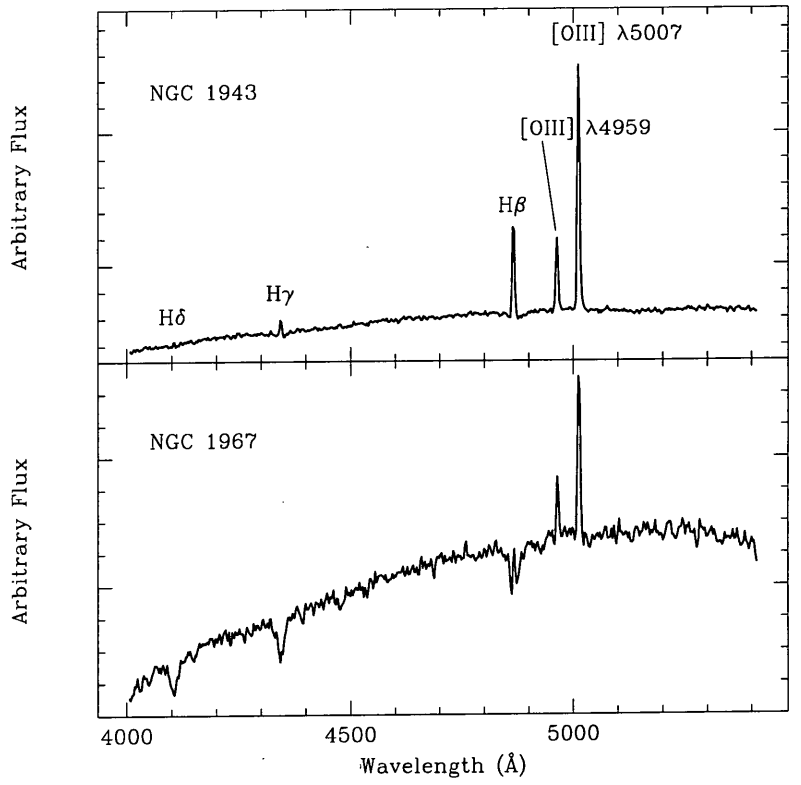

Figure 4.21: Emission lines in two LMC clusters, NGC 1943 and NGC 1967. The filling in of the Hβ absorption line by Hβ emission is clear in the lower panel. NGC 1943 is of SWB type II *(B-V)* = 0.27 whilst NGC 1967 has SWB type I *(B-V)* = 0.05. The SWB type–age relation gives approximate ages for the clusters of $30 < \tau < 70$ and $10 < \tau < 30$ Myr respectively (Bica, Claria, & Dottori 1992).

of Kennicutt (1992) and Dressler & Gunn (1982). Unfortunately, the [OII]λ3727 line is too blue for our data, whereas their other successful calibration, that of Hα against [SII]λ6716,λ6731 is too red. González (1993) corrected for emission in his sample of early-type galaxies by scaling the change in the Hβ index by 0.7 $\times$ [OIII]λ5007. We have attempted to employ this scaling for our data, but have found this to be an unreliable estimate of Hβ emission. As pointed out by Barbaro & Poggianti (1997) this method is unreliable since the strength of the [OIII]λ5007 line is sensitive to the excitation conditions within the emission line region, and may subsequently vary region to region and indeed, galaxy to galaxy.

With these considerations in mind, we chose *not* to correct for emission, but simply flag in our sample those which are affected. We identify the clusters with emission in two ways:

- **By Eyeball:** some of the clusters (e.g. Figure 4.21) show clear emission in their spectrum. The strongest line is generally [OIII]λ5007, although for some of the clusters (e.g. NGC 1967), emission is seen *in* the Hβ index itself.

- **Comparison of Hβ, Hγ and Hδ:** as one moves to higher-order Balmer lines, the strength of emission due to recombination processes decreases. The ratio of emission in Hβ : Hγ : Hδ is approximately 4:2:1 for the temperature range $2500 \leq$ T(K) ≤ 20000 (Osterbrock 1989). We therefore compare these indices for each cluster using the model grids of W94 (we do not use the KFF99 grids here because they do not model the higher-order Balmer lines). We use a scheme whereby if for a given age, the line-strength of the Hβ index is weaker (i.e. older) than that predicted by Hγ and Hδ (taking into account the uncertainties in the index), we flag the cluster as emission affected. Moreover, we use the wider Balmer definitions (H$\gamma_{\rm A}$ and H$\delta_{\rm A}$) since these are a factor of two less sensitive to emission than the narrower 'F' definitions (Worthey & Ottaviani 1997).

In Figure 4.22 we compare the Hβ, H$\gamma_{\rm A}$ and H$\delta_{\rm A}$ indices for two clusters, M-OB4 (SWB I) and NGC 1754 (SWB VII).

NGC 1754 is an old GC, with Fe/H=-1.42 $\pm$ 0.15 and an age of $\simeq$ 15 Gyr (Olsen et al. 1998). The W94 models predict the same age (within the uncertainties) from the Hβ, H$\gamma_{\rm A}$ and H$\delta_{\rm A}$ indices. M-OB4 is a young star cluster ($\tau \sim 30$ Myr), and its spectrum shows clear emission in [OIII]λ5007. As one goes to higher-order Balmer lines, the W94 models predict *younger* ages for this cluster, since they become progressively less influenced by emission. An important point to note is that, due to the non-orthogonality of the SSP grids, as the cluster increases in Balmer line-strength, its predicted metallicity also increases. It is also clear from Figure 4.22 that the W94 grids do not give age and metallicity predictions for young clusters such as M-OB4. In Table 4.10, we list those clusters which we identify as emission affected.

We note that of the 20 LMC clusters which we identify as having emission in their spectra, 18 have SWB types 0 or I. In fact, of all the LMC clusters in our sample of SWB types 0 and I, only two, KMHK1019 and SL 675 do *not* show any evidence for emission. Operating under the assumption that the origin of the emission in the SWB type 0-I clusters is from hot O and B cluster stars, then we can place an upper limit on these cluster ages of $\tau < 10^8$ yr. Bica et al. (1996) indicate that NGC 1872 (SWB IVA) is superimposed on an emission nebula. This is perhaps the case for NGC 1943, unless it is misclassified as SWB II when it is actually of earlier type.

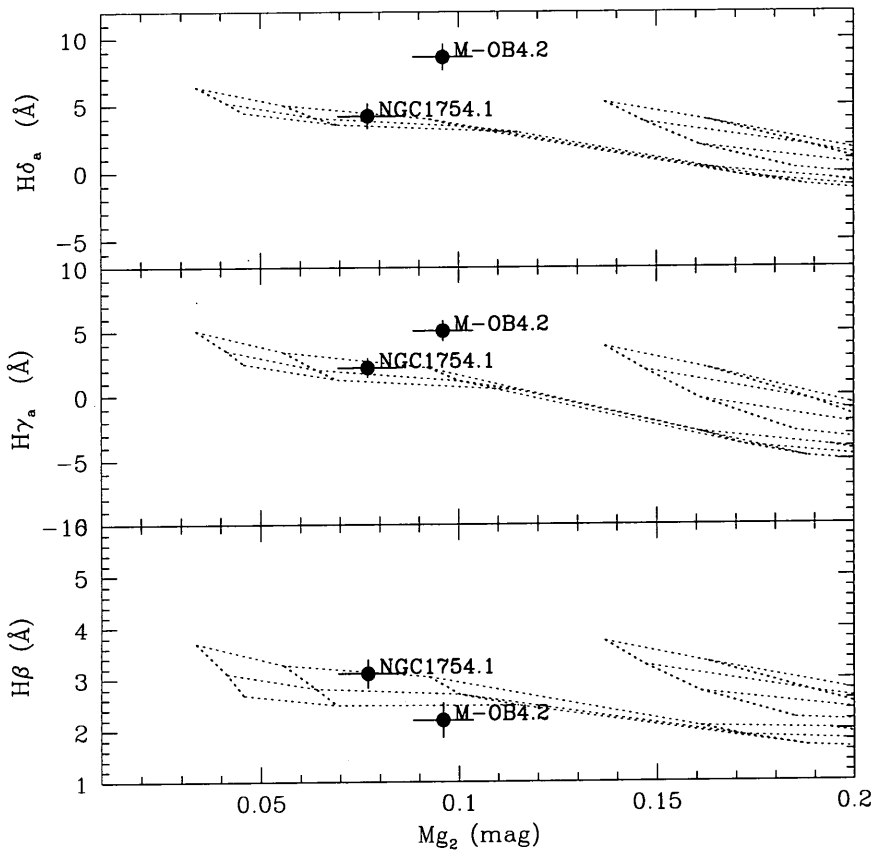

Figure 4.22: The Hβ, Hγ_A and Hδ_A indices versus Mg_2 for the young cluster M-OB4 and the old cluster NGC 1754, compared to the W94 models. The three indices give consistent ages for NGC 1754, whereas emission in Hβ (and to a lesser extent, Hγ_A) lowers the predicted age for M-OB4.

4.6.4 Stochastic Effects

Besides emission and field-star contamination (which we have tried to minimize through the careful selection of core radii for the LMC clusters), stochastic effects in the IMF of the clusters may also affect our age and metallicity determinations (e.g. Barbaro & Bertelli 1977; Chiosi, Bertelli, & Bressan 1988 ; Girardi et al. 1995). For less populous star clusters, the relative light contribution from individual stars becomes increasingly important. Indeed, for very young, low-mass clusters a single bright star can provide a significant fraction of the total integrated flux of the cluster. Such contributions can cause significant dispersions in $U-B$, $B-V$ colours and spectral indices such as Hβ. However, this dispersion is most significant for *very* young ($6 \sim 30$ Myr) star clusters in the red supergiant stage of their evolution (Girardi et al. 1995). After $\sim$ 30 Myr, these

Table 4.10. Star clusters in our spectroscopic sample which we identify as being affected by emission. Where possible, we measure the equivalent widths of the [OIII] lines for completeness. We do not measure the equivalent widths of the Balmer lines since they are superimposed onto absorption lines.
† superimposed on nebula emission.

ID	Emission	Notes
BRHT14b	[OIII]λ5007 (1.4 Å)	SWB I
M-OB4	[OIII]λ5007 (1.2 Å)	SWB I
NGC 1711	[OIII]λ5007 (2.9 Å)	SWB I
NGC 1767	[OIII]λ5007 (1.8 Å)	SWB I
NGC 1815	Hβ, [OIII]λ5007 (0.9 Å)	SWB I
NGC 1825	Hβ, [OIII]λ5007 (0.8 Å)	SWB I
NGC 1834	OIII]λ5007 (0.4 Å)	SWB I
NGC 1872	Hγ, Hβ, [OIII]λ5007 (2.6 Å)	SWB IVA, sup N113†
NGC 1943	Hγ, Hβ, [OIII]λ4956 (10 Å), [OIII]λ5007 (33 Å)	SWB II
NGC 1967	Hβ, [OIII]λ4956 (1.6 Å), [OIII]λ5007 (5.6 Å)	SWB I
NGC 2002	[OIII]λ5007 (0.6 Å)	SWB I
NGC 2004	Hβ, [OIII]λ5007 (0.7 Å)	SWB I
NGC 2100	Hβ, [OIII]λ4956 (0.8 Å), [OIII]λ5007 (2.2 Å)	SWB I
NGC 2102	Hβ, [OIII]λ5007 (2.8 Å)	SWB 0
Rob 1	Hβ, [OIII]λ4956 (0.7 Å), [OIII]λ5007 (2.5 Å)	SWB 0
SL 106	[OIII]λ5007 (0.4 Å)	SWB I
SL 230	[OIII]λ5007 (2.0 Å)	SWB I
SL 360	Hγ, Hβ, [OIII]λ4956 (17 Å), [OIII]λ5007 (52 Å)	SWB 0
SL 586	[OIII]λ5007 (0.6 Å)	SWB 0
SL 601	Hβ, [OIII]λ4956 (1.6 Å), [OIII]λ5007 (5.1 Å)	SWB I

stochastic effects are a decreasing function of age, and become negligible as RGB stars begin to appear at $\sim$ 1.2 Gyr.

4.6.5 Predictions of the Models

We now derive ages and metallicities for our clusters using the SSP model grids. We begin by comparing our full sample of clusters to the W94 and KFF99 models, shown in Figures 4.23

and 4.24. We show our line-strength data with their individual uncertainties, σ_T, after having been corrected by their respective Lick/IDS offsets. For comparison, we over-plot the W94 and KFF99 SSP grids in a similar fashion to Figure 4.17. The age and metallicity scales of the models are also the same as for Figure 4.17, but have been omitted for the sake of clarity. In the upper right panel of Figure 4.24, we plot Hβ versus $\langle$Fe$\rangle$. This index is defined by González (1993) as the mean of the Fe5270 and Fe5335 indices, with the purpose of reducing the statistical uncertainties in these indices.

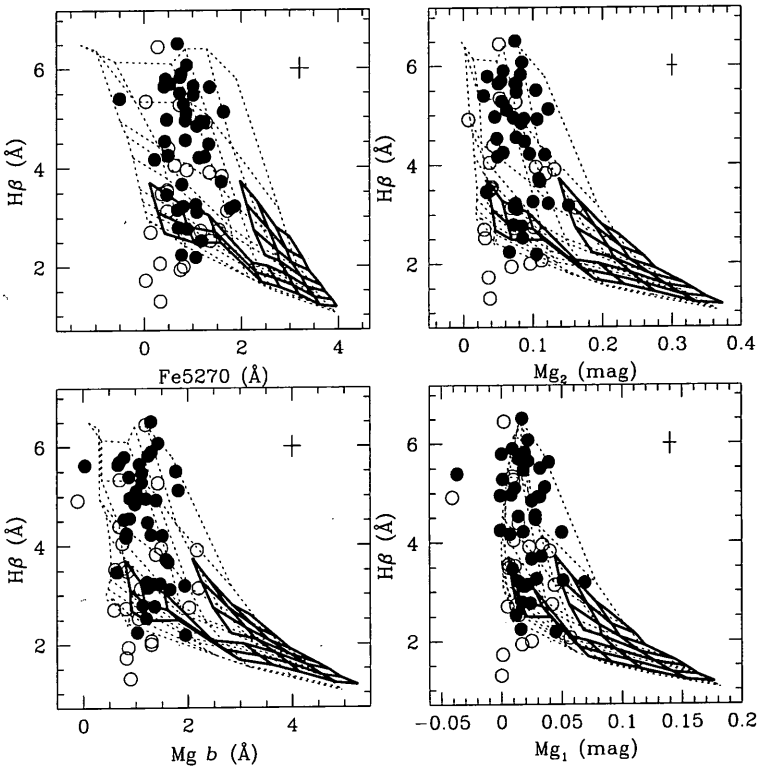

Figure 4.23: The Hβ index versus Fe5270, Mg *b*, Mg$_1$ and Mg$_2$ indices of the LMC clusters, compared to the SSP grids of W94 (thick lines) and KFF99 (dashed lines). Circles indicate the position of the LMC clusters on the age-metallicity plane. Open symbols indicate the clusters affected by emission. The age and metallicity range of the SSP grids are shown in Figure 4.17.

It is apparent from Figures 4.23 and 4.24 that the clusters cover a wide range in age, and generally have metallicities well below solar values. It is gratifying to note that the majority of the indices for each cluster are consistent between models. The clusters are generally confined to the model grids, although there are a few notable exceptions. Some four or five clusters (depending upon the model) drop off the bottom of the grids, apparently implying that they are

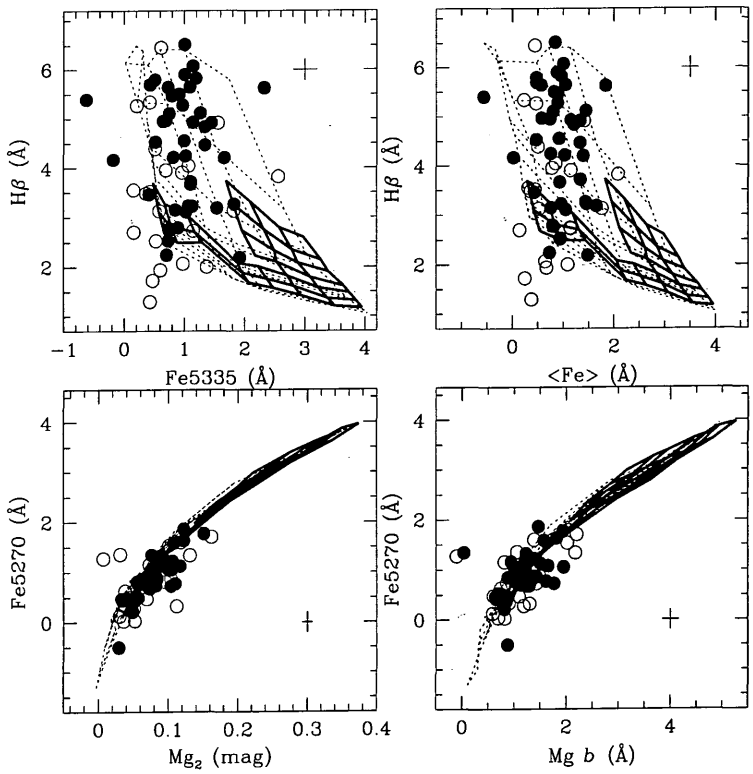

Figure 4.24: Index-index plots for the LMC clusters, compared to the SSP grids of W94 and KFF99. Symbols are the same as for Figure 4.23.

very old. However, it is significant that most have open symbols, indicating that they are affected by emission, which is acting to fill in their measured Hβ absorption. These clusters are, in fact, all very young. However, two clusters are not affected by emission but still lie on or below the oldest SSP isochrone. These clusters, NGC 1898 and NGC 1916 have both been identified as having ages comparable to Milky Way GCs (Suntzeff et al. 1992) (see later).

Inspection of the upper left panel of Figure 4.24 reveals that many of the LMC clusters fall to the left of the Fe5335–Hβ SSP model predictions, which we attribute to a combination of effects. The Fe5335 index is quickly reaching saturation point as it approaches [Fe/H] $\sim$ -2.0; the nature of the feature is such that, as it approaches zero, it loses all predictive power. This can be seen in Figure 4.24 where, for the lowest metallicities, both the W94 and KFF99 grids become degenerate. This has the effect of making many clusters pile-up to the left of the models. However, perhaps more importantly, not only is the scatter in the Fe5335 index much larger than it is for the other grids, but there are indications of shifts between the Fe5335 index and the other indices which are significantly larger than formal the measurement error. This appears to be a

problem for our Fe5335 measurements, perhaps hinted at by our relatively poor repeatability of this index of r = 0.66 (Table 4.6). Clearly, this problem will also effect the $\langle$Fe$\rangle$ index, although to a lesser extent. We still use this index in the age–metallicity determinations, but bear these factors in mind. Five of the clusters, seemingly unaffected by emission, show very poor agreement between indices, leading to very different predictions for their ages and metallicities for a given SSP grid. The afflicted clusters are NGC 1951 (SWB II), NGC 2031 (SWB III), NGC 2065 (SWB III), NGC 2136 (SWB III), and SL 741 (SWB IVA). Whilst these clusters are all of SWB II type or later, it is not inconceivable that they are also affected by emission which fell below our detection threshold. We note that a large number of the clusters with $\tau < 4$ Gyr seem to follow the [Fe/H] $\sim$ -0.5 line relatively closely. This effect is most noticeable in the upper left and right panels of Figure 4.23.

In the two lower panels of Figure 4.24, we show index-index plots of Fe5270 versus Mg_2 and Fe5270 versus Mg b. In principle, these figures give an insight into any α-element enhancement of the LMC star clusters. The [α/Fe] ratio, commonly measured as [Mg/Fe], indicates the degree of enrichment produced by Type II supernovae (SNe) (which produce mainly α-elements) compared to that from Type Ia SNe which produce both α and iron-peak elements in similar quantities. Since the progenitors of Type II SNe are massive stars ($M \geq 10$ $M_\odot$), an enhanced [α/Fe] ratio is indicative of either a skewed IMF (towards higher mass stars) and/or a violent and rapid phase of star formation. As we can see in Figure 4.24, the data and models agree very well. Since the W94 models are scaled-solar, we conclude that there is no indication of enhanced [Mg/Fe] ratios for the LMC clusters. This is unlike the situation for bright elliptical galaxies (e.g. Worthey, Faber, & Gonzalez 1992 ; Davies, Sadler, & Peletier 1993), which can show [Mg/Fe] ratios in excess of 0.3 dex compared to solar values. However, it should be noted that even our most metal-rich star clusters have [Fe/H] $\sim$ -0.4 dex, whereas the affected giant ellipticals typically have abundances of solar or higher.

By plotting the entire LMC cluster sample, it is not particularly clear if any structure is present on the SSP grids. Therefore, in Figures 4.25–4.33 we show our data compared to the models separated by SWB type. We comment upon each in turn:

- **SWB 0** all of these clusters are strongly affected by emission, therefore the age-metallicity predictions of the SSP grids for these data are unreliable. However, we do note that Rob 1, even though its spectrum is strongly contaminated with emission, is predicted to be less than

0.5 Gyr old. The poor agreement between the metallicity-sensitive indices in Figure 4.25 is indicative that these lines are also affected by emission in the clusters.

- **SWB I** again the majority of these clusters are emission-affected, some so strongly that their Hβ absorption is approaching zero.

- **SWB II** the behaviour of these clusters is somewhat surprising. The clusters have a reasonably narrow spread in metallicity, [Fe/H] $\sim$ -0.5, but cover a broad range in age, $0.5 \leq \tau \leq 3$ Gyr. This spread to older ages is possibly indicative of emission contamination, though we do note that the majority if the SWB II clusters follow the 1 Gyr locus of the KFF99 models fairly closely. The one cluster at $\sim$ 5.0 Gyr is NGC 1951 which we previously identified as being 'problematic'.

- **SWB III** these clusters show a very narrow spread in metallicity, [Fe/H] $\sim$ -0.4, and are all less than 2 Gyr old. The three apparently more metal-poor clusters are NGC 2031, NGC 2065 and NGC 2136.

- **SWB IVA** these clusters have $\tau < 1.5$ Gyr and have metallicities of approximately 1/3 solar (with the exception of SL 741, which is displaced to the left of the Fe5270 and Mg_1 grids).

- **SWB IVB** despite the fact that we identify two of the three SWB IVB clusters as being affected by emission, all three exhibit similar characteristics. They lie near the 2 Gyr line of the models at [Fe/H] $\sim$ -0.4.

- **SWB V** two of the clusters, NGC 1806 and NGC 1852, display very similar properties; however NGC 1751 appears to be younger and somewhat more metal-rich (indeed, near solar values).

- **SWB VI** the clusters lie in the 2–4 Gyr line of the grids, ranging from -1.0 $\sim$ -0.4 in metallicity.

- **SWB VII** eight of the nine SWB VII star clusters populate the old, metal-poor region of the model grids. As previously mentioned, two of these clusters (NGC 1898 and NGC 1916) fall *below* the oldest isochrones of the W94 models. We find no evidence of emission in these spectra, and it is hard to find other effects which act to lower the Hβ line-strengths of these clusters. These clusters are separated by $\sim$ 0.25 deg from each other and are both in the crowded bar regions of the LMC. Blue field stars might add a contribution to these spectra, but these would act to enhance the clusters' Balmer indices. Moreover, as noted by Olsen et al. (1998), their high surface brightnesses, in particular NGC 1916, probably preclude such

contamination. Two other clusters, NGC 1754 and NGC 2005 have somewhat stronger Hβ absorption than the other SWB VII 'old' clusters. Interestingly, Olsen et al. (1998) find indications of the presence of a significantly blue horizontal branch in NGC 2005, which, if well populated, may contribute to its Hβ enhancement. However, one cluster, namely NGC 1865, does not subscribe to the interpretation of being 'GC like'. The models predict that this cluster is some 1.0 dex more metal-rich, and is $\sim$ 1 Gyr old. Indeed, although Bica et al. (1996) identify this cluster as SWB type VII, CMDs have since shown this cluster to be $\sim$ 1.0 Gyr old (Geisler et al. 1997), in agreement with our findings. This misclassification probably arose due to a combination of contamination from field stars and the stochastic effects due to bright stars in the cluster.

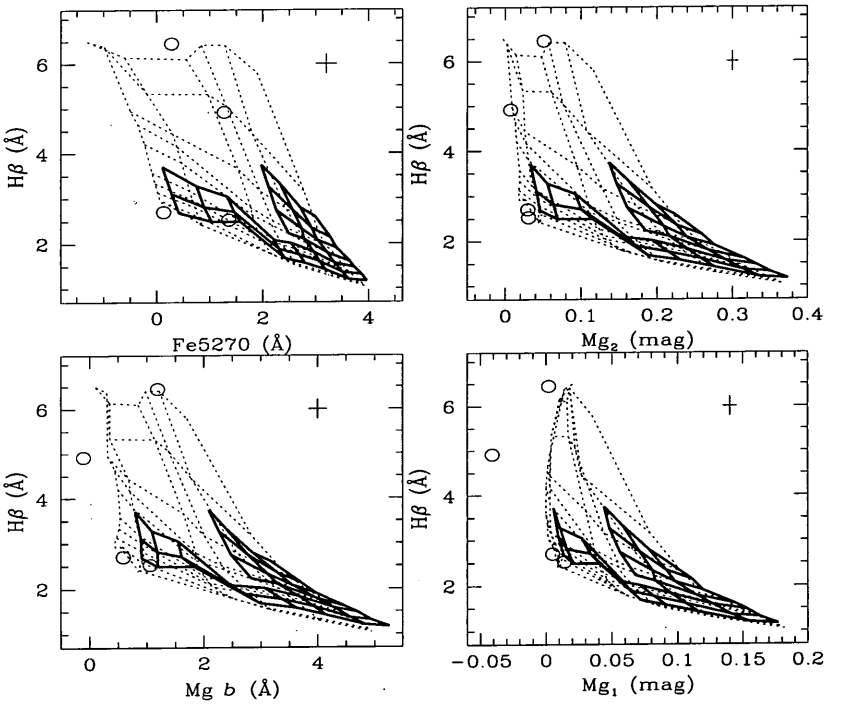

Figure 4.25: Comparison of SWB 0 clusters with SSP grids of W94 and KFF99. Symbols are as for Figure 4.23.

We derive ages and metallicities from the SSP grids using a FORTRAN programme based upon the bivariate interpolation method of Renka & Cline (1984). The programme, using STARLINK PDRA libraries, constructs a surface $\mathcal{F}(x, y)$ through a set of m scattered data points (i.e. age and metallicity for two given indices) (x_r, y_r, f_r), for r = 1,2,...,m. Where the data points (or, more frequently, the uncertainties) extend beyond the parameter space bounded by the grids, we

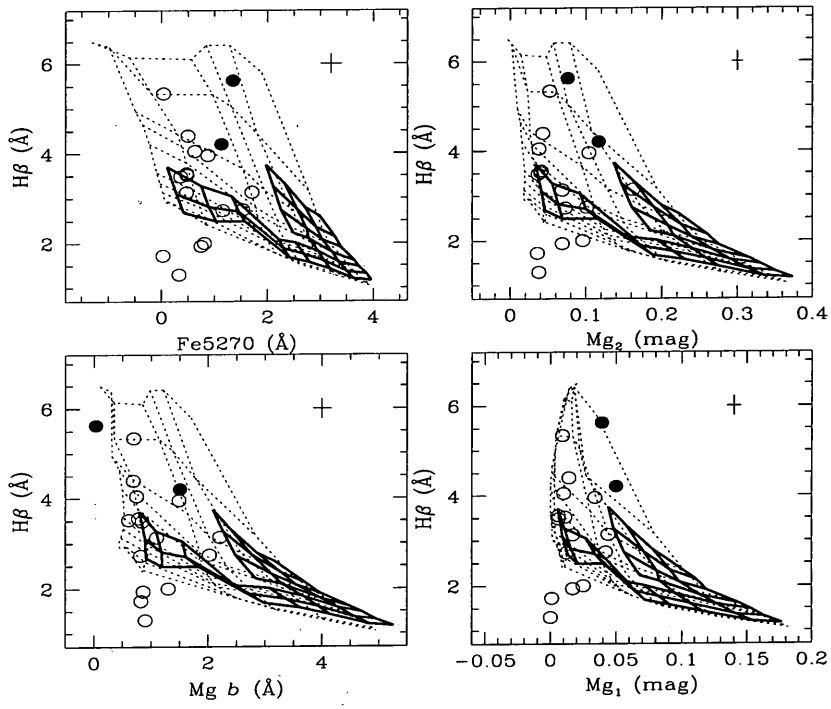

Figure 4.26: Comparison of SWB I clusters with SSP grids of W94 and KFF99. Symbols are as for Figure 4.23.

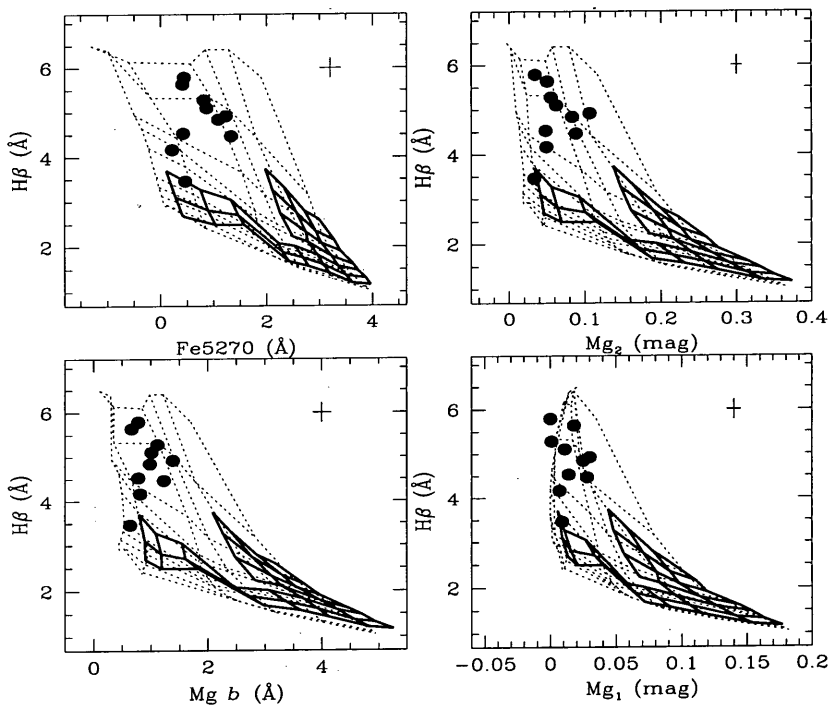

Figure 4.27: Comparison of SWB II clusters with SSP grids of W94 and KFF99. Symbols are as for Figure 4.23.

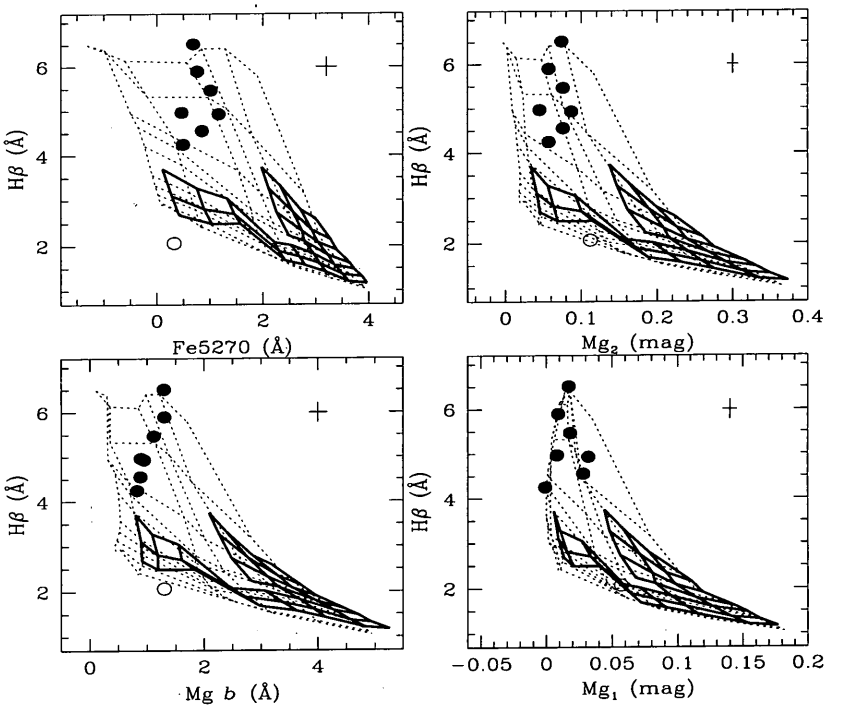

Figure 4.28: Comparison of SWB III clusters with SSP grids of W94 and KFF99. Symbols are as for Figure 4.23.

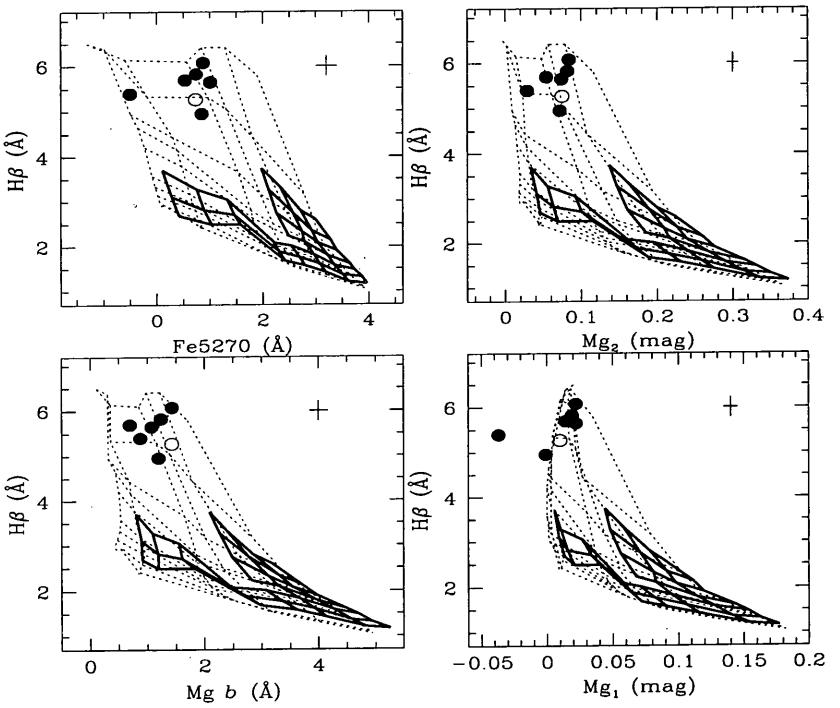

Figure 4.29: Comparison of SWB IVA clusters with SSP grids of W94 and KFF99. Symbols are as for Figure 4.23.

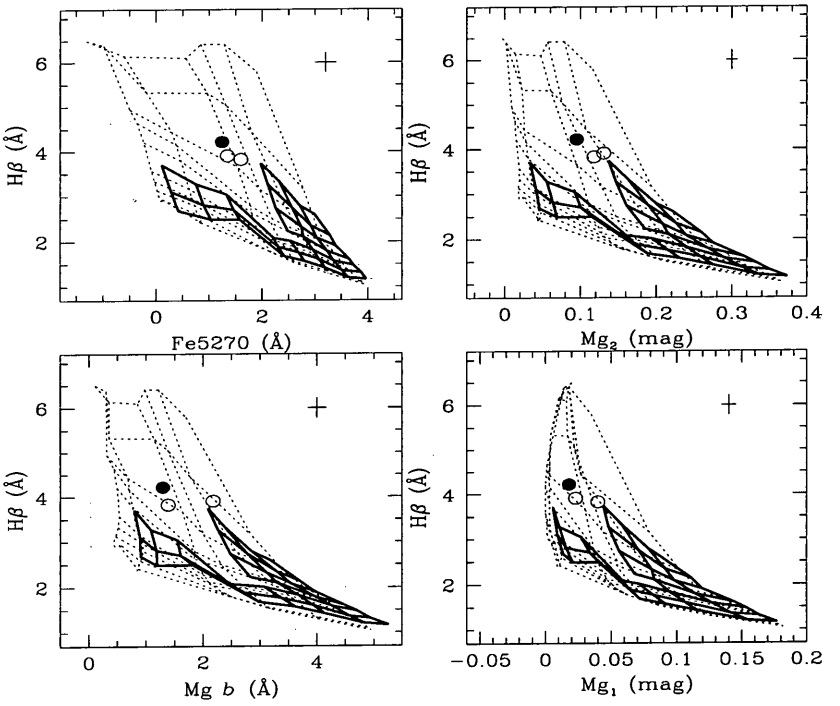

Figure 4.30: Comparison of SWB IVB clusters with SSP grids of W94 and KFF99. Symbols are as for Figure 4.23.

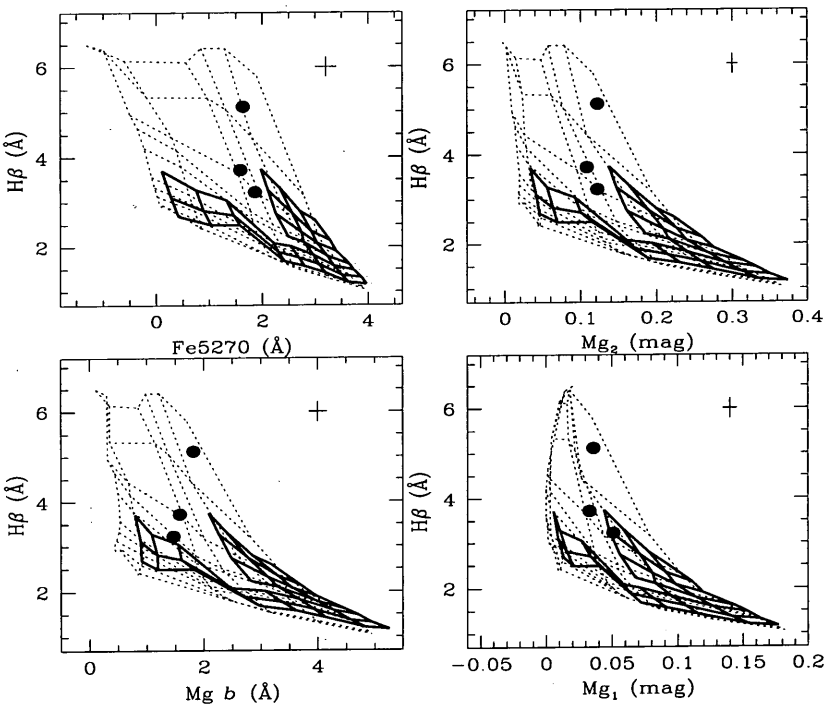

Figure 4.31: Comparison of SWB V clusters with SSP grids of W94 and KFF99. Symbols are as for Figure 4.23.

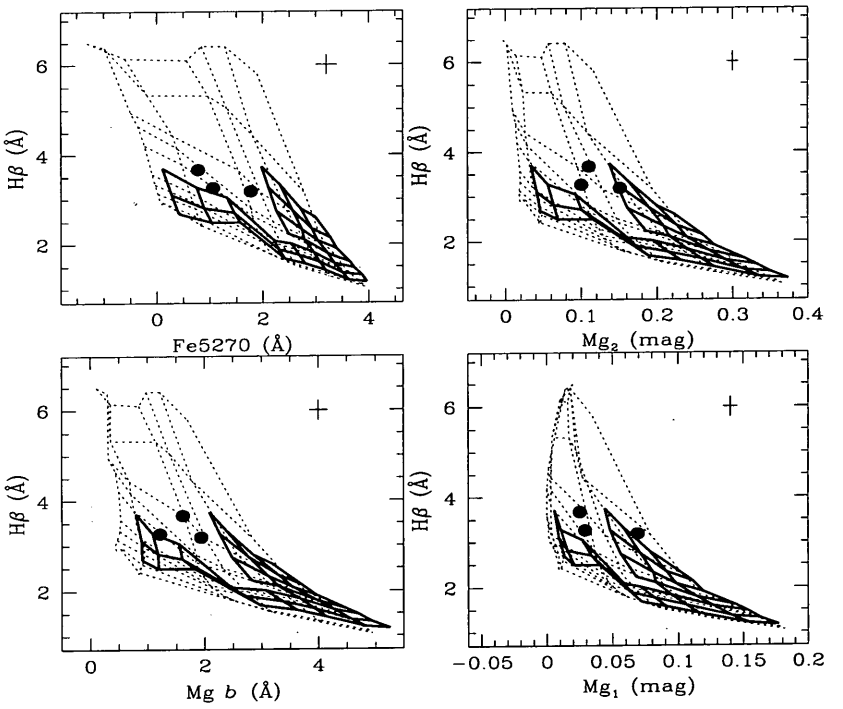

Figure 4.32: Comparison of SWB VI clusters with SSP grids of W94 and KFF99. Symbols are as for Figure 4.23.

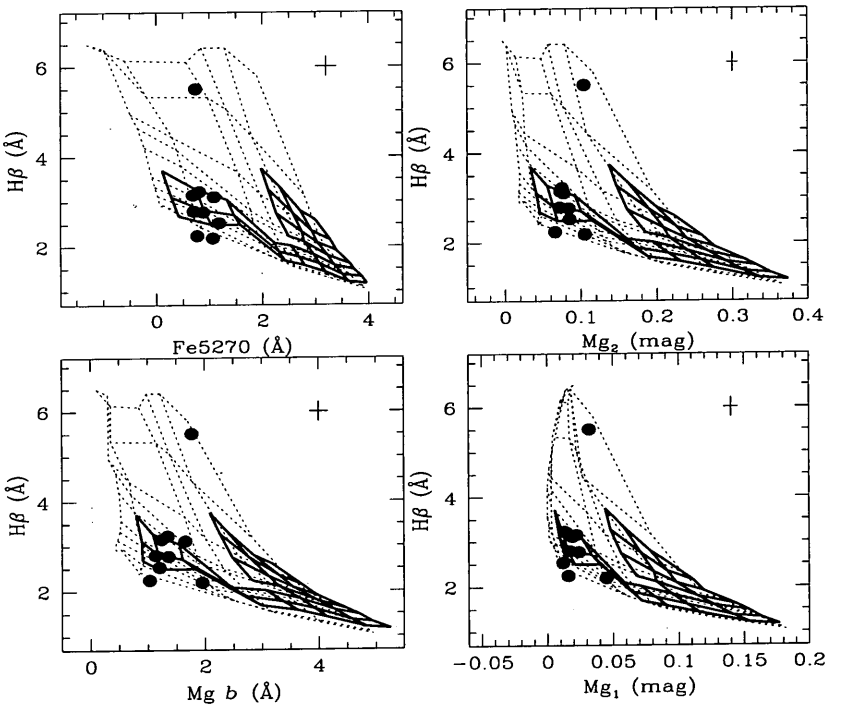

Figure 4.33: Comparison of SWB VII clusters with SSP grids of W94 and KFF99. Symbols are as for Figure 4.23.

extrapolate the models. Clearly the larger the extrapolation required, the larger the uncertainty in the age and metallicity determination. The principle requirement of the algorithm is that the data-points must be uniquely described. This presents a problem for the KFF99 models at old ages and low metallicities since these grids become degenerate. For a given a star cluster of metallicity [Fe/H] = -1.65 and Hβ = 2.58 Å, the KFF99 models predict ages of 10 Gyr *or* 16 Gyr. Moreover, the grids show a saddle-point minima at $\sim$ 12 Gyr for [Fe/H] $\leq$ -1.00, it is not obvious how to extrapolate for points which lie below these grids. We address this problem by determining two different ages and metallicities for the clusters in these regions, one determination from the W94 models, one from those of KFF99. We adopt the younger of the two ages predicted by the KFF99 grids, so avoiding the uncertainty of extrapolation for the majority of the clusters.

We derive ages and metallicities for the LMC clusters from the predictions of the Fe5270, Fe5335, Mg_2 and Mg *b* indices, in conjunction with the Hβ index. We have chosen not to include metallicity determinations derived from Mg_1. This molecular index is the equivalent of Burstein et al.'s MgH index, and since we obtain metallicities from Mg *b* and Mg_2 (MgH $\sim$ Mg *b* + Mg_2), using Mg_1 will give unjustified weight to these magnesium indices. Moreover, in terms of metallicity, inspection of the Hβ–Mg_1 grid (e.g. lower right panel, Figure 4.33) indicates that Mg_1 has little predictive power for the most metal-poor clusters. We obtain the uncertainties in age and metallicity for each index prediction by creating an 'error-ellipse' about each measurement, with its principle axes being defined by the index uncertainties. We then minimize and maximize the index values for this ellipse, yielding minimum and maximum values in age and metallicity for each cluster. The uncertainties derived for the clusters are not always symmetric. The SSP grids are non-orthogonal in age and metallicity; the degree of 'squashing' of the grid varies from index to index and is highly position dependent. Where the error-ellipse maps onto more than one grid-square, the magnitude of the difference between the + and - uncertainty can vary considerably.

We list our derived ages and metallicities for the LMC clusters in Table 4.11. We give the weighted mean age and metallicity predicted for each cluster, with weights assigned on the basis of our uncertainty in each index.

For clusters of SWB-types 0 and I which show emission, we place an upper limit on the ages of the cluster of τ = 0.5 Gyr (log[τ/yr] = 8.70), which is the lowest computed age of the KFF99 models. We then derive metallicities for these clusters from the KFF99 models, adopting this age.

Table 4.11.: Age and metallicity predictions for the LMC clusters.
Columns are : (1) ID, suffix w = W94 model predictions; * = emission affected,
(2) [Fe/H] (this work), (3) age (log [τ/yr]), (4) literature [Fe/H](colon denotes assumed metallicity by authors),
(5) literature age (log [τ/yr]), (6) references; 1: Bomans, Vallenari, & de Boer (1995), 2: Brocato et al. (1997),
3: Dolphin & Hunter (1998), 4: Olsen et al. (1998), 5: Olszewski et al. (1991),
6: Vallenari et al. (1994), 7: Geisler et al. (1997), 8: Sagar, Richtler, & de Boer (1991),
9: Corsi et al. (1994), 10: Dirsch et al. (2000), 11: Elson & Fall (1988).
Column(7) : source, StrP = Strömgren Photometry, Spec. = Spectroscopy of late-type giants,
CMD = ground-based Colour-Magnitude diagram, *HST* CMD = *HST* Colour-Magnitude diagram
problematical = poor agreement between indices.

ID	[Fe/H]	log (Age[y])	$[Fe/H]_{lit}$	$\log (Age[y])_{lit}$	Reference	Notes
BRHT 14b*	$-0.72^{+0.11}_{-0.11}$	$8.70^{+0.00}_{-0.00}$				
KMHK 1019*	$-0.60^{+0.26}_{-0.30}$	$8.81^{+0.28}_{-0.34}$				
M-OB 4*	$0.04^{+0.16}_{-0.16}$	$8.70^{+0.00}_{-0.00}$				
NGC 1711*	$-0.72^{+0.12}_{-0.12}$	$8.70^{+0.00}_{-0.00}$	-0.57±0.17	7.7±0.05	10	StrP.
NGC 1718	$-0.80^{+0.28}_{-0.21}$	$9.48^{+0.28}_{-0.15}$		9.26±0.08	11	CMD
NGC 1735	$-1.33^{+0.22}_{-0.25}$	$9.40^{+0.30}_{-0.32}$				
NGC 1751	$0.01^{+0.24}_{-0.26}$	$8.81^{+0.29}_{-0.32}$	-0.18±0.2		5	Spec.
NGC 1754	$-1.15^{+0.12}_{-0.13}$	$9.60^{+0.18}_{-0.19}$	-1.42±0.15	10.19±0.06	4,5	*HST* CMD
NGC 1754w	$-1.25^{+0.14}_{-0.14}$	$9.90^{+0.09}_{-0.09}$	...	...	...	...
NGC 1755	$-0.80^{+0.30}_{-0.33}$	$9.04^{+0.11}_{-0.08}$				
NGC 1767*	$-0.75^{+0.17}_{-0.17}$	$8.70^{+0.00}_{-0.00}$				
NGC 1774	$-0.77^{+0.18}_{-0.20}$	$8.70^{+0.11}_{-0.08}$				
NGC 1782	$-1.49^{+0.15}_{-0.29}$	$9.26^{+0.20}_{-0.06}$				
NGC 1786	$-1.45^{+0.23}_{-0.19}$	$9.98^{+0.10}_{-0.09}$	-1.87±0.2	10.02	2,5	CMD, Spec.
NGC 1786w	$-1.51^{+0.17}_{-0.11}$	$10.10^{+0.06}_{-0.06}$	...	...	...	...
NGC 1801	$-0.77^{+0.33}_{-0.45}$	$8.78^{+0.10}_{-0.07}$				
NGC 1806	$-0.40^{+0.23}_{-0.34}$	$9.35^{+0.24}_{-0.29}$	-0.71±0.24	8.7±0.1	12,5	StrP.
NGC 1815*	$-0.78^{+0.25}_{-0.25}$	$8.70^{+0.00}_{-0.00}$				
NGC 1825*	$0.22^{+0.09}_{-0.09}$	$8.70^{+0.00}_{-0.00}$				
NGC 1830	$-0.71^{+0.23}_{-0.24}$	$9.09^{+0.12}_{-0.16}$				
NGC 1834*	$-0.19^{+0.21}_{-0.21}$	$8.70^{+0.00}_{-0.00}$		7.90±0.2	13	CMD
NGC 1835	$-1.27^{+0.22}_{-0.27}$	$9.93^{+0.12}_{-0.17}$	-1.62±0.15	10.21±0.07	4,5	*HST* CMD, Spec.
NGC 1835w	$-1.38^{+0.20}_{-0.23}$	$10.09^{+0.09}_{-0.07}$	....	...	...	...
NGC 1846	$-0.65^{+0.23}_{-0.26}$	$9.33^{+0.17}_{-0.10}$	-0.70±0.2		5	Spec.
NGC 1852	$-0.60^{+0.29}_{-0.25}$	$9.29^{+0.22}_{-0.05}$				
NGC 1856	$0.00^{+0.18}_{-0.17}$	$8.81^{+0.06}_{-0.07}$		8.08±0.14	11	CMD
NGC 1863	$-1.19^{+0.33}_{-0.33}$	$8.99^{+0.10}_{-0.08}$		7.94±0.2	11	CMD
NGC 1865	$-0.04^{+0.27}_{-0.41}$	$8.76^{+0.18}_{-0.18}$		8.95	7	CMD
NGC 1872*	$-0.68^{+0.29}_{-0.31}$	$8.70^{+0.16}_{-0.07}$				

continued from previous page

ID	[Fe/H]	log (Age[y])	$[Fe/H]_{lit}$	$\log (Age[y])_{lit}$	Reference	Notes
NGC 1878	$-0.17^{+0.22}_{-0.21}$	$8.81^{+0.09}_{-0.08}$				
NGC 1898	$-0.97^{+0.22}_{-0.22}$	$10.02^{+0.15}_{-0.08}$	-1.18±0.16	10.13±0.07	4,5	*HST* CMD, Spec.
NGC 1898w	$-1.28^{+0.22}_{-0.22}$	$10.30^{+0.06}_{-0.06}$	...	...	...	...
NGC 1916	$-1.57^{+0.16}_{-0.14}$	$10.11^{+0.09}_{-0.09}$	-2.08±0.2		5	Spec.
NGC 1916w	$-1.74^{+0.24}_{-0.24}$	$10.31^{+0.05}_{-0.05}$	...	...	...	...
NGC 1939	$-1.39^{+0.25}_{-0.26}$	$9.72^{+0.14}_{-0.09}$				
NGC 1939w	$-1.41^{+0.17}_{-0.20}$	$9.95^{+0.06}_{-0.06}$				
NGC 1940	$-0.15^{+0.18}_{-0.26}$	$8.93^{+0.15}_{-0.09}$				
NGC 1943*	—	—				no correction appl.
NGC 1951	$-0.50^{+0.61}_{-0.66}$	$9.40^{+0.21}_{-0.11}$				problematical
NGC 1967*	$-0.60^{+0.23}_{-0.23}$	$8.70^{+0.00}_{-0.00}$				
NGC 1978	$-0.35^{+0.16}_{-0.18}$	$9.28^{+0.14}_{-0.16}$	-0.42±0.2	9.34	5,1	Spec., CMD
NGC 1987	$-0.51^{+0.22}_{-0.25}$	$9.37^{+0.13}_{-0.06}$	-0.4:	8.76	9	CMD
NGC 2002*	$-0.33^{+0.15}_{-0.15}$	$8.70^{+0.00}_{-0.00}$				
NGC 2004*	$-0.22^{+0.24}_{-0.23}$	$8.70^{+0.00}_{-0.00}$	-0.4	7.19±0.15	3	CMD
NGC 2005	$-1.15^{+0.37}_{-0.38}$	$9.62^{+0.16}_{-0.15}$	-1.35±0.15	10.22±0.11	4,5	*HST* CMD, Spec.
NGC 2005w	$-1.24^{+0.22}_{-0.28}$	$9.89^{+0.13}_{-0.13}$	...	...	...	...
NGC 2019	$-1.37^{+0.16}_{-0.18}$	$10.19^{+0.10}_{-0.10}$	-1.23±0.15	10.21±0.08	4,5	*HST* CMD, Spec.
NGC 2019w	$-1.45^{+0.19}_{-0.66}$	$10.23^{+0.09}_{-0.09}$	...	...	...	...
NGC 2031	$-1.27^{+0.41}_{-0.42}$	$9.13^{+0.16}_{-0.11}$	-0.52±0.21	8.2±0.1	10	StrP., problematical
NGC 2038	$-0.54^{+0.30}_{-0.33}$	$9.15^{+0.22}_{-0.18}$				
NGC 2041	$-0.51^{+0.23}_{-0.35}$	$9.00^{+0.17}_{-0.10}$				
NGC 2051	$-0.43^{+0.23}_{-0.29}$	$8.95^{+0.07}_{-0.08}$				
NGC 2056	$-0.28^{+0.22}_{-0.22}$	$8.79^{+0.07}_{-0.02}$				
NGC 2065	$-1.66^{+0.98}_{-0.24}$	$9.08^{+0.10}_{-0.20}$		8.03± 0.20	11	CMD, problematical
NGC 2100*	$-0.73^{+0.17}_{-0.17}$	$8.70^{+0.00}_{-0.00}$	-0.4:	7.40±0.06	8	CMD
NGC 2102*	$-0.10^{+0.24}_{-0.24}$	$8.70^{+0.00}_{-0.00}$				
NGC 2107	$-0.30^{+0.21}_{-0.23}$	$8.86^{+0.07}_{-0.03}$	-0.4:	8.37	9	CMD
NGC 2108	$-0.21^{+0.29}_{-0.25}$	$9.29^{+0.16}_{-0.14}$	-0.4:	8.77	9	CMD
NGC 2127	$-0.51^{+0.28}_{-0.39}$	$9.01^{+0.17}_{-0.12}$				
NGC 2134	$0.01^{+0.38}_{-0.35}$	$8.65^{+0.18}_{-0.16}$	-0.4	8.28	6	CMD
NGC 2135	$-0.70^{+0.23}_{-0.33}$	$8.81^{+0.09}_{-0.06}$				
NGC 2136	$-1.09^{+0.39}_{-0.34}$	$9.25^{+0.13}_{-0.13}$	-0.55±0.23	8.0±0.1	10	StrP., problematical
Rob 1*	$-0.45^{+0.18}_{-0.18}$	$8.70^{+0.00}_{-0.00}$				
SL 106*	$-0.71^{+0.22}_{-0.22}$	$8.70^{+0.00}_{-0.00}$				
SL 230*	$0.06^{+0.16}_{-0.16}$	$8.70^{+0.00}_{-0.00}$				
SL 250	$-0.43^{+0.31}_{-0.35}$	$9.44^{+0.15}_{-0.18}$				
SL 360*	$0.19^{+0.25}_{-0.25}$	$8.70^{+0.00}_{-0.00}$				

continued from previous page

ID	[Fe/H]	log (Age[y])	[Fe/H]$_{lit}$	log (Age[y])$_{lit}$	Reference	Notes
SL 586 *	$-1.15^{+0.14}_{-0.14}$	$8.70^{+0.00}_{-0.00}$				
SL 601*	$-0.36^{+0.25}_{-0.25}$	$8.70^{+0.00}_{-0.00}$				
SL 675	$-0.19^{+0.36}_{-0.36}$	$9.16^{+0.19}_{-0.15}$				
SL 709	$-0.66^{+0.19}_{-0.27}$	$8.98^{+0.09}_{-0.05}$				
SL 741	$-0.50^{+0.69}_{-0.97}$	$9.32^{+0.36}_{-0.28}$				problematical

4.7 The Cluster Ages and Metallicities

4.7.1 Literature Comparisons

In order to compare our results with the literature, we have compiled a list of ages and metallicities for our clusters (where available) from a number of sources. We have given highest priority to data from *HST* CMDs and spectroscopic observations of individual cluster stars. For ground-based CMDs, we have placed a strict magnitude limit of $V = 21.0$ to act as a rough 'quality control' (e.g. Dirsch et al. 2000). The list is less than complete, whilst a large number of the clusters in Table 4.11 have literature age and metallicity determinations from integrated photometry and/or spectroscopy, there are many examples of strong disagreement for the same clusters. For five of the six old clusters in their *HST* sample, Olsen et al. (1998) quote two metallicity values, from the stellar spectroscopy of Olszewski et al. (1991), and using the method of Sarajedini (1994). This latter technique uses the height of the red giant branch above the horizontal branch to simultaneously determine the metallicity and reddening of the cluster and we have chosen to adopt the metallicities obtained using this approach. As pointed out by Olsen et al. (1998), the admirable metallicity determinations of Olszewski et al. (1991), which rely upon observations of one or two late-type giant stars, are extremely difficult to perform and somewhat susceptible to small sample sizes. The metallicities determined by Olszewski et al. (1991) are up to 0.5 dex *lower* than those using the CMD-morphology technique.

In Figure 4.34 we plot our metallicity determinations against literature values given in Table 4.11. We apply a linear weighted fit to the data (dotted line in Figure 4.34), and compare it to the line of unit slope (solid line). It may be argued that the relation between metallicities in Figure 4.34 is non-linear, and may perhaps be better fit by some polynomial. However without extra information (i.e. more data-points or some underlying physical justification), we apply a

linear fit for the sake of simplicity. Using the KFF99-derived values for the metal-poor clusters, we obtain a slope of almost unity (c = 0.97) and an offset of + 0.12 dex, and an rms, σ = 0.21 dex. Using the W94-derived metallicities (again, only for the metal-poor clusters) yields c = 0.99, an offset of + 0.10 dex and σ = 0.20 dex.

The agreement between these data is generally good, however at [Fe/H] $\leq$ -1.4, there is evidence that we derive higher metallicities than the literature values. Indeed, as one goes to lower abundances, our metallicity predictions become flatter than unit slope. The origin of this divergence between the model predictions and literature values is unclear. For two of the GCs in our sample, NGC 1754 and NGC 2005, we predict significantly younger ages than is indicated by their CMDs (see later). Moving the clusters to younger ages on the SSP grids would indeed have the effect of increasing their predicted metallicities. However, the divergence seen in Figure 4.34 appears *systematic*, and perhaps indicates that the models under predict metallicities at the lowest abundances.

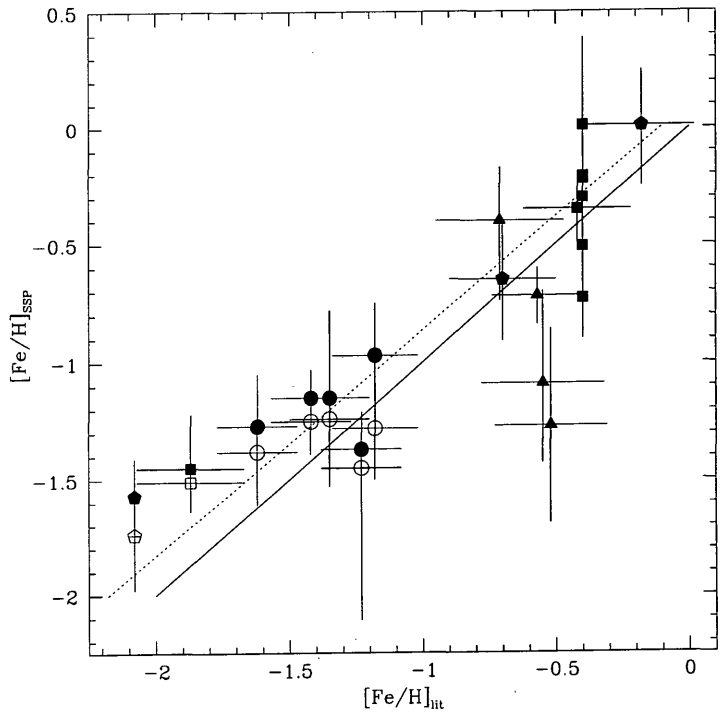

Figure 4.34: Comparison between our metallicity determinations and those of the literature. Circles : *HST* CMDs, squares : ground-based CMD, triangles : Strömgren Photometry, pentagons : stellar spectroscopy (see Table 4.11 for sources). Solid symbols indicate metallicities derived from KFF99 models, open symbols show alternative metallicity derived using W94 models (for the metal-poor clusters). The solid line is of unit slope, the dotted line is a linear-fit to these data (see discussion in text).

Nevertheless, we do find that within the uncertainties, and with the exception of NGC 1786 and NGC 1916, our metallicities for the clusters are consistent with the literature determinations. For both NGC 1786 and NGC 1916, we have used the metallicities of Olszewski et al. (1991) ($[Fe/H]_{N1786}$ = -1.86 $\pm$ 0.2; $[Fe/H]_{N1916}$ = -2.08 $\pm$ 0.2), since Olsen et al. (1998) could not derive a value for NGC 1916, due to the effects of crowding and differential reddening and NGC 1786 was not in their sample. We obtain $[Fe/H]_{N1786} = -1.42^{+0.12}_{-0.13}$, $[Fe/H]_{N1786} = -1.51^{+0.17}_{-0.11}$ and $[Fe/H]_{N1916} = -1.57^{+0.16}_{-0.14}$, $[Fe/H]_{N1916} = -1.74^{+0.24}_{-0.24}$ using the KFF99 and W94 models respectively for these clusters. In each case, we predict metallicities which are $\sim$ 0.4 dex higher than those given by Olszewski et al. (1991).

With regards to the more metal-rich clusters, we find that two are inconsistent with the literature. For NGC 2031 and NGC 2136 we obtain [Fe/H] = $-1.27^{+0.41}_{-0.42}$ and $-1.09^{+0.39}_{-0.34}$ respectively, whereas the metallicities given in Table 4.11 are -0.52 $\pm$ 0.21 and -0.55 $\pm$ 0.23 (both values derived from the Strömgren photometry of Dirsch et al. 2000). However, as previously mentioned both NGC 2031 and NGC 2136 show inconsistencies between different indices (reflected by their large uncertainties) and both are of rather low S/N ($\sim$ 30). For these reasons, we have excluded these two clusters from the following age comparisons.

In Figure 4.35 we compare our ages derived for the LMC star clusters to the literature values. In order to compare the clusters on a linear age scale, Figure 4.35 has been split into three panels; the top panel for clusters with literature ages younger than $\tau < 0.5 \times 10^9$ yr, middle panel for clusters with $0.5 < \tau < 3.0$ Gyr and the lower panel for star clusters older than 3 Gyr. Again, we show a line of unit slope in the figure (dotted line). For star clusters with literature ages less than $\sim$ 0.5 Gyr we consistently derive higher ages using the SSP models. In the mean, we obtain ages $\sim$ 0.7 Gyr older than the literature values. This discrepancy has several origins. The most obvious is the fact that on the basis of emission in their spectra, we have assigned four of the clusters (indicated by the open symbols in the top panel) an age of 0.5 Gyr. However, less trivially, with the exception of NGC 2134, none of these clusters lie above the 0.5 Gyr line of the KFF99 grids. This could be due to either: i) emission affecting these clusters at a level which we could not detect, ii) stochastic effects are affecting these youngest clusters (see § 4.6.4) or iii) the KFF99 models overestimate Hβ at these very young ages. Clearly, if the clusters did lie above the 0.5 Gyr line of the KFF99 grid, the youngest age predicted by these models, their derived ages would still be uncertain due to the subsequent extrapolation required.

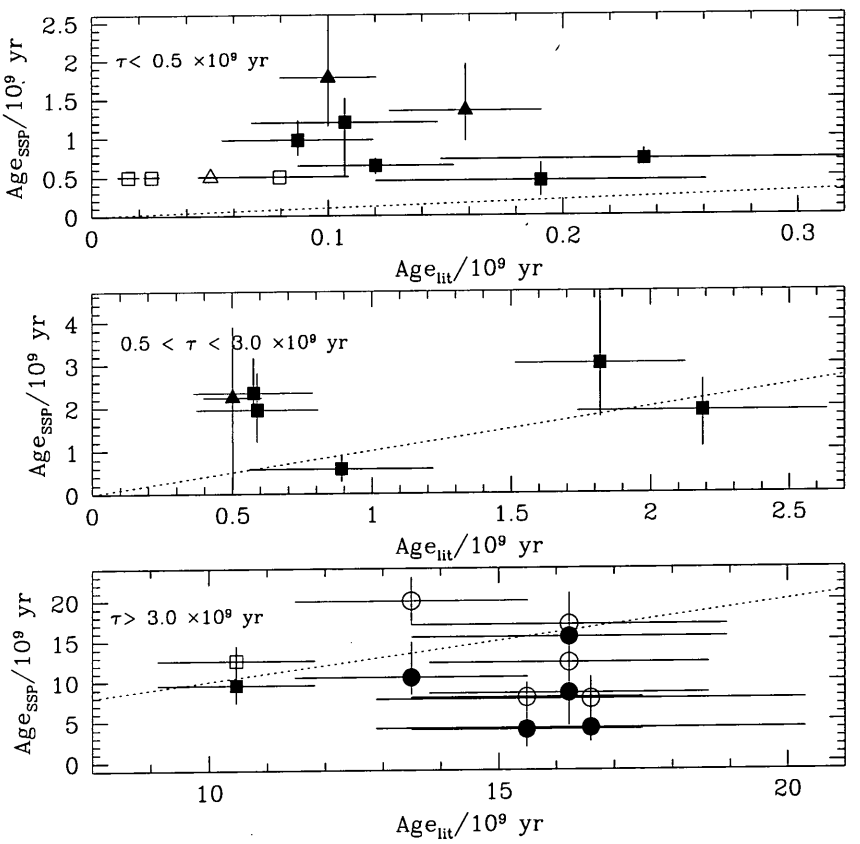

Figure 4.35: Comparison between our age determinations and those of the literature. The top panel shows clusters with literature ages $< 0.5 \times 10^9$ yr, middle panel clusters with $0.5 < \tau < 3.0$ Gyr and the lower panel shows clusters older than 3 Gyr. Symbols indicate origin of literature age determinations; circles : *HST* CMDs, squares : ground-based CMD, triangles : Strömgren Photometry, pentagons : stellar spectroscopy (see Table 4.11 for sources). Solid black symbols indicate ages derived using the KFF99 models. In the top panel, open symbols indicate the emission-affected clusters which we have assigned an age of 0.5 Gyr. Open symbols in the bottom panel indicate alternative ages derived using W94 models (for the old, metal-poor clusters), the dotted lines are of unit slope (see discussion in text).

The SSP and literature ages for the intermediate-age clusters ($0.5 \sim 3.0$ Gyr) are generally in good agreement, although admittedly the number of clusters we have for comparison at these ages is low (i.e. 6). We predict slightly higher ages from our integrated spectra, but this is not significant given the uncertainties.

Our derived ages for the old clusters are in reasonably good agreement with the literature. As discussed in § 4.6.1 the W94 models typically predict ages which are several Gyr older than those of KFF99 (dependent on metallicity). The locus of the W94 derived ages is in somewhat better agreement with the unit slope than those derived using the KFF99 grids. As seen in Figure 4.34,

the metallicities for these clusters are generally 0.1–0.3 dex higher than the literature; decreasing the metallicity of these clusters on the SSP grids by this amount will age the clusters by $\sim$ 1–2 Gyr. Our derived ages for NGC 1786, and NGC 2019 are both in excellent agreement with the literature values, as is W94-derived age for NGC 1835 ($12.3^{+1.5}_{-2.1}$ Gyr) which is consistent with the age found by Olsen et al. (1998). We find that the age of NGC 1898 as predicted by the W94 models ($\tau = 20 \pm 3$ Gyr) is older than found by Olsen et al. (13.5 ± 2.3 Gyr) and better agreement is found using KFF99 (10.4 Gyr). However, two of the clusters in the lower panel of Figure 4.35 depart significantly from the ages derived by Olsen et al. (1998). We find that both NGC 1754 and NGC 2005 are predicted by the W94 models to be $\sim$ 8 Gyr younger than the ages found by Olsen et al.. NGC 2005 is in a dense bar region, and is perhaps affected by field-star contamination. Moreover, as indicated in § 4.6.5, this cluster also shows hints of a very blue horizontal branch. Both these factors could in principle enhance the Hβ measured in this clusters spectrum, yielding artificially young ages from the SSP models. However, NGC 1754 is in an area of relatively low stellar density, and whilst it shows some signs of a horizontal branch extending bluewards (Olsen et al. 1998), it is no bluer than the horizontal branches of NGC 1835 and NGC 2019.

4.7.2 Age and Metallicity Distribution

We have seen that the ages and metallicities of our cluster sample are generally in agreement with the literature values. We now look at the age and metallicity distributions within our sample, and the age–metallicity relation (AMR) of the LMC clusters inferred from these data.

In Figure 4.36 we show the age and metallicity distribution of our cluster sample. The age distribution (top panel) shows a clear break, with no clusters of ages $3.0 \leq \tau \leq 9.0$ Gyr. This separation of 'old' and 'young' clusters, with none of intermediate ages, is a principle characteristic of the LMC cluster system (e.g. Westerlund 1997). The pile-up of clusters at the very youngest ages of the models is artificial, the majority of these clusters are those which we have assigned an age of 0.5 Gyr due to emission contamination. In reality these clusters should have much younger ages.

In the lower panel of Figure 4.36 we show the metallicity distribution of the LMC clusters, compared to that of the Milky Way GCs (taken from the McMaster catalogue of Harris 1996). In the Galaxy, there are a greater number of metal-poor ($\leq$ -0.8) 'halo' GCs than metal-rich GCs (those commonly associated with the thick-disk), in the approximate ratio 3:1 (Ashman & Zepf 1998). This is in the opposite sense to the LMC distribution, with a far greater number of the star

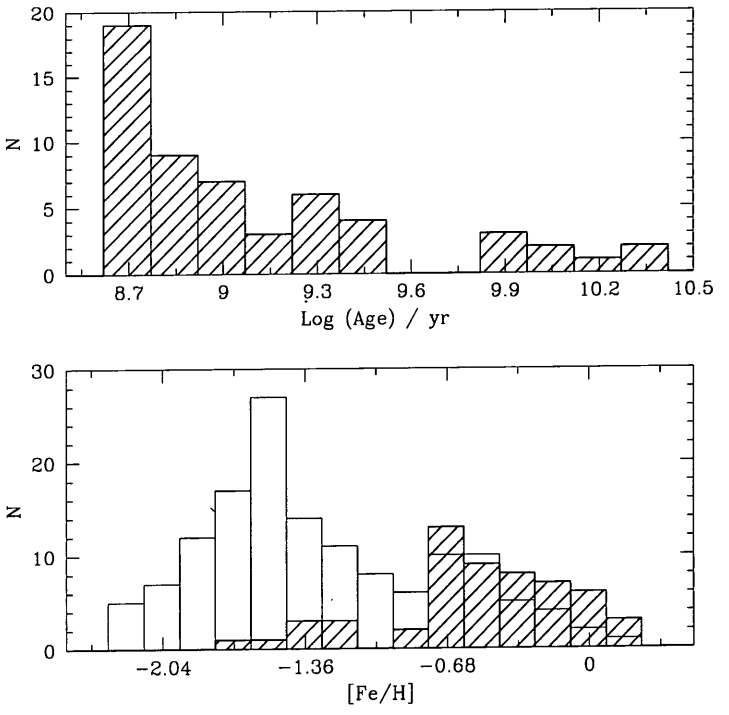

Figure 4.36: Top panel: logarithmic age distribution of our cluster sample, Lower panel: metallicity distribution of LMC clusters (shaded histogram). The open histogram shows the metallicity distribution of the Milky Way GCS (Harris 1996).

clusters at the metal-rich end of the distribution. However, these younger clusters in the LMC are generally more akin to the *open* clusters of the Galaxy, in terms of mass, age and metallicity.

The KMM mixture-modelling test (Ashman, Bird, & Zepf 1994) was applied to the metallicities of the clusters. This test determines the confidence level at which subpopulations may be present within a dataset, and finds the relative contribution from each subpopulation. We find that, for the homoscedastic case[12], the likelihood that the metallicities of the LMC clusters belong to two populations is $> 99\%$ confidence, with peaks at -0.45, $\sigma = 0.31$ and -1.40, $\sigma = 0.2$. As is the case for the Milky Way GCs, the LMC metallicity distribution is bimodal.

The situation is not quite so clear cut for the age distribution, mainly due to the pile-up of the clusters at 0.5 Gyr. Moreover, the ages clearly do not follow a Gaussian distribution, and are more like a power-law. However, by simply separating the populations at $\tau = 4$ Gyr (i.e. the gap in the the age histogram) we find the young and old populations have mean ages of 0.8 Gyr, $\sigma =$ 0.24 Gyr and 12.6 Gyr, $\sigma = 5.0$ Gyr respectively. This mean age for the younger population

[12] i.e. A common covariance

should certainly be regarded as an upper limit in these data. There are 48 star clusters in the young population, and 8 to the older group. Whilst this ratio of 6:1 has no particular significance (our cluster selection deliberately targeted a range of ages), it is illustrative that the number of young clusters far outweighs that of the older population.

The absence of clusters between $3.0 \leq \tau \leq 9.0$ Gyr implies that the LMC clusters are useful probes of the chemical enrichment of this galaxy, but *cannot* be used for deriving star formation rates.

4.7.3 The Age–Metallicity Relation

Efforts to determine the AMR of the LMC clusters have been undertaken using broad-band photometry (Westerlund 1997). Work in this vein has been continued by Bica et al. (1998) using the Washington system and by Dirsch et al. (2000) using Strömgren photometry. de Freitas Pacheco, Barbuy, & Idiart (1998) plot an AMR for LMC clusters, with ages and metallicities determined using Lick/IDS indices compared to the SSP models of Borges et al. (1995) (see figure 2 in de Freitas Pacheco, Barbuy, & Idiart 1998). However, few conclusions can be drawn from the AMR they plot, since their sample only comprises of 8 clusters. Here, we construct an AMR for our sample of LMC clusters, and show this in Figure 4.37.

The bimodal nature of the clusters can be clearly seen in the figure, both in terms of age and metallicity. The solid line in Figure 4.37 indicates the AMR of the LMC field stars derived from the Strömgren photometry of Dirsch et al. (2000). The mean metallicity of the field stars at $\tau < 10^9$ yr is -0.4 $\pm$ 0.2, identical to the mean metallicity for our youngest clusters. However, in the age range 1.5–3 Gyr, our clusters are more metal-rich than the field stars by $\sim$ 0.3 dex . This is in the opposite sense to that found by Dirsch et al. (2000), and is more consistent with the data of Bica et al. (1998), who obtain a mean metallicity of $\langle$[Fe/H]$\rangle$ $\simeq$ -0.56 $\pm$ 0.1 dex from the Washington photometry of 13 clusters and their surrounding fields. Indeed, Dirsch et al. (2000) indicate the possibility of a zero-point difference of up to 0.2 dex between their data and the literature, which would make our data consistent with that of Dirsch et al. (2000).

We show two models of chemical enrichment for the LMC; the closed-box models of Geha et al.(1998) (dashed lines) and that of Pagel & Tautvaisiene (1998) (dotted line), which account for inflow and a homogeneous galactic wind in the Cloud. Dirsch et al. (2000) find that the models of Geha et al. (1998) are consistent with their field-star AMR. These authors present enrichment models based upon the star formation histories (SFHs) of Vallenari et al. (1996) and Holtzman

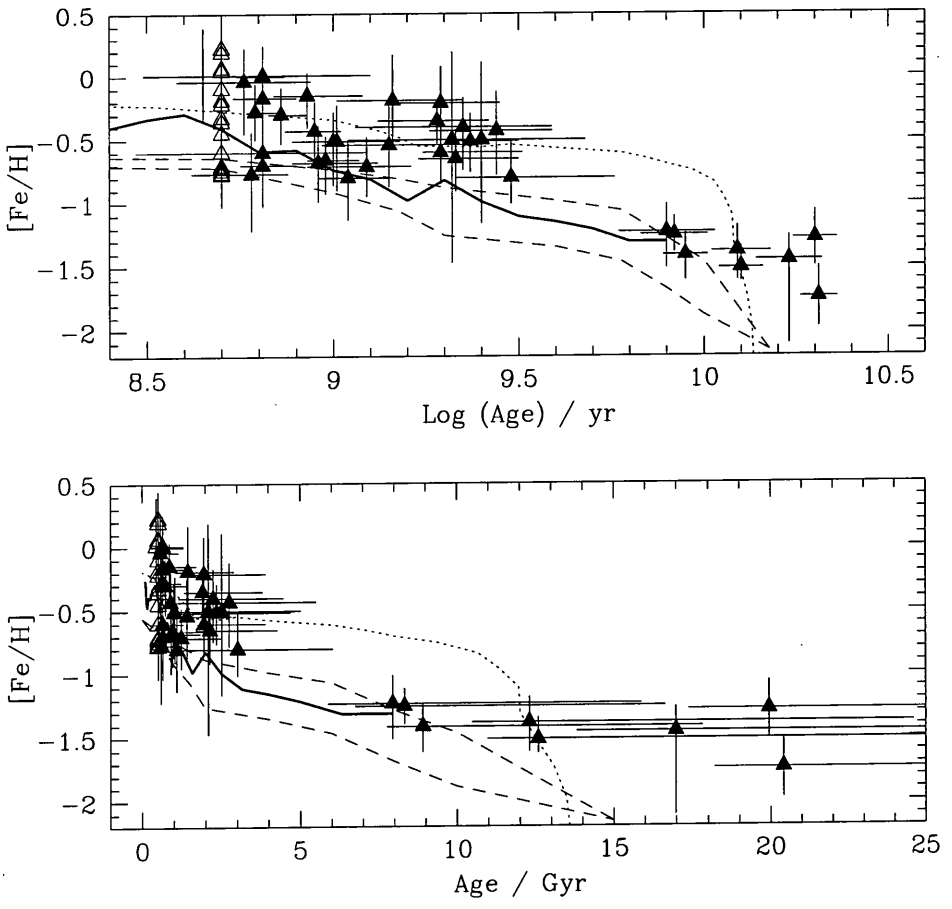

Figure 4.37: Age–metallicity relation for our cluster sample on both logarithmic (top panel) and linear age scale. Triangles represent the LMC clusters, open symbols indicate the emission-affected clusters. We also show the AMR of the LMC field stars (solid line) taken from Dirsch et al. (2000), in addition to the chemical-enrichment models of Pagel & Tautvaisiene (1998) (dotted line) and those of Geha et al. (1998) (dashed lines).

et al. (1997). Both these SFHs indicate a long period of quiescent star-formation, followed by a sharp increase some 2 Gyr ago, leading to increased metal enrichment. The principle difference between the two SFHs being the degree of enrichment, that of Holtzman et al. (1997) indicates metallicity increased by a factor of ~ 3, whereas Vallenari et al.'s shows a factor of 5 increase in the past 2 Gyr. Moreover, Dirsch et al. (2000) find that the model of Pagel & Tautvaisiene (1998), based upon observations of planetary nebulae by Dopita et al. (1997), is inconsistent with the AMR of their field-stars. The Pagel & Tautvaisiene (1998) models would seem predict too steep a rise in metallicity at early times.

To investigate this matter further, we re-plot the chemical enrichment models of Geha et al.(1998) and Pagel & Tautvaisiene (1998), the field-star AMR of Dirsch et al. (2000) and our star cluster AMR in Figure 4.38.

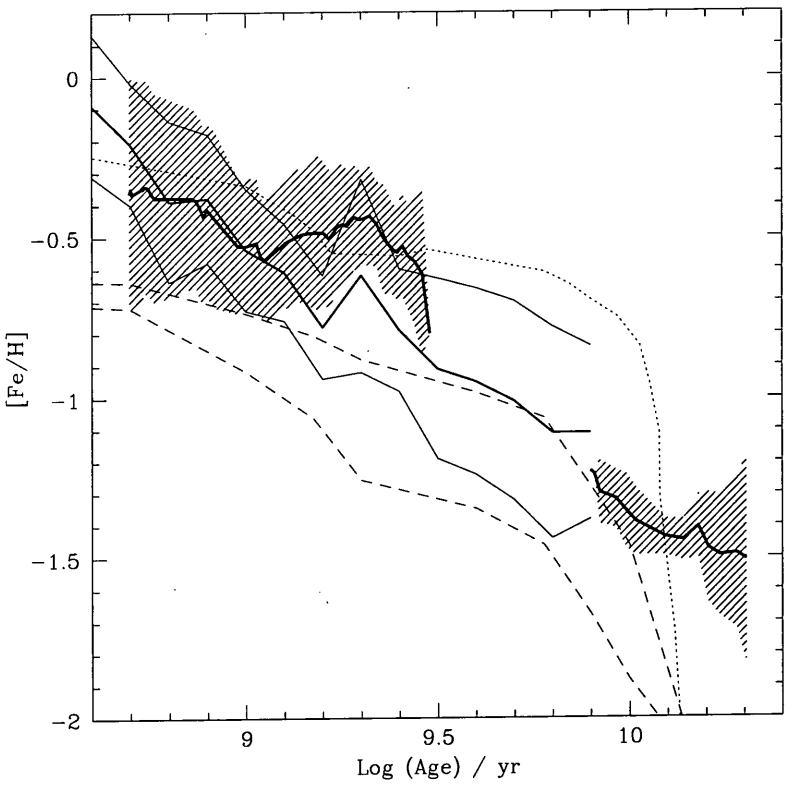

Figure 4.38: Comparison of our smoothed star cluster AMR (thick solid line) with the field star data of Dirsch et al. (2000) (thin solid line) and the chemical enrichment models of Geha et al.(1998) (dashed lines) and Pagel & Tautvaisiene (1998) (dotted line). The shaded region indicates our 1-σ uncertainties in metallicity, the points are correlated with a smoothing length of 0.1 in log (age). We have added an offset of +0.2 dex to the data of Dirsch et al. (2000) and indicate their 1-σ uncertainties (faintest solid lines).

For comparison to the field-star AMR of Dirsch et al. (2000), we have smoothed our data with a Gaussian kernel of width 0.1 in log (age), and show the formal 1-σ uncertainties from this smoothing (shaded region). We have added a constant of 0.2 dex to the data of Dirsch et al. (2000) operating under the (possibly incorrect) assumption of a zero-point offset in their data.

Interestingly, the overall behaviour of the AMR of the younger ($\leq$ 3.0 Gyr) clusters closely mimics that of the fields stars, even to the point of showing a slight increase in mean metallicity at $\sim$ 2.0 Gyr. The gap between $10^{9.5} \sim 10^{9.9}$ yr indicates the lack of clusters in this region. Whilst unequivocally dangerous, a linear extrapolation across this region would remain consistent with

the field-star AMR. In any event, these data do not argue for a decoupled enrichment history for the star clusters and LMC field stars.

Comparing our data to the enrichment models, we find that for the young clusters, our AMR is inconsistent with Geha et al.(1998) (dashed lines) both for the Vallenari et al. (1996) SFH, and for that of Holtzman et al. (1997).

Conversely, we find that the young clusters, our data is in much better agreement with the inflow and galactic wind models of Pagel & Tautvaisiene (1998). However, as found by Dirsch et al. (2000), the models of Pagel & Tautvaisiene (1998) predict to steep an enrichment for our metal-poor clusters. Even by using ages derived for the old clusters by the KFF99 models, which predict somewhat younger ages and higher metallicities, we cannot reconcile the Pagel & Tautvaisiene (1998) model with our data at early times.

4.8 Summary and Conclusions

We have measured Lick/IDS indices in the integrated spectra of 64 star clusters in the Large Magellanic Cloud. We have derived ages and metallicities for these clusters using the single stellar population models of Worthey (1994) and Kurth, Fritze-v. Alvensleben, & Fricke (1999). We compare these predictions with literature values derived from colour-magnitude diagrams, photometry and spectroscopy and find:

- The metallicities predicted for the clusters are in good agreement with the literature values. However, in the mean, we derive metallicities which are + 0.15 dex more metal-rich than those derived from CMDs and/or spectroscopy. This offset is primarily driven by the old, metal-poor (i.e. globular) clusters; at [Fe/H] $\leq$ -1.4, the models yield increasingly higher metallicities than the literature values.

- The ages of the LMC star clusters obtained from the SSP models, are in generally good agreement with literature values. However, for the youngest clusters, we systematically derive ages some 0.7 Gyr older than those ages given in the literature. We find that for these clusters, and those clusters in areas of active star formation, emission acts to fill-in the Hβ index, making accurate age determinations difficult. This emission, coupled with possible stochastic effects in the IMF of the clusters and a lack of adequate fitting functions at the youngest ages, makes these SSP models unsuitable for star clusters younger than $\sim$ 1.0 Gyr. We find that the ages derived for the older star clusters ($\tau \geq$ 1.0 Gyr) and GCs ($\tau \geq$ 10 Gyr) are consistent with

CMD-derived ages. This good correspondence for the GCs indicates that, to first order at least, the assumptions in the models concerning horizontal-branch morphology and mass-loss are correct. Two significant departures from the literature values are the GCs NGC 1754 and NGC 2005, which are predicted to be $\sim$ 8.0 Gyr too young by the models. This perhaps stems from our inability to measure the Hβ indices of these clusters adequately (e.g. due to contamination from the field), or from a strong contribution due to the horizontal branch morphology of these clusters.

- We confirm the presence of an age-gap in the LMC cluster system, with no clusters of ages in the range $3.0 \leq \tau \leq 9.0$ Gyr. This age-gap has a corresponding metallicity gap at -1.2 $\leq$ [Fe/H] $\leq$ -0.8. Either no detectable clusters were formed during this period of the LMC's history, or they have been preferentially destroyed by some mechanism efficient at these times.

- We obtain an age–metallicity relation for our cluster sample. This in good agreement with the AMR of the LMC field stars derived from Strömgren photometry, arguing for a close degree of coupling between the enrichment histories of the clusters and field stars. We find our cluster AMR is inconsistent with closed-box chemical enrichment models. The AMR of the younger ($\tau < 3.0$ Gyr) clusters is better represented by enrichment models which account for inflow and a homogeneous galactic wind in the Large Cloud.

In Summary: the ages and metallicities of the LMC star clusters, obtained from integrated spectra, are consistent with those derived from CMDs, spectroscopy and photometry of individual stars. For the very young clusters, ages are uncertain due to a lack of model constraints and the effects of emission and possible stochastic effects. For the older stellar populations, the principle uncertainties originate from assumptions in horizontal-branch morphology and the possible effects of field-star contamination.

Providing the data is adequately calibrated to the adopted spectral system (e.g. the Lick/IDS), integrated spectral indices, coupled with the latest stellar population models provide an accurate method for deriving ages and metallicities of unresolved stellar systems.

Chapter 5

Conclusions

Abstract.

In this Section, a summary of the principle findings and conclusions of this thesis are presented. We discuss the problems inherent in searching for GCs in low-luminosity, late-type spirals, which are hampered by their small number of GCs and confusion with the disk of the galaxy. We then look at future avenues of research in this area.

Having clearly distinguished chemically and kinematically between the two GC subpopulations associated with NGC 4472 in Chapter 3, we try and understand their origin. We show the first results of a project employing a semi-analytical galaxy formation model to predict the observable properties of the GCS of elliptical galaxies. Assuming that GCs are formed in gas-rich mergers and in gaseous disks, we obtain bimodal and multi-modal metallicity distributions of striking similarity to those observed from broad-band colours. We find that the majority of GCS of elliptical galaxies will be bimodal, irrespective of galaxy luminosity. We find no correlation between either the blue or red peaks with host galaxy luminosity, with the red GCs showing large scatter at all luminosities. We conclude that GC formation is consistent with models of hierarchical clustering, and that mergers naturally lead to multimodal metallicity distributions, whilst forming GCS in a preferentially single mode is difficult.

We discuss the use of simple stellar population models in age-dating GCS from integrated spectra. We find that despite of the still present uncertainties in the stellar population models, their age and metallicity predictions are reasonable. We discuss that the principle uncertainty in measuring ages for metal-poor GCs arises from the uncertain contribution of blue horizontal-branch stars to the Balmer indices, and discuss an alternative to age-dating extragalactic GCs.

5.1 Summary and Conclusions

5.1.1 The GCS of Late-Type Spirals

In Chapter 2, we presented a spectroscopic survey of the GCS of two late-type spiral galaxies, based upon published catalogues of GC candidates. On the basis of their radial velocities and image parameters, we identified 14 GCs associated with the Sculptor Group spiral NGC 253, and one

probable GC belonging to NGC 55. From co-added spectra of the 14 NGC 253 GCs, we obtained a mean metallicity of [Fe/H] = -1.23 $\pm$ 0.19. Using the objects identified spectroscopically as GCs, foreground stars and background galaxies, in conjunction with COSMOS plate scans, we defined new samples of globular cluster candidates for these two galaxies. We estimated the total GC populations of NGC 55 and NGC 253 to be 24 $\pm$ 12 and 68 $\pm$ 18 respectively, yielding specific frequencies of 0.4 $\pm$ 0.2 and 0.7 $\pm$ 0.2. These specific frequencies, and the mean metallicity of the NGC 253 GCS, are consistent with the values expected for these galaxies' morphological type.

The contamination of the samples from field stars and background galaxies was 85% for the NGC 253 sample and 98% for NGC 55. This contrasts with a contamination of $\sim$ 20% for the spectroscopy of NGC 4472 GCs described in Chapter 3. Two principle factors are responsible for such a large number of objects which are not GCs entering into the NGC 253 and NGC 55 samples. The GCS of faint, late-type spirals are very poor compared to bright, early-type spiral and elliptical galaxies–for instance the GCS of NGC 4472 is a factor of $\sim$ 100 richer than that of NGC 253. Moreover, broad-band colours are an unreliable method of classifying GCs if the effects of reddening are uncertain - certainly the case for the samples of Liller & Alcaino (1983), Liller & Alcaino (1983) and Blecha (1986) which only employed $B - V$ colours. The level of contamination in the Liller & Alcaino and Blecha samples indicates the difficulty faced when undertaking searches of this type based on geometrical and/or photometric properties, especially in relatively poor cluster systems.

At the distance of Sculptor ($\sim$ 2.5 Mpc), GCs will be marginally resolved, with median diameters on the sky of $\sim 2\farcs5$, whilst the angular extent of these galaxies is $\sim 30'$. Assuming that the absolute magnitude of the turn-over of the GCLF for spirals occurs at M_V = -7.6 (Harris 1999), then the observed peak of the GCLF in Sculptor will occur at $V \sim 19.5$. Therefore, in order to identify a significant fraction of these galaxies GCS requires a survey in the presence of good seeing, with a wide-field and with relatively deep exposures. Such a survey has been undertaken by Bright & Olsen (2000), with the intention of spectroscopic follow-up. These authors have obtained CTIO 4-m mosaiced images for the Sculptor Galaxies NGC 24, NGC 45, NGC 55, NGC 247, NGC 253, NGC 300, and NGC 7793. On the basis of measured isophotal area, isophotal flux, ellipticity, $C - R$ and $M - R$ colours, they have identified 100-150 GC candidates for each galaxy, with properties similar to the GCs identified in this study. They estimate their contamination to be $\sim$ 50%, similar to that of our newly defined NGC 253 sample.

With the identification of *bona fide* GCs associated with the Sculptor Group galaxies, comes the prospect of building CMDs for these clusters–a project well within the capabilities of *HST*. Indeed, Harris, Poole, & Harris (1998) obtained *HST* WFPC-2 images of *N5128-C44* in NGC 5128, to date the most distant GC for which a colour-magnitude diagram has been constructed ($d \sim 4$ Mpc). With an integration time totalling 12800s in both V and I, Harris, Poole, & Harris (1998) reached two magnitudes down the giant branch of this GC, allowing them to derive a metallicity of [Fe/H] $\sim$ -1.3, and compare its stellar population with the galaxy halo. Since the distance to the Sculptor group is fully 1.5 magnitudes brighter than NGC 5128, equivalent observations would reach to the horizontal branch of Sculptor GCs, with stellar crowding in the cluster reduced by a factor of two.

5.1.2 The GCS of NGC 4472

In Chapter 3 we obtained 87 new spectra for GCs associated with the giant Virgo elliptical NGC 4472, using the multi-spectrograph at the CFHT. These data, combined with spectra from the study of Sharples et al. (1998), has yielded a dataset of 144 GCs for which we have obtained line-strengths from co-added spectra and kinematics from their measured radial velocities.

We find that our sample of GCs have metallicities of approximately -1.6 $\leq$ [Fe/H] $\leq$ 0, with the metallicity determinations derived from stellar population models, empirical line-strength calibrations, and from their integrated $C - T_1$ colours all in good agreement. We find some evidence for a radial gradient in the GCs, apparently not originating from the changing spatial distribution of the red and blue GCs. If real, this points towards some level of dissipation in the NGC 4472 GCS.

Using Galactic GCs as calibrators for the Worthey (1994) models, the metal-poor (blue) population of GCs have an age of 14.5 $\pm$ 4 Gyr and the metal-rich (red) population are 13.8 $\pm$ 6 Gyr old. From Monte Carlo simulations, we have placed lower limits on the ages of the GCs of 6 Gyr at the 95% confidence level. Therefore, we find that within the uncertainties, the GCs are old and coeval, implying that the bimodality seen in their broadband colours primarily reflects differences in metallicity and not in age. These results are in agreement with a previous study (Puzia et al. 1999), but do not rely upon the assumption of identical mass distributions for the red and blue GCs.

From analysis of the GCS kinematics, we obtain a velocity dispersion of $\sigma = 356 \pm 25$ km s^{-1} for the blue GCs, whilst the red GCs have $\sigma = 221 \pm 22$ km s^{-1}, similar to the velocity dispersion of the NGC 4472 spheroid (Fisher, Franx, & Illingworth 1995). We find evidence for moderate

rotation ($\sim$100 km s^{-1}) in the blue clusters, but little or no rotation in the red GCs, for which we derive an upper limit of $(v/\sigma)_{\rm proj} < 0.34$ at the 99% confidence level.

These strong kinematical and chemical differences between the blue and red GCs lead us to conclude that they form distinct subpopulations, hitherto only inferred from their bimodal colour distributions. Moreover, the lack of rotation in the red GCs requires the efficient transport of angular momentum out of this dynamical system, which is perhaps most easily explained if NGC 4472 has undergone a major merger.

Finally, we obtain a mass profile for the GCs which is in good agreement with X-ray estimates, indicating that our assumptions about the orbital anisotropy of the GCs is roughly correct. We find a steeply rising $\mathcal{M}/L$ ratio with radius, indicative of a massive dark matter halo surrounding this galaxy.

5.1.3 Globular Clusters in the Hierarchical Model

Of the four principle models of GCS formation discussed in Chapter 3, three are constructed implicitly within the framework of the hierarchical formation of structure.[1]

In the 'primordial GCs' model, GCs are the first structure to form after recombination. These objects, the blue GCs, will thus be the oldest stellar systems in the Universe, composed of relatively un-enriched material. The red GCs then form later, from gas enriched after the first star formation (e.g. Rosenblatt, Faber, & Blumenthal 1988; West 1993; Kissler-Patig, Forbes, & Minniti 1998; Burgarella, Kissler-Patig, & Buat 2000).

In the merger model, gas-rich spirals merge to form elliptical galaxies (e.g. Toomre 1977), and in the process form GCs (e.g. Ashman & Zepf 1992). The blue GCs are those associated with the progenitor spirals, whilst the red GCs are formed from enriched gas during this merger process.

In the accretion scenario, the galactic halo is created in part (or entirely) from infalling satellites, either 'proto-Galactic' fragments (Searle & Zinn 1978), or dwarf galaxies (e.g. Mateo 1996; Hilker 1998; Cote, Marzke, & West 1998). In the model developed by Cote, Marzke, & West (1998), the latter is the case; dwarf galaxies become accreted to become part of the galaxy halo, whilst their GCs are stripped and subsequently join the GCS of the accreting galaxy. In this picture, the blue

[1] This is not to say that the *in-situ* collapse model operates outside the hierarchical scheme, but it does not necessarily require it.

GCs originate from the ongoing stripping of dwarf galaxies, whilst the red GCs are formed early, during the dissipational collapse of the proto-galaxy.

Whilst these latter two models differ in the precise details of which GC subpopulation belongs to which galaxy component, they are actually rather similar; both operate under the premise that large galaxies form from the coalescence of their smaller brethren.

In recent years, 'semi-analytic' models of galaxy formation have been enjoying much success in calculating the formation and subsequent evolution of galaxies in hierarchical clustering cosmologies (e.g. White & Rees 1978; Blumenthal et al. 1984; Kauffmann, White, & Guiderdoni 1993; Cole et al. 1994; Cole et al. 2000). Such models calculate galaxy formation *ab initio*; they model the behaviour of gas and stars beginning with the spectrum of primordial density fluctuations to the present day, using physically motivated analytic recipes. The dominant (by mass) dark matter component is dealt with by either direct N-body simulations, or by a Monte Carlo approach to hierarchical merging.

It is, therefore, perhaps a natural question to ask *what do semi-analytic models predict for the GCS of these galaxies?* We have begun to try and answer this question, and present a few first results here. A somewhat more quantitative treatment will be forthcoming.

The semi-analytic model we use in this study is GALFORM (Cole et al. 1994; Cole et al. 2000). Since this is a complex model, we refer the reader to Cole et al. (2000) for a full description, and Baugh et al. (1998) for an example of its application in interpreting observational data. Briefly, from an initial power-spectrum of density fluctuations described by a given set of cosmological parameters, dark matter halos are formed, and galaxies form within these halos. These halos then coalesce in 'merger trees', and the future of their associated galaxies is governed by the dynamical friction time-scale acting in these halos. If long, the galaxies will continue to orbit within the halo, if short the galaxy will infall and merge with the central dominant galaxy. We show such a merger tree in Figure 5.1. The figure shows the evolution of small galaxies within a dark matter halo, which merge over time (the y-axis is redshift) to create a present-day massive elliptical. The width of the branches reflects the mass of the galaxy at a given epoch, in the case of Figure 5.1, this elliptical galaxy has undergone several fairly significant mergers, and numerous minor ones.

In the semi-analytic scheme, the behaviour of many processes are calculated; the angular momentum and density profiles of the dark matter halos, the cooling of gas and formation of disks, 'passive' star formation in disks, violent star formation in bursts, feedback from supernovae

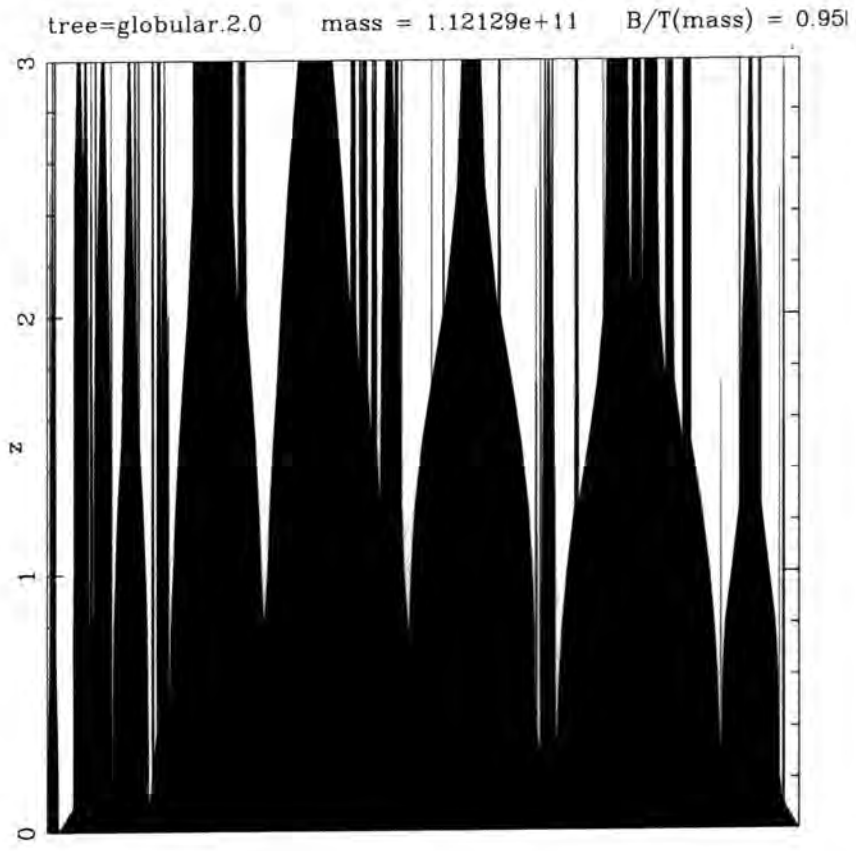

Figure 5.1: Merger tree for an elliptical galaxy of mass $\sim 1.1 \times 10^{11}$ $M_{\odot}$. The width of the 'branch' reflects the mass of the merger product, starting at redshift 3, and running up to the present day.

and the re-heating of gas, dynamical friction of the galaxies, properties of galactic spheroids and resulting observables predicted by stellar population models.

The GALFORM model used in this present study operates within the ΛCDM cosmology, assuming a mean mass density, $\Omega_0 = 0.3$, cosmological constant, $\Lambda_0 = 0.7$ and Hubble constant, $H_0 = 100\,h\,\mathrm{kms}^{-1}\mathrm{Mpc}^{-1}$ (here, $h = 0.7$). For our purposes the GALFORM machinery is a closed box; for a given halo mass the models run for a Hubble time, star formation proceeds in the cold gas disks of galaxies, some of these galaxies then merge, forming more massive galaxies coupled with bursts of star formation.

Whether or not a starburst occurs during a galaxy merger is determined by the ratio of the mass of the satellite galaxy M_{sat} to the central galaxy, M_{cen}. If $M_{\mathrm{sat}}/M_{\mathrm{cen}} \geq f_{\mathrm{ellip}}$ then the merger is classified as a 'major burst'. The gas in the disks of the galaxies then form into stars following a prescription for star formation and chemical enrichment. The resultant merger product is an

elliptical galaxy composed of its original stellar content, material from the satellite[2] galaxy, and any newly formed stellar population from the starburst. If $M_{\rm sat}/M_{\rm cen} < f_{\rm ellip}$, then no burst of star formation occurs, and the stellar content of the central galaxy and satellite merge into the final elliptical, whilst any residual cold gas is accreted to the gas disk of the resulting galaxy. For these models we adopt $f_{\rm ellip} = 0.3$, determined by the morphological mix for $L\star$ galaxies (Cole et al. 2000). Selecting lower values results in a higher proportion of bulge-dominated galaxies in a given halo.

In making a GCS from the SFHs produced by GALFORM, we make several simplifying assumptions, since we wish to keep the complexity of the model to a minimum. Our principle assumption is that one GC subpopulation (turning out to be the red GCs) is formed during gas-rich mergers of disk galaxies, whilst the blue population is associated with the progenitor spiral galaxies. Both these populations then go to make up the resulting GCS of the merger product. For the rest of this discussion, we will refer to the red GCs as 'burst' GCs, and the blue GCs as 'disk' GCs, thereby avoiding the implicit assumption that the GC subpopulations belong to a certain mode. We emphasize that when we say 'disk' GCs, this does *not* to mean that they end up in gas disks (i.e. of spirals), but that they were formed in these structures.

A key parameter in the model is the formation efficiencies of the burst and disk GCs. By efficiency, we mean the fraction of GCs formed relative to the *stars*, we currently do not consider the hot, X-ray gas associated with the elliptical galaxies (e.g. McLaughlin 1999). Several workers have argued for a 'universal' efficiency of GC formation (e.g. di Fazio & Capuzzo Dolcetta 1987; McLaughlin & Pudritz 1996; Harris 1999; McLaughlin 1999), whilst other studies indicate that star and GC formation efficiency in starbursts and interactions may be significantly higher than the in the 'quiescent' mode (e.g. Elmegreen & Efremov 1997; e.g. **?** 1998; Zepf et al. 1999; Rownd & Young 1999). Suffice to say, the exact nature of GC formation and their relative formation efficiencies in different environments is still poorly understood (e.g. Elmegreen & Efremov 1997; Larsen & Richtler 1999).

In the semi-analytic models, the majority of star formation occurs in disks rather than bursts (e.g. Kauffmann 1996; Cole et al. 2000). If we were to adopt a universal efficiency for GCs, then in all cases the disk GCs would dominate (by mass) the burst GCs, by about a factor of $\sim$ 4–7, dependent upon the merger history of the parent galaxy.

[2] Although the term 'satellite' is used, this could be an equal mass merger.

Therefore, we have chosen to normalize the numbers of GCs to those observed in the prototypical (and well studied) bimodal GCS of NGC 4472. This galaxy has some 3600 blue GCs and 2400 red GCs (Geisler, Lee, & Kim 1996), giving $N_{\rm blue}/N_{\rm red} = 1.5$. Moreover, we have chosen to calculate absolute numbers of GCs rather than consider their observed luminosity function, and adopt a mean GC mass corresponding to that of the Milky Way GCs of $\sim 3.0 \times 10^5 {\rm M}_\odot$ (from the McMaster catalogue of Harris 1996). Having several galaxies in our 'sample' with a similar luminosity to NGC 4472 ($M_V \sim$ -22.7), all with roughly the same numbers and proportions of burst:disk GCs, we scale these numbers until they match those observed in NGC 4472. This then yields efficiencies (ϵ) for the burst and disk GCs. For our adopted mean GC mass, we obtain $\epsilon_{\rm burst} = 0.0035$ and $\epsilon_{\rm disk} = 0.001$, i.e. the burst GCs are a factor of 3.5 more efficient at forming than their disk counterparts. These efficiencies imply that in bursts, 1 GC will be formed for every 8.8 $\times 10^7$ M$_\odot$ of stars formed, whilst in disks, 3.5 $\times 10^8$ M$_\odot$ masses of stars are required to form a GC. These efficiencies bracket the universal value found by McLaughlin (1999) of $\epsilon = 0.0026 \pm 0.0005$.

We neglect the effects of dynamical evolution and destruction of the GCs, which can also be significant (e.g. Aguilar, Hut, & Ostriker 1988; Ostriker & Gnedin 1997). We note that whilst the absolute numbers of GCs *will* be affected (and perhaps the blue:red ratio), the common turn-over in the GCLF across all galaxy morphologies indicates that the mass spectrum of GCs is relatively robust to this process (Ostriker & Gnedin 1997),

At some level, the line between 'mergers' and 'accretions' becomes blurred, and is perhaps governed by the amount of gas available to form stars. In spirit, our model is closely associated with the Ashman & Zepf picture, however a key difference is that we assume the GCs associated with the progenitor spirals form *passively* in the disks of these galaxies. This may seem an odd assumption at first; there are no young massive star clusters (YMCs) seen forming in the disk of the Milky Way. However, YMCs are seen to form in spiral galaxies which show *no* signs of recent mergers or interactions (e.g. Christian & Schommer 1988; Bresolin, Kennicutt, & Stetson 1996), and perhaps the Milky Way is unusual in this respect. From a survey of 21 nearby spiral galaxies, Larsen & Richtler (1999) found that the majority of seemingly 'normal' spirals possessed YMCs, many comparable in mass to the most luminous GCs seen in the Milky Way. Furthermore, it is worth noting that much of the star formation in the Ashman & Zepf picture is expected to occur at look-back times where the dominant mode of star formation in disks is still not well understood (e.g. Gallagher 1999).

With these assumptions, we construct the elliptical galaxies' GCS as follows: for a given halo, GALFORM outputs SFHs for stars formed both in disks and in bursts, predicting stellar mass, hot gas mass, cold gas mass, metallicities and look-back times. To form the blue GCs, we simply take a fraction of the cumulative total of stars formed in disks, dictated by the GC formation efficiency and mean GC mass. This yields age and metallicity distributions for the metal-poor GCs which are a reflection of the star formation of the disk-formed stellar component. Then, for each major merger, red GCs are created providing that a high enough mass of stars are formed in the burst. These nascent GCs are assigned ages and metallicities corresponding to the age and metallicity of the burst. Since each burst is instantaneous, the metallicity distributions of red GCs form a series of δ-functions, separated by the time of each burst. We convert the ages and metallicities of each GC into observable quantities, such as $V-I$ and $V-K$ using SSP models, in this case those of Kurth, Fritze-v. Alvensleben, & Fricke (1999). Finally, the colours of the GCS are assigned photometric errors typically achievable for the colour indices used, for instance for $V-I$ we adopt $\sigma_{V-I} = 0.05$ mag.

We show our results for a typical bright elliptical galaxy, with $M_V = -22.63$, in Figure 5.2, and a 'low-luminosity' elliptical ($M_V = -20.32$) in Figure 5.3.

Inspection of the age histogram in Figure 5.2 reveals that all the bursts in this galaxy happened fairly quickly, yielding burst GCs with mean ages of $\sim$ 12 Gyr. This is actually a generic prediction of semi-analytic models of hierarchical galaxy formation, where the most massive halos collapse at relatively early times (Cole et al. 2000). The bulk of the disk GCs also form early; some 80% may be considered 'coeval' with their burst counterparts. However, the rate of formation of the disk GCs shows an exponential-like decay, with a non-negligible number of GCs forming until relatively recently ($\sim$ 4 Gyr). This is an important prediction; if this picture is correct then a small fraction of disk-formed GCs in ellipticals will be detectably young.

The metallicity distributions for the burst and disk GCs shows that their enrichment histories are distinctly different. The disk GCs show a very broad distribution, spanning over two decades in metal abundance with -2.0 $\leq$ [Fe/H] $\leq$ 0. The peak of this distribution occurs at $\sim$ -0.8, and its position remains fairly constant over our entire range of galaxy luminosities. In contrast, the burst GCs are somewhat more sharply peaked in metallicity. In the case of this galaxy, they have a mean metallicity just below solar values. We find that for this galaxy, $N_{\rm burst}/N_{\rm disk} \simeq 1$.

Significantly, both the 'observed' $V-I$ and $V-K$ colour histograms of the total GCS appear bimodal in Figure 5.2, a point we return to shortly.

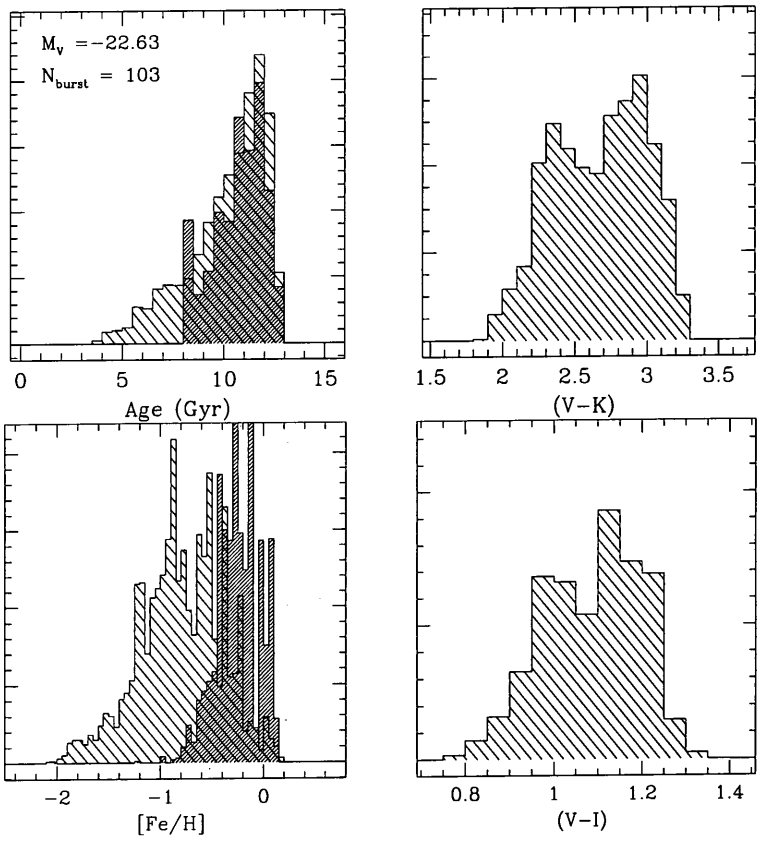

Figure 5.2: Age, metallicity and colour distributions for the GCS of an elliptical with $M_V = -22.63$. In the left-hand panels, the disk GCs are represented by the lightly shaded histograms, the burst GCs formed during major mergers are represented by the dark histograms. Top left : age distribution of the GCS (in Gyr), bottom left : metallicity distribution of the GCS, top right $V - K$ colours of the resultant GCS, bottom right : $V - I$ colours of the resultant GCS (see text). N_{burst} refers to the total number of major mergers experienced by this galaxy, in this case 103.

The low-luminosity elliptical GCS (Figure 5.3) shows a somewhat different story. The metallicities of the disk GCs do not extend to the low metallicities seen in Figure 5.2, which is largely due to the overall reduced GC numbers. The metallicities of the bursts show a spread ($\sim$ 0.5 dex), with no obvious peak, arising principly from the large variation in age of the bursts. The burst GCs are formed in four clearly distinct epochs. In $V - I$ the GCs look unimodal, and indeed the KMM test points towards a unimodal distribution. However, this arises due to a combination of the small numbers of burst GCs, and the existence of very young burst GCs, which pull the mean $V - I$ colours to the blue.

Our entire sample of simulated galaxies span a magnitude range of -23.3 $\geq M_V \geq$ -19.5, with 550 galaxies in total. Surprisingly, we find that the *majority* of the galaxies appear to have broad or

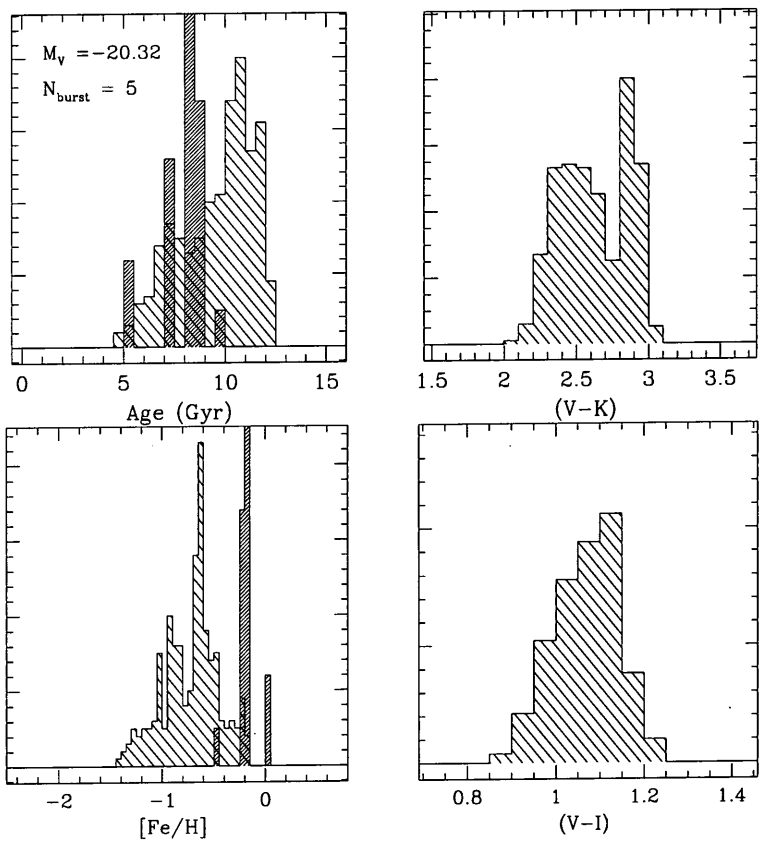

Figure 5.3: Age, metallicity and colour distributions for the GCS of a 'low luminosity' elliptical with $M_V = -20.32$.

bimodal colour distributions. By using the KMM test, with 95% as the lower confidence level, we find that more than 90% indeed exhibit bimodality in $V-I$ with mean peaks at 1.03 and 1.21, with mean metallicities of -0.86 and -0.11 for the disk and burst GCs respectively. The surprising result is that nearly all the galaxies have bimodal GCS *regardless of the luminosity of the parent galaxy.* This result is in stark disagreement with the notion that 'low-luminosity' ellipticals have narrow, unimodal distributions, which has been used as a principle argument against these galaxies being formed in mergers (Kissler-Patig, Forbes, & Minniti 1998). Our results are consistent with the recent study of Kundu (1999). He found evidence for bimodality in the GCS of his elliptical galaxy sample for all parent galaxy luminosities, and subsequently stated *'...this is a fairly important discovery which has significant implications on the formation models.'* Clearly more investigation is required in this very interesting result.

In Figure 5.4 we show the predicted specific frequencies for our galaxy sample, separated into burst and disk GC components. For our adopted efficiencies, we find that the mean S_N of the burst

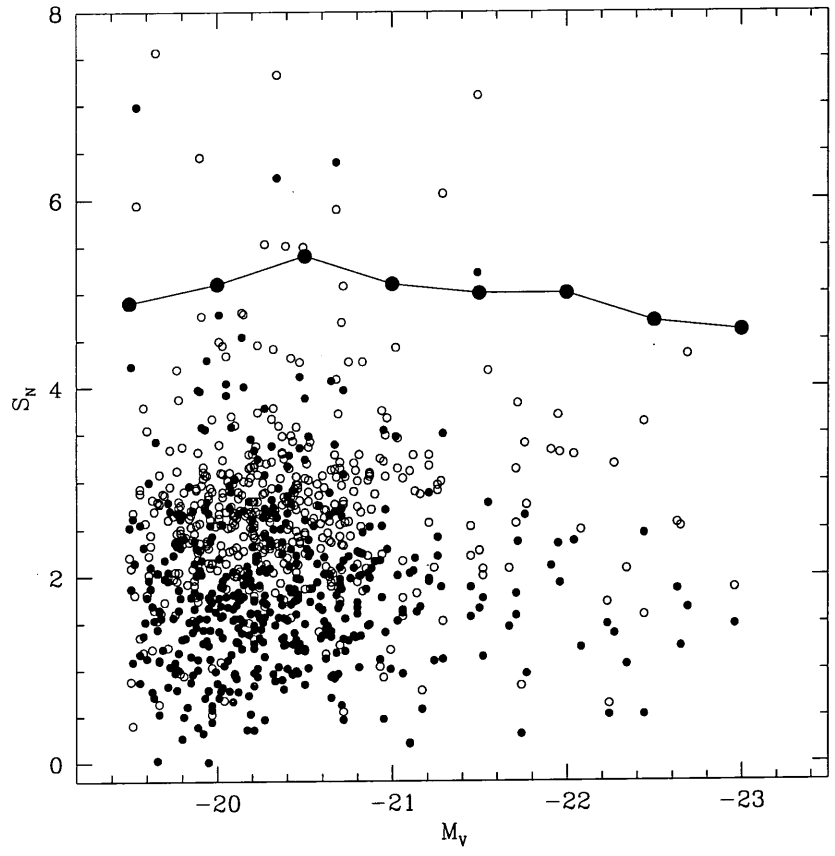

Figure 5.4: Specific frequencies of the disk (open circles) GCs and burst (filled circles) GCs. The mean specific frequencies of the combined GCs are shown by the large filled connected circles.

GCs is ~ 2, and for the disk GCs, $S_N \sim 3$. This gives a total mean S_N of ~ 5 for all galaxy luminosities. This specific frequency of the GCS is in general agreement with the average value found for bright ellipticals of $\sim$ 3–5 (Ashman & Zepf 1998). However, this is not particularly surprising, since we based our GC formation efficiencies upon the observed GCS of NGC 4472 with $S_N = 5.6 \pm 1.7$ (Geisler, Lee, & Kim 1996). We note that the scatter in S_N is large at all magnitudes, although in contrast to the observed trend, seems to decrease slightly with magnitude (Harris 1999). However, we have very few of the brightest ellipticals in our sample for comparison, since these BCGs are rare (both in the GALFORM models and in the Universe). The fact that the mean S_N shown Figure 5.4 is flat, indicates that a constant number of GCs are formed per unit starlight and arises because our GC formation efficiency is defined purely with respect to the mass of stars formed.

GALFORM does not explicitly predict morphologies of the resulting galaxies, but rather gives a ratio of bulge to disk luminosity (B/T). This ratio is known to correlate (with some scatter) with

morphological type. For this study, we have selected galaxies with $B/T \geq 0.6$, corresponding to 'elliptical' galaxies.

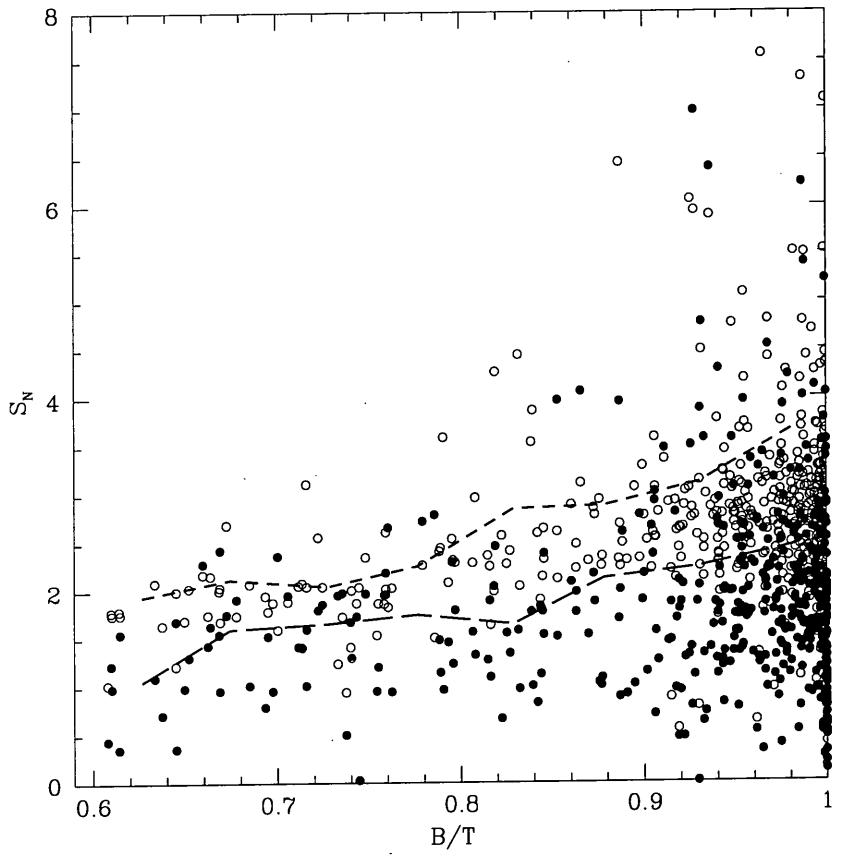

Figure 5.5: Specific frequency plotted against bulge to disk ratio. Open circles represent disk GCs, filled circles are for the burst GCs. The short and long dashed lines show the mean S_N for the disk and burst GC respectively.

We plot the S_N of our GCS against B/T in Figure 5.5. We find that the specific frequency increases noticeably with increasing B/T ratio. This implies that the more 'bulge-dominated' ellipticals tend to produce more GCs for their starlight than their more 'disky' counterparts. In the GALFORM model, bright ellipticals are formed during nearly equal-mass mergers of disk galaxies. However, spheroids also arise from multiple accretions of smaller, gas-poor galaxies which have their stellar content completely deposited into the bulge component of the accreting galaxy. The correlation seen in Figure 5.5 therefore implies that galaxies which have undergone many mergers (e.g. cluster ellipticals) generally have higher S_N than 'field' ellipticals. A future avenue of investigation is whether this extends to lenticular ($B/T \sim 0.5$) and spiral galaxies ($B/T < 0.5$).

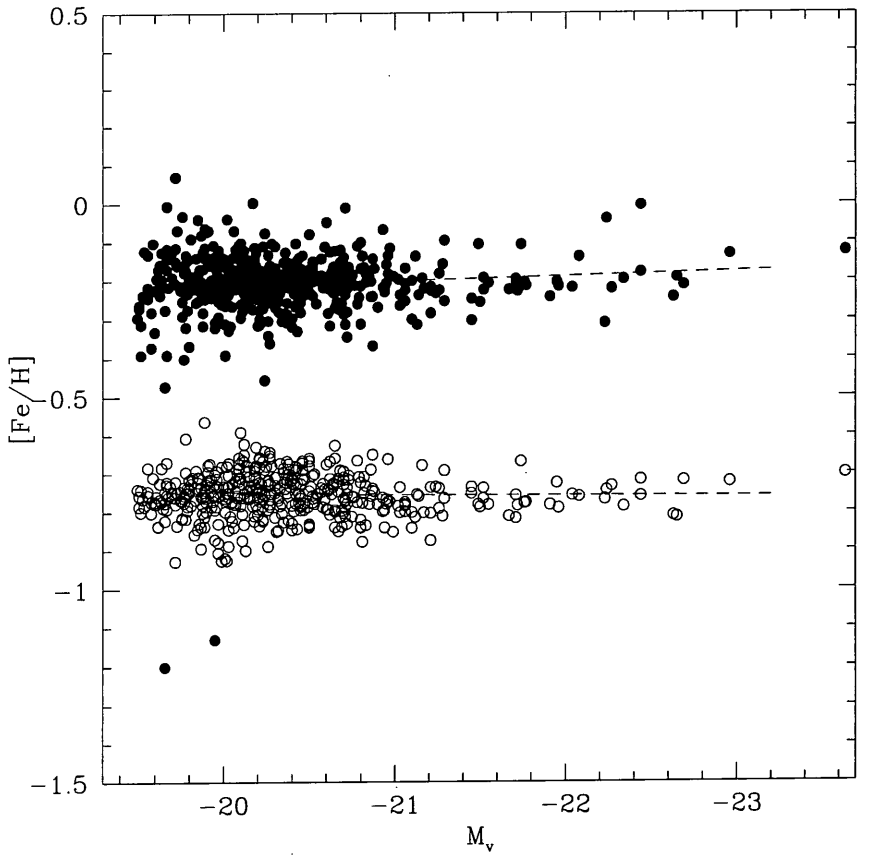

Figure 5.6: The relation between the mean metallicities of the GCS and luminosity of the host galaxy. The burst GCs are indicated by filled circles and the disk GCs are indicated by open circles. The dashed lines indicate a least-squares fit to these data.

Before bringing this brief look at the models to an end, we show one more interesting result in Figure 5.6. Here, we plot the mean metallicity of the burst and disk GCs against the luminosity of their parent galaxy. We find that the distributions of the disk GCs *and* burst GCs are completely flat. The disk GCs show a reasonably tight relation, with $\sigma \sim 0.06$ dex, whilst the burst GCs exhibit larger scatter ($\sigma \sim 0.1$ dex) at all magnitudes. A flat [Fe/H]-M_V relation for the burst (red) GCs is at odds with the findings of Forbes, Brodie, & Grillmair (1997) and Forbes & Forte (2000). These authors found that, whilst the blue GCs showed no correlation, the mean metallicity of the red GCs in bimodal GCS correlated with the luminosity of the host galaxy, in the sense that brighter ellipticals have increasingly metal-rich, red GCs. These authors found a slope for [Fe/H]-M_V corresponding to approximately -0.2 dex. Again, we note that our results are consistent those of Kundu (1999) who found no significant trend in his sample (see discussion in § 1.4.2).

We find no correlation in the burst or disk GCs, however the mean metallicity of the combined GCS is known to increase with increasing galaxy luminosity (e.g. Brodie & Huchra 1991; Durrell et al. 1996; Forbes et al. 1996). The only way in which our data could reproduce this trend is if the *ratio* of disk to burst GCs changes with a slope corresponding to approximately $Z \propto L^{0.4}$ (Brodie & Huchra 1991), i.e. the number of burst GCs must increase more rapidly than disk GCs with increasing galaxy luminosity. However, despite the fact that our burst GCs are a factor of 3.5 more efficient at forming with respect to the field stars than the disk GCs, the ratio of the burst to disk GCs essentially remains constant. We therefore currently find no correlation between the mean metallicity of the entire GCS and the luminosity of the host galaxy.

In summary; from our models, we find that we can reproduce the bimodal colour distributions of GCS associated with elliptical galaxies rather well. Moreover, we find that galaxies of *all* luminosities should generally contain bimodal GCS, reflecting bimodal metallicity distributions. However, a small number ($\sim 5\%$) will appear unimodal since their ages and metallicities 'conspire' to look single-peaked in broad-band colours. We find no dependence of the mean metallicity of either the red or blue GCs on host galaxy luminosity, and any Z-L relation for GCS must originate from a changing ratio of blue:red GCs which is currently not reproduced by the models.

Clearly, the results presented here are dependent upon several unknowns, particularly with regards to the formation efficiencies of burst and disk GCs (and, indeed, *if* true GCs form in disks at all.) However by making simple assumptions, we conclude that the semi-analytic models of galaxy formation are a powerful way of probing the formation history of GCS, a technique which will be extensively developed in the future.

5.1.4 Integrated Spectra of the LMC Clusters

In Chapter 4 we derived ages and metallicities from the integrated spectra of 64 star clusters in the LMC, using the stellar population models of Worthey (1994) and Kurth, Fritze-v. Alvensleben, & Fricke (1999). We compared these data with ages and metallicities in the literature obtained from CMDs, spectroscopy and Strömgren photometry.

We find that in general, agreement between metallicities is very good, and we achieve a mean uncertainty in the metallicities of the clusters of ~ 0.22 dex. However, we do find that in the mean our data is 0.15 dex more metal-rich than the literature values. This offset is driven by the metal-poor clusters, for which the stellar population models systematically under-predict their metallicities; an offset which increased with decreasing metallicity. We see no evidence for a

systematic under-prediction of ages for these clusters, which would yield higher metallicities, and conclude that this cannot be the origin of this difference.

Our ages for the clusters, derived using the two-dimensional plane of Hβ–metal index, are also consistent with the literature values, although the older star clusters ($\tau > 1$ Gyr) show somewhat better agreement than the very youngest clusters. Besides the very obvious emission in some of the youngest clusters and contribution from possible stochastic effects, it seems that perhaps the Kurth, Fritze-v. Alvensleben, & Fricke (1999) models are not well constrained in the $\tau \sim 1$ Gyr, [Fe/H] ≤ -0.3 region of the grids. The lack of young, metal-poor empirical calibrators has long been recognised (e.g. Rabin 1982; Worthey 1994; Idiart & Pacheco 1995), and was a reason why Worthey (1994) did not cover this region of parameter space.[3] With large, homogeneous libraries of star clusters such as those obtained in this thesis, we may attempt to redress the balance.

There are still many uncertainties in the input physics of stellar models, such as the relative importance of diffusion in stars, atmospheric opacities, α-element enhancement and diffusion (e.g. Cassisi et al. 1999). However, as discussed by Maraston & Greggio (1999) and Maraston & Thomas (2000), the principle uncertainty in deriving ages for largely metal-poor GCs lies in the Balmer indices. Depending upon the adopted assumptions about the behaviour of the HB phase, different SSP models predict differences in Hβ of up to ~ 1.5 Å at low metallicities; one model's old stellar population maybe another's young population. Until such discrepancies are resolved, deriving even *relative* ages for GCs in the low-metallicity régime using SSP models carries considerable uncertainty

Despite these modelling uncertainties, we find the agreement for the ages of the LMC *globular* clusters in our sample particularly satisfying, since we used the Worthey models in Chapter 3 to derive ages for the NGC 4472 GCs. This consistency between the predictions of the SSP models and the literature is a good indication that to first order at least, the assumptions about the HB contribution to the Hβ index is correct.

In the previous Section, we discussed a model whereby the GCS of a galaxy forms hierarchically. One prediction was that significant age variations in the GCS of elliptical galaxies should be present. If we wish to test these predictions, how may we proceed?

Broadband colours such as $V - I$, or the more sensitive $B - I$ and $C - T_1$, have proven themselves as accurate measures of metallicity in old stellar systems. However, for un-resolvable

[3] Coupled with the fact that elliptical galaxies have much higher metallicities.

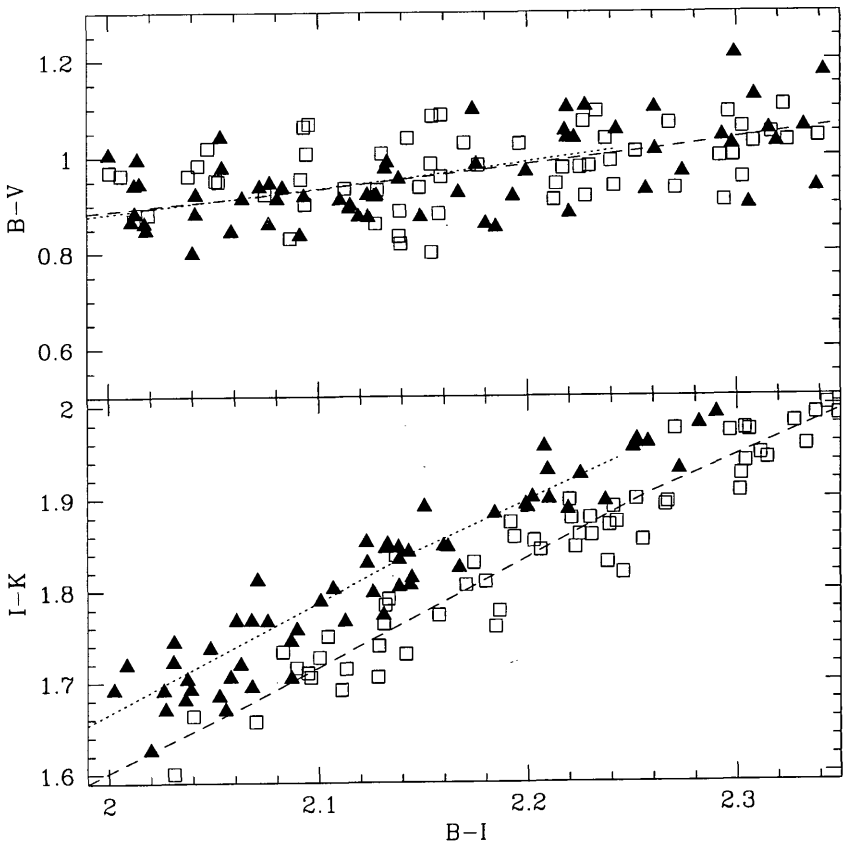

Figure 5.7: The predicted $B-V$, $B-I$ and $I-K$, $B-I$ colours for a subset of NGC 4472 GCs (Geisler, Lee, & Kim 1996), using the stellar population models of Vazdekis (in preparation). Solid triangles represent the red ($C-T_1 \geq 1.625$) GCs, assigned an age of 10 Gyr, open squares represent the blue GCs, with an assumed age of 15 Gyr. We have included a representative observational scatter of 0.05 mag in the colours. The top panel highlights the degeneracy between age and metallicity in optical broadband colours, whereas the inclusion of the K-band (lower panel) can distinguish between the ages of the two GC populations. Dashed and dotted lines indicate the 15 Gyr and 10 Gyr isochrones of the models respectively.

extragalactic GCS, spectroscopy is the only way of unambiguously identifying *bona fide* GCs on the basis of their radial velocities. Moreover, in addition to estimating ages for these GCs from Balmer indices, spectroscopy is the only way of investigating possible α-element enhancement in the GCs.

However, building up statistically significant samples of high S/N spectra for GCs is time consuming, even in the era of 8 and 10-metre class telescopes. An alternative route towards disentangling the ages and metallicities for GCs is through the use of two colour photometry, with the inclusion of an infrared passband (Kissler-Patig 2000). Since SSP models of broadband optical

colours are effectively degenerate in age and metallicity, isochrones in these models are largely superposed upon lines of constant metallicity. However, a colour such as $I - K$ directly measures the temperature of the RGB in evolved stellar populations, which is dependent almost entirely on metallicity. By constructing a plane of metallicity sensitive colour against an age/metallicity sensitive colour allows the extraction of age information, providing high enough photometric accuracies can be achieved.

In Figure 5.7 we illustrate the effect of including the K-band in two-colour SSP model predictions. We have taken a subset of $\sim$ 300 NGC 4472 GCs from the catalogue of Geisler, Lee, & Kim (1996), and have assigned the blue GCs an age of 15 Gyr, and the red GCs an age of 10 Gyr. We then plot the predictions of the SSP models of Vazdekis (in preparation) for the $B - V$, $B - I$ and $I - K$, $B - I$ planes at these ages and metallicities. We have included an 'observational' uncertainty of 0.05 mag in the colour indices. The optical colours are clearly degenerate, but the inclusion of the K-band provides a powerful discriminant between age and metallicity.

The absolute magnitude of the turn-over in the GCLF occurs at M_K = -9.9, at the distance of the Virgo cluster, this corresponds to $K \sim 21.1$. In order to sample a significant fraction of the GCS in a Virgo elliptical, with maximum uncertainties of $\sim$ 0.05 mag, will require integrations of $\sim$ 5 hours on an 8-metre class telescope. Including off-source sky exposures, this implies an entire nights' observing. Whilst this is clearly quite an observational overhead, the scientific returns for such a project would be high.

Appendix A

Contamination in the M 49 Sample

Table A.1. Foreground stars and background galaxies near NGC 4472 identified in MOS spectra.

ID	RA (1950.0)	DEC (1950.0)	V_{helio} ($km\,s^{-1}$)	Object
4415	12 27 09.108	08 16 36.67	45000	Galaxy
2597	12 27 12.905	08 14 34.16	20000	Galaxy
2431	12 27 19.222	08 14 20.44	14800	Galaxy
1746	12 26 47.590	08 13 22.50	222	Star
2430	12 27 03.464	08 14 20.37	-60	Star
7790	12 26 47.971	08 20 34.73	11334	Galaxy
8113	12 27 06.929	08 21 02.14	10982	Galaxy
7569	12 27 35.790	08 20 16.31	10706	Galaxy
7039	12 27 43.904	08 19 34.18	34686	Galaxy
8062	12 27 30.612	08 20 58.75	83	Star
9103	12 27 36.561	08 22 35.62	224	Star
3900	12 27 16.980	08 16 00.03	10600	Galaxy
3217	12 27 36.547	08 15 16.30	28868	Galaxy
1922	12 27 37.078	08 13 36.65	32278	Galaxy
1024	12 27 14.180	08 12 12.53	200	Star
1621	12 27 27.575	08 13 11.02	159	Star
2935	12 27 40.190	08 14 57.60	133	Star
1955	12 27 11.629	08 13 39.38	31000	Galaxy
8224	12 27 17.371	08 21 11.44	11700	Galaxy
6302	12 27 33.741	08 18 38.24	12000	Galaxy

References

Abbreviations

MNRAS; Monthly Notices of the Royal Astronomical Society

ApJ; The Astrophysical Journal

ApJ Lett.; The Astrophysical Journal Letters

ApJS; The Astrophysical Journal Supplement

AJ; The Astronomical Journal

AAP; Astronomy & Astrophysics

ARA&A; Annual Review of Astronomy & Astrophysics

References

Aaronson M., Cohen J. G., Mould J., Malkan M., 1978, ApJ, 223, 824

Ables H. D., Newell E. B., O'Neil E. J., 1974, P.A.S.P., 86, 311

Aguilar L., Hut P., Ostriker J. P., 1988, ApJ, 335, 720

Ajhar E. A., Blakeslee J. P., Tonry J. L., 1994, AJ, 108, 2087

Alcaino G., Liller W., 1984, AJ, 89, 814

Alvarez H., Aparici J., May J., 1987, AAP, 176, 25

Armandroff T. E., 1988, in Bulletin of the American Astronomical Society, Vol. 20, p. 708

Arp H., 1961, Science, 134, 810

Ashman K. A., Bird C. M., Zepf S. E., 1994, AJ, 108, 2348

Ashman K. M., Bird C. M., 1993, in American Astronomical Society Meeting, Vol. 183, p. 7415

Ashman K. M., Zepf S. E., 1992, ApJ, 384, 50

Ashman K. M., Zepf S. E., 1998, "Globular cluster systems". Globular cluster systems / Keith M. Ashman, Stephen E. Zepf. Cambridge, U. K. ; New York : Cambridge University Press, 1998. (Cambridge astrophysics series ; 30) QB853.5 .A84 1998 ($69.95)

Baade W., 1951, Publ. Obs. Univ. of Michigan, 10, 7

Barbaro C., Bertelli C., 1977, AAP, 54, 243

Barbaro G., Poggianti B. M., 1997, AAP, 324, 490

Barbuy B., 1994, ApJ, 430, 218

Barmby P., Huchra J. P., Brodie J. P., Forbes D. A., Schroder L. L., Grillmair C. J., 2000, AJ, 119, 727

Baugh C. M., Cole S., Frenk C. S., Lacey C. G., 1998, ApJ, 498, 504

Baum W. A., 1955, P.A.S.P., 67, 328

Beard S. M., MacGillivray H. T., Thanisch P. F., 1990, MNRAS, 247, 311

Bertelli G., Mateo M., Chiosi C., Bressan A., 1992, ApJ, 388, 400

Bessell M. S., Scholz M., 1989, in IAU Colloq. 106: Evolution of Peculiar Red Giant Stars, p. 67

Bhatia R. K., Read M. A., Tritton S., Hatzidimitriou D., 1991, AAPS, 87, 335

Bica E., Claria J. J., Dottori H., 1992, AJ, 103, 1859

Bica E., Claria J. J., Dottori H., Santos J. F. C., Piatti A. E., 1996, ApJS, 102, 57

Bica E., Dottori H., Santos J. F. C., Claria J. J., Piatti A., 1991, ApJ Lett., 381, L51

Bica E., Geisler D., Dottori H., Clariá J. J., Piatti A. ., Santos. J. . C., 1998, AJ, 116, 723

Bica E. L. D., Schmitt H. R., 1995, ApJS, 101, 41

Bica E. L. D., Schmitt H. R., Dutra C. M., Oliveira H. L., 1999, AJ, 117, 238

Binney J., Merrifield M., 1998, Galactic astronomy. Galactic astronomy / James Binney and Michael Merrifield. Princeton, NJ : Princeton University Press, 1998. (Princeton series in astrophysics) QB857 .B522 1998 ($35.00)

Binney J., Tremaine S., 1987, Galactic dynamics. Princeton, NJ, Princeton University Press, 1987, 747 p.

Blakeslee J. P., Tonry J. L., Metzger M. R., 1997, AJ, 114, 482

Blecha A., 1986, AAP, 154, 321

Blumenthal G. R., Faber S. M., Primack J. R., Rees M. J., 1984, Nature, 311, 517

Bolte M., 1989, AJ, 97, 1688

Bomans D. J., Vallenari A., de Boer K. S., 1995, AAP, 298, 427

Borges A. C., Idiart T. P., de Freitas Pacheco J. A., Thevenin F., 1995, AJ, 110, 2408

Bothun G. D., Harris H. C., Hesser J. E., 1992, P.A.S.P., 104, 1220

Bothun G. D., Thompson I. B., 1988, AJ, 96, 877

Bresolin F., Kennicutt R. C., Stetson P. B., 1996, AJ, 112, 1009

Bressan A., Chiosi C., Tantalo R., 1996, AAP, 311, 425

Bridges T. J., Ashman K. M., Zepf S. E., Carter D., Hanes D. A., Sharples R. M., Kavelaars J. J., 1997, MNRAS, 284, 376

Bright J., Olsen K., 2000, in American Astronomical Society Meeting, Vol. 196, p. 2805

Brocato E., Castellani V., Ferraro F. R., Piersimoni A. M., Testa V., 1996, MNRAS, 282, 614

Brodie J. P., Huchra J. P., 1990, ApJ, 362, 503

Brodie J. P., Huchra J. P., 1991, ApJ, 379, 157

Buonanno R., 1993, in ASP Conf. Ser. 48: The Globular Cluster-Galaxy Connection, p. 131

Buonanno R., Corsi C. E., Castellani M., Marconi G., Fusi Pecci F., Zinn R., 1999, AJ, 118, 1671

Buonanno R., Corsi C. E., Pulone L., Fusi Pecci F., Bellazzini M., 1998a, AAP, 333, 505

Buonanno R., Corsi C. E., Zinn R., Fusi Pecci F., Hardy E., Suntzeff N. B., 1998b, ApJ Lett., 501, L33

Burgarella D., Kissler-Patig M., Buat V., 2000, in ASP Conf. Ser. 211: Massive Stellar Clusters, p. 288

Burstein D., Faber S. M., Gaskell C. M., Krumm N., 1984, ApJ, 287, 586

Burstein D., Faber S. M., Gonzalez J. J., 1986, AJ, 91, 1130

Butcher H., 1977, ApJ, 216, 372

Buzzoni A., 1995, ApJS, 98, 69

Cannon A. J., 1929, Bull. Harvard Coll. Obs., 868

Cardiel N., Gorgas J., Cenarro J., Gonzalez J. J., 1998, AAPS, 127, 597

Carlberg R. G., 1984, ApJ, 286, 403

Carlson M. N. et al., 1999, AJ, 117, 1700

Carretta E., Gratton R. G., 1997, AAPS, 121, 95

Carretta E., Gratton R. G., Clementini G., Fusi Pecci F., 2000, ApJ, 533, 215

Cassisi S., Castellani V., degl'Innocenti S., Salaris M., Weiss A., 1999, AAPS, 134, 103

Castellani V., degl'Innocenti S., 1999, AAP, 344, 97

Catelan M., de Freitas Pacheco J. A., 1993, AJ, 106, 1858

Chiosi C., Bertelli G., Bressan A., 1988, AAP, 196, 84

Christian C. A., Schommer R. A., 1988, AJ, 95, 704

Cohen J. G., 1982, ApJ Lett., 260, L45

Cohen J. G., 1988, AJ, 95, 682

Cohen J. G., 2000, AJ, 119, 162

Cohen J. G., Blakeslee J. P., Ryzhov A., 1998, ApJ, 496, 808

Cohen J. G., Ryzhov A., 1997, ApJ, 486, 230

Cole S., Aragon-Salamanca A., Frenk C. S., Navarro J. F., Zepf S. E., 1994, MNRAS, 271, 781

Cole S., Lacey C. G., Baugh C. M., Frenk C. S., 2000, MNRAS, 319, 168

Copetti M. V. F., Pastoriza M. G., Dottori H. A., 1986, AAP, 156, 111

Corsi C. E., Buonanno R., Fusi Pecci F., Ferraro F. R., Testa V., Greggio L., 1994, MNRAS, 271, 385

Cote P., Marzke R. O., West M. J., 1998, ApJ, 501, 554

Couture J., Harris W. E., Allwright J. W. B., 1990, ApJS, 73, 671

Couture J., Harris W. E., Allwright J. W. B., 1991, ApJ, 372, 97

Cowley A. P., Hartwick F. D. A., 1982, ApJ, 259, 89

Da Costa G. S., 1991, in IAU Symp. 148: The Magellanic Clouds, Vol. 148, p. 183

Da Costa G. S., Graham J. A., 1982, ApJ, 261, 70

Da Costa G. S., Hatzidimitriou D., 1998, AJ, 115, 1934

Danziger I. J., 1973, ApJ, 181, 641

Davidge T. J., 2000, ApJS, 126, 105

Davies R. L., Sadler E. M., Peletier R. F., 1993, MNRAS, 262, 650

de Freitas Pacheco J. A., Barbuy B., Idiart T., 1998, AAP, 332, 19

de Vaucouleurs G., 1970, ApJ, 159, 435

de Vaucouleurs G., 1975, ApJ, 202, 319

de Vaucouleurs G., de Vaucouleurs A., Corwin J. R., Buta R. J., Paturel G., Fouque P., 1991, in Third reference catalogue of bright galaxies (1991), p. 0

de Vaucouleurs G., Freeman K. C., 1972, Vistas in Astronomy, 14, 163

di Fazio A., Capuzzo Dolcetta R., 1987, AAP, 184, 263

Dickens R. J., Croke B. F. W., Cannon R. D., Bell R. A., 1991, Nature, 351, 212

Dirsch B., Richtler T., Gieren W. P., Hilker M., 2000, astro-ph/0004009, 15, 10

Dolphin A. E., Hunter D. A., 1998, AJ, 116, 1275

Dopita M. A. et al., 1997, ApJ, 474, 188

Dressler A., Gunn J. E., 1982, ApJ, 263, 533

Durrell P. R., Harris W. E., Geisler D., Pudritz R. E., 1996, AJ, 112, 972

Edvardsson B., Andersen J., Gustafsson B., Lambert D. L., Nissen P. E., Tomkin J., 1993, AAP, 275, 101

Eggen O. J., Lynden-Bell D., Sandage A. R., 1962, ApJ, 136, 748

Elmegreen B. G., Efremov Y. N., 1997, ApJ, 480, 235

Elmegreen B. G., Efremov Y. N., Larsen S. ., 2000, ApJ, 535, 748

Elson R. A., Fall S. M., 1988, AJ, 96, 1383

Elson R. A. W., Gilmore G. F., Santiago B. X., 1997, MNRAS, 289, 157

Elson R. A. W., Grillmair C. J., Forbes D. A., Rabban M., Williger G. M., Brodie J. P., 1998, MNRAS, 295, 240

Elson R. A. W., Santiago B. X., 1996, MNRAS, 278, 617

Elson R. A. W., Santiago B. X., Gilmore G. F., 1996, New Astronomy, 1, 1

Faber S. M., 1972, AAP, 20, 361

Faber S. M., Friel E. D., Burstein D., Gaskell C. M., 1985, ApJS, 57, 711

Faber S. M., Gallagher J. S., 1979, ARA&A, 17, 135

Faber S. M., Worthey G., Gonzales J. J., 1992, in IAU Symp. 149: The Stellar Populations of Galaxies, Vol. 149, p. 255

Fagotto F., Bressan A., Bertelli G., Chiosi C., 1994, AAPS, 105, 39

Feast M. W., Catchpole R. M., 1997, MNRAS, 286, L1

Ferrarese L. et al., 1996, ApJ, 464, 568

Fischer P., Hesser J. E., Harris H. C., Bothun G. D., 1990, P.A.S.P., 102, 5

Fisher D., Franx M., Illingworth G., 1995, ApJ, 448, 119

Fluks M. A., Plez B., The P. S., de Winter D., Westerlund B. E., Steenman H. C., 1994, AAPS, 105, 311

Forbes D. A., 1996, AJ, 112, 1409

Forbes D. A., Brodie J. P., Grillmair C. J., 1997, AJ, 113, 1652

Forbes D. A., Brodie J. P., Huchra J., 1997, AJ, 113, 887

Forbes D. A., Forte J. . C., 2000, astro-ph/0005481

Forbes D. A., Franx M., Illingworth G. D., Carollo C. M., 1996, ApJ, 467, 126

Forbes D. A., Grillmair C. J., Williger G. M., Elson R. A. W., Brodie J. P., 1998, MNRAS, 293, 325

Forbes D. A., Hau G. K. T., 2000, MNRAS, 312, 703

Forte J. C., Strom S. E., Strom K. M., 1981, ApJ Lett., 245, L9

Freeman K. C., Illingworth G., Oemler A., 1983, ApJ, 272, 488

Frenk C. S., Fall S. M., 1982a, MNRAS, 199, 565

Frenk C. S., Fall S. M., 1982b, MNRAS, 199, 565

Freytag B., Salaris M., 1999, ApJ Lett., 513, L49

Gallagher J. S., 1999, in American Astronomical Society Meeting, Vol. 195, p. 6702

Gascoigne S. C. B., 1962, in IAU Symp. 15: Problems of Extra-Galactic Research, Vol. 15, p. 49

Gebhardt K., Kissler-Patig M., 1999, AJ, 118, 1526

Geha M. C. et al., 1998, AJ, 115, 1045

Geisler D., Bica E., Dottori H., Claria J. J., Piatti A. E., Santos J. F. C., 1997, AJ, 114, 1920

Geisler D., Forte J. C., 1990, ApJ Lett., 350, L5

Geisler D., Lee M. G., Kim E., 1996, AJ, 111, 1529

Gelatt A. E., Hunter D. A., Gallagher J. S., 2000, astro-ph/0010515

Girardi L., Bica E., 1993, AAP, 274, 279

Girardi L., Chiosi C., Bertelli G., Bressan A., 1995, AAP, 298, 87

Goodwin S. P., 1997, MNRAS, 286, L39

Gorgas J., Faber S. M., Burstein D., Gonzalez J. J., Courteau S., Prosser C., 1993, ApJS, 86, 153

Goudfrooij P., Emsellem E., 1996, AAP, 306, L45

Goudfrooij P., Mack J., Kissler-Patig M., Meylan G., Minniti D., 2000, astro-ph/0010275

Graham J. A., 1982, ApJ, 252, 474

Green E. M., Demarque P., King C. R., 1987, "The revised Yale isochrones and luminosity functions". The revised Yale isochrones and luminosity functions, New Haven: Yale Observatory, 1987

Grillmair C. J., Forbes D. A., Brodie J. P., Elson R. A. W., 1999, AJ, 117, 167

Grillmair C. J., Freeman K. C., Bicknell G. V., Carter D., Couch W. J., Sommer-Larsen J., Taylor K., 1994, ApJ Lett., 422, L9

Hanes D. A., 1976, Ph.D. thesis, UNIVERSITY OF TORONTO (CANADA).

Hanes D. A., 1977a, MNRAS, 179, 331

Hanes D. A., 1977b, MNRAS, 180, 309

Hanes D. A., 1979, MNRAS, 188, 901

Hanes D. A., Brodie J. F., 1980, in IAU Symp. 85: Star Formation, Vol. 85, p. 451

Hanes D. A., Brodie J. P., 1986, ApJ, 300, 279

Hanes D. A., Grieve G. R., 1982, MNRAS, 198, 193

Harris G. L. H., Geisler D., Harris H. C., Hesser J. E., 1992, AJ, 104, 613

Harris G. L. H., Poole G. B., Harris W. E., 1998, AJ, 116, 2866

Harris H. C., Canterna R., 1977, AJ, 82, 798

Harris H. C., Harris G. L. H., Hesser J. E., 1988, in IAU Symp. 126: The Harlow-Shapley Symposium on Globular Cluster Systems in Galaxies, Vol. 126, p. 205

Harris H. C., Harris G. L. H., Hesser J. E., MacGillivray H. T., 1984, ApJ, 287, 185

Harris W. E., 1974, Ph.D. thesis, UNIVERSITY OF TORONTO (CANADA).

Harris W. E., 1986, AJ, 91, 822

Harris W. E., 1991, ARA&A, 29, 543

Harris W. E., 1996, AJ, 112, 1487

Harris W. E., 1999, "Saas-Fee Advanced Course on Star Clusters". Saas-Fee Advanced Course on Star Clusters / William E. Harris, Swiss Society for Astrophysics and Astronomy, Springer, in press.

Harris W. E., Smith M. G., 1976, ApJ, 207, 1036

Harris W. E., van den Bergh S., 1981, AJ, 86, 1627

Hartwick F. D. A., Sargent W. L. W., 1978, ApJ, 221, 512

Heggie D. C., Hut P., 1996, in IAU Symp. 174: Dynamical Evolution of Star Clusters: Confrontation of Theory and Observations, Vol. 174, p. 303

Henize K. G., Aller L. H., Doherty L., 1953, AJ, 58, 215

Henry R. B. C., Worthey G., 1999, P.A.S.P., 111, 919

Hernquist L., 1993, ApJ, 409, 548

Hesser J. E., McClure R. D., Harris W. E., 1984, in IAU Symposia, Vol. 108, p. 47

Hilker M., 1998, Ph.D. thesis, Sternw. Bonn, (1998)

Hodge P., 1988, P.A.S.P., 100, 1051

Hodge P. W., 1960, ApJ, 131, 351

Hodge P. W., Dolphin A. E., Smith T. R., Mateo M., 1999, ApJ, 521, 577

Hodge P. W., Sexton J. A., 1966, AJ, 71, 363

Holland S., 1998, P.A.S.P., 110, 759

Holtzman J. A. et al., 1992, AJ, 103, 691

Holtzman J. A. et al., 1997, AJ, 113, 656

Horne K., 1986, P.A.S.P., 98, 609

Hubble E., 1932, ApJ, 76, 44

Huchra J. P., Kent S. M., Brodie J. P., 1991, ApJ, 370, 495

Idiart T. P., Pacheco J. A. D., 1995, AJ, 109, 2218

Irwin J. A., Sarazin C. L., 1996, ApJ, 471, 683

Jasniewicz G., Thevenin F., 1994, AAP, 282, 717

Johnson J. A., Bolte M., 1996, in American Astronomical Society Meeting, Vol. 189, p. 7118

Jorgensen I., 1997, MNRAS, 288, 161

Kaluzny J., Stanek K. Z., Krockenberger M., Sasselov D. D., Tonry J. L., Mateo M., 1998, AJ, 115, 1016

Kauffmann G., 1996, MNRAS, 281, 487

Kauffmann G., White S. D. M., Guiderdoni B., 1993, MNRAS, 264, 201

Kennicutt R. C., 1992, ApJ, 388, 310

Kim E., Lee M. G., Geisler D., 2000, MNRAS, 314, 307

Kim S., 1998, in American Astronomical Society Meeting, Vol. 193, p. 2803

King I. R., 1966, AJ, 71, 64

Kissler-Patig M., 1997, AAP, 319, 83

Kissler-Patig M., 2000, in ASP Conf. Ser. 211: Massive Stellar Clusters, p. 157

Kissler-Patig M., Ashman K. M., Zepf S. E., Freeman K. C., 1999, AJ, 118, 197

Kissler-Patig M., Brodie J. P., Schroder L. L., Forbes D. A., Grillmair C. J., Huchra J. P., 1998, AJ, 115, 105

Kissler-Patig M., Forbes D. A., Minniti D., 1998, MNRAS, 298, 1123

Kissler-Patig M., Gebhardt K., 1998, AJ, 116, 2237

Kobayashi C., Arimoto N., 1999, ApJ, 527, 573

Kontizas M., Morgan D. H., Hatzidimitriou D., Kontizas E., 1990, AAPS, 84, 527

Korista K. T. et al., 1995, ApJS, 97, 285

Kormendy J. et al., 1996, in IAU Symp. 171: New Light on Galaxy Evolution, Vol. 171, p. 105

Kundu A., 1999, Ph.D. thesis, UNIVERSITY OF MARYLAND COLLEGE PARK

Kundu A., Whitmore B. C., Sparks W. B., Macchetto F. D., Zepf S. E., Ashman K. M., 1999, ApJ, 513, 733

Kuntschner H., 1998, Ph.D. thesis, University of Durham, Department of Physics, South Road, Durham DH1 3LE

Kuntschner H., Davies R. L., 1998, MNRAS, 295, L29

Kurth O. M., Fritze-v. Alvensleben U., Fricke K. J., 1999, AAPS, 138, 19

Kurucz R. L., 1979, ApJS, 40, 1

Langer G. E., Fischer D., Sneden C., Bolte M., 1998, AJ, 115, 685

Larsen S., Richtler T., 1998, Astronomische Gesellschaft Meeting Abstracts, Abstracts of Contributed Talks and Posters presented at the Annual Scientific Meeting of the Astronomische Gesellschaft at Heidelberg, September 14–19, 1998, poster #P82, 14, 82

Larsen S. S., Richtler T., 1999, AAP, 345, 59

Larson R. B., 1974, MNRAS, 166, 585

Lauberts A., 1982, "ESO/Uppsala survey of the ESO(B) atlas". Garching: European Southern Observatory (ESO), 1982

Lee H., Yoon S., Lee Y., 2000, AJ, 120, 998

Lee M. G., Geisler D., 1993, AJ, 106, 493

Lee M. G., Kim E., 2000, AJ, 120, 260

Lee M. G., Kim E., Geisler D., 1998, AJ, 115, 947

Leitherer C. et al., 1996, P.A.S.P., 108, 996

Lejeune T., Cuisinier F., Buser R., 1997, AAPS, 125, 229

Liller W., Alcaino G., 1983b, ApJ, 265, 166

Liller W., Alcaino G., 1983a, ApJ, 264, 53

Lindsay E. M., Mullan D. J., 1963, Irish Astronomical Journal, 6, 51

Loxen J., 1997, Ph.D. thesis, Ph.D thesis Universität Göttingen, (1997)

Lucke P. B., 1974, ApJS, 28, 73

Lutz D., 1991, AAP, 245, 31

MacGillivray H. T., Stobie R. S., 1984, Vistas in Astronomy, 27, 433

Maraston C., Greggio L., 1999, in ASP Conf. Ser. 192: Spectrophotometric Dating of Stars and Galaxies, p. 295

Maraston C., Thomas D., 2000, ApJ, 541, 126

Martinez-Roger C., Perez-Fournon I., Sanchez F., ed, 1999, Globular clusters : X Canary Islands Winter School of Astrophysics

Mateo M., 1996, in ASP Conf. Ser. 92: Formation of the Galactic Halo...Inside and Out, p. 434

Mayall N. U., 1946, ApJ, 104, 290

McLaughlin D. E., 1999, AJ, 117, 2398

McLaughlin D. E., Harris W. E., Hanes D. A., 1994, ApJ, 422, 486

McLaughlin D. E., Pudritz R. E., 1996, ApJ, 457, 578

McNamara D., 1997, P.A.S.P., 109, 1221

Meylan G., Heggie D. C., 1997, A&AR, 8, 1

Mighell K. J., Rich R. M., Shara M., Fall S. M., 1996, AJ, 111, 2314

Morgan D. H., Watson F. G., Parker Q. A., 1992, AAPS, 93, 495

Mould J. R., Oke J. B., de Zeeuw P. T., Nemec J. M., 1990, AJ, 99, 1823

Neilsen E. H., Tsvetanov Z. I., 1999, ApJ Lett., 515, L13

O'Connell R. W., 1976, ApJ, 206, 370

Olsen K. A. G., Hodge P. W., Mateo M., Olszewski E. W., Schommer R. A., Suntzeff N. B., Walker A. R., 1998, MNRAS, 300, 665

Olszewski E. W., 1988, in IAU Symp. 126: The Harlow-Shapley Symposium on Globular Cluster Systems in Galaxies, Vol. 126, p. 159

Olszewski E. W., Schommer R. A., Suntzeff N. B., Harris H. C., 1991, AJ, 101, 515

Olszewski E. W., Suntzeff N. B., Mateo M., 1996, ARA&A, 34, 511

Osterbrock D. E., 1989, "Astrophysics of gaseous nebulae and active galactic nuclei". Research supported by the University of California, John Simon Guggenheim Memorial Foundation, University of Minnesota, et al. Mill Valley, CA, University Science Books, 1989, 422 p.

Ostriker J. P., Gnedin O. Y., 1997, ApJ, 487, 667

Ostrov P., Geisler D., Forte J. C., 1993, AJ, 105, 1762

Pagel B. E. J., Tautvaisiene G., 1998, MNRAS, 299, 535

Parker Q. A., Watson F. G., 1995, "FLAIR Handbook. Part 1: User Guide". AAO UM (User Manual), Epping: Anglo-Australian Observatory (AAO), —c1995, Version 1.0, November 1995

Parry I., Sharples R. M., 1988, in ASP Conf. Ser. 3: Fiber Optics in Astronomy, p. 93

Pecci F. F. et al., 1996, AJ, 112, 1461

Peebles P. J. E., Dicke R. H., 1968, ApJ, 154, 891

Pence W. D., 1980, ApJ, 239, 54

Perelmuter J., Brodie J. P., Huchra J. P., 1995, AJ, 110, 620

Peterson C. J., King I. R., 1975, AJ, 80, 427

Puche D., Carignan C., 1988, AJ, 95, 1025

Puche D., Carignan C., van Gorkom J. H., 1991, AJ, 101, 456

Puche D., Carignan C., Wainscoat R. J., 1991, AJ, 101, 447

Puzia T. H., Kissler-Patig M., Brodie J. P., Huchra J. P., 1999, AJ, 118, 2734

Puzia T. H., Kissler-Patig M., Brodie J. P., Schroder L. L., 2000, AJ, 120, 777

Rabin D., 1982, ApJ, 261, 85

Racine R. ., 1968, P.A.S.P., 80, 326

Racine R., 1980, in IAU Symp. 85: Star Formation, Vol. 85, p. 369

Racine R., Oke J. B., Searle L., 1978, ApJ, 223, 82

Reed B. C., Hesser J. E., Shawl S. J., 1988, P.A.S.P., 100, 545

Reimers D., 1975, Memoires of the Societe Royale des Sciences de Liege, 8, 369

Rhode K., Zepf S. E., 2000, AJ, astro-ph/0010065

Rich R. M., 1988, AJ, 95, 828

Robertson J. G., 1986, P.A.S.P., 98, 1220

Robinson L. B., Wampler E. J., 1972, P.A.S.P., 84, 161

Rosenblatt E. I., Faber S. M., Blumenthal G. R., 1988, ApJ, 330, 191

Rownd B. K., Young J. S., 1999, AJ, 118, 670

Sagar R., Richtler T., de Boer K. S., 1991, AAPS, 90, 387

Salaris M., Groenewegen M. A. T., Weiss A., 2000, AAP, 355, 299

Sandage A., 1968, ApJ Lett., 152, L149

Sandage A., Tammann G. A., 1981, A revised Shapley-Ames Catalog of bright galaxies. Washington: Carnegie Institution, 1981, Preliminary version

Sandage A., Wallerstein G., 1960, ApJ, 131, 598

Sarajedini A., 1994, AJ, 107, 618

Sarajedini A., Geisler D., Harding P., Schommer R., 1998, ApJ Lett., 508, L37

Schommer R. A., Christian C. A., Caldwell N., Bothun G. D., Huchra J., 1991, AJ, 101, 873

Schweizer F., 1982, ApJ, 252, 455

Schweizer F., 1987, in Nearly Normal Galaxies. From the Planck Time to the Present, p. 18

Schweizer F. ., Seitzer P., 1998, AJ, 116, 2206

Schweizer F., Miller B. W., Whitmore B. C., Fall S. M., 1996, AJ, 112, 1839

Searle L., 1984, in IAU Symposia, Vol. 108, p. 13

Searle L., Wilkinson A., Bagnuolo W. G., 1980, ApJ, 239, 803

Searle L., Zinn R., 1978, ApJ, 225, 357

Secker J., Geisler D., McLaughlin D. E., Harris W. E., 1995, AJ, 109, 1019

Shapley H., 1951, Publ. Obs. Univ. of Michigan, 10, 79

Shapley H., 1957, "The inner metagalaxy". New Haven: Yale University Press, 1957

Shapley H., Lindsay E. M., 1963, Irish Astronomical Journal, 6, 74

Shara M. M., Fall S. M., Rich R. M., Zurek D., 1998, ApJ, 508, 570

Sharples R., 1988, in IAU Symp. 126: The Harlow-Shapley Symposium on Globular Cluster Systems in Galaxies, Vol. 126, p. 545

Sharples R. M., Zepf S. E., Bridges T. J., Hanes D. A., Carter D., Ashman K. M., Geisler D., 1998, AJ, 115, 2337

Smith M. G., Weedmann D. W., 1976, ApJ, 205, 709

Strom S. E., Strom K. M., Wells D. C., Forte J. C., Smith M. G., Harris W. E., 1981, ApJ, 245, 416

Suntzeff N. B., Schommer R. A., Olszewski E. W., Walker A. R., 1992, AJ, 104, 1743

Tantalo R., Chiosi C., Bressan A., 1998, AAP, 333, 419

Tantalo R., Chiosi C., Bressan A., Fagotto F., 1996, AAP, 311, 361

Taylor J. R., 1982, "An introduction to error analysis. The study of uncertainties in physical measurements". A Series of Books in Physics, Oxford: University Press, and Mill Valley: University Science Books, 1982

Tonry J., Davis M., 1979, AJ, 84, 1511

Toomre A., 1977, "Evolution of Galaxies and Stellar Populations". eds., B.M. Tinsley and R.B.Larson,New Haven:Yale University Observatory, p.401

Trager S. C., 1997, Ph.D. thesis, UNIVERSITY OF CALIFORNIA, SANTA CRUZ

Trager S. C., King I. R., Djorgovski S., 1995, AJ, 109, 218

Trager S. C., Worthey G., Faber S. M., Burstein D., Gonzalez J. J., 1998, ApJS, 116, 1

Tripicco M. J., Bell R. A., 1995, AJ, 110, 3035

Vallenari A., Aparicio A., Fagotto F., Chiosi C., Ortolani S., Meylan G., 1994, AAP, 284, 447

Vallenari A., Chiosi C., Bertelli G., Aparicio A., Ortolani S., 1996, AAP, 309, 367

van den Bergh S., 1975, ARA&A, 13, 217

van den Bergh S., 1981, AAPS, 46, 79

Vandenberg D. A., 1985, ApJS, 58, 711

Vandenberg D. A., Bell R. A., 1985, ApJS, 58, 561

Vandenberg D. A., Laskarides P. G., 1987, ApJS, 64, 103

Vandenberg D. A., Stetson P. B., Bolte M., 1996, ARA&A, 34, 461

Vazdekis A., Casuso E., Peletier R. F., Beckman J. E., 1996, ApJS, 106, 307

Walker A. R., 1990, AJ, 100, 1532

Walker A. R., 1992, ApJ Lett., 390, L81

Warren W. H., Sturch C. R., Lasker B. M., Jahreiss H., Luyten W. J., 1989, AJ, 97, 1480

Watson A. M. et al., 1996, AJ, 112, 534

West M. J., 1993, MNRAS, 265, 755

Westerlund B. E., 1997, The Magellanic Clouds

Westerlund B. E., Linde P., Lynga G., 1995, AAP, 298, 39

White R. E., Shawl S. J., 1987, ApJ, 317, 246

White S. D. M., Rees M. J., 1978, MNRAS, 183, 341

Whitmore B. C., Schweizer F., 1995, AJ, 109, 960

Worthey G., 1993, ApJ Lett., 415, L91

Worthey G., 1994, ApJS, 95, 107

Worthey G., Faber S. M., Gonzalez J. J., 1992, ApJ, 398, 69

Worthey G., Faber S. M., Gonzalez J. J., Burstein D., 1994, ApJS, 94, 687

Worthey G., Ottaviani D. L., 1997, ApJS, 111, 377

Wyse R. F. G., Gilmore G., 1992, MNRAS, 257, 1

Zepf S. E., Ashman K. M., 1993, MNRAS, 264, 611

Zepf S. E., Ashman K. M., English J., Freeman K. C., Sharples R. M., 1999, AJ, 118, 752

Zepf S. E., Ashman K. M., Geisler D., 1995, ApJ, 443, 570

Zepf S. E., Beasley M. A., Bridges T. . J., Hanes D. A., Sharples R. M., Ashman K. M., Geisler D., 2000, AJ, in press

Zinn R., 1985, ApJ, 293, 424

Zinn R., West M. J., 1984, ApJS, 55, 45